Optical imaging of dopamine dynamics and decoding its role in arousal and salience

Thesis by

Jounhong Ryan Cho

In Partial Fulfillment of the Requirements for

the degree of

Doctor of Philosophy

CALIFORNIA INSTITUTE OF TECHNOLOGY

Pasadena, California

2019

Defended May 23, 2019

Jounhong Ryan Cho
ORCID: 0000-0001-9542-716X

ACKNOWLEDGEMENTS

I would like to begin by thanking my wonderful advisor, Professor Viviana Gradinaru. Viviana has been a truly exceptional mentor throughout my doctoral training. Ever since I started my rotation project in her lab, I knew that this was the place to be. She has helped promote my development as an independent thinker and researcher by letting me pursue my own ideas and guiding me through the right path. I have always admired the fact that her office door is always open and she is passionate and happy to discuss data with us, although we all know that she has lots of other important things to do: she has always put her lab members and our science as utmost priority. I truly feel blessed to work with her as she has always provided me with invaluable advice, unlimited resource to pursue science, and positive lab environments. She also had my back when I was going through rough patches, and I am sincerely grateful for her support. She has set up a standard as a successful scientist and exemplar leader that I would like to follow, and I believe my PhD experience with her will take me many steps closer to that goal.

I would like to thank my committee members for their support and guidance throughout my PhD training as well: Professors Thanos Siapas, David Anderson, and Yuki Oka, who are in my PhD defense committee, and Professors Richard Andersen, Markus Meister, and David Prober, who served in my oral qualification and candidacy committees. I would like to specifically mention Thanos and David, as their courses in systems neuroscience have really taught me how to critically read papers and think like a scientist. It goes without saying that they are lauded scientists who stand up as examples to follow for young people like me. They were always willing to discuss my projects and give me guidance to solve problems and

move things forward. I would like to thank Professor Daniel Wagenaar as well: it would not have been possible to pursue my interest in single cell imaging in vivo without his help.

For early career scientists, it is so important to meet talented and exemplar senior scientists who can teach and guide you on the right path. In this regard, I feel very fortunate to have worked with and been trained by wonderful senior scientists in Viviana's lab, including Drs. Jennifer Treweek, Lindsay Bremner, and Cheng Xiao. Jenny and Lindsay taught me almost all of the experimental skills that I needed to work in this lab. Without them, I would not even be interested in studying dopamine at all. Cheng was a perfect example of a hard-working, dedicated scientist, and I enjoyed working with him on the cholinergic PPN project.

I would like to thank Professor Lin Tian and Dr. Tommaso Patriarchi in UC Davis for giving me the opportunity to work with them on the dopamine sensor project. I still remember the excitement when I first saw fluctuating dopamine signals from their sensor in freely moving mice – ever since, we have worked together to design experiments and analyze data (thank you Slack!), eventually with unexpectedly great success. I am fortunate to have met these wonderful scientists, and I hope I can keep working with them to make more interesting discoveries about dopamine.

Obtaining one's PhD is a long process and often involves ups and downs, so it would not be easy to go through all of those without friends and companions who know and understand the process. For that, I would like to specifically mention Ken Chan and Nick Flytzanis in Viviana's lab. They were second year graduate students when I first joined Viviana's lab,

who welcomed me with their warm hearts. We had a great time inside and outside of the lab, and I am proud that I am the one who introduced interesting Korean culture to them. I would like to thank Claire Bedbrook, Alon Greenbaum, Priya Kumar, Xinhong Chen, Ben Deverman, and Michael Altermatt, who have always been there when I needed them.

I am also thankful to Drs. Elliott Robinson and Anat Kahan, who are fellow systems neuroscientists in the lab. We have always had fun building tools and writing MATLAB codes together to share, and our loud discussions on data and papers were always enjoyable. I also want to thank Elisha Mackey and Pat Anguiano, who are wonderful lab managers: nothing in the lab would be possible without these two invaluable people. I am of course grateful to all past and present lab members for making my time here delightful: this includes Min Jee Jang, Collin and Rose Challis, Nick Goedon, Xiaozhe Ding, Gerry Coughlin, David Brown, Tatyana Dobreva, Miggy Chuapoco, Acacia Hori, and Bin Yang.

I would regret if I did not mention my fellow CNS students: Vinny Augustine, Gabi Tavares, Janis Hesse, Mason McGill, and Juri Minxha. They were my first friends since I arrived in Caltech, and our friendship over the years is really something that I cherish and hope to continue for the future as well. To me, our CNS parties are still the best ones I have ever had here in LA. I am happy to see that all of them have blossomed to great scientists now, and that they have or are ready to move on to the next chapter of their lives. I also want to mention my Korean fellow neuroscientists at Caltech, who we call “K-neuros”; Kyu Hyun Lee, Sangjun Lee, Dong-wook Kim, Yonil Jung, Hyung Chan Jo, and Sangjin Yoo for our scientific discussion over bottles of Korean drinks and wine.

In addition, I would like to recognize my previous mentors: Drs. Seung Bong Hong and Eun Yeon Joo from the Samsung Medical Center, Dr. Brian Litt from Penn, Dr. Jee Hyun Choi from KIST, and Drs. Stan Anderson and Piotr Franszczuk from Hopkins, all of whom have guided and helped me to step on the right path for a scientific career.

I am blessed that I have lots of caring friends from Korea, who have given me support across the country and across the Pacific Ocean: Kevin Park, Junhwan Ko, Jaekyung Koh, Myungkyun Kye, Hwarang Kim, Jeehoon Jang, Jaeho Lee, Euisung Baek, Yongsuk Song, Jungmin Ryu, Don Lee, Kihyuk Hong, Eunji Ju, Christina Jeon, Soorin Chung, Hanjoon Lee, and Hyun Shik Yun. They all helped me get through this hard time.

Last but certainly not least, I would like to thank my family. It would not be possible to go through this journey without their caring and support. My dad is always an inspiration for me in his dedication to the family, and he was the reason entering the biomedical field. My mom is always the one who gives me unconditional love and support, no matter what I do and where I am at. My sister is also my biggest supporter and I am so proud that she is having a great career as a doctor. I also would like to thank my aunt, Dr. Sung Nam Cho, who has always been an example of a dedicated scholar and leader in academia.

Thank you all, and I dedicate this thesis to all of you.

ABSTRACT

Dopamine (DA) is a key neuromodulator in the brain that can exert a profound impact on brain physiology and cognitive functions. There is consensus that DA plays critical roles in reward prediction error, reinforcement learning, and motor control, and that dysregulation of DA signaling is common in many neuropsychiatric diseases, such as Parkinson's disease, drug addiction, and depression. Although the tools to study the functional roles of DA have considerably expanded with novel genetic tools and optical imaging methods, we are still limited in our ability to record or visualize DA release in vivo with long-term stability and high spatiotemporal resolution. This is an unmet need in DA research, as DA release at the post-synaptic sites can be decoupled from DA cell body firing due to local circuit interaction and influence from other afferent activities. In parallel, there is growing evidence that DA is functionally heterogeneous beyond its classically described roles for reward and movement, based on its anatomical location, projection target, electrophysiological properties, and response patterns to stimuli with motivational valence. Pharmacological and genetic studies have provided indirect evidence that DA can promote strong behavioral arousal and signal salience, but the precise neural substrates for these functions remain largely unknown. Towards this end, my thesis work has been focused on 1) developing and characterizing optical tools to visualize DA release in vivo and 2) utilizing such optical and genetic tools to study the overlooked, sparse DA populations in the dorsal midbrain, demonstrating that they are functionally unique DA cells for broadcasting arousal and salience signals to the forebrain targets.

As neuromodulatory systems exert profound influences on brain function, understanding how these systems modify the operating mode of target circuits requires spatiotemporally precise measurement of neuromodulator release. Towards this goal, in Chapter II, my colleagues and I developed dLight1, an intensity-based genetically encoded DA indicator, to enable optical recording of DA dynamics with high spatiotemporal resolution in behaving mice. We demonstrated the utility of dLight1 by imaging DA dynamics simultaneously with pharmacological manipulation, electrophysiological or optogenetic stimulation, and calcium imaging of local neuronal activity. dLight1 enabled chronic tracking of learning-induced changes in millisecond DA transients in mouse striatum. Further, we used dLight1 to image spatially distinct, functionally heterogeneous DA transients relevant to learning and motor control in mouse cortex. We also validated our sensor design platform for developing norepinephrine, serotonin, melatonin, and opioid neuropeptide indicators. Together, this tool provides a unique opportunity to optically monitor DA release dynamics in vivo with long-term stability and unprecedented spatiotemporal resolution.

In Chapter III, I have characterized the functional roles of sparse DA populations in the dorsal raphe nucleus (DRN) and discovered that these neurons play key roles in promoting behavioral arousal. I first demonstrated that DRN^{DA} neurons are activated by diverse forms of motivationally salient stimuli, irrespective of valence. Simultaneous fiber photometry and polysomnographic recordings showed that DRN^{DA} neuronal activity is correlated with distinct sleep-wake states, showing highest activities during wakefulness over sleep states. Optogenetic activation of DRN^{DA} neurons was sufficient to cause immediate sleep-to-wake

transitions and promote longer wakefulness upon sustained stimulation. On contrary, DRN^{DA} inhibition via chemogenetics reduced wakefulness and promoted non-rapid eye movement sleep, even in the presence of ethologically relevant salient stimuli. Taken together, this pinpoints DRN^{DA} neurons as the critical contributor of arousal-promoting DA system in the brain.

In Chapter IV, I further characterized the encoding dynamics of DRN^{DA} neurons during classical conditioning tasks where mice learned the association between neutral cues and outcomes with positive or negative outcomes. DRN^{DA} neurons developed phasic, positive responses to cues predicting both positive and negative unconditioned stimuli across learning, suggesting that these populations track motivational salience rather than valence. In addition, DRN^{DA} neurons encoded unsigned prediction error, demonstrating higher neuronal activity to unexpected reward or punishment over fully expected outcomes. Collectively with Chapter III, these results expand on the existing literature on functionally heterogeneous roles of DA in the brain and propose that DRN^{DA} neurons play critical roles in signaling arousal and motivational salience to the forebrain regions to coordinate appropriate behavior, depending on the nature of environmental stimuli.

PUBLISHED CONTENT AND CONTRIBUTIONS

[1] Patriarchi, T. and Cho, J. R. et al. (2018). “Ultrafast neuronal imaging of dopamine dynamics with designed genetically encoded sensors.” In: *Science* 360.6396, pii: eaat4422. doi: 10.1126/science.aat4422.

J.R.C participated in the experimental designs, collected and analyzed in vivo data, prepared relevant figures, and wrote a significant portion of the manuscript as a co-first author.

[2] Cho, J. R. et al. (2017). “Dorsal raphe dopamine neurons modulate arousal and promote wakefulness by salient stimuli.” In: *Neuron* 94.6, pp. 1205-1219.e8. doi: 10.1016/j.neuron.2017.05.020.

J.R.C. designed and performed experiments, collected and analyzed all data, prepared figures, and wrote a manuscript as a first author.

[3] Xiao, C. et al. (2016). “Cholinergic mesopontine signals govern locomotion and reward through dissociable midbrain pathways.” In: *Neuron* 90.2, pp. 334-347. doi: 10.1016/j.neuron.2016.03.028.

J.R.C. designed and performed experiments, and prepared figures.

TABLE OF CONTENTS

Chapter 1

INTRODUCTION

1.1 Dopamine as a neuromodulator

Neurons communicate with each other in electrochemical language, where electrical signals such as action potentials are translated into chemical transmission by releasing neurotransmitters or neuromodulators from synaptic terminals to the post-synaptic targets, which in turn convert into electrical potentials via ion channels or triggers biochemical signaling cascade through G-protein coupled receptors (GPCR). One such media for the neuronal transmission is dopamine (DA), which exerts a profound influence on neural circuit dynamics and behavior.

DA is an organic chemical neurotransmitter within the catecholamine family. It is synthesized in a particular group of neurons in the brain (see Chapter 1.3 for details) and cells in the medulla of the adrenal glands to be used as circulatory hormone. Several metabolic pathways exist for DA synthesis but they all start from L-Phenylalanin, which is converted to L-Tyrosine with biopterin-dependent aromatic amino acid hydroxylase. In the primary pathway, L-Tyrosine is converted to L-DOPA, a precursor of DA, by the rate-limiting enzyme tyrosine hydroxylase. Finally, DA is synthesized from L-DOPA by the enzyme DOPA decarboxylase. DA can be used as an independent neurotransmitter, but at the same time in a subset of catecholamine neurons, it is used as a precursor for

synthesizing another aminergic neurotransmitters norepinephrine with the enzyme dopamine b-hydroxylase.

DA mediates its effects in downstream regions by binding to and activating DA receptors. All DA receptor types are GPCRs, which suggest that they exert their post-synaptic effects through biochemical signal cascade and second messenger system and indirectly influence neuronal excitability. DA receptors are often divided into two subtypes, D1-like and D2-like. The D1-like family consists of D1 and D5 receptors, both of which are G_s-coupled ones to increase the intracellular level of cyclic adenosine monophosphate (cAMP) by activating adenylyl cyclase. In most cases, the ultimate effect of activating D1-like receptors is to increase the excitability of the post-synaptic neurons by diverse mechanisms, including opening of sodium channels. The D2-like family is composed of D2, D3, and D4 receptors, all of which are G_i-coupled to decrease the intracellular level of cAMP by inhibiting adenylyl cyclase. Upon activating D2-like receptors, post-synaptic cells are mostly inhibited, in part through the opening of potassium channels. Therefore, it is not straightforward to describe the post-synaptic action of DA either as excitatory or inhibitory, as it depends on the type of DA receptors expressed in the post-synaptic neurons and the type of GPCR they are coupled to.

DA is synthesized in the cell bodies or axons of dopaminergic neurons, and they are transported to the synaptic vesicles from the cytosol via vesicular monoamine transporter. Synaptic vesicles containing DA molecules can be released into the synaptic cleft either via action potential firing or via activation of intracellular trace amine-associated receptors.

Once DA is released from synaptic terminals, it can bind to post-synaptic DA receptors or pre-synaptic auto-receptors (mostly D2 receptors). After activation, DA can be rapidly unbound from them and absorbed back into the presynaptic cells by the dopamine transporter (DAT). The relative concentration of DAT on axon terminals can dictate the spatiotemporal window of DA action in the post-synaptic circuits: for example, DA axons in the prefrontal cortex show sparse immunoreactivity to DAT (Sesack et al. 1998), unlike the DAT-enriched striatum, therefore showing reduced DA reuptake and longer distance of volume transmission (Cass and Gerhardt, 1995).

There are two modes of DA neuronal firing and subsequent DA release: 1) tonic mode, where DA cells continuously fire in 2-5 Hz like pacemakers, and 2) phasic mode, where DA neurons fire high-frequency bursts, usually not longer than 500 ms (Grace et al., 2007). Tonic firing ensures the consistent release of DA into the post-synaptic targets. Phasic firing of DA neurons rapidly and transiently elevates extracellular DA levels, reaching up to ~100 uM in the striatum, and preferentially activates D1-like receptors with lower affinity (Grace et al., 2007; Dreyer et al., 2010). The interaction between tonic and phasic transmission modes is important in modulating downstream circuit functions, as the post-synaptic effect of phasic firing is dependent on the basal level of dopamine (from tonic firing) within the synaptic environment (Wanat et al., 2009).

Through decades of research, DA has been implicated in a wide range of cognitive function and behavior, such as motor control, reward, motivation, reinforcement, executive function, and arousal. Tools to detect DA release in vivo have also been developed to study

the functional role of DA, and they will be discussed in the following Chapter 1.2. Specific functions of DA signaling mediated by separate sub-groups will be discoursed in the Chapter 1.3. One critical function of DA most relevant to this thesis is its role in promoting behavioral arousal. Systemic change of DA tone in the brain is demonstrated to modulate the level of behavioral arousal. For example, some recreational and addictive drugs such as cocaine or amphetamine cause strong behavioral arousal, in part by increasing extracellular DA concentration through blocking the reuptake action of DAT (Arias-Carrion et al., 2011). Another pharmacological evidence comes from Modafinil, one of the most clinically effective drugs to treat patients with narcolepsy and other sleep disorders, and DAT blocking action contributes to its wake-promoting mechanism (Zolkowska, et al., 2009). In mice, selective knockout of DAT gene reduced non-rapid eye movement sleep and increased wakefulness, arguing for DA's stimulant role in promoting wakefulness (Wisor et al., 2001). Overall, it is well accepted that systemic increase of DA tone in the brain does promote behavioral arousal, but the neural substrate or specific group of DA neurons responsible for its action and its specific encoding properties are not well known.

1.2 Tools for measuring dopamine release in vivo

In order to investigate the functional roles of DA on post-synaptic circuits and behavior, it is critical to detect DA release in vivo. With the recent success of genetically encoded calcium indicator GCaMP family (Chen et al., 2013), Ca^{2+} imaging of dopamine neurons or axons contributed to revealing novel insights on DA dynamics during behavior. For example, fiber photometry and two-photon imaging of GCaMP-expressing DA axons revealed rapid and phasic signaling associated with locomotion in the dorsal striatum, which could be differentiated from separate axons that signal reward (Howe and Dombeck, 2016). In addition, multi-site fiber photometry recording of DA axons revealed heterogeneous responses to reward and punishment depending on projection targets (Kim et al., 2016).

While these type of studies may reveal novel insights on DA *firing or neuronal activity* associated with specific behavior, these findings cannot be directly generalizable to DA *release dynamics* since the relationship between Ca^{2+} dynamics of DA axons (as an indirect measure of DA action potential firing) and actual DA release to post-synaptic targets is nonlinear. Other factors, such as local acetylcholine signaling, autoreceptors, and various neuropeptides, can contribute to DA release in vivo, in addition to DA neuronal firing (Sulzer et al., 2016). Indeed, it was recently shown from simultaneous electrochemical and single-unit recordings that striatal DA release can be decoupled from DA cell firing (Mohebi et al., 2018). Therefore, it is important to have complementary recording techniques to directly measure DA release within a defined target circuit, preferably with high spatiotemporal resolution. There have been a number of existing methods to detect DA release in vivo, such

as microdialysis, fast scan cyclic voltammetry (FSCV), and optical sensors. While they have been widely used to study DA function, each of method suffers from some critical weaknesses.

Microdialysis is a chemical sampling technique that requires the insertion or implantation of a small probe into the tissue of interest. This probe mimics a blood capillary with semi-permeable membrane and has inlet/outlet tubing for allowing the perfusion of aqueous solution, such as artificial cerebrospinal fluid if used in the brain. When the probe is inserted in a tissue, small solutes or molecules can pass through the semi-permeable membrane by passive diffusion, and the concentration of these solutes can be measured and analyzed. Key advantages of microdialysis include easy construction of probes and its versatility. Practically, it can detect any neurotransmitter or neuromodulator of interest, including DA, and is well tolerable in in vivo experiments. The most critical disadvantage, however, is its poor temporal resolution: as it takes minutes to collect enough samples for analysis, concentration of molecules can only be resolved in minute-scale, usually resulting in 10-15 minutes as a single temporal step. This limits the number of compatible behavioral assays that can be paired with microdialysis, since it cannot measure faster component of DA release dynamics. Another disadvantage is that it samples DA (or other molecules of interest) in the extracellular space where the probe is located, and therefore it does not necessarily correlate with its concentration near the post-synaptic targets.

Another prevalent method in measuring DA release is the FSCV, which utilizes the inserted carbon-fiber microelectrodes and oxidization-reduction capabilities of DA depending on

voltage levels. Once the carbon-fiber microelectrode is inserted into the brain region of interest, the potential at the microelectrode is ramped up and down at a high scan rate. When dopamine is oxidized to dopamine-o-quinone, it donates two electrons that can be measured as electrical current. As the potential scan rate is fast enough (~400 V/s), the key strength of this method is its capability to measure DA concentration at millisecond time scale. This is a vital reason that FSCV has been the gold standard to investigate fast DA transients in response to short-lived stimuli or behavioral tasks. However, it also suffers from several limitations. First, similar to microdialysis, the measurement takes place in the extracellular space, and therefore it does not necessarily match with actual DA concentration acting on post-synaptic receptors. Second and more importantly, FSCV cannot differentiate DA from norepinephrine (NE), another catecholamine neurotransmitter, due to its similarity in chemical structures. As NE shows same oxidization-reduction properties as dopamine, the current measured from the microelectrode cannot differentiate the relative contributions from two distinct catecholamine molecules. This has limited the application of FSCV for DA studies only in the striatum, where dense DA projections are existent without NE innervation. Therefore, this method is not feasible to measure DA release dynamics in other areas, such as the cortex where both of DA and NE signaling are present.

Recently, there have been attempts to using optical methods for detecting DA release in vivo. One such tool is CNiFER (cell-based neurotransmitter fluorescent engineered reporters), which utilize the G-protein-coupled receptor (GPCR) and its biochemical pathway to detect DA (Muller et al., 2014). CNiFER is derived from HEK293 cells and expresses chimeric D2 dopamine receptor and TN-XXL, a genetically encoded FRET-based Ca^{2+} sensor. Once DA

binds and activates the GPCR, it triggers signal cascade through the phospholipase C-inositol triphosphate pathway and increases cytosolic Ca^{2+} concentration. This increased Ca^{2+} inside the cell leads to a fluorescent increase in FRET from the TN-XXL. While this method is compatible in vivo and can differentiate DA release from NE action, it is relatively slow (second to minute scale) due to endogenously slow temporal kinetics of GPCR signaling pathway, and the signal-to-noise ratio of FRET sensor is suboptimal. Another recently developed technique to detect DA release in vivo is iTango, a light- and ligand-gated gene expression system (Lee et al., 2017). As iTango expresses reporter gene (such as fluorescent protein) or Cre recombinase depending on the presence of both ligand and blue light, it can visualize or even manipulate cells affected by DA during specific, user-defined temporal window. For example, Lee et al. (2017) labeled striatal cells affected by DA during locomotion (by delivering blue light only during locomotion) and showed that optogenetic activation of these cells in turn triggers locomotion, but not from neurons labeled during reward consumption. Although iTango system allows for visualization or manipulation of cells influenced by DA in a genetically and functionally defined manner, it again suffers from poor temporal resolution, as it cannot report the dynamic DA concentration in real-time.

Current limitations of these existing methods hint at some of desired properties for novel dopamine sensor. First, it is desirable for such system to be based on endogenous dopamine receptors for high specificity over other chemically similar neurotransmitters. Second, it has to have fast kinetics to capture sub-second changes in DA signaling. Third, optical readout methods are preferable to others to quantify DA levels through visualization, potentially at cellular or even sub-cellular level. Finally, this sensor should be expressed in the membrane

in a genetically specific manner in order to measure DA in close proximity to defined post-synaptic cells. In Chapter II, I present dLight1, an intensity-based optical sensor for dopamine based on D1 receptor, to meet such needs for measuring DA release in vivo. My colleagues and I further demonstrate the utility of dLight1 in various settings, from ex vivo slice setups to measuring DA release in freely moving animals, and to monitoring cortical DA dynamics in vivo at the cellular resolution.

1.3 Anatomical and functional heterogeneity of dopamine system

DA has been best known as the neurotransmitter responsible for reinforcement learning, reward-seeking behavior, and motor control, because seminal studies have shown its unique role in encoding reward prediction error (RPE; Schultz et al., 1997). Moreover, dysregulation of the DA pathways is implicated in relevant pathological conditions, such as drug addiction and Parkinson's disease (Volkow et al., 2017; Charvin et al, 2018). However, it is increasingly recognized that DA has more diverse functions beyond reward and movement, and can encode aversion, alertness, arousal, and salience (Bromberg-Martin et al., 2010; Lammel et al., 2014).

Although most of DA studies have focused on the ventral midbrain populations, there is a great degree of anatomical and functional heterogeneity within DA systems in the brain. Dopaminergic populations were first systemically described by Dahlstroem and Fuxe, who labeled monoaminergic neurons starting with the letter A for "aminergic" (Dahlstroem and Fuxe, 1964). In their description, A1-A7 populations denote the groups containing norepinephrine, while A8-A14 groups consist of anatomically segregated DA populations. Substantia nigra pars compacta (SNc or A9) and ventral tegmental area (VTA or A10) are located in the ventral midbrain and the most well-studied DA groups. SNc^{DA} neurons mostly project to the dorsal striatum, terms as "nigrostriatal" pathway, and are known to regulate motor function, action learning, and movement vigor (Groenewegen, 2003; Howe and Dombeck, 2016; da Silva et al., 2018). SNc^{DA} populations are specifically vulnerable to neurodegeneration, and severe loss of these DA neurons can result in motor symptoms of

Parkinson's disease (Charvin et al., 2018). There is evidence for molecular and functional diversity even within the A9 group: for example, SNc^{DA} neurons defined by distinct genetic or molecular markers showed differential vulnerability to Parkinsonian attack (Poulin et al., 2014). In addition, SNc^{DA} neurons in the most lateral side, which uniquely co-express glutamatergic marker (vglut2) and project to the tail of the striatum, were shown to contain little information about movement but to encode the presence of salient or aversive stimuli in order to reinforce avoidance behavior (Poulin et al., 2018; Menegas et al., 2017 and 2018).

VTA^{DA} (A10) populations are another relatively well-studied group in the ventral midbrain, sending projections mainly to the ventral striatum (including the nucleus accumbens) and prefrontal cortex, but also to the amygdala, hippocampus, and olfactory bulb. VTA^{DA} neurons, especially the mesolimbic pathway projecting to the nucleus accumbens (NAc), have been widely recognized for its function in reward-seeking behavior and reinforcement learning, as VTA^{DA} neurons encode reward prediction error (Schultz, 1997; Bromberg-Martin et al., 2010), gate associative learning (Steinberg et al. 2013), and support intracranial self-stimulation through operant conditioning (Witten et al., 2011). Mesolimbic DA pathway is heavily implicated in neural mechanisms of drug addiction, as many drugs for substance use can "hijack" this DA-dependent reward circuitry through maladaptive learning mechanisms (Chen et al., 2010). While the activity profiles of most VTA^{DA} neurons are compatible with its proposed role in positive reinforcement learning and RPE encoding (Schultz et al., 1997; Cohen et al., 2012; Witten et al., 2011), there are some VTA^{DA} neurons described to signal aversion, showing phasic responses to non-rewarding, aversive stimuli (Brischoux et al. 2009; Matsumoto and Hikosaka, 2009). Consistent with this idea, it has

recently been demonstrated by optical recordings that VTA^{DA} terminals in the ventral NAc medial shell are excited by aversive outcomes and their cues (de Jong et al., 2019). Similarly, VTA^{DA} terminals in the mPFC and basolateral amygdala were also excited by aversive events (Kim et al., 2016), suggesting that positive and negative valences may be separately encoded by distinct VTA^{DA} neurons defined by projection targets. This functional diversity within VTA^{DA} subgroups may arise in part from distinct input patterns (Lammel et al., 2012), indicating that complex anatomical connectivity can give rise to divergent functions in a seemingly homogenous population. These studies expand from the reward-centric view of VTA^{DA} neurons and provide novel mechanisms on how they carry distinct diverse information, such as aversion, alertness, or salience, to the forebrain regions (Bromberg-Martin et al., 2010).

Other DA neuronal groups are found in distinct sub-regions within the hypothalamus, but their functional roles are not well known. A11 group in the posterior hypothalamus projects to the spinal cord and may contribute to coordinating limb movements, as its dysfunction is implicated in restless leg syndrome (Paulus and Schomburg, 2006). Small portions of these neurons also project to the inferior colliculus and the auditory brainstem, suggesting its potential role in auditory processing (Nevue et al., 2016). DA neurons in the arcuate and periventricular nucleus of the hypothalamus, or A12 group, consist of the tuberoinfundibular pathway projecting to the pituitary gland and inhibits the release of the hormone prolactin. A subpopulation of this A12 group was recently shown to govern maternal behavior by controlling the level of oxytocin secretion through its projection to

the paraventricular hypothalamus (Scott et al., 2015). The functional property of A13 DA neurons in the zona incerta is not known, as there have not been much of studies on this group, but some anatomical studies demonstrated their projections to diverse regions including basal forebrain, central amygdala and dorsolateral periaqueductal gray (Eaton et al., 1994; Messanvi et al., 2013).

Another poorly characterized DA neuronal population is found within the dorsal raphe nucleus (DRN), a heterogeneous brainstem region that contains diverse neuronal cell types including serotonin, glutamate, GABA, dopamine, and various neuropeptides. Historically, this group was labeled "A10dc", the dorsocaudal extension of A10 VTA group. As it is correct that DRN^{DA} neurons are continuously extended from VTA^{DA} neurons through dorsal and caudal directions, these neurons were often overlooked, and hence their functions were simply assumed to be equivalent as A10 group. However, some of recent studies propose against this notion. For example, A10dc group may be directly involved in regulating sleep-wake states. Whereas the role of ventral midbrain DA neurons in sleep-wake regulation has been ambiguous as these neurons do not change their mean firing rate across different behavioral states (Miller et al., 1983), DA neurons in the DRN and ventral periaqueductal gray were more activated during wake or forced wake period over sleep states, as shown by increased *c-fos* expression (Lu et al., 2006). Further, selective neurotoxic lesion of DRN^{DA} cells, while sparing other neighboring types of cells, resulted in hypersomnia phenotype where rats spent ~20 % more time in sleep during both dark and light cycles, suggesting that their endogenous role may be to promote wakefulness (Lu et al., 2006). Another study characterized DRN^{DA} neurons in the regulation of pain

perception, demonstrating that chemogenetic activation of these neurons mediated supra-spinal anti-nociceptive effect (Li et al., 2016).

A recently study on DRN^{DA} neurons by Matthews and colleagues unraveled novel ideas about physiology, anatomical connectivity and function of these neurons (Matthews et al, 2016). They first showed that DRN^{DA} neurons preferentially project to the extended amygdala structures, both central amygdala and bed nucleus of stria terminalis, unlike VTA^{DA} neurons mostly projecting to the ventral striatum and prefrontal cortex. They also confirmed that these neurons release DA to those downstream regions via FSCV detection methods, and some of them express molecular marker for glutamate (vglut2) to co-release glutamate. Importantly, optogenetic activation of DRN^{DA} neurons promoted social interaction but did not support operant conditioning. Rather, phasic photostimulation of DRN^{DA} neurons resulted in mild aversion to the light-paired chamber. Additionally, with ex vivo and in vivo recording data that DRN^{DA} neurons are activated by social targets and sensitive to the experience of acute social isolation, they suggested that increased social interaction results from negative reinforcement mechanisms and DRN^{DA} neuronal activity represents the “loneliness-like” emotional state.

These seemingly disparate roles suggested for DRN^{DA} neurons imply that they may play more general roles than representing specific aspects of behavior. All of these studies on sleep-wake regulation, anti-nociception, and social isolation suggest one fundamental link in common: these neurons may signal arousal or alertness towards external, motivationally salient stimuli. During my doctoral training, I have devoted a significant amount of my

time to understanding the unique functional roles of DRN^{DA} neurons using novel optical and genetic tools. In Chapter III, I demonstrate that these neurons are indeed critical modulators of sleep-wake regulation, showing that DRN^{DA} neuronal activity was highest at wake over sleep states and that bi-directional manipulation of these neurons can affect the level of arousal. In Chapter IV, I further show that these neurons encode motivational salience and unsigned prediction error. Collectively, these data propose that DRN^{DA} neurons are fundamentally distinct from VTA^{DA} neurons in both anatomical connectivity and functional property, and that their endogenous role is to signal arousal and salience to the selected forebrain targets to guide appropriate behavior.

1.4 Reference

Arias-Carrion, O., Stamelou, M., Murillo-Rodriguez, E., Menendez-Gonzalez, M., Poppel, E. (2010). Dopaminergic reward system: a short integrative review. Int Arch Med. 3, 24.

Brischoux, F., Chakraborty, S., Brierley, D.I., Ungless, M.A. (2009). Phasic excitation of dopamine neurons in ventral VTA by noxious stimuli. Proc Natl Acad Sci U S A. 106(12), 4894-9.

Bromberg-Martin, E.S., Matsumoto, M., and Hikosaka, O. (2010). Dopamine in motivational control: rewarding, aversive, and alerting. Neuron 68, 815–834.

Cass, W.A. and Gerhardt, G.A. (1995). In vivo assessment of dopamine uptake in rat medial prefrontal cortex: comparison with dorsal striatum and nucleus accumbens. J Neurochem. 65, 201-207.

Charvin, D., Medosi, R., Hauser, R.A., Rascol, O. (2018). Therapeutic strategies for Parkinson disease: beyond dopaminergic drugs. Nat Rev Drug Discov. 17, 804-822.

Chen, B.T., Hopf, F.W., Bonci, A. (2010). Synaptic plasticity in the mesolimbic system: therapeutic implications for substance use. Ann N Y Acad Sci. 1187, 129-139.

Chen, T.W. et al. (2013). Ultrasensitive fluorescent proteins for imaging neuronal activity. Nature 499, 295–300.

Cohen, J.Y., Haesler, S., Vong, L., Lowell, B.B., and Uchida, N. (2012). Neuron- type-specific signals for reward and punishment in the ventral tegmental area. Nature 482, 85–88.

da Silva, J.A., Tecuapetla, F., Paixao, V., Costa, R.M. (2018). Dopamine neuron activity before action initiation gates and invigorates future movements. Nature 554(7691), 244-248.

Dahlstroem, A. and Fuxe, K. (1964). Evidence for the existence of monoamine-containing neurons in the central nervous system. I. Demonstration of monoamines in the cell bodies of brain stem neurons. Acta Physiologica Scandinavica. Supplementum. 232, 1-55.

de Jong, J.W. et al. (2019). A neural circuit mechanism for encoding aversive stimuli in the mesolimbic dopamine system. Neuron 101, 133-151.

Dreyer, J.K., Herrik, K.F., Berg, R.W., Hounsgaard, J.D. (2010). Influence of phasic and tonic dopamine release on receptor activation. J Neurosci. 30, 14273-83.

Eaton, M.J., Wagner, C.K., Moore, K.E., Lookingland, K.J. (1994). Neurochemical identification of A13 dopaminergic neuronal projections from the medial zona incerta to the horizontal limb of the diagonal band of Broca and the central nucleus of the amygdala. Brain Res. 659, 201-7.

Grace, A.A., Floresco, S.B., Goto, Y., Lodge, D.J. (2007). Regulation of firing of dopaminergic neurons and control of goal-directed behaviors. Trends Neurosci. 30, 220-227.

Groenewegen, H.J. (2003). The basal ganglia and motor control. Neural Plast. 10, 107-120.

Hokfelt, T., Martensson, R., Bjorklund, A., Kleinau, S., and Goldstein, M. (1984). Distribution Maps of Tyrosine-Hydroxylase-Immunoreactive Neurons in the Rat Brain (Elsevier).

Howe, M.W. and Dombeck, D.A. (2016). Rapid signalling in distinct dopaminergic axons during locomotion and reward. Nature 535, 505–510.

Kim, C.K., Yang, S.J., Pichamoorthy, N., Young, N.P., Kauvar, I., Jennings, J.H., Lerner, T.N., Berndt, A., Lee, S.Y., Ramakrishnan, C., et al. (2016). Simultaneous fast measurement of circuit dynamics at multiple sites across the mammalian brain. Nat. Methods 13, 325–328.

Lammel, S. et al. (2012). Input-specific control of reward and aversion in the ventral tegmental area. Nature 491(7423), 212-7.

Lammel, S., Lim, B.K., Malenka, R.C. (2014). Reward and aversion in a heteroneous midbrain dopamine system. Neuropharm. 76, 351-59.

Lee, D., et al. (2017). Temporally precise labeling and control of neuromodulatory circuits in the mammalian brain. Nat Methods. 14, 495-503.

Li, C. et al. (2016). Mu opioid receptor modulation of dopamine neurons in the periaqueductal gray/dorsal raphe: a role in regulation of pain. Neuropsychopharmacology 41, 2122-32.

Lu, J., Jhou, T.C., and Saper, C.B. (2006). Identification of wake-active dopaminergic neurons in the ventral periaqueductal gray matter. J. Neurosci. 26, 193–202.

Matsumoto, M. and Hikosaka, O. (2009). Two types of dopamine neuron distinctly convey positive and negative motivational signals. Nature 459(7248), 837-41.

Matthews, G.A., et al. (2016). Dorsal raphe dopamine neurons represent the experience of social isolation. Cell 164, 617–631.

Menegas, W., Akiti, K., Amos, R., Uchida, N., Watabe-Uchida, M. (2018). Dopamine neurons projecting to the posterior striatum reinforce avoidance of threatening stimuli. Nat Neurosci. 21(10), 1421-30.

Menegas, W., Babayan, B.M., Uchida, N., Watabe-Ushida, M. (2017). Opposite initialization to novel cues in dopamine signaling in ventral and posterior striatum in mice. Elife. 6. pii: e21886.

Messanvi, F., Eggens-Meijer, E., Roozendaal, B., van der Want, J.J. (2013). A discrete dopaminergic projection from the incertohypothalamic A13 cell group to the dorsolateral periaqueductal gray in rat. Front Neuroanat. 7, 41.

Miller, J.D., Farber, J., Gatz, P., Roffwarg, H., German, D.C. (1983). Activity of mesencephalic dopamine and non-dopamine neurons across stages of sleep and waking in the rat. Brain Res. 273, 133-141.

Mohebi, A., et al. (2018). Forebrain dopamine value signals arise independently from midbrain dopamine cell firing. bioRxiv 334060.

Muller, A., Joseph, V., Slesinger, P.A., Kleinfeld, D. (2014). Cell-based reporters reveal in vivo dynamics of dopamine and norepinephrine release in murine cortex. Nat Methods. 11, 1245-52.

Nevue, A.A., Felix, R.A. 2nd, Portfors, C.V. (2016). Dopaminergic projections of the subparafascicular thalamus nucleus to the auditory brainstem. Hear Res. 241, 202-209.

Paulus, W. and Schomburg, E.D. (2006). Dopamine and the spinal cord in restless legs syndrome: does spinal cord physiology reveal a basis for augmentation? Sleep Med Rev. 10(3), 185-96.

Poulin, J.F. et al. (2014). Defining midbrain dopaminergic neuron diversity by single-cell gene expression profiling. Cell Rep. 9, 930-943.

Poulin, J.F. et al. (2018). Mapping projections of molecularly defined dopamine neuron subtypes using intersectional genetic approaches. Nat Neurosci. 21, 1260-71.

Schultz, W., Dayan, P., Montague, P.R. (1997). A neural substrate of prediction and reward. Science 275(5306), 1593-9.

Scott, N., Prigge, M., Yizhar, O., Kimchi, T. (2015). A sexually dimorphic hypothalamic circuit controls maternal care and oxytoxin secretion. Nature 525, 519-22.

Sesack, S.R., Hawrylak, V.A., Matus, C., Guido, M.A., Levey, A.I. (1998). Dopamine axon varicosities in the prelimbic division of the rat prefrontal cortex exhibit sparse immunoreactivity for the dopamine transporter. J Neurosci. 18, 2697-2708.

Steinberg, E.E. et al. (2013). A causal link between prediction errors, dopamine neurons and learning. Nat Neurosci. 16(7), 966-73.

Sulzer, D., Cragg, S.J., Rice, M.E. (2016). Striatal dopamine neurotransmission: regulation of release and uptake. Basal Ganglia 6, 123-148.

Volkow, N.D., Wise, R.A., Baler, R. (2017). The dopamine motive system: implications for drug and food addiction. Nat Rev Neurosci. 18, 741-52.

Wanat, M.J., Willuhn, I., Clark, J.J., Phillips, P.E.M. (2009). Phasic dopamine release in appetitive behaviors and drug addiction. Curr Drug Abuse Rev. 2, 195-213.

Wisor, J.P. et al. (2001). Dopaminergic role of stimulant-induced wakefulness. J Neurosci. 21, 1787-94.

Witten, I.B. et al. (2011). Recombinase-driver rat lines: tools, techniques, and optogenetic application to dopamine-mediated reinforcement. Neuron 72, 721–733.

Zolkowska et al. (2009). Evidence for the involvement of dopamine transporter in behavioral stimulant effect of modafinil. J Pharmacol Exp Ther. 329, 738-46.

Chapter 2

ULTRAFAST NEURONAL IMAGING OF DOPAMINE DYNAMICS WITH DESIGNED GENETICALLY ENCODED SENSORS

[1] Patriarchi, T. and Cho, J. R. et al. (2018). "Ultrafast neuronal imaging of dopamine dynamics with designed genetically encoded sensors." In: *Science* 360.6396, pii: eaat4422. doi: 10.1126/science.aat4422.

2.1 Summary

INTRODUCTION: Neuromodulators, such as dopamine, norepinephrine, or serotonin, exert powerful control over neural circuit dynamics that give rise to diverse neural function and behavior. Altered neuromodulator signaling is a key feature of virtually all human neurological and psychiatric disorders, including Parkinson's disease, schizophrenia, depression, and addiction. Hence, drugs that mimic or block neuromodulators have become important components in the treatment of these disorders. Much work is devoted to determining exactly what information neuromodulatory neurons represent, but very little is known about how these signals alter the function of their target circuits.

RATIONALE: To address this problem, scientists need to be able to monitor the spatiotemporal dynamics of neuromodulatory signals in target circuits while also measuring and manipulating the elements of the circuit during natural behavior. However, existing technologies for detecting neuromodulators, such as analytic chemical or cell-based approaches, have limited spatial or temporal resolution, thus preventing high-resolution measurement of neuromodulator release in behaving animals. We recognized

the potential of combining genetically encoded indicators based on fluorescent proteins with modern microscopy to support direct and specific measurement of diverse types of neuromodulators with needed spatial and temporal resolution.

RESULTS: We report the development and validation of dLight1, a novel suite of intensity-based genetically encoded dopamine indicators that enables ultrafast optical recording of neuronal dopamine dynamics in behaving mice. dLight1 works by directly coupling the conformational changes of an inert human dopamine receptor to changes in the fluorescence intensity of a circularly permuted green fluorescent protein. The high sensitivity and temporal resolution of dLight1 permit robust detection of physiologically or behaviorally relevant dopamine transients. In acute striatum slices, dLight1 faithfully and directly reports the time course and concentration of local dopamine release evoked by electrical stimuli, as well as drug-dependent modulatory effects on dopamine release. In freely moving mice, dLight1 permits deep-brain recording of dopamine dynamics simultaneously with optogenetic stimulation or calcium imaging of local neuronal activity. We were also able to use dLight1 to chronically measure learning-induced dynamic changes within dopamine transients in the nucleus accumbens at subsecond resolution. Finally, we show that two-photon imaging with dLight1 revealed a high-resolution (cellular level) dopamine transient map of the cortex showing spatially distributed, functionally heterogeneous dopamine signals during a visuomotor learning task.

CONCLUSION: To overcome the major barriers of current methods and permit high-resolution imaging of dopamine dynamics in the mammalian brain, we developed and

applied a new class of genetically encoded indicators. This work validates our sensor design platform, which could also be applied to developing sensors for other neuromodulators, including norepinephrine, serotonin, melatonin, and opioid neuropeptides. In combination with calcium imaging and optogenetics, our sensors are well poised to permit direct functional analysis of how the spatiotemporal coding of neuromodulatory signaling mediates the plasticity and function of target circuits.

2.2 Introduction

Animal behavior is influenced by the release of neuromodulators such as dopamine (DA), which signal behavioral variables that are relevant to the functioning of circuits brainwide. Projections from dopaminergic nuclei to the striatum and cortex, for example, play important roles in reinforcement learning, decision-making, and motor control. Loss of DA or dysfunction of its target circuits has been linked to disorders such as Parkinson's disease, schizophrenia, and addiction (Tritsch and Sabatini, 2012; Wise, 2004; Dudman and Krakauer, 2016).

Much work has been devoted to determining how neural representations of behavioral states are encoded in the firing patterns of neuromodulatory neurons (Schultz et al., 1997; Lee and Dan, 2012; Marder, 2012; Schultz, 2016; Pan et al., 2005; Cohen et al., 2012), but very little is known about how the precise release of neuromodulators alters the function of their target circuits (Howe and Dombeck, 2016; Cui et al., 2013). To address this problem, an essential step is to monitor the spatiotemporal dynamics of neuromodulatory signals in target circuits while also measuring and manipulating the elements of the circuit during behavior.

Analytical techniques such as microdialysis and electrochemical microsensors have provided useful insights about neuromodulator presence (Jaquins-Gerstl et al., 2015; Genesana et al., 2017) but suffer from poor spatial and/or temporal resolution and cannot be targeted to cells of interest. Optical approaches such as injected cell-based systems

(CNiFERs) (Muller et al., 2014) and reporter gene–based iTango (Lee et al., 2017) can reveal DA release with high molecular specificity. However, these systems are limited by poor temporal resolution (seconds to hours), preventing direct detection of DA release events that occur on a subsecond time scale (Ford et al., 2009 and 2010).

High-quality single fluorescence protein (FP)– based sensors that report calcium or glutamate transients with subsecond temporal resolution have recently been developed and are widely used (Chen et al., 2013; Marvin et al., 2013). Here, we report the development of a set of single FP–based DA sensors, named dLight1, that enables imaging of DA transients with high spatiotemporal resolution in behaving animals.

2.3 Sensor engineering

Sensitive optical readout of changes in DA concentration was achieved by directly coupling the DA binding–induced conformational changes in human DA receptors to changes in the fluorescence intensity of circularly permuted green fluorescent protein (cpGFP). We did this by replacing the third intracellular loop (IL3) of the human dopamine D1 receptor (DRD1), D2 receptor (DRD2), and D4 receptor (DRD4) with a cpGFP module from the genetically encoded calcium indicator GCaMP6 (Fig. 1A).

To determine the insertion site of cpGFP in IL3 that produces maximal coupling of ligand-induced conformational changes to cpGFP fluorescence, we aligned the sequences of DRD1 and DRD4 with that of the b2 adrenergic receptor (B2AR) (Fig. 1B), for which both active and inactive structure are available (Manglik et al., 2015). The initial variant, obtained by inserting a cpGFP module with original linker sequences (LSSLE-cpGFP-LPDQL) between Lys^{232} and Lys^{269} of DRD1, was well expressed at the plasma membrane of human embryonic kidney (HEK293) cells and showed a fluorescence decrease (DF/F_{max} = –19.4 ± 0.02%) in response to puffed DA (Fig. S1A). To obtain a positive-response sensor, we screened a library of 585 variants in HEK cells (Fig. 1C and Fig. S1B). The variant with the largest positive fluorescence response (max DF/F_{max} = 230 ± 9%) and excellent membrane localization was named dLight1.1 (Fig. 1D). In situ DA titration on HEK cells revealed submicromolar apparent affinity of dLight1.1 (affinity constant K_d = 330 ± 30 nM; Fig. 1E).

We next sought to further tune the dynamic range and affinity of the sensor. Mutation of Phe^{129}, a highly conserved residue among many G protein–coupled receptors (GPCRs) (Rasmussen et al., 2011), into Ala (dLight1.2) slightly increased dynamic range (max$\Delta F/F_{max}$ =340±20%, K_d =770±10nM; Fig. 1, D and E). Optimizing the cpGFP insertion site in dLight1.1 and dLight1.2 (Fig. S1, C to G) greatly increased the dynamic range but also reduced the affinity to micromolar range (dLight1.3a: $\Delta F/F_{max}$=660±30%, K_d=2300±20nM,Fig.S2, A and B; dLight1.3b: $\Delta F/F_{max}$ = 930 ± 30%, K_d = 1680 ± 10 nM; Fig. 1, D and E). Insertion of the cpGFP module into DRD4 and DRD2 produced dLight1.4 and dLight1.5, respectively, which exhibited nanomolar affinity with a relatively small dynamic range [dLight1.4: $\Delta F/F_{max}$ = 170 ± 10%, K_d = 4.1 ± 0.2 nM, Fig. 1, B, D, and E; dLight1.5: DA,$\Delta F/F_{max}$=180±10%,K_d=110±10nM; quinpirole (synthetic agonist of D2 dopamine receptors), $\Delta F/F_{max}$ = 124 ± 19%, Fig. S2, A to C]. In addition, we engineered a control sensor by incorporating a D103A mutation in dLight1.1 to abolish DA binding (control sensor: $\Delta F/F$ = 0.4 ± 4%, Fig. 1E) (Strader et al., 1988). Because dLight1.1 and dLight1.2 produced large responses at low DA concentration (e.g., 100 nM) without approaching response saturation (Fig. 1E, inset) and had submicro-molar affinity, we further characterized these two sensors.

2.4 Sensor characterization

These two sensors showed peak emissions at 516 nm and 920 nm for one- and two-photon illumination in HEK cells, respectively (Fig. S3). In situ titration on dissociated hippocampal neurons and on HEK293 cells showed similar apparent affinities to DA (Fig. 1E and Fig. S4, A to C). Single 5-ms pulses of uncaged DA were robustly detected on the dendrites of cultured neurons, and the fluorescence response tracked uncaging pulse duration (Fig. S4, D to F). In cultured hippocampal slices, dLight1 could reliably detect submicromolar DA concentration changes at dendrites and single dendritic spines (Fig. S4, G to I).

We then investigated the endogenous and pharmacological molecular specificity of the sensor. dLight1 was less sensitive to norepinephrine and epinephrine than to DA by factors of ~70 and ~40, respectively; negligible responses were observed to all other neuromodulators tested (Fig. S5). The amplitude of the response to each pharmacological compound reflected the efficacy of drugs on the wild-type receptors, with the largest response to the full agonist dihydrexidine (DF/F = 300 ± 10%), followed by partial agonists (Fig. 1F). The response to DA was abolished in the presence of the DRD1 antagonists SKF-83566 and SCH-23390 but was unaffected by the DRD2 antagonists haloperidol and sulpiride (Fig. 1F).

To investigate the possible interference of sensor expression with G protein signaling, we first measured the effect of sensor expression on the ligand-induced cyclic adenosine

monophosphate (cAMP) response (Fig. S6) (Irannejad et al., 2013). Transiently transfected dLight1.1 and dLight1.2 triggered no significant cAMP response in HEK cells, similar to the negative control (EGFP), whereas wild-type DRD1 receptor significantly did (Fig. S6A). The conversion of DRD1 to a fluorescent sensor thus apparently blocked the scaffold's ability to bind G protein and trigger the signaling cascade. When introduced into a cell line that endogenously expressed DRD1 (U2OS), dLight1 did not significantly alter the dose-response curve for DA ($P = 0.96$, Fig. S6B). dLight1 also showed a significant reduction in agonist-induced internalization, a readout of DRD1 engagement of b-arrestin (Vickery and von Zastrow, 1999), when compared to wild-type DRD1 (Fig. S6C). Total internal reflectance fluorescence (TIRF) imaging verified that dLight1 remained diffusely distributed in the plasma membrane, without any detectable internalization, during a complete cycle of ligand-dependent fluorescence change (Fig. S6, D to F). Taken together, these results indicate that the dLight sensors are suitable for use on the cell membrane without affecting endogenous signaling through G proteins or engagement of b-arrestins.

2.5 Versatile application to other neuromodulators

We next applied the design strategy of dLight1 to modularly develop a class of intensity-based sensors for various neuromodulators and neuropeptides. We selected a subset of GPCRs, including G_s-coupled b_1 and b_2 adrenergic receptors (B1AR and B2AR); G_i-coupled k- and m-type opioid receptors (KOR, MOR) and a_2 adrenergic receptor (A2AR); and G_q-coupled 5-hydroxytryptamine (serotonin) receptor-2A (5HT2A) and melatonin type-2 receptor (MT2). As with dLight1, we replaced IL3 with cpGFP, with insertion sites chosen to preserve the conserved positive charges (Fig. S7A). All sensors localized to the membrane and showed positive fluorescence responses to their respective agonists (Fig. S7B).

2.6 Two-photon imaging of DA release in dorsal striatum ex vivo and in vivo

We next used dLight1 to measure the time course and concentration of endogenous DA release triggered by electrical stimulation and drug modification in acute striatal slices with two-photon imaging (Fig. 2A). Two to four weeks after injection of an adeno-associated virus encoding dLight1 (AAV9.hSynapsin1.dLight1.2) into the dorsal striatum, we observed both broadly distributed and localized fluorescence transients across the field of view (Fig. 2, B and C, and Fig. S8, A to C) in response to a single electrical stimulus. Fast line scan at these hotspots (Fig. 2C) revealed a rapid onset of fluorescence increase (rise $t_{1/2}$ = 9.5 ± 1.1 ms) followed by a plateaued peak (averaged DF/F = 220 ± 50%) for about 150 ms, which decayed to baseline in about 400 ms (decay $t_{1/2}$ = 90 ± 11 ms, Fig. 2D). We observed robust and reproducible fluorescent transients to low-frequency stimuli over a prolonged imaging period, whereas subsequent higher-frequency stimuli elicited significantly smaller responses (Fig. 2, E and F), indicating strong depression from an initially high probability of release. Blockade of DA reuptake with cocaine significantly prolonged the decay of fluorescence from peak to baseline (Fig. 2, G and H), but with equivocal effect on response amplitude (Fig. 2, G and H). Application of the competitive antagonist SKF83566 eliminated the responses (Fig. S8F), confirming that fluorescent signals are indeed attributable to DA binding.

We next used dLight1 to estimate released DA concentration induced by a brief electrical stimulus. By comparison with a concentration-response curve (Fig. S8, D, E, and G), the

fluorescence response suggested a DA release of 10 to 30 mM (Fig. 2I), which is one to two orders of magnitude higher than previously reported in ventral striatum using fast-scan cyclic voltammetry (FSCV) (Yorgason et al., 2017) and is similar to that reported by measuring DRD2 activation (Coutney and Ford, 2014). Addition of saturating amphetamine (10 mM in the presence of 400 mM sulpiride) increased tonic DA to 3.3 mM (Fig. S8, F and G).

We then examined the action of known modulators of DA release using dLight1 (Fig. 2, J to L). Activation of D2 autoreceptors with quinpirole decreased the electrically evoked fluorescence transients; this effect was significantly reversed by the application of sulpiride (Fig. 2J). Perfusion with a k-opioid receptor agonist (U69,593) caused a small decrease in the amplitude, which was completely blocked by naloxone (Fig. 2J). We then imaged the effects of nicotinic receptor activation in mediating the probability of DA release.

Blockade of nicotinic receptors with hexamethonium profoundly reduced the fluorescence transient, which depended on the number of stimuli (Fig. 2, K and L). In the absence of hexamethonium, the amplitude of the fluorescence remained consistent regardless of the stimulation protocol (Fig. 2, K and L) (Mamaligas et al., 2016).

Next, we asked whether dLight1 could reliably report DA signals associated with mouse locomotion in dorsal striatum, which was labeled with AAV1.hSynapsin1.dLight1.1/1.2 and AAV1.hSynapsin1.flex.tdTomato. We measured DA transients with two-photon imaging during rest and self-initiated locomotion (Fig. S9). Consistent with in vivo two-

photon calcium imaging of substantia nigra pars compacta (SNc) axon terminals in dorsal striatum (Howe and Dombeck, 2016), dLight1 reliably showed widespread and synchronous subsecond transients associated with spontaneous locomotion, which was clearly distinguishable from motion artifacts (Fig. S9, A to E). The DA transients were rapidly and bidirectionally modulated with respect to locomotion. Accelerations were associated with an increase and decelerations with a decrease in fluorescence (peak mean cross-correlation 240 ms Fig. S9, F to L).

In summary, dLight1 faithfully and directly reports the time course and concentration of local DA release and drug-dependent modulatory effects on DA release in an acute striatum slice. In addition, dLight1 enables direct visualization of locomotion-triggered DA release in behaving mice.

2.7 Deep brain recording of DA dynamics simultaneously with optogenetics or calcium imaging

The nucleus accumbens (NAc) receives projections from dopaminergic neurons in the ventral tegmental area (VTA). To directly probe DA release in freely moving mice, we delivered AAV9. CAG.dLight1.1 or AAV9.CAG.control_sensor in NAc, followed by fiber photometry imaging (Fig. 3 and Fig. S10, A and B). dLight1 revealed visible spontaneous DA transients, which were absent in the imaging sessions using the control sensor (Fig. S10C).

To optically activate VTA dopaminergic neurons, we infected VTA of TH::IRES-Cre mice with AAV5.hSynapsin1.flex.ChrimsonR.tdTomato (Gunaydin et al., 2014) (Fig.3,AtoC, Fig.S11, A and B, and Fig.S12, A and D). The high temporal resolution of dLight1 enabled detection of individual peaks of DA transients in response to 5-, 10-, and 20-Hz photostimulation (Fig. 3D and Fig. S13, A to C). The amplitude of fluorescence increase was correlated with the frequency of photostimulation (Fig. 3, D and F). In contrast, no fluorescence changes were observed with the control sensor using 20-Hz stimuli (Fig. 3, D and E). Relative to saline-injected controls, systemic administration of SCH-23390 significantly reduced optogenetically induced dLight1 responses, whereas the re-uptake inhibitor GBR-12909 enhanced them (Fig. 3, G and H).

Next, we examined whether dLight1 can report inhibition of DA transients. To induce transient inhibition of VTA dopaminergic neurons, we optogenetically stimulated VTA g-

aminobutyric acid–releasing (GABAergic) neurons in VGAT:: IRES-Cre mice (Tan et al., 2012) (Fig. 3I). Histology confirmed ChrimsonR expression in VTA GABAergic neurons (Fig. S12, B, C, and E). We observed rapid and reversible reductions in dLight1 fluorescence in response to VTA GABAergic neuron photoactivation at 40 Hz (Fig. 3, J and K, and Fig. S13D), indicating that dLight1 can report bidirectional changes in local DA release.

Motivationally salient stimuli modify DA neuron firing and downstream NAc activity (Cohen et al., 2012; Tan et al., 2012; Brischoux et al., 2009). To link the DA release to local neuronal activity, we performed dual-color measurements with dLight1 and the red-shifted calcium indicator jRGECO1a (Dana et al., 2016) in lateral core/shell regions (Fig. 3L and Figs. S10B, S11A, and S12F). When mice voluntarily consumed a reward (50 ml of 5% sucrose), we observed a concordant increase of DA concentration and local population activity (Fig. 3, M and N, and Fig. S13E), similar to a class of NAc single units showing excitation upon reward (Taha and Fields, 2005). In contrast, footshocks suppressed DA release while enhancing local neuronal activity, indicating dissociation between DA dynamics and local circuit activity (Fig. 3, O and P, and Fig. S13F).

2.8 Chronic imaging of DA dynamics throughout cue-reward learning

We next examined the utility of dLight1 in reporting modulation of DA signaling in response to conditioned stimuli (CS) and unconditioned stimuli (US) throughout Pavlovian conditioning (Fig. 4A) (Pan et al., 2005; Day et al., 2007; Clark et al., 2010). Mice successfully learned to associate the predictive cues to the reward, as shown by increasing number of licks during CS over the course of training and by decreasing numbers of licks during extinction learning (Fig. 4B).

Repeated fiber photometry recordings in NAc revealed two types of DA transients modulated during associative learning: increased DA response to the predictive cues and decreased response to reward consumption across sessions. In the first session, a small and time-locked phasic DA signal was present at the CS onset, whereas after US the DA signal was larger and also more temporally spread (Fig. 4, C and D), consistent with US consumption onsets being highly variable at early stages (Fig. S14, A and B). Aligning to consumption onset revealed large DA signal to the US at the first session (Fig. 4C and Fig. S14A). Upon repeated cue-reward pairings, the amplitude of CS response significantly increased (Fig. 4, C, D, F, and H, and Fig. S14C). On the other hand, US response, when aligned to the consumption onset, showed a monotonic decrease across learning sessions (Fig. 4, G and H, and Fig. S14D) (Cohen et al., 2012; Day et al., 2007). During extinction, we observed an attenuated phasic CS response (Fig. 4, E, F, and H). The amplitude of the phasic CS response was correlated with CS-triggered licking behavior during both learning and extinction sessions (Fig. S14E).

We further investigated whether dLight1 can report signals correlated with “reward prediction error” (Schultz and Dayan, 1997). After the animals had fully learned CS-US association, mice underwent “unexpected reward availability” sessions (in which the US was occasionally made available without the CS) between normal paired trials (Fig. 4I). Unexpected availability of reward elicited significantly higher fluorescence than did expected consumption (Fig. 4, J and K). In the “unexpected reward omission” session, where the US was occasionally omitted after the predictive CS, fluorescence decreased below the pre-CS baseline after the time at which the US would have normally become available after CS presentation (Fig. 4, L and M).

2.9 Cellular-level imaging of functionally heterogeneous DA transients in mouse cortex

Finally, we tested whether two-photon imaging with dLight1 could reveal the spatiotemporal release of DA associated with reward in the cortex. The cortex receives projection axons from both SNc and VTA. Inputs from these nuclei carry distinct dopaminergic signals influencing motor control and reward learning, respectively (Howe and Dombeck, 2016; da Silva et al., 2018). To demonstrate the utility of dLight1 in detecting behavior-related DA signals, we broadly labeled frontal/motor cortex with AAV9.hSynapsin1. dLight1.2, followed by two-photon imaging of dLight1-expressing layer 2/3 neurons in head-fixed mice. The animals had fully learned a visuomotor association task that required them to run in response to a visual "Go" cue in order to receive a water reward (Fig. 5, A and B). We observed task-related DA transients, distinguishable from motion artifacts (Fig. S15), across cell-sized regions of interest (ROIs) across the field of view (Fig. 5C and Fig. S16).

Aligning the DA transients to trial/stand-still phase onset, we found two types of task-relevant DA responses during the reward expectation and reward delivery intervals. An average of 63% of responsive ROIs showed significantly increased DA transients that correlated with reward, which were abolished by unexpected reward omission (20% of randomly selected trials) (Fig. 5D, right). A subset of ROIs (~37%) showed significantly increased DA transients that lasted during the short phase of "Go" stimulus presentation for both rewarded and non-rewarded trials (Fig. 5D, left). These transient increases during

the stimulus presentation phase were not caused by the stimulus appearance itself, because no significant increase in DA levels was observed during miss trials during which the animal saw the stimulus but did not respond (Fig. 5D, yellow traces).

To investigate whether these early responses shown in 37% of ROIs reflect increased DA levels during reward expectation or correlate with locomotion, we aligned the trials at running onset (Fig. 5E, group averages; Fig. S16G, single ROIs) and compared the DA transients of runs triggered by the "Go" stimulus (when the animals expected a reward) with spontaneous runs that erroneously occurred during the standstill phase (with no reward expectation). A small subset of responsive ROIs (5%) showed significant increases in DA transients during reward expectation but not spontaneous running (Fig. 5E, center), whereas the other 32% of ROIs correlated with locomotion (Fig. 5E, left). The 63% of ROIs responsive to reward only (Fig. 5D, right) also showed increased DA transients during the early stimulus presentation phase consisting of both locomotion- and reward expectation–related responses (Fig. 5E, right). All three types of responses were consistently seen across animals. Comparing the heterogeneity of response transients between layer 1 and layers 2/3 of cortical area M1 (Fig. S16, E and F), we found that layer 2/3 showed more ROIs active during reward. A similar number of ROIs responded to locomotion and reward expectation in both layers (Fig. S16H). Mesocortical dopaminergic projections are thus spatially intermingled, and activation of these inputs leads to spatiotemporally heterogeneous DA signals in the cortex whose dynamics depends on motor behavior, reward expectation, and consumption.

2.10 Conclusion

We developed and applied a new class of genetically encoded indicators that overcome major barriers of current methods to permit high-resolution imaging of DA dynamics in acute brain slices and in behaving mice. The sub-micromolar affinity and fast kinetics of dLight1 offer fast temporal resolution (10 ms on, 100 ms off) to detect the physiologically or behaviorally relevant DA transients with higher molecular specificity relative to existing electrochemical or cell-based probes (Muller et al., 2014). For example, in NAc of freely behaving mice, longitudinal measurements revealed different changes in time-resolved DA signals encoding either predictive cue or reward consumption across learning.

The disparate contributions of synaptic, extra-synaptic, and spillover DA events to circuit function are not addressable without fast, robust, and genetically encoded sensors. In a dorsal striatal slice, dLight1 reliably detected the concentration and time course of DA transients and their modifications by pharmacological compounds. The rapid rise of fluorescence (10 ms) and the peak concentration (10 to 30 mM) of DA after electrical stimulation indicates that the initial measures of DA are closely associated with the site of release (Coutney and Ford, 2014). The decline of fluorescence, particularly in the presence of cocaine, results primarily from re-uptake and diffusion of DA away from release sites.

dLight1 also permits measurement of functionally heterogeneous DA transients at the cellular level with high spatial resolution. In the cortex, two-photon imaging with dLight1 revealed a DA transient map with spatially distributed, functionally heterogeneous DA

signals during a visuomotor learning task. Simultaneous calcium imaging can further determine how spatiotemporal differences in DA levels relate to ongoing neural activity and influence associative learning or goal-directed behavior.

dLight1.1 and dLight1.2 are optimized sensor variants that can be immediately applied to ex vivo or in vivo studies, as they offer a good balance between dynamic range and affinity. Other dLight variants may be suitable for measuring synaptic release (dLight1.3) or tonic DA transients (dLight1.4). Given the broadly tunable affinity and dynamic range of dLight1, protein engineering and high-throughput screening efforts can further optimize the signal-to-noise ratio and molecular specificity (Piatkevich et al., 2018) as well as the performance of other neuromodulator indicators.

In combination with calcium imaging and optogenetics, our sensors are well poised to permit direct functional analysis of how the spatiotemporal coding of neuromodulatory signaling mediates the plasticity and function of target circuits.

2.11 Main figures

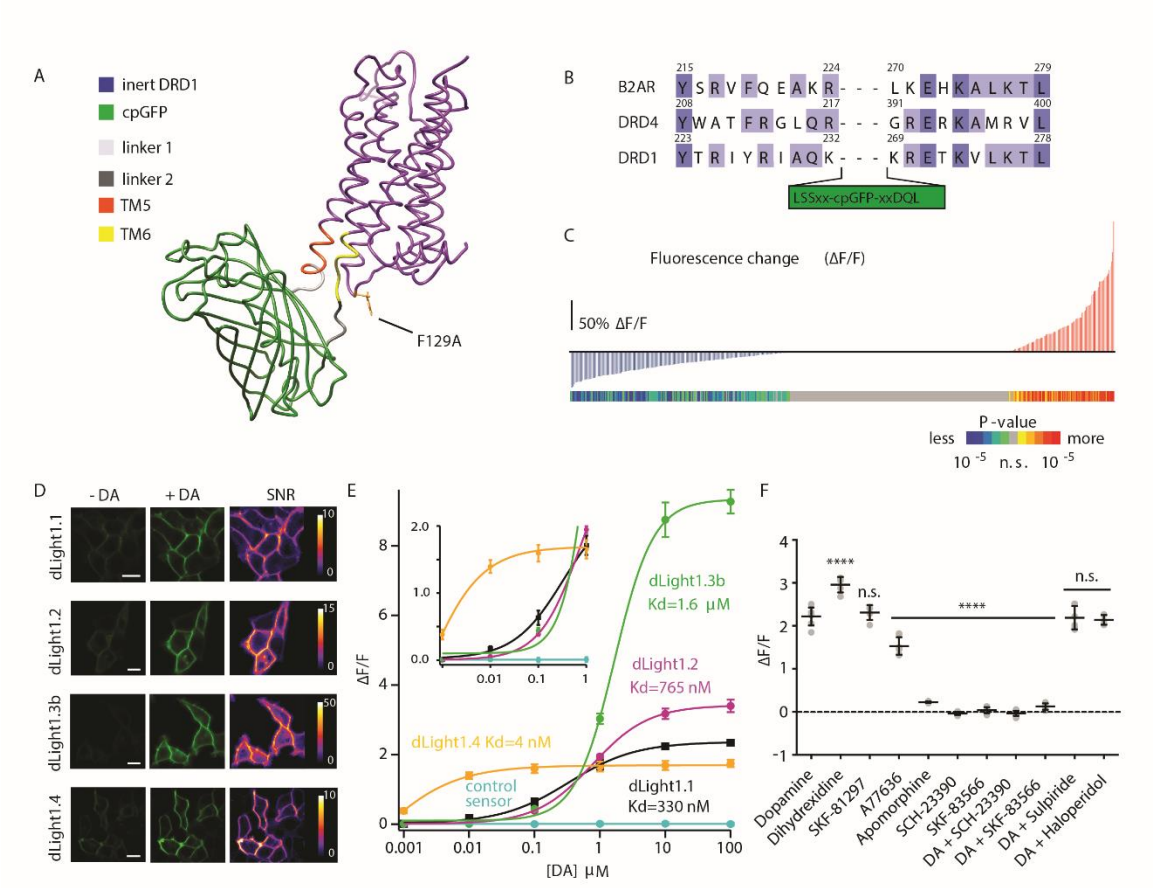

Fig. 1. Development and characterization of dLight1. (A) Simulated structure of dLight1 consisting of DRD1 and cpGFP module. **(B)** Sequence alignment of transmembrane (TM) domain 5 and 6 in b2AR, DRD1, and DRD4. Library design is shown. Amino acid abbreviations: A, Ala; D, Asp; E, Glu; F, Phe; G, Gly; H, His; I, Ile; K, Lys; L, Leu; M, Met; Q, Gln; R, Arg; S, Ser; T, Thr; V, Val; W, Trp; Y, Tyr. **(C)** Screening result of 585 linker variants. Red and blue vertical bars indicate fluorescence changes (DF/F) in response to 10 mM DA; significance values of DF/F are shown by colored bars and scale (n = 3 trials, two-tailed t test). **(D)** Expression of dLight variants in

HEK cells. Fluorescence intensity and signal-to-noise ratio of apo and sat state are shown. Scale bars, 10 mm. **(E)** In situ titration of DA on HEK cells. Data were fitted with the Hill equation (n = 5). **(F)** Pharmacological specificity of dLight1.1. DRD1 full agonist (dihydrexidine, 295 ± 8%, n = 5); DRD1 partial agonists (SKF-81297, 230 ± 7.7%, n = 5; A77636, 153 ± 7.8%, n = 7; apomorphine, 22 ± 0.8%, n = 6); DRD1 antagonists (SCH-23390, –0.04 ± 0.01%, n = 7; SKF-83566, 0.04 ± 0.03%, n = 7); DRD2 antagonists (sulpiride, 213 ± 5.1%, n = 5; haloperidol, 219 ± 11%, n = 6). Data are means ± SEM. ****P < 0.0001 [one-way analysis of variance (ANOVA), Dunnett posttest]; n.s., not significant.

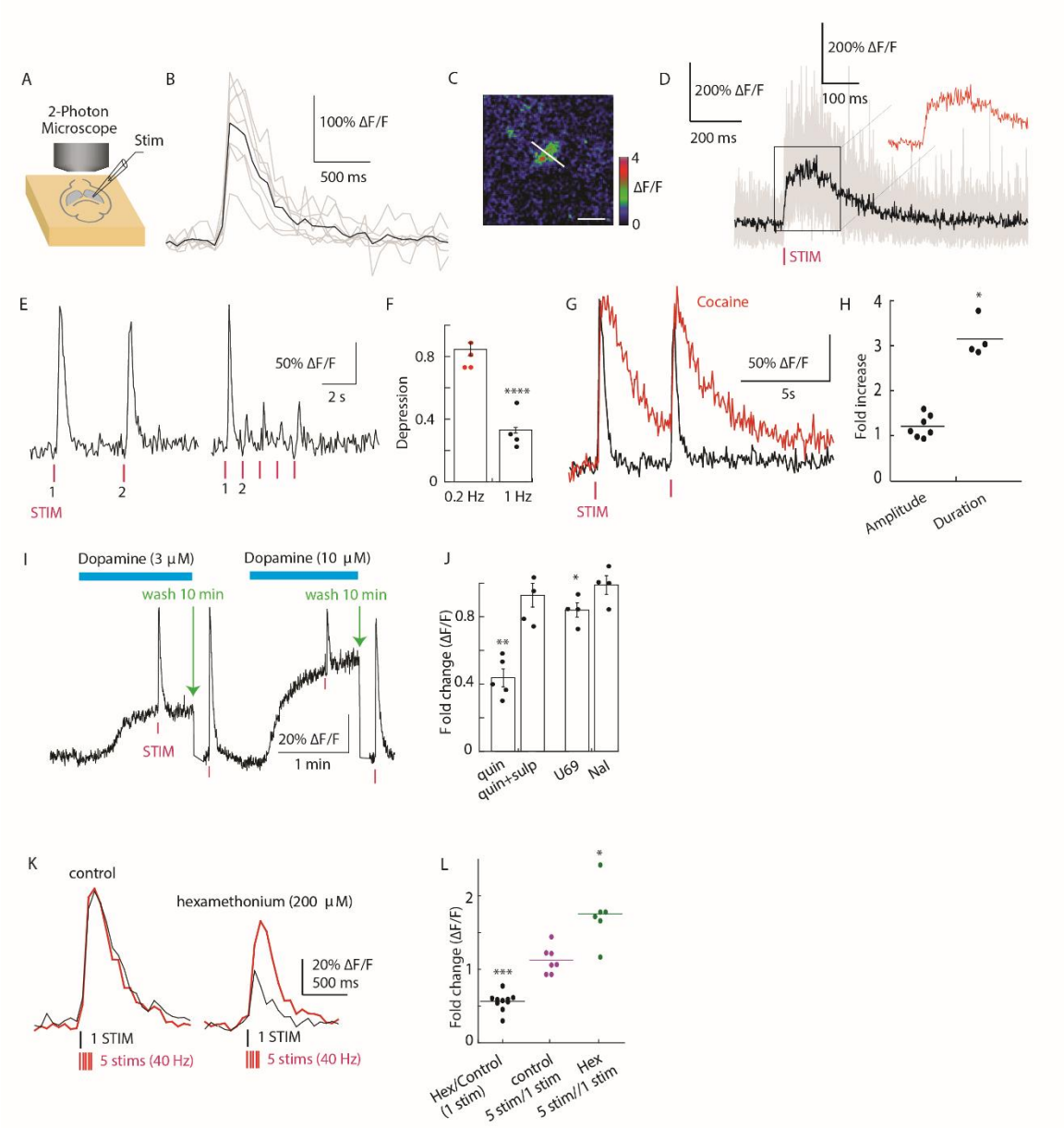

Fig. 2. Imaging electrically evoked and pharmacologically modulated dopamine release in acute dorsal striatum slices. (A) Schematics of experimental setup. **(B)** Single-trial fluorescence response (average in black) in response to a single stimulus (0.5 ms). Images were acquired at 15 Hz using two-photon light at 920 nm. Averaged DF/F = 182 ± 21% across seven trials, mean ± SEM. **(C)** Representative hotspot (DF/F) for line scan.

Scale bar, 20 mm. **(D)** Individual fluorescence traces during line scan (500 Hz) in response to a single stimulus (average in black across 13 trials). Inset shows zoomed-in view of the fluorescence plateau. **(E)** Fluorescence responses to low- and high-frequency stimuli (left, 0.2 Hz; right, 1 Hz). **(F)** Quantification of data in (E) [relative (fold) change in DF/F = 0.506 ± 0.061 at 1 Hz across five trials]. **(G)** Single-trial fluorescence response in the presence of cocaine (10 mM) triggered by a single stimulus, overlaid with trace without cocaine. **(H)** Quantification of fold change in peak fluorescence amplitude (1.056 ± 0.095, n = 7, P = 0.056) and duration (3.15 ± 0.213, n = 4). **(I)** Estimation of released DA concentration (single-trial trace shown). **(J)** Quantification of fold change in peak fluorescence in the presence of 1 mM quinpirole (0.437 ± 0.052, n = 5), 400 nM sulpiride and 1 mM quinpirole (quin+sulp, 0.926 ± 0.070, n = 5), 1 mM U69,593 (0.838 ± 0.042, n = 4), and 1 mM naloxone (1.022 ± 0.053, n = 4), all bath-applied. **(K)** Single-trial fluorescence response to either a single pulse (black) or a train of five pulses at 40 Hz (red) in the absence (left) and presence (right) of the nicotinic acetylcholine receptor blocker hexamethonium (200 mM). **(L)** Quantification of fold change in peak fluorescence response in (K) (Hex/Control: 0.561 ± 0.038, n = 10; control 5stim/1stim: 1.13 ± 0.069, P = 0.06, n = 7; Hex 5stim/1stim: 1.76 ± 0.16, n = 6). *P < 0.05, **P < 0.01, ***P < 0.001, ****P < 0.0001 (paired t test).

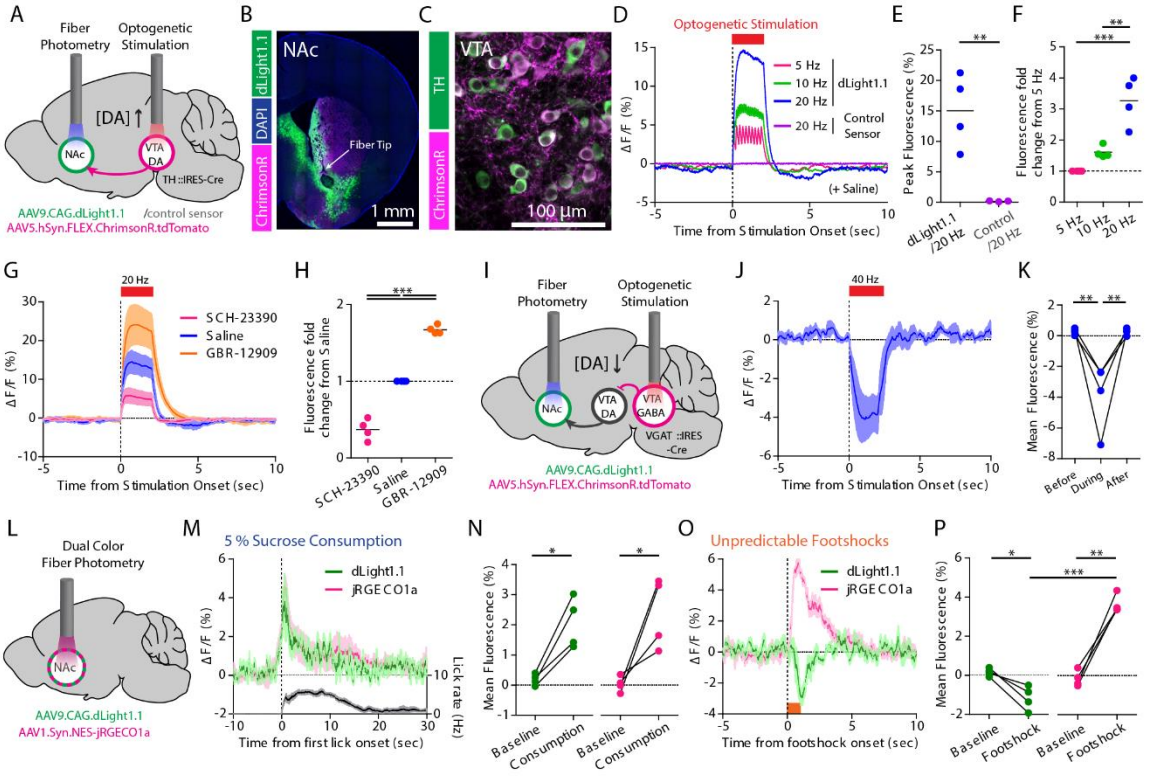

Fig. 3. Deep brain imaging of DA release triggered by optogenetic stimulation and combined with calcium imaging in freely behaving mice. (A) Schematics showing fiber photometry recording of dLight1.1 or control sensor in NAc while stimulating VTA DA neurons by optogenetics. **(B)** Expression of dLight1.1 in NAc around fiber tip location and ChrimsonR-expressing axons from midbrain. **(C)** ChrimsonR-expressing TH^+ DA neurons in VTA. **(D)** Averaged fluorescence increase in response to optogenetic stimuli (n = 5 mice). **(E)** Quantification of peak fluorescence at 20 Hz. **(F)** Fluorescence fold changes relative to 5 Hz. **(G and H)** Optogenetically induced fluorescence increase of dLight1.1 after systemic administration of saline, D1 antagonist (SCH-23390, 0.25 mg/kg), and DA reuptake inhibitor (GBR-12909, 10 mg/kg) (n = 5 mice). **(I)** Schematics showing fiber photometry recording of dLight1.1 in NAc and optogenetic stimulation of VTA GABA

neurons that inhibits VTA DA neurons. **(J and K)** Averaged fluorescence decrease in response to optogenetic stimulation at 40 Hz (n = 4 mice) and quantification of mean fluorescence. **(L)** Dual-color fiber photometry recording of DA release with dLight1.1 and local neuronal activity with jRGECO1a. **(M and N)** Increase of dLight1.1 (green) and jRGECO1a (magenta) fluorescence during 5% sucrose consumption with lick rate (black, n = 5 mice) and quantification of mean fluorescence. **(O and P)** Fluorescence decrease in dLight1.1 (green) and increase in jRGECO1a (magenta) during unpredictable footshock delivery (0.6 mA for 1 s, n = 5 mice) and quantification of mean fluorescence. Data shown are means ± SEM. *P < 0.05, **P < 0.01, ***P < 0.001 (paired or unpaired t tests for two-group comparisons; one-way ANOVA by post hoc Tukey test for multiple-group comparisons).

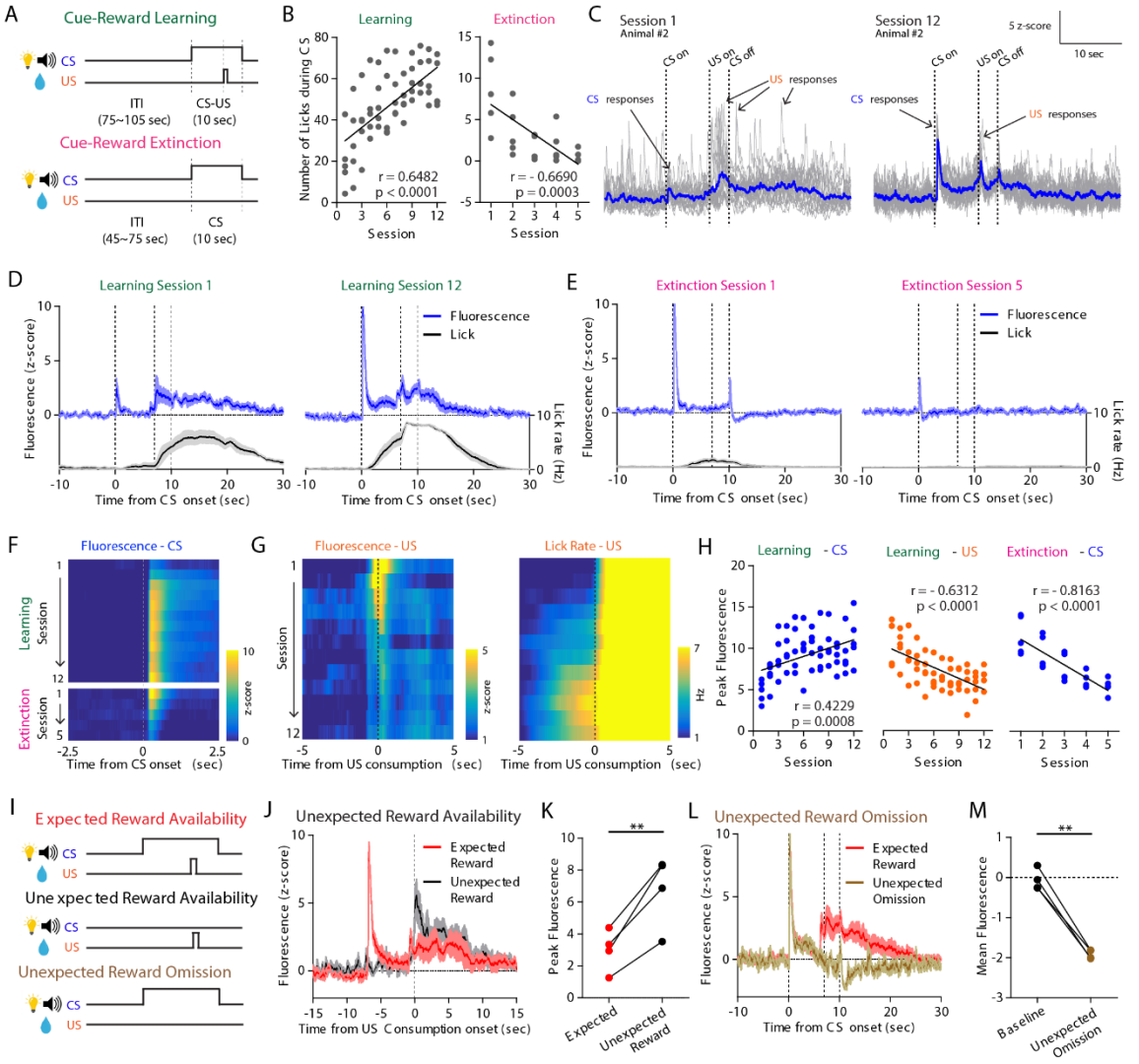

Fig. 4. Dynamic changes of NAc DA signaling during appetitive Pavlovian conditioning and reward prediction error. (A) Pavlovian conditioning procedures involved learning to associate neutral cues (CS; house light and 5-kHz tone) with a sucrose reward (US; 50 ml of 5% sucrose) and subsequent extinction. **(B)** Change of CS-evoked licks across cue-reward learning (left) and extinction (right). **(C and D)** dLight1.1 dynamics in response to CS and US in first and last sessions of cue-reward learning, shown in single (gray) and averaged (blue) trials (n = 20 trials) from a single animal (C) or

averaged across all trials and animals (n = 5 mice) (D). Lick rate is shown in black. **(E)** Same as (D) for cue-reward extinction (n = 5 mice). In (D) and (E), dotted lines indicate CS onset, US onset, and CS offset, respectively. **(F to H)** Evolution of CS-evoked (F) and US-evoked [(G), left] average fluorescence and US-triggered licks [(G), right] across learning and extinction sessions. (H) Quantification of peak fluorescence across learning and extinction. **(I)** Reward prediction error procedure. **(J)** Fluorescence response during expected (red) versus unexpected (black) reward consumption (n = 4 mice). **(K)** Peak fluorescence evoked by expected (red) and unexpected (black) reward consumption. **(L)** Fluorescence response during expected (red) versus unexpected (brown) reward omission (n = 4 mice). Second and third dotted lines indicate US onset and CS offset, respectively. **(M)** Mean fluorescence during baseline and after unexpected reward omission. Data are means ± SEM. **P < 0.01 (Pearson correlation coefficient and paired t test).

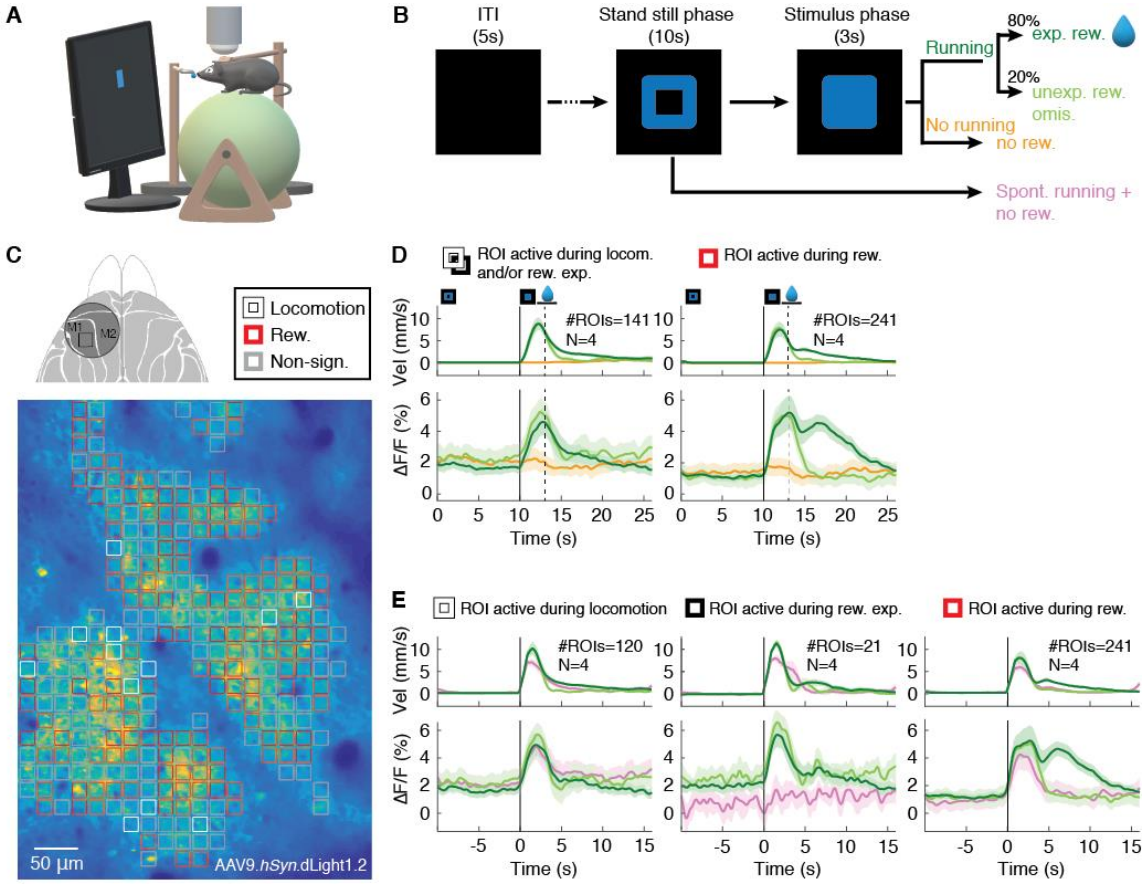

Fig. 5. Spatially resolved imaging of cortical dopamine release during a visuomotor association task. (A) Schematics of experimental setup. **(B)** A trial was initiated when mice were required to stand still for 10 s after a visual cue (blue square). If mice started to run during the stimulus phase ("hit trials"), a water reward was given. In 20% of randomly selected hit trials, the reward was withheld. If no run was triggered by stimulus presentation, the trials were counted as "miss trials." Erroneous or spontaneous runs during the standstill phase ended the trial (no "Go" cue or reward). **(C)** Top: Dorsal view of mouse cortex with the chronic cranial window (circle) and imaging location indicated (square). Bottom: Heat map of dLight1.2 expression pattern in layer 2/3 of M1 cortex. The image is overlaid with computationally defined regions of interest (ROIs, ~17 mm × 17 mm).

Colored ROIs indicate the type of fluorescence responses observed during the task. **(D)** Population data (N = 4 mice, n = 19 recording sessions) showing average task-related dLight1.2 transients (bottom) and mouse running velocity (top) aligned to trial/standstill cue onset (0 s). The solid vertical line indicates “Go” cue onset. The dashed line marks the end of the reward expectation phase during unrewarded hit and miss trials. The period during which running velocity–dependent reward consumption occurred is indicated by the horizontal line. Left: ROIs showing significantly increased responses during reward expectation/locomotion. Right: ROIs showing significant fluorescence increases to reward (dark green) but not unexpected reward omission (light green). Shaded areas of DF/F traces indicate SD. **(E)** Population data realigned to running onset (vertical black line). ROIs with “Go” cue responses [(D), left] can be subdivided into ROIs responsive to locomotion in all trials (left) and responsive to reward expectation only (center), with no fluorescence increases during spontaneous runs (pink). $P < 0.05$ (Wilcoxon test, Bonferroni-corrected for multiple comparisons).

2.12 Supplementary figures

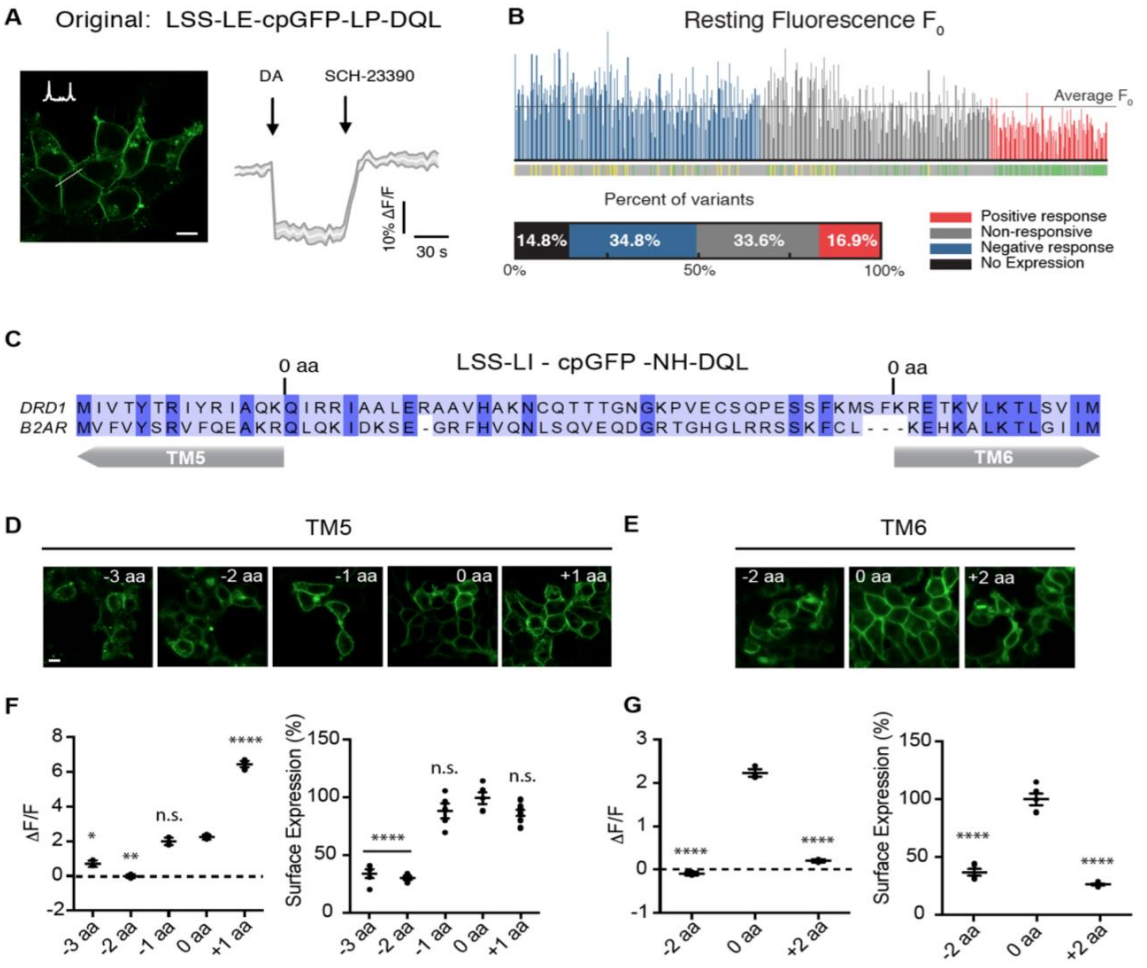

Fig. S1. Screening dLight1 variants. (**A**) Membrane expression and response of original dopamine sensor built by inserting the original GCaMP6 cpGFP module (LSS-LE-cpGFP-LP-DQL) into DRD1. Peak response (-19.4 ± 0.02 % ΔF/F, mean ± SEM, n=12 cells). Inset shows membrane intensity profile. Scale bar, 10 μm. (**B**) Resting fluorescence for all screened variants that showed expression. Proportion of response type in horizontal bar. Color-coding indicates significance value (n=3). (**C-G**) Optimizing insertion site of cpGFP in DRD1. (**C**) Sequence alignment of DRD1 and β_2 adrenergic receptor encompassing

TM5-TM6 (replacement sites was indicated as 0 aa in each TM region) is shown. (**D, E**) Representative images showing membrane expression of dLight1 variants. Scale bar, 10 μm. (**F**) Quantification of ΔF/F and surface expression from variants shown in **D**. ΔF/F: -3 aa, 70.1 ± 10.8 %; -2 aa, -1.3 ± 6.7 %; -1 aa, 199.4 ± 13.1 %; 0 aa, 223.2 ± 8.2 %; +1 aa, 652.3 ± 9.8 %. Surface expression values quantified in arbitrary units and normalized to 0 aa control (-3 aa, 33.6 ± 4 %; -2 aa, 30 ± 1.8 %; -1 aa, 88.8 ± 6.4 %; +1 aa, 87 ± 2.7 %). (**G**) Quantification of fluorescent signal changes and surface expression from variants shown in e. ΔF/F values: -2 aa, -9.2 ± 2.3 %; 0 aa, 223.2 ± 8.2 %; +2 aa, 205 ± 21 %). Surface expression values quantified in arbitrary units and normalized to 0 aa control: -2 aa, 36.4 ± 2.9 %; +2 aa, 25.9 ± 0.86 %. All values are shown as mean ± SEM. *$p<0.05$, **$p<0.01$, ****$p<0.0001$ versus 0 aa position control, One-way ANOVA with Dunnett's post-hoc test.

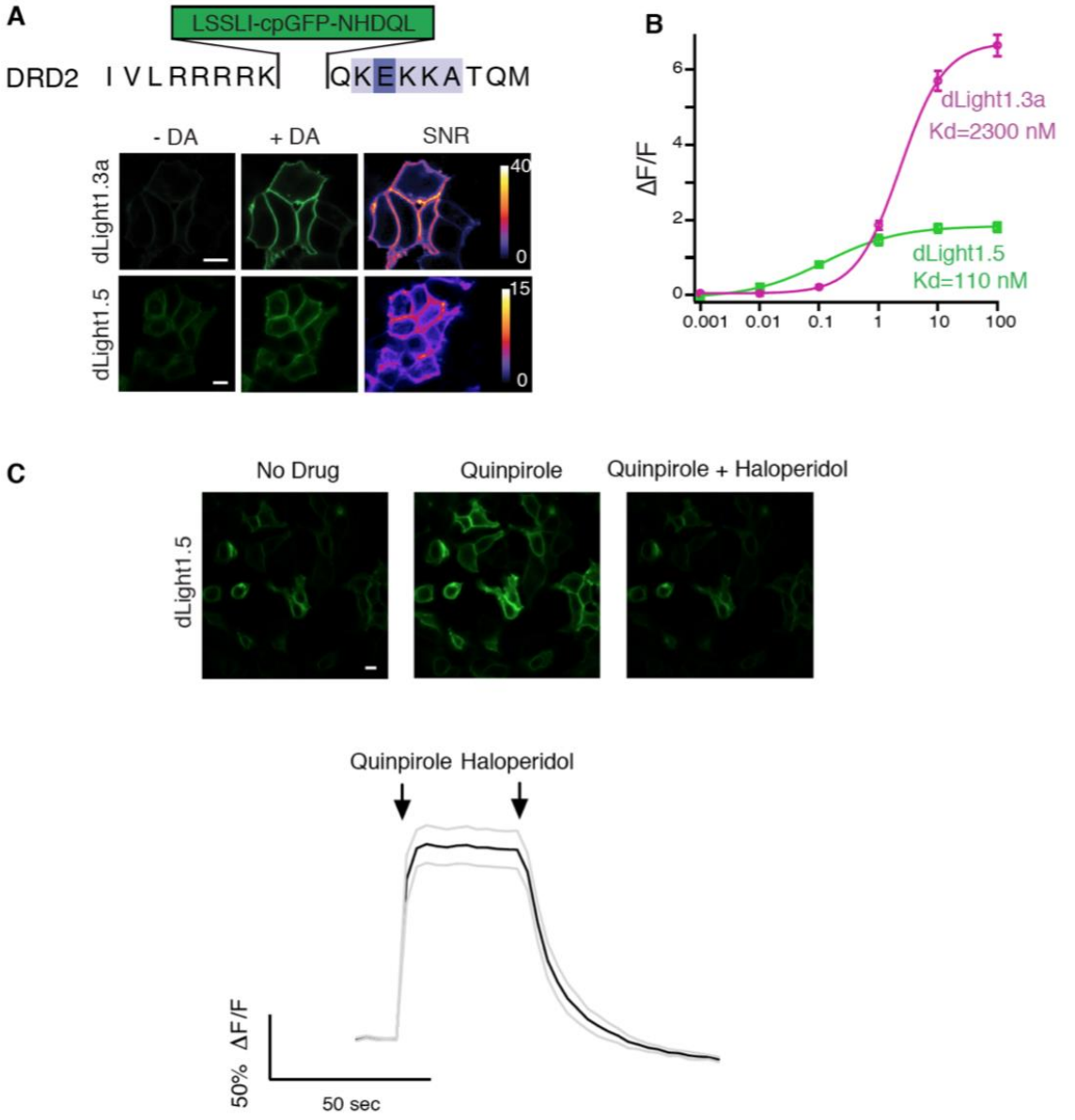

Fig. S2. Characterization of dLight1.3a and dLight1.5. (**A**) Top, amino acid sequence of DRD2 insertion site for the cpGFP module. Bottom, representative images of dLight1.3a and dLight1.5 expressed on HEK293 cells before and after addition of DA (10 μM) and corresponding SNR heatmaps. Scale bars, 10 μm. (**B**) Quantification of fluorescence response of dLight1.3a (n=12) and dLight1.5 (n=4) to DA titrations on HEK293 cells. Data

were fit with Hill equation (EC50: dLight1.3a, 2300 ± 20 nM; dLight1.5, 110 ± 10 nM). (**C**) Representative images of dLight1.5 under basal conditions, after addition of quinpirole (10 μM) and haloperidol (50 μM), and trace showing quantification of fluorescence response during bath application of drugs (n=15). All data are shown as mean ± SEM.

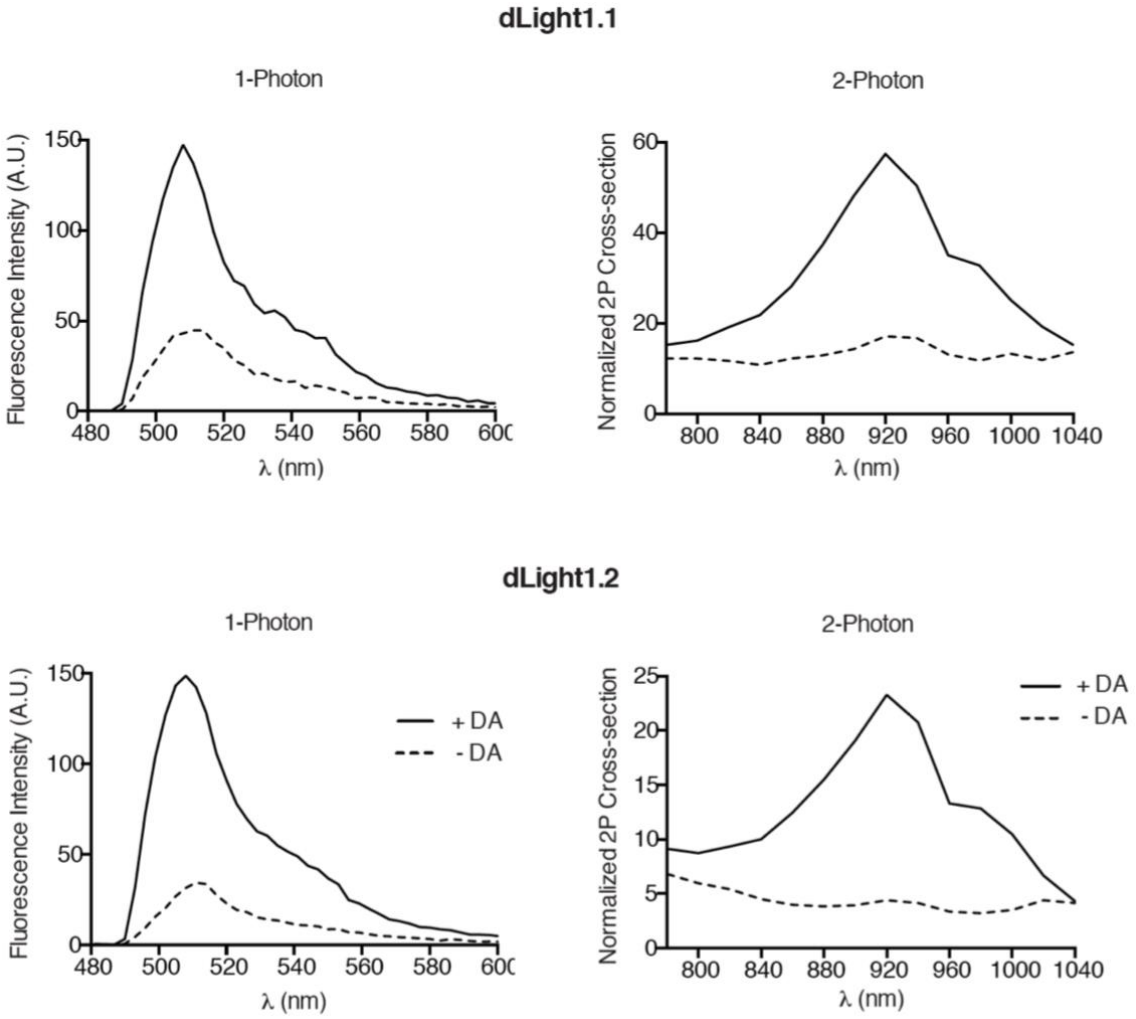

Fig. S3. One photon emission spectrum and two-photon cross-section of dLight1 expressed in HEK293T cells. Emission spectrum of both dLight1.1 and dLight1.2 peaks at 517 nm. Under 2P illumination, emission peaks are driven at 920 nm.

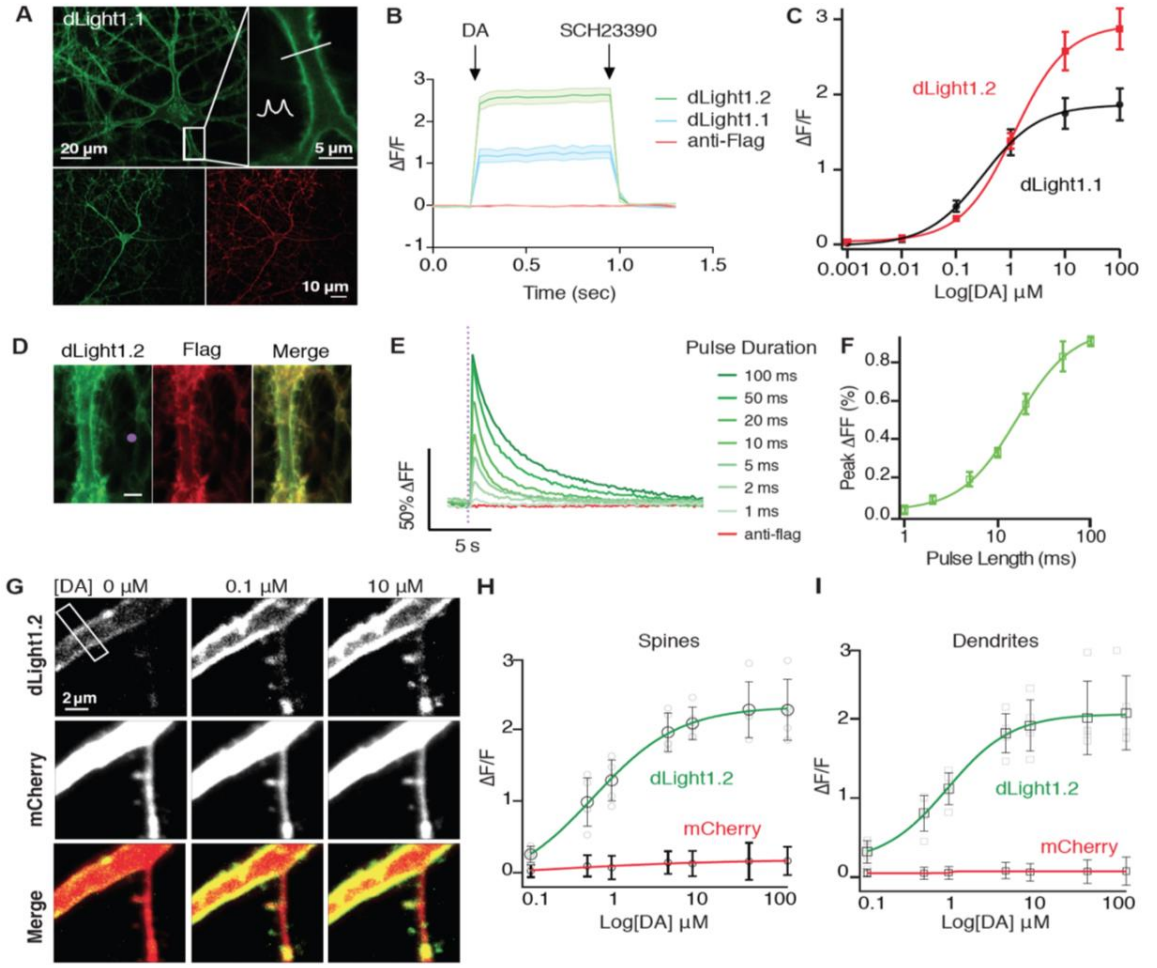

Fig. S4. Characterization of dLight1 in cultured hippocampal neurons and organotypic hippocampal slice. (**A**) Representative images showing membrane localization of dLight1.1 (GFP fluorescence in green, Alexa-564-conjugated anti-flag labeling in red) in cultured hippocampal neurons. Inset shows membrane intensity profile. (**B**) dLight1.1 and dLight1.2 responses to dopamine perfusion, which were abolished immediately with the addition of a DRD1 antagonist (mean ± SEM, n=4 sessions). (**C**) In situ titration on neurons (mean ± SEM, n=7 cells). Fitted with Hill equation (EC50: dLight1.1, 311 ± 26 nM; dLight1.2, 1,157 ± 44 nM). (**D**) Representative images showing uncaging spots (purple circle, 2 µm diameter, 40% laser power 405 nm light). Scale bar, 5

μm. (**E**) Representative traces of dLight1.2 fluorescence in response to increasing duration of uncaging light pulses (1ms per pulse). (**F**) Quantification of peak ΔF/F values which is correlated with the number of uncaging pulses (1 ms, 2.7 ± 0.01 %; 2 ms, 8.2 ± 2.2 %; 5 ms, 18.9 ± 3.9; 10 ms, 32.8 ± 2.5; 20 ms, 58.4 ± 5.3; 50 ms, 83.4 ± 7.8; 100 ms, 91.1 ± 6 %; n=3, mean ± s.d.). (**G**) Representative dLight1.2 responses to bath applied DA from sparsely-labeled CA1 pyramidal neurons in organotypic slice cultures. mCherry expression was used as a cell fill to visualize dendritic and synaptic structures (shown in rectangular and circular boxes, respectively) and to provide reference fluorescence. (**H-I**) Quantification of both green and red (control) fluorescence signal change at single spines and dendrites in response to a titration of DA concentrations. Maximal ΔF/F% fold change in the green channel were: synaptic spines, 227 ± 39; dendrites 201 ± 46 (mean ± s.d., n=5). EC50 values were: spines, 844 nM; dendrites, 883 nM.

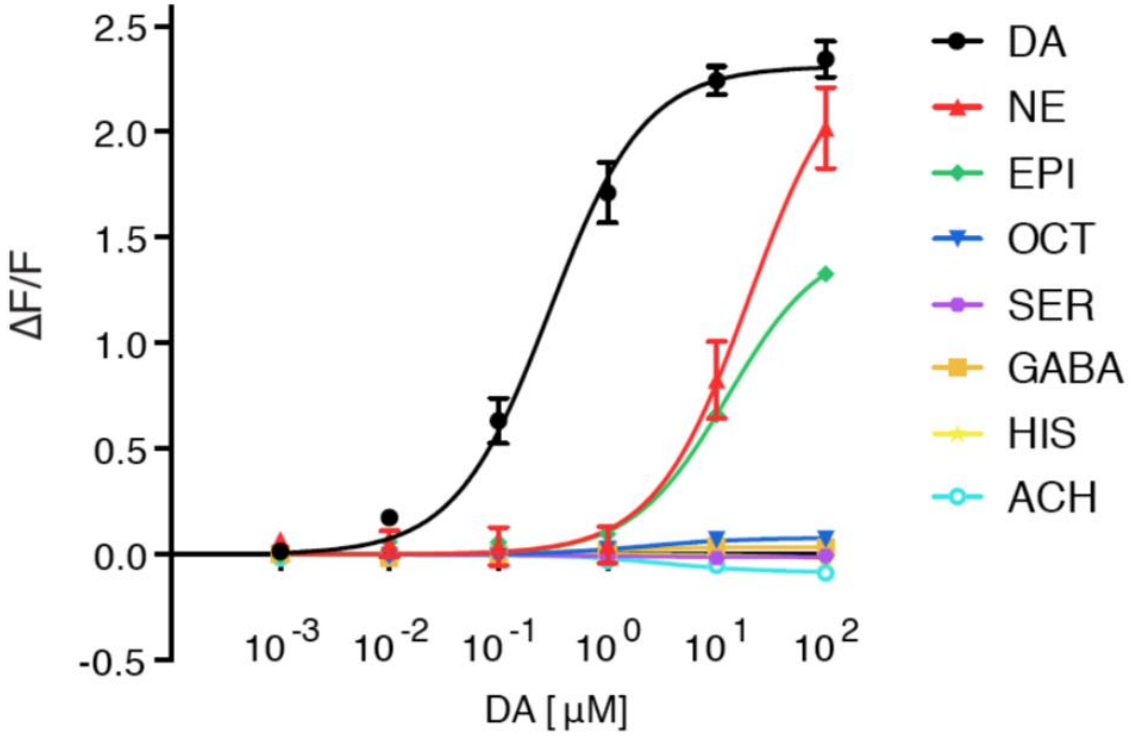

Fig. S5. Specificity of dLight1. Specificity of dLight1 response was determined by titrations of a panel of 8 different neuromodulators on dLight1.1-expressing HEK293 cells. Acetylcholine, ACH; histamine, HIS; γ-aminobutyric acid, GABA; serotonin, SER; octopamine, OCT; epinephrine, EPI; norepinephrine, NE; dopamine, DA. Kd values for DA, NE and EPI were: 330 ± 28 nM, 19,850 ± 2,644 nM, 12,680 ± 1,559 nM, respectively. Results shown as mean ± SEM, (n=3).

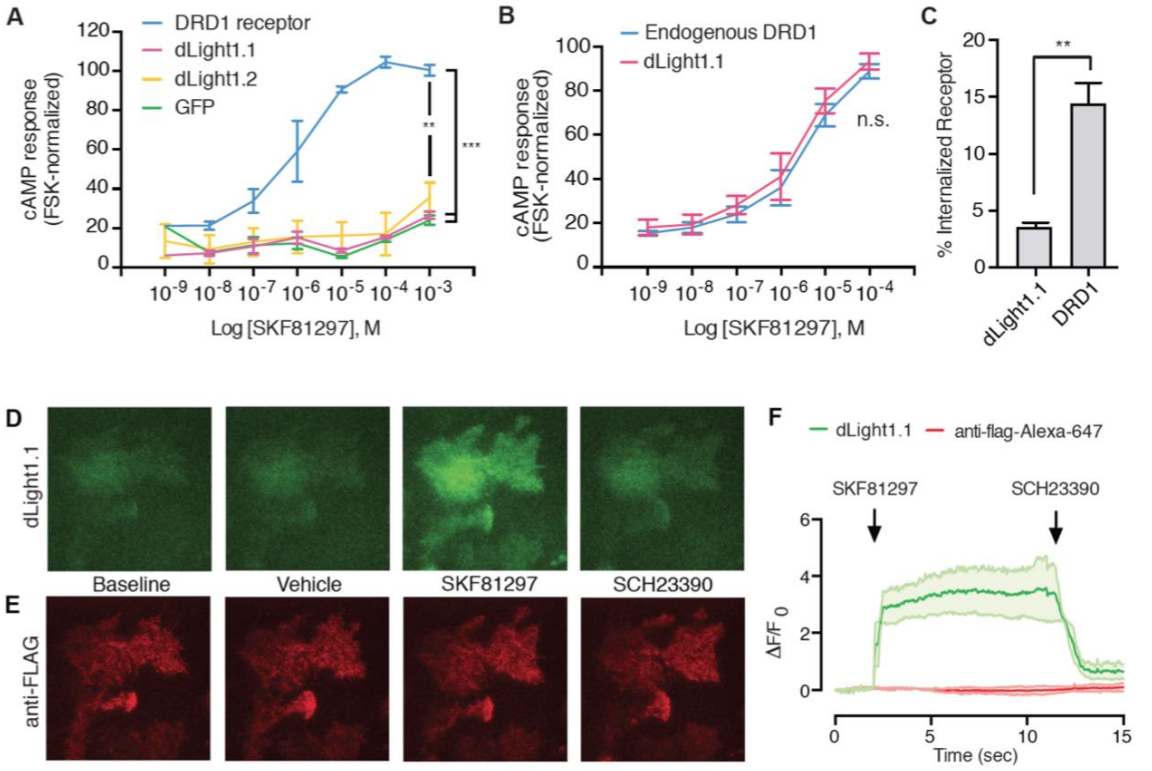

Fig. S6. Functional analysis of dLight1 signaling properties. (**A**) cAMP response curve to a titration of DA in HEK293T cells expressing wild-type human DRD1 receptor or dLight1.1 or dLight1.2 or GFP. No significant cAMP response were observed in cells expression dLight1.1 (n=3, **p<0.01, ***p<0.001, one-way ANOVA, Dunnett's post test). (**B**) cAMP response curves of a cell line endogenously expressing DRD1 (U2OS). Overexpression of dLight1.1 did not alter the cAMP response to DA (n=3, p=0.192, two-way ANOVA with Tukey's post-hoc test. (**C**) dLight1.1 internalization is significantly reduced compared to wild type DRD1 as assayed via flow cytometry (% internalized receptor: dLight1.1, 3.4 ± 0.5 %; DRD1, 14.3 ± 1.9 %; **p<0.01, unpaired t test). (**D**) TIRF microscopy visualization of dLight1.1 shows the fluorescent response to a DRD1 agonist (SKF81297) in green channel but not in red channel, which was immediately abolished by

applying antagonist (SCH23390). (**E**) In situ surface staining with an Alexa-647 conjugated anti-flag antibody further confirmed the lack of internalized punctae. (**F**) Quantification of fluorescence responses in (**D**) and (**E**).

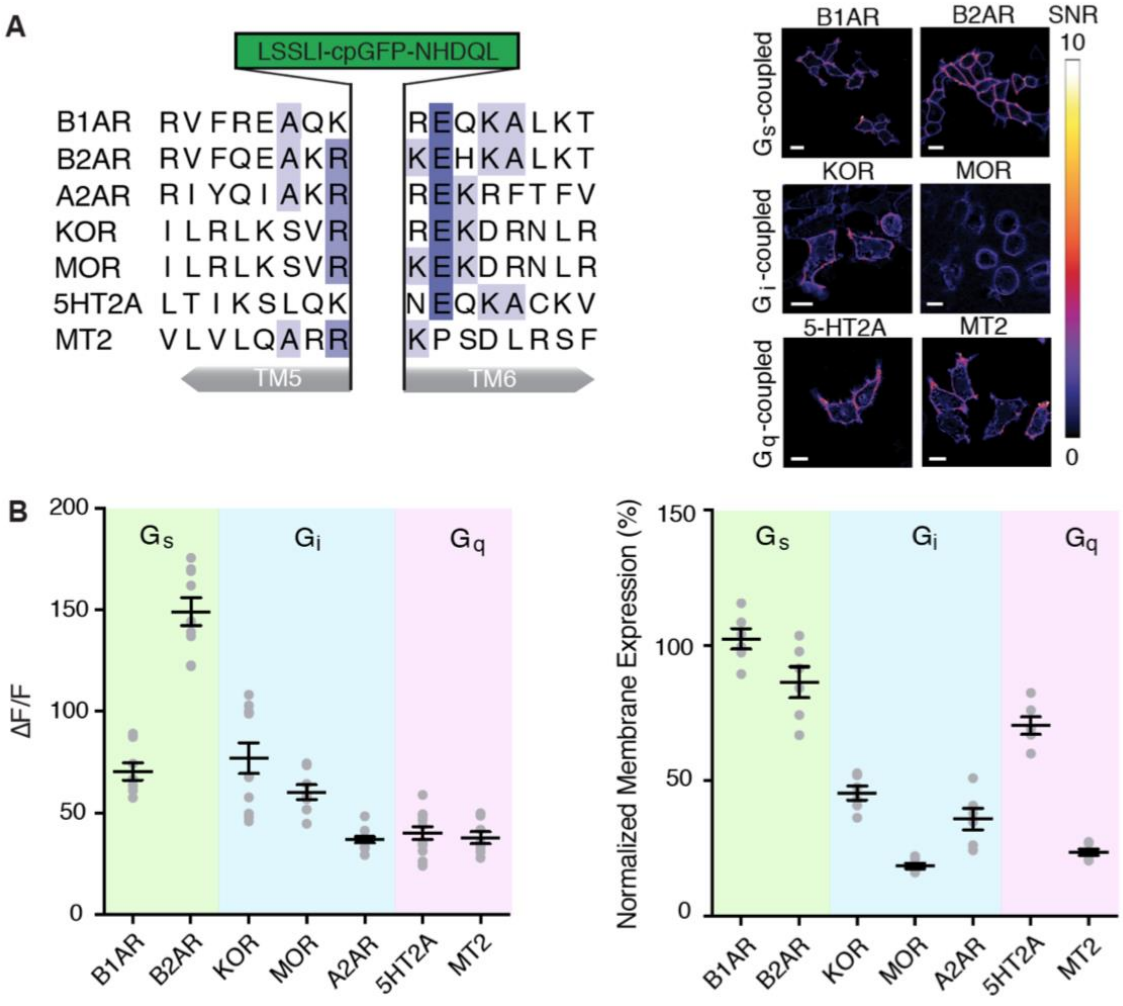

Fig. S7. Versatility of engineering approach to generate other GPCR-sensors. (A) Left, aligned sequences of TM 5 and TM6 from 7 GPCRs with insertion site for cpGFP module. To maximize ΔF/F in the B2AR and MT2 constructs the "QLQKID" sequence was inserted between TM5 (after the last R) and before LSS. Scale bars: 10 μm. Right, SNR heatmaps for a subset of GPCR sensors expressed in HEK cells. (**B**) Quantification of fluorescence response and membrane expression for each GPCR-sensor construct. Max ΔF/F of each sensor to bath applied agonist (B1AR: 70 ± 4%, n=8; B2AR: 149 ± 7%, n=9; A2AR: 77 ± 8%, n=11; KOR: 60 ± 4%, n=8; MOR: 37 ± 2%, n=10; 5HT2A: 40 ± 3%, n=12; MT2: 38

± 3%, n=8). Agonists used were: norepinephrine for B1AR, B2AR, A2AR (100 μM); U50488 for KOR (10 μM); [D-Ala2, NMe-Phe4, Gly-ol5]-enkephalin (DAMGO) for MOR (10 μM); serotonin for 5HT2A (10 μM); melatonin for MT2 (10 μM). Membrane expression was calculated as membrane-to-cytosol ratio and normalized to dLight1.1 (B1AR, 102 ± 4%; B2AR, 86 ± 6%; DRD2, 39 ± 4%; A2AR, 36 ± 4%, KOR, 45 ± 3%; MOR, 19 ± 1%; 5HT2A, 70 ± 3%; MT2, 24 ± 1%; n=6). Individual datapoints are shown. mean ± SEM shown in black.

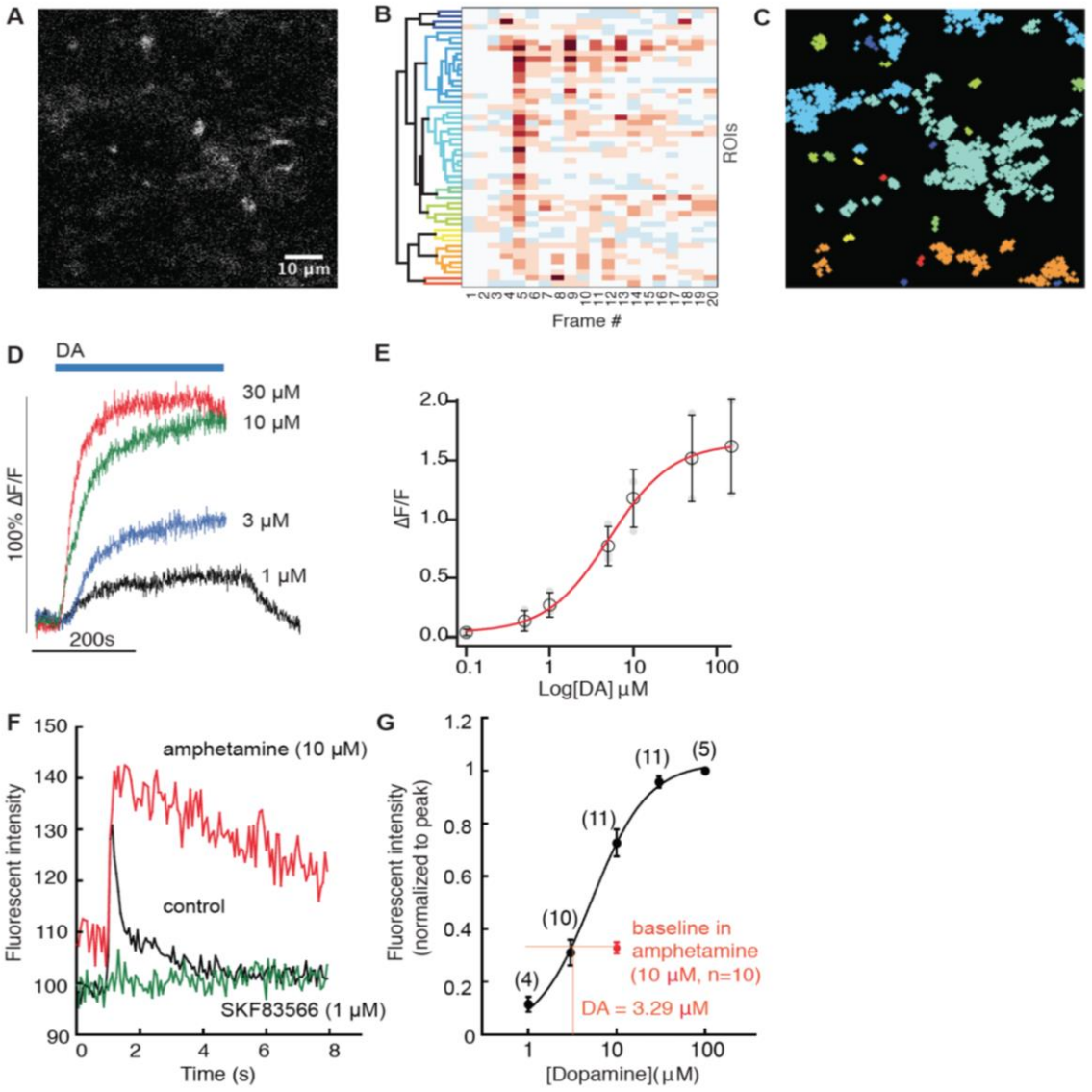

Fig. S8. Characterization of dLight1 performance in striatal brain slice. (**A-C**) Spatially-distinct responses triggered by electrical stimuli in acute rat striatum slice. (**A**) Representative field of view for two-photon imaging of acute striatum slice infected with AAV9.*hSynapsin1*.dLight1.2. (**B**) ROIs hierarchically clustered based on correlations in the time course of their fluorescence values. (**C**) ROIs location relative to (**A**), with color-coding corresponding to the dendrograms from the hierarchical clustering. (**D**) A steady-

state concentration response curve with bath application of specified DA concentrations in the presence of cocaine (10 μM) and sulpiride (400 μM) to block D2-autoreceptors. The increase in fluorescence to each known concentration of DA (1-100 μM) was measured after reaching a steady level in 3-10 min. (**E**) Quantification of concentration-dependent fluorescence responses from (**D**). The fluorescence response reached half-maximal levels at about 5 μM DA and approached saturation at 30-100 μM. Curve was fitted with a Hill equation (EC50 = 5.3 ± 0.4 μM; mean ± s.d.; n=3). (**F**) Fluorescence response to a single-pulse stimulation in the presence of amphetamine (10uM) or the DRD1 antagonist SKF83566 (1 μM). (**G**) Estimate of basal DA concentration in the presence of amphetamine at saturated concentration by interpolation on a dose-response curve, normalized to peak value (n numbers are shown for each concentration).

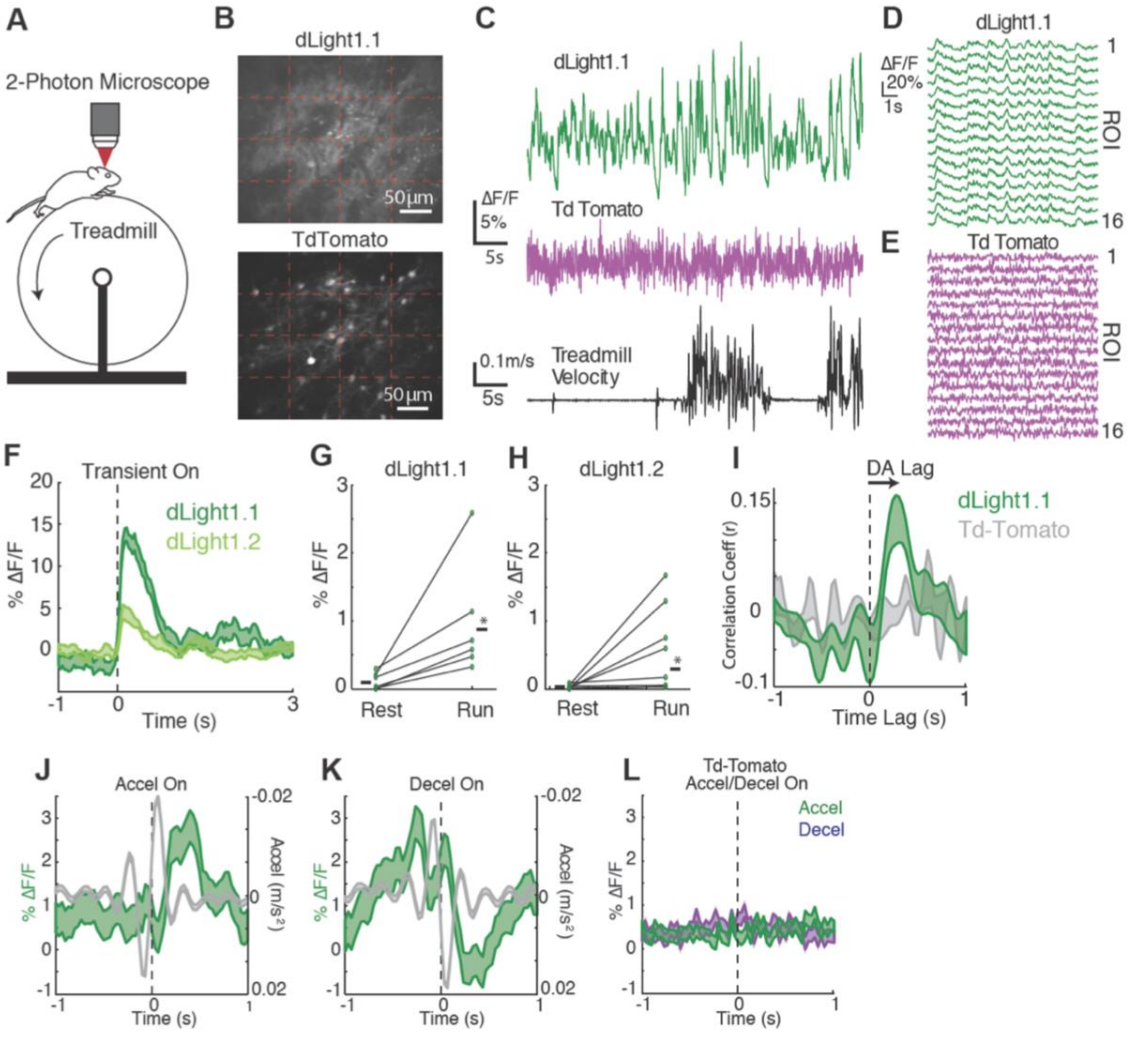

Fig. S9. Two photon imaging of locomotion related bi-directional dopamine transients in dorsal striatum. (**A**) Schematics of two-photon imaging of head-fixed mouse during treadmill locomotion. (**B**) Mean fluorescence projection from a representative imaging field showing green dLight1.1 expression (top) and red td-Tomato expression (bottom). (**C**) Average fluorescence changes in the field of whole in green (ΔF/F, green, top), red fluorescence (magenta, center), and treadmill velocity (black, bottom) for a representative imaging session. (**D-E**) Mean ΔF/F traces for 16 equal-sized ROIs tiling the imaging field pictured in (**C**) (red-dashed lines) in green and red. Note large positive-going transients

and the high synchrony across ROIs in dLight1.1 fluorescence, but not in td-Tomato fluorescence. (**F**) Mean ΔF/F for all significant positive-going transients in mice expressing either dLight1.1 (n = 2 mice, 131 transients) or dLight1.2 (n = 2 mice, 31 transients). (**G-H**) Mean transient ΔF/F during rest and run for all fields in dLight1.1 (n = 2 mice, 5 fields) and dLight1.2 (n = 2 mice, 8 fields) (**I**) Cross correlation between acceleration and ΔF/F for dLight1.1 during run periods (peak mean cross correlation 240ms). (**J**-**L**) DA transients were rapidly and bi-directionally modulated by accelerations and decelerations. Mean ΔF/F from dLight1.1 aligned on the zero crossing of all large accelerations (**J**) or decelerations (**K**). Note the significant peak in ΔF/F following the acceleration peak (**J**) or the decrease below baseline following decelerations (**K**). (**L**) Same as (**J**, **K**) but for the td-Tomato traces. Note the lack of significant peaks or troughs to accelerations or decelerations. Shaded regions and error bars indicate SEM. Asterisks indicate $p < 0.0001$ with Wilcoxon rank-sum test.

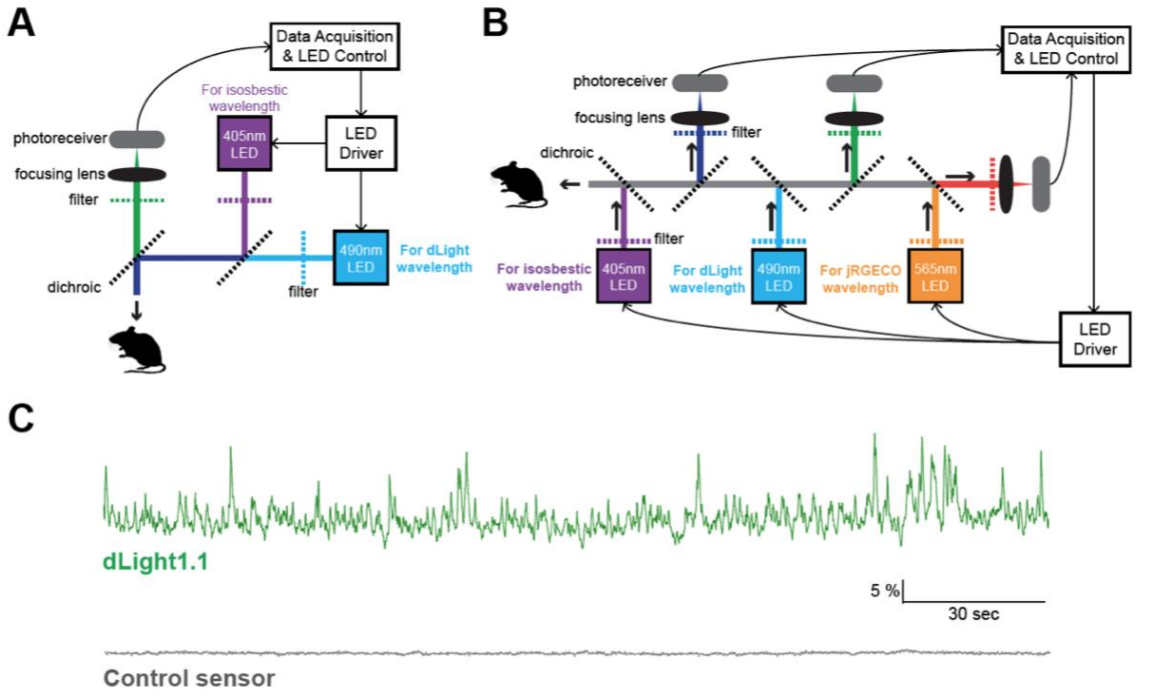

Fig. S10. Fiber photometry setups and spontaneous DA transients in NAc. (**A**) Schematics of fiber photometry setup for dLight1 imaging. Two LEDs were used: 490 nm for dLight1.1 excitation and 405 nm for an isosbestic wavelength (*63*). These two LEDs were modulated at different frequencies and demodulated with lock-in functions implemented in the custom software. (**B**) Schematics of "dual color" fiber photometry setup. Compared to conventional fiber photometry, an additional 565 nm LED was added to excite red-shifted Ca^{2+} indicator jRGECO1a (*31*). Emitted fluorescence was divided into three channels based on their spectral profiles, detected by separate photoreceivers and then demodulated. (**C**) Representative traces of dLight1.1 (green) and control sensor (gray). Note that there are clear fluctuations of fluorescence in dLight1.1 with occasional bursts, while no apparent change of fluorescence is observed with control sensor.

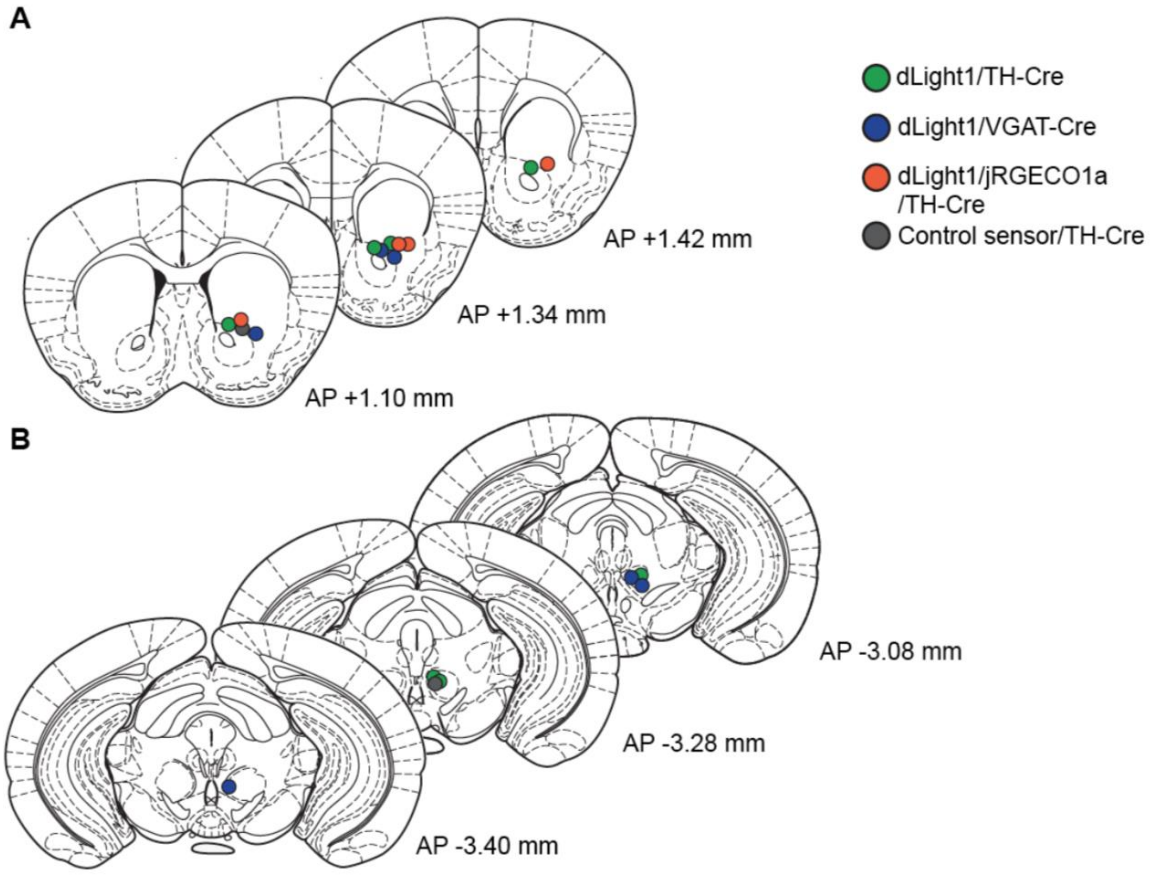

Fig. S11. Histological verification of fiber tip locations during fiber photometry recordings. (**A**) Histologically verified anatomical positions of implanted fibers for photometry in the NAc. (**B**) Histologically verified anatomical positions of implanted fibers for optogenetic stimulation in the VTA. Histological brain images were reproduced from Paxinos and Franklin's the Mouse Brain in Stereotaxic Coordinates (Academic Press, 2012).

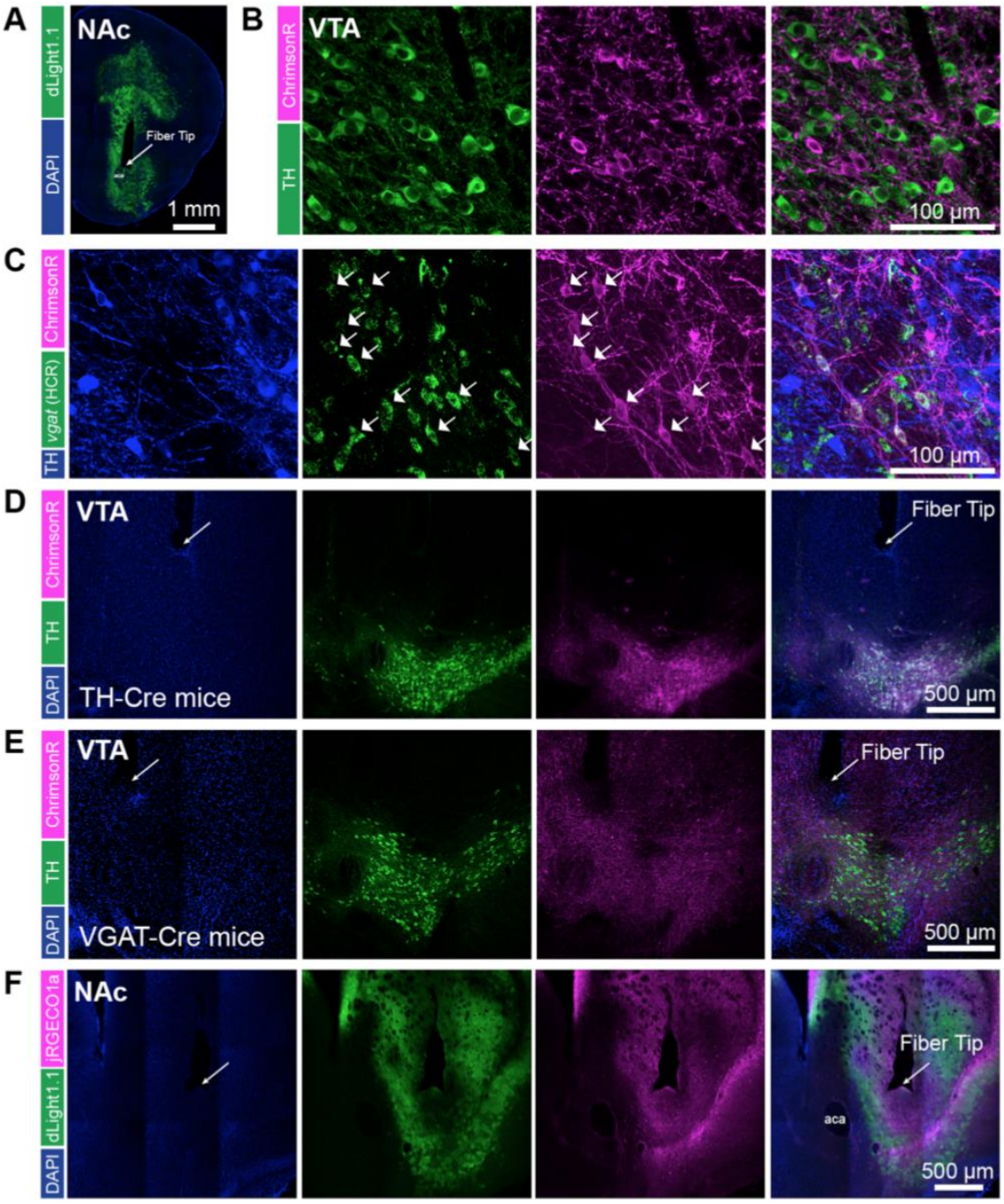

Fig. S12. Histological verification of virus expression in the NAc and VTA. (**A**) Histological image of dLight1.1 (green) expression in the NAc with fiber tip location in a VGAT-Cre mouse. Blue indicates nuclear staining DAPI. (**B**) Histological images showing

that ChrimsonR-expressing (magenta) neurons do not overlap with DA (green for tyrosine hydroxylase $(TH)^{+}$) neurons in the VTA. **(C)** Histological images showing that ChrimsonR-expressing (magenta) neurons in the VTA co-localize with *vgat* mRNA (green, detected by hybrid chain reaction in situ hybridization, see supplementary information for details), but not with TH protein (blue, by IHC). Thick arrows indicate neurons co-expressing ChrimsonR and *vgat* mRNA. (**D**) Representative low-magnification images of VTA regions in TH-Cre mice showing optical fiber tip locations (best visible in DAPI section) and virus expressions in the VTA. Blue is DAPI, green TH+ DA neurons, and magenta ChrimsonR+ neurons. (**E**) Same as (**D**) above, but for a VGAT-Cre mice. (**F**) Histological images of a NAc region with co-expression of dLight1.1 (green) and jRGECO1a (magenta).

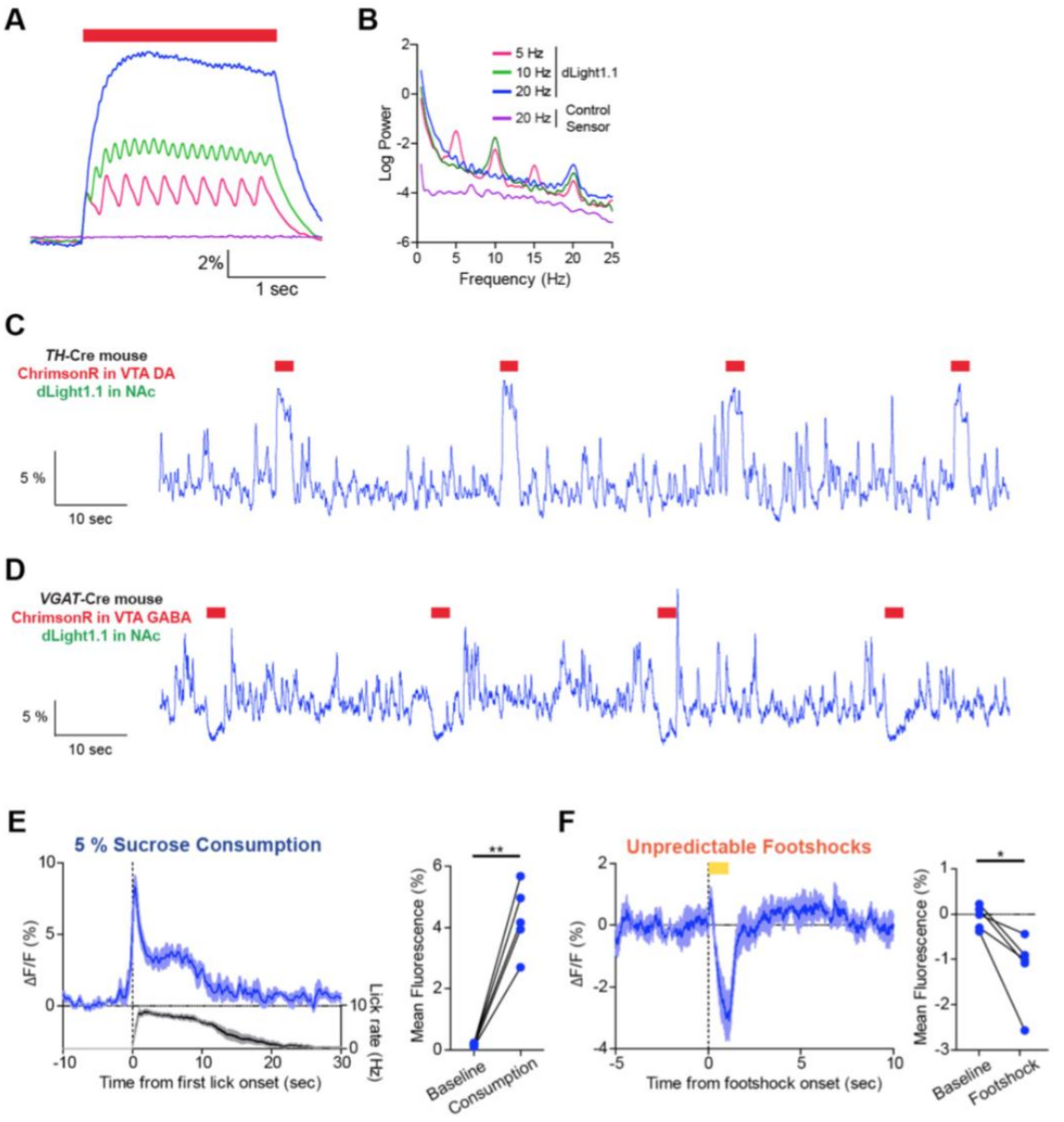

Fig. S13. dLight1 fluorescence in response to optogenetic stimulation of VTA DA or GABA neurons and NAc DA dynamics underlying natural behaviors. (**A**) Magnified version of traces in **Fig. 3D**. Note that there are clear peaks of DA transients corresponding to each optogenetic stimulation pulses, even at 20 Hz. (**B**) Power spectral density analysis reveals peaks at matching stimulation frequencies (and harmonics) in dLight1.1, while the control sensor shows no clear peak in any frequency ranges. **(C)** Raw trace of a TH-Cre

mouse expressing dLight1.1 during VTA DA photostimulation. Optogenetic stimulation of VTA DA neurons caused evident and time-locked increase in fluorescence from spontaneously fluctuating transients. **(D)** Raw trace of a VGAT-Cre mouse expressing dLight1.1 during VTA GABA photostimulation. Fluorescence is decreased from baseline fluctuations upon optogenetic stimulation of VTA GABA neurons. (**E**) DA dynamics during natural behavior recorded from conventional fiber photometry with separate mouse cohort expressing dLight1.1 alone in the NAc. Mice consumed 5% sucrose water. Consistent with dual color fiber photometry results shown in **Fig 3M** and voluntary reward consumption was associated with increase of dLight1.1 fluorescence (mean fluorescence increase was quantified; paired t-test, $t4 = 8.495$, $p = 0.0011$). (**F**) DA dynamics while mice expressing dLight1.1 only in the NAc received unpredictable footshocks. Footshock caused transient depression of dLight1.1 fluorescence, which is consistent with dual color fiber photometry results shown in **Fig 3O** (mean fluorescence decrease were quantified; paired t-test, $t4 = 3.765$, $p = 0.0197$).

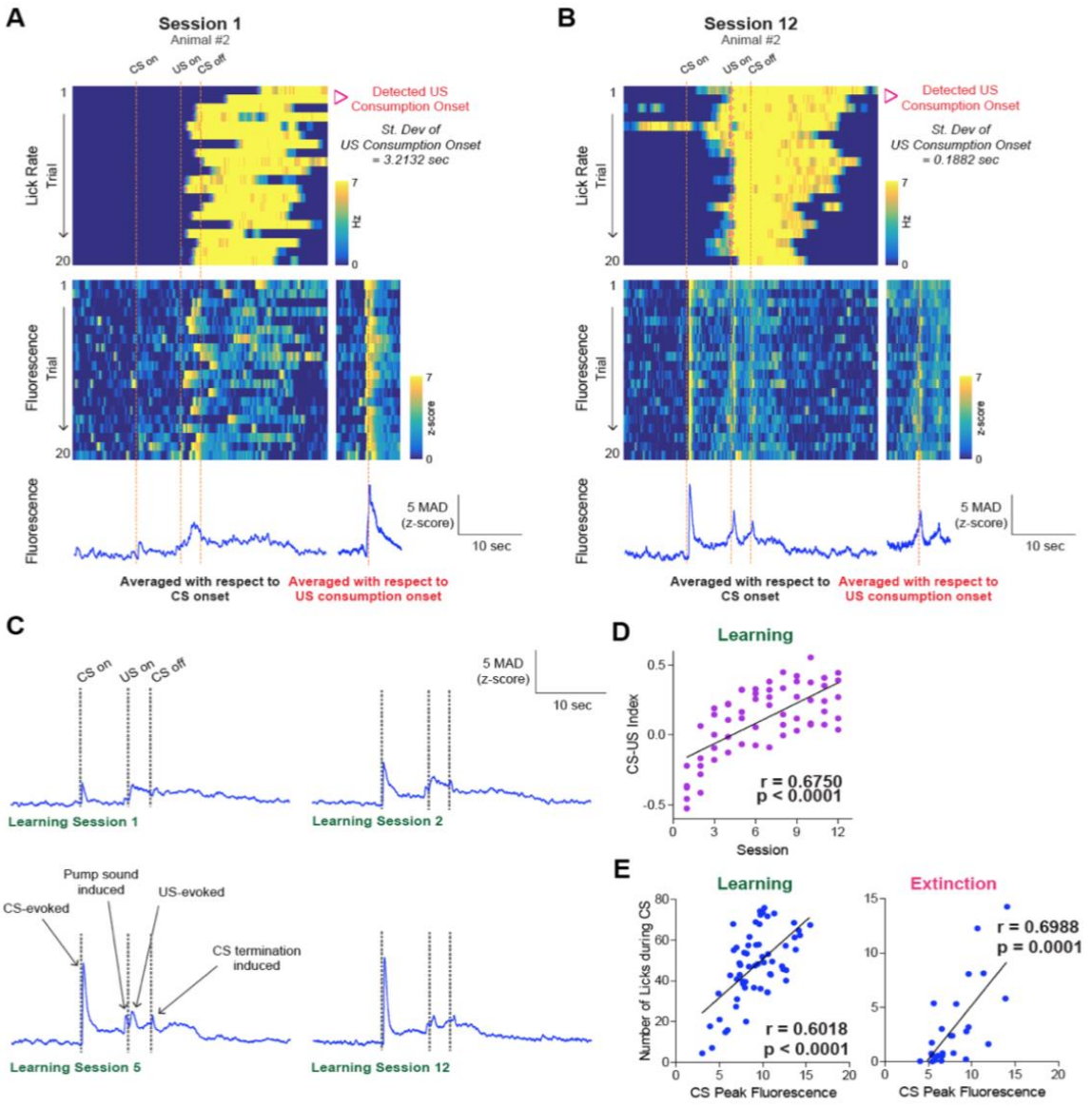

Fig. S14. Detection of US consumption onsets and details of DA dynamics after learning. (A) Individual trial heatmap data of lick rate (top) and fluorescence (bottom) from a mouse in learning session 1. Notice that lick onsets (indicated as magenta triangles or sudden color change from blue to yellow) are highly variable in this early session. When fluorescence is averaged from CS onset, fluorescence response from US is averaged or canceled out. However, when fluorescence is averaged from US consumption onset

(defined as lick onset after US is available), fluorescence peaks are aligned and results in higher US response. **(B)** Same as (A), but from learning session 12. After cue-reward association, mice show anticipatory lick behaviors in most of trials, therefore most lick onsets correspond to the time when US is available (t = 7 s after CS onset or second dotted line). Therefore, US response values are almost identical when fluorescence are averaged from CS onset or US consumption onset. (**C**) Averaged photometry traces from learning sessions 1, 2, 5, and 12. We observed total of four peaks in dLight1 fluorescence (best visible at the session 5): 1) CS-evoked (right after time = 0, which was dynamically modulated across learning and extinction), 2) pump sound induced (after time = 6), 3) US-evoked (after time = 7) and 4) CS termination induced (after time = 10) peaks. (**D**) CS-US index (see supplementary information for definition) increases across learning sessions, suggesting that fluorescence response is transferred from US to CS. **(E)** Positive correlations between CS peak fluorescence and licks during CS presentation, both in learning (left) and extinction (right) sessions.

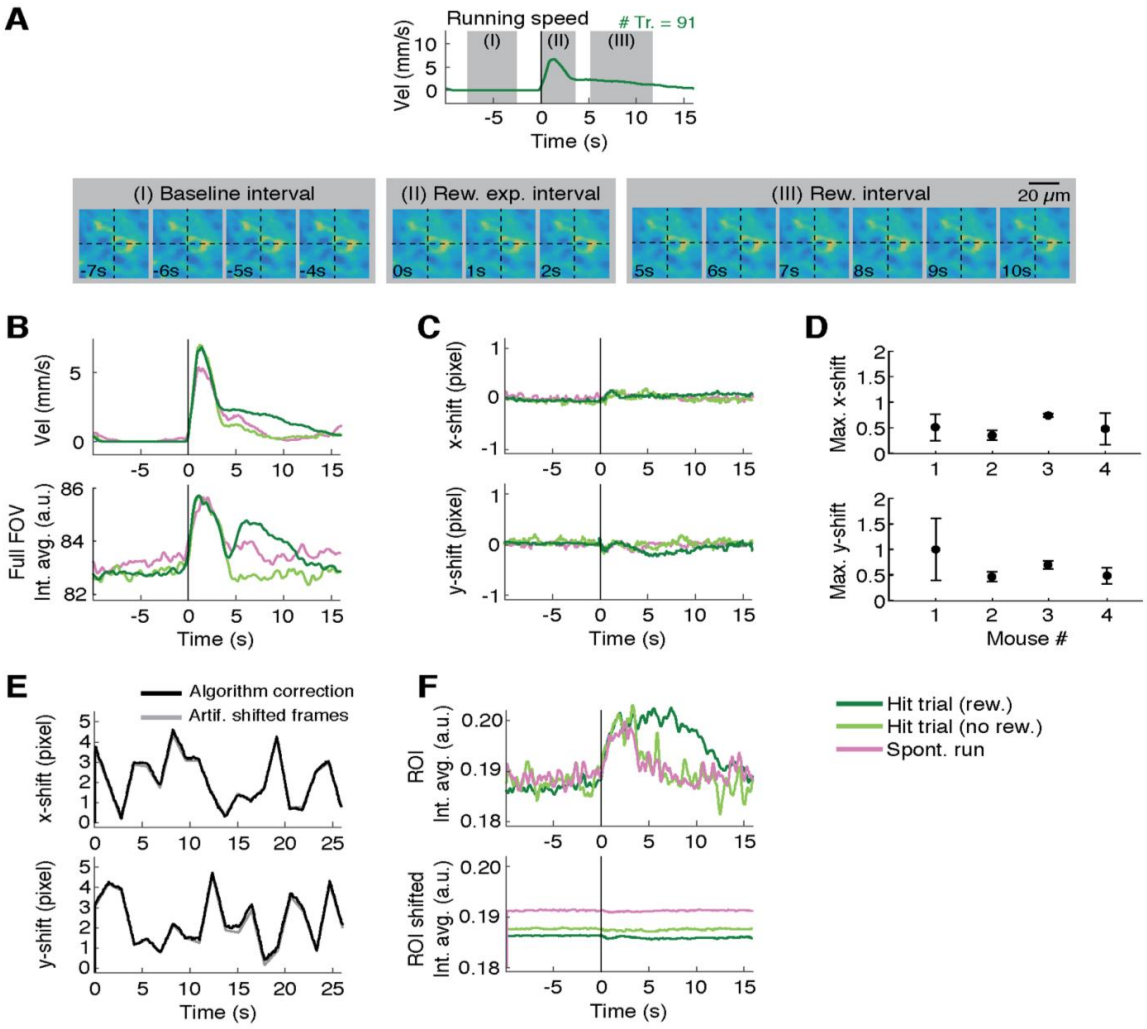

Fig. S15. Cortical dLight1 transients during animal behavior cannot be explained by image motion artifacts. (**A**) Top, average mouse running velocity for rewarded "Hit trials" from an example recording session. Data were aligned to running onset (vertical black line) prior to averaging. Three time intervals are indicated: "(I) Baseline interval" is part of the interval during which the animal was required to stand still; "(II) Reward expectation interval" defines the interval during which the mouse began to run and expected a reward; and "(III) Reward interval" defines the period during which the water reward was delivered in 80% of "Hit trials". Bottom, 40x45 pixel detail from the corresponding time-lapse

fluorescence imaging data. Image data was motion corrected prior to averaging (Methods). Image comparison (dotted crosshair) indicates that residual image movement was below one pixel within and across the baseline, reward expectation, and reward intervals. (**B**) Top, average mouse running velocity from the same recording session but for all trial types. Bottom, corresponding dLight1.2 fluorescence transients across the entire field of view (FOV). Data was motion corrected prior to averaging. Full FOV transients retain the main characteristics of the single ROI transients (Fig. 5E), but details about the spatio-temporal heterogeneity of DA release are lost. (**C**) Lateral image displacements detected by the motion correction algorithm for the example average data shown in panel B. Image displacements were below one pixel for all trial types. (**D**) Maximum lateral image displacements for all averaged recording sessions and all mice. Error bars indicate SEM. (**E**) The motion correction algorithm reliably detected sub- and supra-pixel image displacements. Artificially introduced shifts (grey) to the data shown in panels A-C were tracked by the algorithm with sub-pixel precision (black). (**F**) Top, task-related dLight1.2 fluorescence transients plotted as intensity average from an example ROI (from Fig. S16G). Bottom, transients extracted from the same ROI when applied to an artificially generated dataset in which the first frame of the top panel dataset was displaced using the lateral residual shifts shown in panel C. Intensity average transients produced by image shifts to the static first frame are negligibly small and distinct from task-related fluorescence transients.

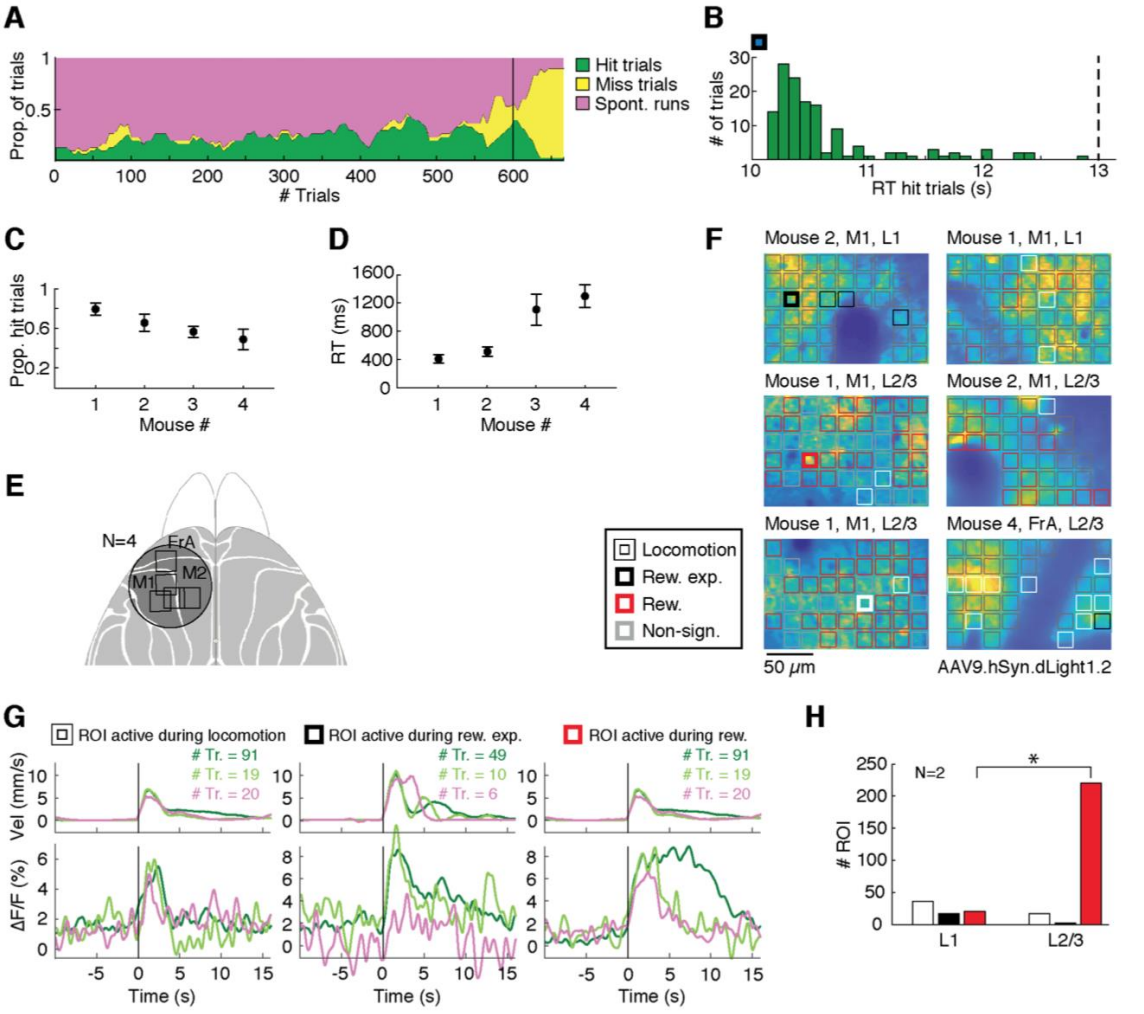

Fig. S16. Behavioral performance and single-session dLight1 transients during cortical two-photon imaging. (**A-D**) Mouse performance on the visuomotor association task during imaging sessions. (**A**) Example performance data from one recording session. Out of all trials in which the "Go" stimulus was presented, the proportion of "Hit trials" (green) was >80%. The "Go" stimulus was not presented in "Spontaneous runs" (pink) during the stand-still phase. Animals typically performed the task successfully for several hundred trials before a steep increase in "Miss trials" (yellow) indicated that they had lost interest in the water reward. Trials beyond that point (black vertical line) were excluded

from analysis. (**B**) Reaction times (RT) from an example recording session. Most "Go" stimulus-triggered runs happened within the first second after stimulus onset indicating that the mouse had learned the task. The dashed line at 13s indicates the "Go" stimulus offset. (**C**) Population data showing mean proportion of "Hit trials" for all mice (N=4) and recording sessions (mouse #1: 4 sessions; mouse #2: 9 sessions; mouse #3: 2 sessions; mouse #4: 4 sessions). (**D**) Mean RTs for all mice and recording sessions. Error bars in panel C and D indicate SEM. (**E**) Dorsal view of the mouse cortex with the imaging locations (square) from all mice indicated. (**F**) Example fluorescence image details showing dLight1.2 expression pattern for different mice and recording locations: M1 cortex, layer 1 and layer 2/3; FrA cortex, layer 2/3. The computationally defined regions of interest (ROIs), colored based on their response type, are overlaid. Single-session fluorescence transients of the highlighted ROIs (bold outlines) are shown in panel G. (**G**) Representative task-related dLight1.2 fluorescence transients from example recording sessions (population averages are shown in Fig. 5E). Top, mouse running speed on the spherical treadmill. Bottom, three common types of task-related fluorescence transients in M1. Left, example ROI showing significantly increased dLight1.2 fluorescence during locomotion but not reward; middle, ROI significantly active during reward expectation but not locomotion; right, ROI with significantly increased dLight1.2 fluorescence during the reward. Each colored trace is an average of the indicated number of trials aligned to running onset (vertical black line). $p<0.05$, Wilcoxon test, Bonferroni corrected for multiple comparisons. (**H**) Population data showing the number of ROIs with significant dLight transients in layer 1 (L1) and layer 2/3 (L2/3) of area M1 sorted by the three response types (see panel G and Fig. 5E). Significantly more reward related responses are seen in deeper

layers. * indicates significance, Binomial test, $p<0.05$, adjusted for total number of ROIs recorded in the respective layer.

2.13 Materials and methods

Molecular Cloning

All constructs were designed using circular polymerase extension cloning (CPEC) (Quan and Tian, 2011), restriction cloning, and gBlock gene fragments (Integrated DNA Technologies). Sequences coding for a hemagglutinin (HA) cleavable secretion motif and a FLAG epitope were placed at the 5'-end of the construct as in (Irannejad et al., 2013). HindIII and NotI cut sites were placed at the 5'- and 3'- end, respectively, for cloning into pEGFP-N1 (Addgene) to generate all pCMV constructs. BamHI and HindIII sites were introduced via PCR for final subcloning onto pAAV.*hSynapsin1* and pAAV.*CAG* vectors.

To maximize coupling between conformational changes and chromophore fluorescence, we chose to use a cpGFP module (LSS-LE-cpGFP-LP-DQL) from GCaMP6 (Chen et al., 2013) for insertion into DRD1 via CPEC. For screening linker variants, we generated a linker library by first creating an insert DNA carrying a 2 aminoacid-long randomized linker on each side of cpGFP (LSS-xx-cpGFP-xx-DQL). Single colonies were manually picked and grown overnight as described in (Tian et al., 2009). All sensor sequences generated in this study are listed in the Supplementary Data S1 file.

Structural modeling and sequence alignments

Sequence alignments were performed using Jalview software (UK) (Waterhouse et al., 2009) using a percentage identity color map. Inactive conformation of the sensor was predicted with rosetta_cm protocol of rosetta 3 (version 2015.31) (Song et al., 2013).

Primary sequence of sensor design was threaded with partial thread routine onto template PDB structures of inactive β_2 adrenergic receptor (Cherezov et al., 2007) (ID: 2RH1) and unbound state of GCaMP3 (Chen et al., 2013) (ID: 4IK3). The threaded structures were then hybridized together with rosetta_cm protocol for membrane protein (Bender et al., 2016). A total of 374 PDB structures were generated by rosetta_script routine. Structure with lowest total score was considered the final model.

Cell culture, imaging and quantification

HEK293T cells (ATCC #1573) and U2OS cells (ATCC #HTB-96) used in this study we cultured and transfected as in (Irannejad et al., 2013; Patriarchi et al., 2018). Primary hippocampal neurons were freshly isolated as previously described (Patriarchi et al., 2016). Neurons were infected using AAVs (1×10^9 GC/ml) at DIV5, two weeks prior to imaging. Prior to imaging, cells were washed with HBSS (Life Technologies). Cell imaging was performed using a 40X oil-based objective on an inverted Zeiss Observer LSN710 confocal microscope with 488/513 ex/em wavelengths. For testing sensor responses, neurotransmitters/drugs were directly applied to the bath during the imaging session. For neurotransmitter titrations, a dual buffer gravity-driven perfusion system was used to exchange buffers between different drug concentrations. Surface labeling was achieved as described previously (Irannejad et al., 2013; Patriarchi et al., 2018). One-photon emission spectrum for the sensors was determined using the lambda-scan function of the confocal microscope. Two-photon emission spectrum was obtained with a 40X water-based objective on a SliceScope (Scientifica) and was used to obtain the normalized two-photon cross-section using a custom-made script on MATLAB. For ROIs selection, masks were

generated either on the cell membrane or around the cytosol, depending on the experiment, using the threshold function in Fiji. We calculated spatial movies and images of $\Delta F/F$ in response to an applied ligand as $F(t) - \bar{F}_{baseline} \Big/ \bar{F}_{baseline}$ with $F(t)$ the pixel-wise fluorescent value at each time, *t*, and mean fluorescence in time points prior to ligand application, $\bar{F}_{baseline}$. To avoid the possibility of infinite pixel values, we added a small offset to each pixel in $\bar{F}_{baseline}$. Based on the $\Delta F/F$ maps we calculated a corresponding SNR map as $\Delta F/F \times \sqrt{\bar{F}_{baseline}}$. $\Delta F/F$ heatmaps were generated using a custom MATLAB script. Surface expression of sensors was quantified as the ratio of membrane fluorescence over cytoplasm fluorescence. For titration curves, Kd values were obtained by fitting the data with a Hill function on Igor Pro (WaveMetrics).

Dopamine-uncaging

Uncaging experiments on neuronal dendrites were performed in the presence of 100 μM caged-dopamine (carboxynitroveratryl-DA, CNV-DA (Robinson et al., 2017)) in the HBSS. Optical recordings were performed at 153 ms/frame scan rate. Uncaging was achieved by shining 405 nm light (40% laser power) on a 2 μm wide circular region selected 10 μm away from the dendrite surface.

Internalization assay with flow cytometry

24 hours post transfection, cells were re-plated onto 6 well dishes. The following day, surface levels of receptors were assayed by addition of Alexa-647-conjugated M1 antibody (Sigma) for 45 minutes, as described previously (Irannejad et al., 2013). Fluorescence

intensity profiles of cells populations (>5000 cells) were measured using a FACS-Calibur instrument (BD Biosciences). Each condition was performed in duplicate. Internalization was calculated by measuring the fraction of surface fluorescence remaining after 30 minutes of 1 μM SKF81297 (Tocris) and divided by the non-treated condition.

Luminescence-based cAMP assay

Experiments were conducted as previously described (Irannejad et al., 2013). Briefly, cells were transfected with the cyclic-permuted luciferase pGLOSensor-20F plasmid (Promega) and then treated with luciferin (GoldBio) in phenol and serum free media for 1 hour in a 24 well dish. Luminescence values for SKF81297 (Tocris) treated conditions were measured at their peaks and normalized with reference to 10 μM forskolin (Sigma) at its peak.

Total Internal Reflection Fluorescence Microscopy (TIRF-FM) Live Imaging

Live cell TIRF-FM was conducted with a Nikon Ti-E inverted microscope at 37°C in a controlled humidity and CO_2 controlled chamber as described previously (Irannejad et al., 2013). D1 specific agonist SKF81297 (Tocris) was added at 1 μM while D1 antagonist SCH23390 (Tocris) was added at 10 μM.

Preparation and transfection of cortical organotypic slice cultures

Rat hippocampal slice cultures were prepared from P6 – P7 pups as previously described (Stoppini et al., 1991; Zhong et al., 2009). pCMV-dLight1.2 (12μg) and pCMV-mCherry

(3μg) were mixed with single cell electroporation solution (160 mM NaCl , 5.4 mM KCl, 12mM $MgCl_2$, 2 mM $CaCl_2$, 5 mM HEPES, pH 7.4) to total volume of 36 μl. One-week old hippocampal cultured slices were transfected with single cell electroporation (Otmakhov and Lisman, 2012). 5 – 7 days after transfection, single hippocampal cultured slice was transferred to the imaging chamber in a custom built two-photon imaging setup. Slices were perfused in 10ml gassed artificial cerebral spinal fluid (ACSF) containing 4mM Ca^{2+}, 4mM Mg^{2+}, 0.5 μM TTX and 10μM cocaine (DA transporter blocker) during imaging.

AAV viral production

All dLight1 AAV constructs were cloned in the laboratory, and viruses were produced by the UC Davis Vision Center Vector Design and Packaging Core facility. The viral titers of the viruses used in this study were: AAV1.*CAG*.flex.tdTomato, ~8 x 10^{12} genome copies (GC)/mL (University of Pennsylvania); AAV5.*hSynapsin1*.flex.ChrimsonR.tdTomato, ~4 x 10^{12} GC/mL (University of North Carolina); AAV1. *hSynapsin1*.NES-jRGECO1a, ~3 x 10^{13} GC/mL (University of Pennsylvania); AAV1. *hSynapsin1*.dLight1.1, ~1 x 10^{12} GC/mL; AAV1. *hSynapsin1*.dLight1.2, ~2 x 10^{12} GC/mL; AAV9. *hSynapsin1*.dLight1.2, ~4 × 10^{12} GC/mL; AAV9.*CAG*.dLight1.1, ~7 × 10^{11} GC/mL; AAV9.*CAG*.control_sensor, ~1 x 10^{12} GC/mL.

Animals

Animal studies were conducted in compliance with the Guide for the Care and Use of

Laboratory Animals of the National Institutes of Health and approved by the Institutional Animal Care and Use Committee (IACUC) at the University of California, Davis or the relevant institutional regulatory body. Wild type rats were used in this study (0-2 months old) for neuronal and organotypic slice culture preparation and two-photon imaging in brain slice. Dopamine receptor-D1 (Drd1)-Cre mice (4-6 months old, Jackson Labs, Strain B6; 129- Tg(Drd1-cre)120Mxu/MMJax) were used for two-photon imaging in the dorsal striatum. Vesicular GABA transporter (VGAT)::IRES-Cre (Vong et al., 2011) (Jackson Labs, Slc32a1tm2(cre)Lowl/J) and Tyrosine hydroxylase (TH)::IRES-Cre (Lindeberg et al., 2004) (Jackson Labs, B6.129X1-Thtm1(cre)Te/Kieg) knock-in mice between 3 and 5 months old were used for in vivo imaging using fiber photometry and for optogenetic manipulations. Wild type male mice (2 to 5 months old, C57BL6/J, Jackson Laboratories) were used for two-photon in vivo imaging in the cortex. Sample sizes (number of mice) for each experiment are stated in main text. All animals were group housed in standard plastic cages on a 12-hour light/dark cycle with food and water available *ad libitum*, except for mice trained on the visuomotor association task (see below). These mice were house individually on a reverse 12-hour light/dark cycle. Anesthesia was performed with 4.5% isoflurane for induction and 2% for maintenance.

Viral injections

Injection procedures were essentially identical to those described in (Howe and Dombeck, 2016; Tufail et al., 2017; Matsui et al., 2014; Cardin et al., 2010) with a few exceptions.

For dopamine imaging in brain slice, male and female Sprague-Dawley rats (p23-27) were

used for intracerebral microinjections. Briefly, anesthetized rats were immobilized in a Stereotaxic Alignment System (Kopf Instruments). AAV1.*hSynapsin1*.dLight1.2 (200 nl) was injected unilaterally into the dorsal striatum using the following coordinates from bregma (in mm): 0.48 anteroposterior (AP), ±2.19 mediolateral (ML), 4.69 dorsoventral (DV).

For dopamine imaging in the dorsal striatum, mice were injected in the dorsal striatum at two caudal locations (+0.6 and +0.2 AP and 2.1mm ML to bregma) and 3 depths below the surface (-1.6mm, -1.9mm, and -2.2mm; 100 nL at each depth, total 0.6uL) with either AAV1. *hSynapsin1*.dLight1.1 or AAV1. *hSynapsin1*.dLight1.2 in combination with AAV1.*CAG*.flex.tdTomato (diluted 1:100 in PBS). The flex-tdTomato in our experiments is expressed in roughly half of the SPNs (Drd1-cre mice) to avoid potential issues, such as competition of expression when two AAVs are co-expressed in the same neurons.

For dopamine imaging using fiber photometry, AAV9.*CAG*.dLight1.1 or AAV9.*CAG*.control_sensor was injected into the NAc (+1.3 mm AP, -1.25 mm ML, -4.25 mm DV) and cre-dependent AAV encoding ChrimsonR-tdTomato was injected into the VTA (-3.3 mm AP, -0.5 mm ML, -4.3 mm DV). For dual color photometry experiments, AAV encoding jRGECO1a was 1:1 mixed with dLight1.1 virus and injected into the NAc region (+1.3 mm AP, -1.5 mm ML, -4.25 mm DV). A 10 μL NanoFil microsyringe (World Precision Instruments) with a blunt 35-gauge needle was used for viral injection and manipulated by a microsyringe pump (UMP3, World Precision Instruments) and a controller (Micro4, World Precision Instruments). 500 nL of AAV was slowly injected into

the target coordinates over 10 minutes, and additional 10 minutes were waited to allow diffusion. The needle was slowly withdrawn over 10-15 minutes.

For dopamine imaging in the cortex, anesthetized animals (4% isoflurane for induction; ~1.5% during surgery) were positioned in a computer-assisted stereotactic frame with digital coordinate readout and atlas targeting (Angle Two, Leica Biosystems Inc., Buffalo Grove, IL). Micropipettes were loaded with virus solution and slowly lowered into the brain under a ~32° injection angle until the target depth (~0.2 mm) was reached. Manual pressure was applied to a 30 mL syringe connected to the injection pipette. Virus solution was slowly injected over a period of 5–10 min. Once desired injection volume (200-400 nl) was delivered, the syringe's pressure valve was locked and position maintained for approximately 10 min to allow virus to spread and to avoid backflow upon needle retraction. Each mouse received two injections of AAV9. *hSynapsin1*.dLight1.2 (1:50 dilution). Injection coordinates were (AP 3-3.2 mm, ML 1- 1.2 mm) and (AP 1.5 mm, ML 1-1.5 mm).

Slice preparation

5% isoflurane was used to deeply anesthetize rats prior to decapitation. Brains were rapidly removed and placed in modified Krebs buffer containing (in mM) 126 NaCl, 2.5 KCl, 1.2 $MgCl_2$, 2.4 $CaCl_2$, 1.4 NaH_2PO_4, 25 $NaHCO_3$, 11 D-glucose, and with 10 μM MK-801. Horizontal slices (245 μm) were taken using a Leica vibratome and allowed to recover for at least 30 minutes prior to use in Krebs with MK-801 being continuously bubbled with

95/5% O_2/CO_2. Slicing and recovery was done at elevated temperatures (30-34° C). Following recovery, slices were secured in a recording chamber maintained at 34° C and perfused with modified Krebs at a rate of 3 ml/min.

Surgical procedures for in vivo imaging

Cannula implant for in vivo imaging in dorsal striatum

Two-weeks post-injection, a chronic imaging window was implanted over the external capsule fibers above the striatal injection site as described previously (Howe and Dombeck, 2016). Briefly, a 2.75mm craniotomy was performed on anaesthetized mice, and cortical tissue was slowly aspirated until the white matter of the external capsule was exposed. A thin layer of Kwik-Sil (WPI) was applied over the imaging region, and a metal cannula covered at one end by a glass coverslip was inserted into the aspiration site down to the fiber surface.

Optical fiber implantation for fiber photometry and optogenetics

Mice were anesthetized with isoflurane and carbogen mixture (4-5% for induction, 1.5-2% for maintenance) and carefully placed to a stereotaxic frame (Kopf Instruments) after shaving their hair. Head skin was sterilized with chlorohexidine and a midline incision was made using a sterile scalpel. The skull surface was exposed and cleaned with sterilized cotton swabs. Bregma and lambda points were identified and leveled to be at the same dorsal-ventral axis. Small craniotomy holes were made with drill bits (#73 size, Kyocera) over the nucleus accumbens (NAc) and ventral tegmental area (VTA). After viral delivery,

optical ferrule/fiber (for VTA/optogenetics, 300 μm diameter, 5-6 mm cut length, NA 0.37, home-made; for NAc/photometry, 400 μm diameter, 5 mm cut length, NA 0.48, Doric lenses) was mounted to a stereotaxic cannula holder (Doric lenses). First, a 400 μm fiber was lowered to the NAc through a craniotomy hole and stopped at 200 μm above the virus injection target. A layer of adhesive cement (C&B Metabond, Parkell Inc.) was applied to the anterior portion of skull surface to strongly hold the implanted ferrule. Care was taken not to apply Metabond near the posterior craniotomy sites for VTA. Next, a 300 μm fiber was inserted to the VTA and stopped at 500 μm above the injection site. Another layer of adhesive cement was applied to hold the second fiber. After adhesive cement was fully dried, a thick layer of dental cement (Lang Dental) was applied to build a head cap.

Head plate and cranial window implantation for in vivo imaging in the cortex

A few weeks after viral injections, mice were implanted with a head plate and cranial window on a custom surgical bed (Thorlabs Inc., Newton, NJ). Body temperature was maintained at 36–37 °C with a DC temperature control system and ophthalmic ointment was used to prevent eyes from drying. Skin was cleaned and disinfected with 70% ethanol and Betadine. A small (~10 mm) incision was performed along the midline. The scalp was pulled open and periosteum cleaned. First, a portion of the scalp was surgically removed to expose frontal, parietal, and interparietal skull segments. Then, the metal plate was affixed to the bone with C&B Metabond Quick Adhesive Cement (Parkell Inc., Edgewood, NY). Next, to enable chronic two-photon imaging, a custom-made cranial window was implanted, similar to (*55*). The craniotomy (2.5 mm diameter) was centered around (AP 2

mm and ML 1.5 mm) and sealed with a custom three-layered cover glass assembly (each No.1 thickness) with the two layers closest to the cortex consisting of two pieces of circular 2.5 mm-diameter cover glass and the outermost layer consisting of a circular 4 mm-diameter cover glass that rested on the thinned skull. The dura mater was kept intact.

Behavioral experiments

Sucrose consumption

Mice were handled daily for 5-10 minutes to reduce anxiety associated with experimenter's handling. Following recovery from surgery (~7 days) mice were water-restricted to 1.5 mL per day and maintained at 85-90 % of ad libitum weight. All behavioral experiments were carried out in an operant chamber within a sound-attenuating box (Lafayette Instruments). Behavioral tasks were implemented and controlled by ABET II software (Lafayette Instruments). TTL pulses were used to synchronize with fiber photometry recordings. After at least 7 days of water deprivation, mice were introduced to an operant chamber and allowed to freely explore with a patch cord connected. 50 μL of 5 % sucrose water was delivered every 60 seconds (total 10 times) so that mice can learn the position of a lick port. Lick was detected as a break of infrared beam at the lick port. This habituation session was repeated two to three times for each mouse until they showed robust lick activity (>400 licks per session). At the recording day, mice underwent the same sessions while recording dLight1 fluorescence with fiber photometry. For analysis, mean fluorescence values were obtained from baseline (-10~-5 s from lick onset) and during consumption (0~5 s).

Unpredictable footshock delivery

Mice were placed into an operating chamber with a patch cord connected for photometric recordings. Five electric footshocks (0.6 mA for 1 second) were delivered with variable intervals (randomly chosen from uniform distribution between 45 and 75 seconds) without predictive cues. This was performed after all other experiments, since such aversive stimuli can induce sustained fear and anxiety to the context. For analysis, mean fluorescence values were obtained from baseline (-5~-1 s from lick onset) and during footshock (0~2 s).

Cue-reward learning and extinction

In cue-reward learning sessions, CS was turned on for 10 seconds and US was available 7 seconds after CS onset, after variable inter-trial intervals (ITI). In cue-reward extinction sessions, same CS was turned on for 10 seconds without US delivery after variable ITI. In "expected reward delivery" trials, US was delivered after CS presentation, as in previous learning sessions.

After sucrose consumption experiments, mice started appetitive Pavlovian conditioning, or cue-reward learning, in the same operant chamber. Conditioned stimuli (CS) consisted of house-light and 70 dB 5kHz tone, and were turned on for 10 seconds with variable intervals (randomly drawn from uniform distribution between 75 and 105 seconds). Unconditioned stimulus (US) was 50 μL of 5 % sucrose water, available at the 7th second after each CS onset. Pump sound from liquid dispenser was audible from 6th to 7th seconds. CS-US pairings were repeated 20 times per session (therefore ~30 minutes for each session). Mice

underwent a total of 12 sessions for cue-reward learning. Chambers and lick port were sanitized with Accel and 70% ethanol between animals to remove any odor. For all sessions, lick data and photometry recordings were simultaneously obtained. Two to three days after the last cue-reward learning sessions mice began cue-reward extinction. Identical CS were given 30 times per session with variable intervals (between 45 and 75 seconds), now without US delivery. Mice underwent total of 5 extinction sessions. To quantify CS-triggered behavior, number of licks was counted during CS presentation. For photometry data, peak fluorescence was obtained for CS (0~3 s after CS onset) and US (-2~5 s around US consumption onset). US consumption onset for each trial was defined as the lick bout onset after US is available, where lick bout onset was detected with a threshold of 2 Hz. To examine fluorescence response shift from US to CS (or vice versa), we calculated CS-US index, defined as (CS response – US response) / (CS response + US response).

Unexpected reward delivery and omission

After 12 cue-reward learning sessions, mice underwent reward prediction error experiments. In “unexpected reward delivery” session, animals were exposed to normal CS-US pairing trials; but in 25% of trials, US was delivered without CS, so that mice can explore to the lick port without predictive cues and consume reward in an unexpected manner. Peak fluorescence values after US consumption onset was obtained and compared between expected and unexpected conditions. In “unexpected reward omission” sessions, US delivery was omitted in 4 out of 20 trials (4th, 8th, 13th, and 16th trials) after predictive CS onset. For analysis, mean fluorescence values were obtained from baseline (-10~0 s

from CS onset) and after CS offset (10.5~11.5 s) and compared.

Visuomotor learning task

Prior to surgical preparation and behavioral training, mice were handled/tamed on two consecutive days to reduce stress during experiments. Following recovery from surgery (~7 days) mice were water-restricted to 25 ml kg^{-1} per day and maintained at 80-85% of ad libitum weight. Training was performed in a custom-built setup that included a color LCD monitor (12.1" LCD Display Kit/500cd/VGA, ICP Deutschland GmbH) on which visual stimuli were presented. To reduce noise in optical recordings, the monitor was covered with a color filter (R342 Rose Pink, Rosco Laboratories Inc.). During training, mice were head-fixed with a custom-build head holder and placed on a spherical treadmill (Habitrail Mini Exercise Ball, Animal World Network) facing the LCD display. An optical encoder (E7P OEM, US Digital) attached to the treadmill allowed measurement of both speed and direction of ball movement. Water reward was delivered with a programmable syringe pump (NE-500 OEM Syringe Pump, New Era Pump Systems, Inc.). Behavioral signals were acquired through a data acquisition board (PCI-6221, National Instruments) connected to a breakout box (BNC-2110, National Instruments) and interfaced to MATLAB using the Data Acquisition Toolbox (Version R2010bSP2, The MathWorks Inc.). Behavioral task sequence was controlled by the MATLAB-based software MonkeyLogic (www.monkeylogic.net) (Assad and Eskandar, 2008; Assad et al., 2013). Custom-written functions were added to MonkeyLogic to enable analysis and control of ball rotation parameters. Treadmill encoder signals, trial marker codes (generated by

MonkeyLogic), and imaging data were acquired in synchrony allowing running parameters, behavioral task events, and image frames to be linked.

Once the mouse stopped moving on the ball, a sequence of task events was initiated. First, a blue square frame was displayed on the monitor and required the animal to continue to stand still for a period of 10 s (ball rotation/velocity ≤ 2 mm/s). If the mouse continued to stand still for the entire stand-still phase, a second stimulus, a filled blue square, was presented for 3 s, instructing the mouse to initiate a run. If the mouse initiated sustained movement (ball rotation/velocity >10 mm/s for >1s duration) during the 3s stimulus phase, a water reward was delivered. In 20% of pseudo-randomly selected trials the reward was withheld ("Unexpected reward omissions"; light green traces in Fig. 5, Fig. S15 and S16). If no running occurred, the trials counted as a miss trial. If the animal began to move during the 10 s stand-still phase (ball rotation/velocity > 2 mm/s), the trial was aborted and no water reward was delivered ("Spontaneous run trials"; pink traces). The mouse was able to initiate a new trial after an intertrial interval (ITI) of 5 s.

During the first two days of training, mice spent ~15-30 min/day in the setup to become accustomed to head restraint. Mice were then trained daily for 60-90 min during which they performed ~300-700 trials. Task parameters were adjusted depending on individual animal's performance. Initially, the duration of the stand-still phase was set to 3 s, the stimulus phase to 20 s, and the running threshold to 2 mm/s. This increased the chance for the mouse to receive the task-dependent reward. The stand-still phase was then

progressively extended and the stimulus phase shortened to establish the association between stimulus onset and running onset. Training continued until median reaction times (RT) had dropped below 1500 ms, which indicated that mice had learned to associate the visual cues with the desired behavior. Task proficiency was typically reached within 5-7 days. During the initial training phase all successful "Go" trials were rewarded. Unexpected reward omission trials were introduced during imaging sessions only.

In vivo optogenetic and pharmacological manipulations

For optogenetic experiments, a patch cord (1 m length, 1.25 mm zirconia ferrule, 300 μm diameter fiber, Doric lenses) was used to connect to a ferrule on an animal's head cap and a swivel commutator (fiber-optic rotary joints, Doric lenses) to allow free movement. Another patch cord was connected from the commutator and to a 635 nm diode-pumped solid-state laser (Changchun New Industries Optoelectronics Technology). The intensity of laser was measured with a power meter (PM100D, Thorlabs) and calibrated to be 10 mW at the fiber tip. An external TTL pulse generator (OTPG4, Doric Lenses) was used to control the laser output. For activating VTA DA neurons, 5 Hz, 10 Hz, and 20 Hz of 10 ms pulses were applied for 2 seconds. For activating VTA GABA neurons, 40 Hz pulses were used (Eshel et al., 2015). These pulse trains were repeated 40 times per animal with intervals of 30 seconds. For pharmacological manipulations, the following drugs were used: DRD1 antagonist (SCH-23390, 0.25 mg/kg) and selective DA reuptake inhibitor (GBR-12909, 10 mg/kg) (Park et al., 2011). Animals were injected with these drugs or saline (0.9% sodium chloride) through intraperitoneal delivery 30 minutes before optogenetics/photometry experiments. Mean or peak fluorescence values were obtained

before (-5~-1 s from onset), during (0.5~2 s) or after (4~10 s) photoactivation.

Data acquisition and analysis for ex vivo and in vivo imaging

Ex vivo imaging in rat brain slice

Imaging was carried out in a custom built 2-photon microscope. Data were acquired and collected using ScanImage software (Pologruto et al., 2003). Slices were scanned at different frequencies, depending on the experiment, using 920 nm light. Electrical stimulation through a glass mono-polar electrode placed within the slice near the area of imaging was used to evoke dopamine release. Experiments were carried out with a scan rate of 2 (128x128 pixels) or 15 (32x32 pixels) Hz. The fluorescence over the entire field (20x20 μm) was measured for each frame and plotted against time. Drugs were applied by superfusion. Line scans were taken at a 500 Hz frame rate. To measure the dopamine response curve, two-photon images were taken every minute. Image analysis was performed using custom software written in MATLAB.

In vivo imaging in mouse dorsal striatum

Treadmill velocity and acceleration were sampled at 1000Hz by a rotary encoder (E2-5000, US Digital) attached to the axle of the treadmill. Two-photon imaging was performed as described previously (Sheffield et al., 2017), using the same collection optics, but without the electric lens. 920 nm laser light was used for excitation and 1024x512 pixels time series datasets were acquired at 30 Hz. Imaging sessions began after mice were acclimated to head fixation and ran frequently on the treadmill (~1-3 days). Imaging data was collected over 1-2 days from dorsal striatum fields ranging from 250 to 450μm in diameter. All

analyses were carried out using custom software written in MATLAB. Time series movies were motion corrected on the static red channel using algorithms described previously (Dombeck et al., 2010) and x and y shifts from the red were used to correct the green channel. Mean whole field fluorescence was calculated from a large, hand-selected ROI containing all regions of the field with visible cellular structure in the red tdTomato channel. Fluorescence time series were converted to ΔF/F by normalizing signals to an 8th percentile baseline (Dombeck et al., 2010) within a sliding window (+/-15s around each point) to correct for slow drift and bleaching. Significant positive-going transients were calculated as previously described (Dombeck et al., 2010).

In vivo imaging with fiber photometry

Fiber photometry was performed as in (*28, 63, 64*). For dual color imaging a three LED system was used (FMC7, Doric Lenses): 490 nm for dLight1, 565 nm for jRGECO1a, and 405 nm to be used as isosbestic wavelength for both indicators. The following dichroic filters and excitation/emission filters were used (all from Semrock): Di02-R405, Di02-R442, FF495-Di03, FF552-Di02, FF593-Di03, FF01-405/10, FF01-433/24, FF01-475/28, FF02-520/28, FF01-565/24 and FF02-641/75 (Gunaydin et al., 2014; Lerner et al., 2015; Cho et al., 2017). Acquired photometry data were processed with custom-written codes in MATLAB. Raw data from each channel were low-pass filtered at 25 Hz (for single color imaging) or 12 Hz (for dual color imaging) using a 2nd order Butterworth filter with zero-phase distortion. To calculate ΔF/F time series, a linear fit was applied to the 405 nm signals and aligned to the 490 and 565 nm signals. The fitted 405 nm signal was subtracted

from 490 and 565 nm channels, and then divided by the fitted 405 nm signal to yield ΔF/F values. Dual color imaging data were down-sampled to 100 Hz. In Pavlovian conditioning, ΔF/F time-series signal is further normalized using robust Z-score (subtraction of median and division by median absolute deviation, calculated from the entire session) to account for potential differences in signal variance across animals and sessions. Photometry signals were then extracted around relevant behavioral events (e.g., lick onset, footshock delivery, CS onset) and averaged. Power spectral density was estimated for averaged dLight1/control sensor fluorescence data upon optogenetic stimulation of different frequencies. We used Welch's method with 2-second window size and 50% overlap to estimate power from 0.5 to 25 Hz in 0.1 Hz step.

In vivo two-photon imaging in the cortex

Once mice had reached proficiency on the task, they were imaged daily for up to 9 days. Imaging was performed using a resonant scanning two-photon microscope (Sutter Instrument) equipped with a pulsed femtosecond Ti:Sapphire laser (Chameleon Ultra II, Coherent). dLight1 fluorescence was excited with 910 nm light, and detected using a ET525/70M emission filter (Chroma Technology Corp.) and H7422-40 GaAsP photomultiplier tube (Hamamatsu Photonics). Average excitation power was 40-130 mW depending on imaging depth and dLight1 expression levels/duration. Typical recording depth was 80-150 μm below the pia. Data were acquired using a Nikon 16x 0.8-NA water immersion objective. A custom-made blackout curtain around the microscope's detector was used to reduce light contamination by the LCD monitor. Images (512×512 pixels) were acquired at 30.8 frames/sec. Recording sessions consisted of five to twelve ~10 min

recordings, separated by short imaging breaks (3-5 min). Recordings within a given session were performed at the exact same location to maximize the number of trial repetitions for analysis. Recordings from different sessions were performed at the same injection sites but offset either laterally or axially to maximize tissue volume being sampled.

Analysis of cortical in vivo imaging data

All data were analyzed using custom code written in MATLAB (MathWorks). Data from four animals were included in the analysis. Mouse #1 underwent 4 recording sessions starting 8 weeks after virus injection. Mouse #2 underwent 9 recording sessions starting 3 weeks after injection. Mouse #3 underwent 2 recording sessions starting 2 weeks after injection and Mouse #4 underwent 4 recording sessions starting 6 weeks after injection. Recording locations (M1/M2/FrA) are indicated in Fig. S16E.

To confirm the animals' responsiveness to the "Go" stimulus, we compared proportions of trials in which runs were triggered by "Go" stimulus presentation ("Hit trials") and proportions of trials in which no such response occurred ("Miss trials") (Fig. S16A and C). A steep increase in "Miss trials" at the end of the session indicated that mice had lost interest in the water reward. Trials beyond that point (black vertical line in Fig. S16A) were excluded from analysis. To confirm that mice had learned the task, we analyzed the animals' RTs (defined as the time interval between "Go" stimulus onset and movement onset/ball velocity >10 mm/s) (Fig. S16B and D). RTs below 1500 ms indicated that mice had learned to associate the visual cues with the desired behavior.

To reduce random noise in our time-lapse recordings a sliding average filter was applied (8 frames or 260 ms). This filtering largely retained the temporal dynamics of dLight1 fluorescence signals. Lateral image motion (e.g., due to mouse movement) was corrected using a cross-correlation registration algorithm, with an average image of 50 consecutive frames from the time-lapse recording serving as the reference image. The same reference image was used to correct image motion of other recordings from the same location. Noise in motion-corrected image data was further reduced using a Kalman filter.

To quantify/classify dLight1 transients, we tiled the field of view (FOV) with equally sized (~17x17μm) regions of interest (ROIs). To exclude ROIs with little or no dLight1 expression (e.g., on blood vessels) we first generated a mean fluorescence projection image from the corresponding time-lapse recording. We then calculated the projection image's pixel intensity distribution. ROIs with mean pixel intensity values below the 55^{th} percentile of this distribution were excluded from analysis. To extract fluorescence time traces F(t) from all remaining ROIs, pixel intensities of each ROI were averaged. $\Delta F(t)/F$ was calculated as (F(t) – mean F) / mean F. ROIs that showed transients with negative amplitudes (predominantly located near blood vessels) were excluded from further analysis.

Each ROI's time trace included multiple trials/task repetitions. Based on the animal's performance on the trials, time traces were subdivided into "Expected reward",

"Unexpected reward omission", and "Spontaneous run" trial traces. This was done for all recordings from the same location using the same ROIs. Extracted trial traces were then sorted by trial type, aligned to running onset, and averaged (Fig. S16G, single ROIs). To ensure that cued and spontaneous running bouts were comparable, only traces from spontaneous runs starting > 5 s after stand-still cue onset and with > 5 mm/s ball rotation/velocity were included. To calculate population responses, "Expected reward", "Unexpected reward omission", and "Spontaneous run" trial traces from all animals, all sessions, and all significant ROIs were averaged (Fig. 5E, group average).

To identify ROIs with significant increases in dLight1 fluorescence in response to the task, three analysis intervals were defined (Fig. S15A): (I) Baseline (from -7 to -2 s prior to run onset), (II) reward expectation (from run onset to 3.3 s after run onset), and (III) reward interval (from 4.3 s to 10.8 s after run onset). $\Delta F/F$ traces for each trial were averaged during the three trial intervals respectively. The distributions of the averaged $\Delta F/F$ traces for particular trial types were then statistically compared among each other and between intervals. ROIs that showed significant fluorescence increases during the reward expectation but not the reward interval, and for all trial types compared to the baseline interval, were defined as "ROI active during locomotion" (white squares in Fig. 5 and Fig. S16G). ROIs that showed significant fluorescence increases during the reward expectation but not reward interval for cued/triggered but not spontaneous run trials were classified as "ROI active during reward expectation" (black squares). Finally, ROIs that showed significant fluorescence increases during the reward interval for rewarded but not un-rewarded or spontaneous run trials were defined as "ROI active during reward" (red

squares). Significance was determined using the Wilcoxon's rank-sum test ($p<0.05$), Bonferroni corrected for multiple comparisons.

All ROI analysis was performed on motion corrected image data (see above) averaged across trials of the same type and from the same session. To investigate whether this averaging introduces artifacts in the DA transients (e.g., due to stereotypic running-related image movements) we inspected our data more closely at cellular and population levels. Close observation of a 40x45 pixel detail of the motion corrected image data revealed stable and sharp images even during the most vigorous running periods (Fig. S15A). Next, we plotted the full field of view (FOV) intensity changes for the average data of each trial type aligned at run onset (Fig. S15B). This revealed that the main characteristics of the single ROI transients are retained in the full FOV average, arguing against a pronounced contamination by motion artifacts. Next, to investigate residual lateral shifts in the average image data for each trial type, we applied our motion correction algorithm. The detected residual image motion was <2 pixels for all sessions and mice (Fig. S15C and D). To verify that our motion correction algorithm reliably detects sub- and supra-pixel image displacements we artificially introduced random lateral shifts of up to 5 pixels to the same average image data (Fig. S15E). The error between the introduced shifts and the shifts detected by the algorithm across 100 repetitions was 0.089 ± 0.001 pixels (mean ± SEM). Together, this suggests that DA transients extracted from our 17x17μm ROIs are unlikely an artifact of image motion (Fig. S15F).

Histology

Histological verification of proper sensor expression was as described previously (Cho et al., 2017). Primary antibodies used were: chicken anti-GFP (1:500; GFP-1020, Aves Labs), chicken anti-TH (1:500; TYH, Aves Labs) and rabbit anti-RFP (1:500; 600-401-379, Rockland A&A).

Hybrid chain reaction combined with immunohistochemistry

To assess the expression pattern of ChrimsonR-tdTomato injected into the VTA of VGAT::IRES-Cre mice, we performed combined in situ hybridization for labeling *vgat* mRNA and immunohistochemistry (IHC) for detecting DAergic neurons (with TH). To achieve high-sensitivity in situ hybridization of *vgat* in tissue slices, we used hybridization chain reaction (HCR) (Choi et al., 2014; Choi et al., 2018). First, we designed 22 probes for targeting *vgat* using a custom written software (available at https://github.com/GradinaruLab/HCRprobe). Each probe consists of 20-nt target sequence, 2-nt spacer, and 18-nt initiator. We selected the target sequences that has (1) the GC content of 45-60%, (2) no nucleotide repeats more than 3, (3) no more than 20 hits when blasted, (4) higher than a ΔG of -9 kcal/mol to avoid self-dimers. Then we blasted full sequences (target sequences with spacer and initiator) and calculated Smith-Waterman alignment scores between all possible pairs to exclude probes forming cross-dimers. The designed probes were synthesized by Integrated DNA Technologies.

HCR was performed on 50 μm-thick slices and kept in RNAlater solution (ThermoFisher Scientific). Slices were permeabilized in PBST (1xPBS with 0.1% Triton X-100) for 1 hour at room temperature (RT) and pre-hybridized in hybridization buffer (2x saline-sodium

citrate (SSC) , 10% ethylene carbonate, 10% dextran sulfate) for another hour at 37°C. Then the samples were incubated in pre-warmed hybridization buffer including probes (2 nM for each) at 37°C overnight. After hybridization, we performed stringent washes with wash buffer (2xSSC, 10% ethylene carbonate) for 30 min at 37°C and washes with 2xSSC for 30 min at RT (twice for each). The amplification step was performed as described in (Shah et al., 2016) overnight. For IHC labeling of TH on HCR-labeled tissue slices, we used IHC buffer consisting of 2x SSC, 1% donkey serum, and 0.1% Triton X-100. We incubated the samples in IHC buffer for 1 hour at RT for blocking and added primary antibody (anti-TH, AB152, Millipore, 1:200). Primary antibody reaction was performed for overnight at RT. Following the wash steps with 2xSSC at RT for 30 min twice, the samples were incubated in IHC buffer including secondary antibodies (1:200) for overnight at RT. The samples were rinsed with 2xSSC a few times and mounted on a glass slide with mounting media (Prolong Diamond, ThermoFisher Scientific).

Probe sequences (5'->3')

1	CACTTCATATCACTCACTaaGACACGGAGGTGGCCACATT
2	CACTTCATATCACTCACTaaGCGATGCTCAAAGTCGAGAT
3	CACTTCATATCACTCACTaaCCTGAATGGCATTTGTCACG
4	CACTTCATATCACTCACTaaACCAGGACTTCTGCGACACG
5	CACTTCATATCACTCACTaaTTCTTCAGGAAGGCGCAGGG
6	CACTTCATATCACTCACTaaTTCTCCCAGGCCCAATCACG
7	CACTTCATATCACTCACTaaGTGTAGCTGAACACGATGAT
8	CACTTCATATCACTCACTaaGCGGCGATGTGTGTCCAGTT

9	CACTTCATATCACTCACTaaACTTCCTTGGTCTCGTCGGC
10	CACTTCATATCACTCACTaaCGCGAAGAAGGGCAACGGAT
11	CACTTCATATCACTCACTaaAGGCGCAAGTGGAAGAGGCT
12	CCTTGGCCTGGGACTTGTTGaaCCCAATCTCTATCTACCC
13	ATGTCCATCTGCAGGCCCTGaaCCCAATCTCTATCTACCC
14	TAGGCCCAGCACGAACATGCaaCCCAATCTCTATCTACCC
15	CACCGCTGTGGCTATGATGGaaCCCAATCTCTATCTACCC
16	ACTTGGACACGGCCTTGAGAaaCCCAATCTCTATCTACCC
17	CGTCGATGTAGAACTTCACCaaCCCAATCTCTATCTACCC
18	AGGGCAGGAAGATCTGCGACaaCCCAATCTCTATCTACCC
19	AGAGACCCTTGAGCACGCAGaaCCCAATCTCTATCTACCC
20	CGGGCAGGTTATCCGTGATGaaCCCAATCTCTATCTACCC
21	TTCTCCAGCACTTCGACGGCaaCCCAATCTCTATCTACCC
22	ACAGCAGCTTGCGCCAGAGAaaCCCAATCTCTATCTACCC

Statistical Analysis

All statistical analyses were performed in MATLAB (MathWorks), Igor Pro (WaveMetrics) or Prism (GraphPad). We used both parametric (t-test, one-way ANOVA, two-way ANOVA) and non-parametric (Wilcoxon's rank-sum) tests. Pearson's correlation coefficients and their p-values were calculated to assess how behavior or dLight1 fluorescence evolved across reward learning or extinction. All tests were two-tailed. Error bars are standard error of the mean or standard deviation as indicated in Figure legends and

main text. No statistical methods were used to predetermine sample size.

2.14 Additional information

ACKNOWLEDGMENTS

We thank B. P. McGrew for assistance during in vitro sensor library screening; H. Cheng for producing AAV virus; L. Lavis (Janelia Research Campus) for providing NV-caged DA; E. Carey for performing cortical viral vector injections; and B. Mensh for critical advice in writing and revising the manuscript. This project was made possible with generous help from L. Looger (Janelia Research Campus). **Funding**: Supported by NIH BRAIN Initiative U01NS090604 and U01NS013522, DP2MH107056 (L.T.); DP2NS083038, R01NS085938, P30CA014195 (A.N.); BRAIN Initiative U01NS013522 (J.T.W. and M.v.Z.); BRAIN Initiative U01NS094247 and R01NS104944 (H.Z.); NIH 1R01MH110556 (D.D.); and NIH DP2NS087949, NIH/NIA R01AG047664 (V.G.). K.M. is a DFG research fellow and recipient of a Catharina Foundation postdoctoral scholar award. V.G. is a Heritage Principal Investigator supported by the Heritage Medical Research Institute. **Author contributions**: L.T. and T.P. conceived the project; T.P. and L.T. designed, screened, and optimized sensors and characterized them in mammalian cells and cultured neurons; R.L. simulated the structure of the sensor; A.M. and M.v.Z. characterized signaling properties of the sensor; W.H.X. and H.Z. characterized the sensor in organotypic brain slices; J.T.W. performed characterization in acute brain slices; M.W.H. and D.D. characterized the sensor in vivo in the dorsal striatum; J.R.C. and V.G. performed fiber photometry recordings coupled with optogenetic manipulations, calcium imaging, and behavioral experiments in NAc, analyzed the data, and prepared the related Figures and text; M.J.J. performed hybridization chain reaction experiments and prepared

relevant figures and text with input from J.R.C. and V.G.; K.M., R.W.F., and A.N. performed the two-photon imaging experiments in the cortex of behaving mice, analyzed the data, and prepared the related figures and text; all authors analyzed the data; L.T. led the project; and L.T. and T.P. wrote the paper with contributions from all authors. **Competing interests**: L.T., R.L., and T.P. have submitted a provisional patent application on sensor engineering. **Data and materials availability**: All DNA and viruses have been deposited in NCBI (accession number MH244549-MH244561), ADDGENE, and the University of Pennsylvania Vector Core. All DNA plasmids and viruses are available from UC Davis or designated repository under a material transfer agreement. Computer codes are deposited in github (https://github.com/GradinaruLab/dLight1/). All other data needed to evaluate the conclusion in the paper are present in the paper or the supplementary materials.

2.15 Reference

Asaad, W.F. and Eskandar, E.N. (2008). A flexible software tool for temporally-precise behavioral control in Matlab. J. Neurosci. Methods 174, 245–258.

Asaad, W.F., Santhanam, N., McClellan, S., Freedman, D.J. (2013). High-performance execution of psychophysical tasks with complex visual stimuli in MATLAB. J. Neurophysiol. 109, 249–260.

Bender, B.J. et al. (2016). Protocols for Molecular Modeling with Rosetta3 and RosettaScripts. Biochemistry 55, 4748–4763.

Brischoux, F., Chakraborty, S., Brierley, D.I., Ungless, M.A. (2009). Phasic excitation of dopamine neurons in ventral VTA by noxious stimuli. Proc. Natl. Acad. Sci. U.S.A. 106, 4894–4899.

Cardin, J.A. et al. (2010). Targeted optogenetic stimulation and recording of neurons in vivo using cell-type-specific expression of Channelrhodopsin-2. Nat. Protoc. 5, 247–254.

Chen, T.W. et al. (2013). Ultrasensitive fluorescent proteins for imaging neuronal activity. Nature 499, 295–300.

Chen, Y. et al. (2013). Structural insight into enhanced calcium indicator GCaMP3 and GCaMPJ to promote further improvement. Protein Cell 4, 299–309.

Cherezov, V., et al. (2007). High-resolution crystal structure of an engineered human beta2-adrenergic G protein-coupled receptor. Science 318, 1258–1265.

Cho, J.R. et al. (2017). Dorsal Raphe Dopamine Neurons Modulate Arousal and Promote Wakefulness by Salient Stimuli. Neuron 94, 1205–1219.e8.

Choi, H.M., Beck, V.A., Pierce, N.A. (2014). Next-generation in situ hybridization chain reaction: Higher gain, lower cost, greater durability. ACS Nano 8, 4284–4294.

Choi, H.M.T. et al. (2018). Third-generation in situ hybridization chain reaction: Multiplexed, quantitative, sensitive, versatile, robust. bioRxiv 285213 [preprint].

Clark, J.J. et al., Chronic microsensors for longitudinal, subsecond dopamine detection in behaving animals. Nat. Methods 7, 126–129.

Cohen, J.Y., Haseler, S., Vong, L., Lowerll, B.B., Uchida, N. (2012). Neuron-type-specific signals for reward and punishment in the ventral tegmental area. Nature 482, 85–88.

Courtney, N.A. and Ford, C.P. (2014). The timing of dopamine- and noradrenaline-mediated transmission reflects underlying differences in the extent of spillover and pooling. J. Neurosci. 34, 7645–7656.

Cui, G. et al. (2013). Concurrent activation of striatal direct and indirect pathways during action initiation. Nature 494, 238–242.

da Silva, J.A., Tecuapetla, F., Paixão, V., Costa, R.M. (2018). Dopamine neuron activity before action initiation gates and invigorates future movements. Nature 554, 244–248.

Dana, H. et al. (2016). Sensitive red protein calcium indicators for imaging neural activity. eLife 5, e12727.

Day, J.J., Roitman, M.F., Wightman, R.M., Carelli, R.M. (2007). Associative learning mediates dynamic shifts in dopamine signaling in the nucleus accumbens. Nat. Neurosci. 10, 1020–1028.

Dombeck, D.A., Harvey, C.D., Tian, L., Looger, L.L., Tank, D.W. (2010). Functional imaging of hippocampal place cells at cellular resolution during virtual navigation. Nat. Neurosci. 13, 1433–1440.

Dudman, J.T. and Krakauer, J.W. (2016). The basal ganglia: From motor commands to the control of vigor. Curr. Opin. Neurobiol. 37, 158–166 (2016).

Eshel, N. et al. (2015). Arithmetic and local circuitry underlying dopamine prediction errors. Nature 525, 243–246.

Ford, C.P., Gantz, S.C., Phillips, P.E., Williams, J.T. (2010). Control of extracellular dopamine at dendrite and axon terminals. J. Neurosci. 30, 6975–6983.

Ford, C.P., Phillips, P.E., Williams, J.T. (2009). The time course of dopamine transmission in the ventral tegmental area. J. Neurosci. 29, 13344–13352.

Ganesana, M., Lee, S.T., Wang, Y., Venton, B.J. (2017). Analytical Techniques in Neuroscience: Recent Advances in Imaging, Separation, and Electrochemical Methods. Anal. Chem. 89, 314–341.

Goldey, G.J. et al. (2014). Removable cranial windows for long-term imaging in awake mice. Nat. Protoc. 9, 2515–2538.

Gunaydin, L.A. et al. (2014). Natural neural projection dynamics underlying social behavior. Cell 157, 1535–1551.

Howe, M.W. and Dombeck, D.A. (2016). Rapid signalling in distinct dopaminergic axons during locomotion and reward. Nature 535, 505–510.

Irannejad, R. et al. (2013). Conformational biosensors reveal GPCR signalling from endosomes. Nature 495, 534–538.

Jaquins-Gerstl, A. and Michael, A.C. (2015). A review of the effects of FSCV and microdialysis measurements on dopamine release in the surrounding tissue. Analyst 140, 3696–3708.

Lee, D. et al. (2017). Temporally precise labeling and control of neuromodulatory circuits in the mammalian brain. Nat. Methods 14, 495–503.

Lee, S.H., Dan, Y. (2012). Neuromodulation of brain states. Neuron 76, 209–222.

Lerner, T.N. et al. (2015). Intact-Brain Analyses Reveal Distinct Information Carried by SNc Dopamine Subcircuits. Cell 162, 635–647.

Lindeberg, J. et al. (2004). Transgenic expression of Cre recombinase from the tyrosine hydroxylase locus. Genesis 40, 67–73.

Mamaligas, A.A., Cai, Y., Ford, C.P. (2016). Nicotinic and opioid receptor regulation of striatal dopamine D2-receptor mediated transmission. Sci. Rep. 6, 37834.

Manglik, A. et al. (2015). Structural Insights into the Dynamic Process of b2-Adrenergic Receptor Signaling. Cell 161, 1101–1111.

Marder, E. (2012). Neuromodulation of neuronal circuits: Back to the future. Neuron 76, 1–11 (2012).

Marvin, J.S. et al. (2013). An optimized fluorescent probe for visualizing glutamate neurotransmission. Nat. Methods 10, 162–170.

Matsui, A., Jarvie, B.C., Robinson, B.G., Hentges, S.T., Williams, J.T. (2014). Separate GABA afferents to dopamine neurons mediate acute action of opioids, development of tolerance, and expression of withdrawal. Neuron 82, 1346–1356.

Muller, A., Joseph, V., Slesinger, P.A. (2014). Cell-based reporters reveal in vivo dynamics of dopamine and norepinephrine release in murine cortex. Nat. Methods 11, 1245–1252.

Otmakhov, N. and Lisman, J. (2012) Measuring CaMKII concentration in dendritic spines. J. Neurosci. Methods 203, 106–114.

Pan, W.X., Schmidt, R., Wickens, J.R., Hyland, I. (2005). Dopamine cells respond to predicted events during classical conditioning: Evidence for eligibility traces in the reward-learning network. J. Neurosci. 25, 6235–6242.

Park, J., Takmakov, P., Wightman, R.M. (2011). In vivo comparison of norepinephrine and dopamine release in rat brain by simultaneous measurements with fast-scan cyclic voltammetry. J. Neurochem. 119, 932–944.

Patriarchi, T. et al. (2016). Phosphorylation of Cav1.2 on S1928 uncouples the L-type Ca2+ channel from the β2 adrenergic receptor. EMBO J. 35, 1330– 1345.

Patriarchi, T. et al. (2018) Nanodelivery of a functional membrane receptor to manipulate cellular phenotype. Sci. Rep. 8, 3556.

Piatkevich, K.D. et al. (2018). A robotic multidimensional directed evolution approach applied to fluorescent voltage reporters. Nat. Chem. Biol. 14, 352–360.

Pologruto, T.A., Sabatini, B.L., Svobodam K. (2003). ScanImage: Flexible software for operating laser scanning microscopes. Biomed. Eng. Online 2, 13.

Quan, J. and Tian, J. (2011). Circular polymerase extension cloning for high-throughput cloning of complex and combinatorial DNA libraries. Nat. Protoc. 6, 242–251.

Rasmussen, S.G. et al. (2011). Crystal structure of the b2 adrenergic receptor-Gs protein complex. Nature 477, 549–555.

Robinson, B.G. et al. (2017). Desensitized D2 autoreceptors are resistant to trafficking. Sci. Rep. 7, 4379.

Schultz, W. (2016). Dopamine reward prediction-error signalling: A two-component response. Nat. Rev. Neurosci. 17, 183–195.

Schultz, W., Daya, P., Montague, P.R. (1997). A neural substrate of prediction and reward. Science 275, 1593–1599.

Shah, S. et al. (2016). Single-molecule RNA detection at depth by hybridization chain reaction and tissue hydrogel embedding and clearing. Development 143, 2862–2867.

Sheffield, M.E.J., Adoff, M.D., Dombeck, D.A. (2017) Increased Prevalence of Calcium Transients across the Dendritic Arbor during Place Field Formation. Neuron 96, 490–504.e5.

Song, Y. et al. (2013). High-resolution comparative modeling with RosettaCM. Structure 21, 1735–1742.

Stoppini, L., Buchs, P.A., Muller, D. (1991). A simple method for organotypic cultures of nervous tissue. J. Neurosci. Methods 37, 173–182.

Strader, C.D. et al. (1988). Conserved aspartic acid residues 79 and 113 of the beta-adrenergic receptor have different roles in receptor function. J. Biol. Chem. 263, 10267–10271.

Taha, S.A. and Fields, H.L. (2005). Encoding of palatability and appetitive behaviors by distinct neuronal populations in the nucleus accumbens. J. Neurosci. 25, 1193–1202.

Tan, K.R. et al. (2012). GABA neurons of the VTA drive conditioned place aversion. Neuron 73, 1173–1183.

Tian, L. et al., (2009). Imaging neural activity in worms, flies and mice with improved GCaMP calcium indicators. Nat. Methods 6, 875–881.

Tritsch, N. X. and Sabatini, B.L. (2012). Dopaminergic modulation of synaptic transmission in cortex and striatum. Neuron 76, 33–50.

Tufail, Y. et al. (2017). Phosphatidylserine Exposure Controls Viral Innate Immune Responses by Microglia. Neuron 93, 574–586.e8.

Vickery, R.G. and von Zastrow, M. (1999). Distinct dynamin-dependent and -independent mechanisms target structurally homologous dopamine receptors to different endocytic membranes. J. Cell Biol. 144, 31–43.

Vong, L. et al. (2011). Leptin action on GABAergic neurons prevents obesity and reduces inhibitory tone to POMC neurons. Neuron 71, 142–154.

Waterhouse, A.M., Procter, J.B., Martin, D.M., Clamp, M., Barton, G.J. (2009). Jalview Version 2— a multiple sequence alignment editor and analysis workbench. Bioinformatics 25, 1189– 1191.

Wise, R.A. (2004). Dopamine, learning and motivation. Nat. Rev. Neurosci. 5, 483–494.

Yorgason, J.T., Zeppenfeld, D.M., Williams, J.T. (2017). Cholinergic Interneurons Underlie Spontaneous Dopamine Release in Nucleus Accumbens. J. Neurosci. 37, 2086–2096.

Zhong, H. et al. (2009) Subcellular dynamics of type II PKA in neurons. Neuron 62, 363–374.

Chapter 3

DORSAL RAPHE DOPAMINE NEURONS MODULATE AROUSAL AND PROMOTE WAKEFULNESS BY SALIENT STIMULI

[2] Cho, J. R. et al. (2017). "Dorsal raphe dopamine neurons modulate arousal and promote wakefulness by salient stimuli." In: *Neuron* 94.6, pp. 1205-1219.e8. doi: 10.1016/j.neuron.2017.05.020.

3.1 Summary

Ventral midbrain dopamine (DA) is unambiguously involved in motivation and behavioral arousal, yet the contributions of other DA populations to these processes are poorly understood. Here, we demonstrate that the dorsal raphe nucleus DA neurons are critical modulators of behavioral arousal and sleep-wake patterning. Using simultaneous fiber photometry and polysomnography, we observed time-delineated dorsal raphe nucleus dopaminergic (DRN^{DA}) activity upon exposure to arousal-evoking salient cues, irrespective of their hedonic valence. We also observed broader fluctuations of DRN^{DA} activity across sleep-wake cycles with highest activity during wakefulness. Both endogenous DRN^{DA} activity and optogenetically driven DRN^{DA} activity were associated with waking from sleep, with DA signal strength predictive of wake duration. Conversely, chemogenetic inhibition opposed wakefulness and promoted NREM sleep, even in the face of salient stimuli. Therefore, the DRN^{DA} population is a critical contributor to wake-promoting pathways and is capable of modulating sleep-wake states according to the outside environment, wherein the perception of salient stimuli prompts vigilance and arousal.

3.2 Introduction

In mammals, behavioral arousal fluctuates as inputs are received from both the external environment (e.g., food availability, predator threat) and internal milieu (e.g., hunger, mating drive, homeostatic sleep demand) (Garey et al., 2003; Brown et al., 2012). While the neural circuits that encode these individual stimuli can be highly stimulus specific or tuned to a specific valence (positive or negative), their activation often promotes more general effects on arousal and electrocortical wakefulness through diverse wake-promoting neurons (Aston-Jones and Bloom, 1981; Szymusiak and McGinty, 2008). Akin to how the noradrenergic (NA) neurons of the locus coeruleus (LC) regulate circadian sleep-wake cycling (Takahashi et al., 2010) and promote vigilance during wake (Aston-Jones and Bloom, 1981), multiple neural circuits play roles in electrocortical wakefulness and behavioral arousal to motivationally relevant situations, including cholinergic neurons of the pons and basal forebrain (Jones, 1991; Xu et al., 2015; Pinto et al., 2013), the corticotrophin-releasing hormone (CRH) and hypocretin (orexin) neuropeptide systems (Sakurai et al., 1998; Winsky-Sommerer et al., 2005), and the mesolimbic dopamine (DA) system (Eban-Rothschild et al., 2016; Taylor et al., 2016).

Several lines of basic research and clinical observations converge upon DA as a crucial modulator of wake drive, but the neuroanatomical underpinnings have resisted detailed characterization. For example, persistent elevation of DA tone via pharmacology (i.e., amphetamine [Daberkow et al., 2013], modafinil [Qu et al., 2008]) or genetic ablation of the dopamine transporter gene (*Slc6a3*) (Wisor et al., 2001) is associated with behavioral

arousal, but these manipulations are diffuse and brain-wide rather than localized to a certain region. Recent work has revealed a role for ventral tegmental area (VTA) DA neurons in electrocortical arousal and sleep-wake patterning (Eban-Rothschild et al., 2016; Taylor et al., 2016), which complements its long-standing role in behavioral arousal to motivationally relevant stimuli (Cohen et al., 2012; Lammel et al., 2014; Matsumoto and Hikosaka, 2009). In contrast, diminished DA signaling from the substantia nigra pars compacta (SNc) is associated with insomnia, a major symptom in Parkinson's disease (Gjerstad et al., 2007). Considering the functional (Morales and Margolis, 2017), genetic (Poulin et al., 2014), and anatomical (Lammel et al., 2011, 2012; Margolis et al., 2008) heterogeneity of midbrain DA neurons, distinct DA subgroups may exert diverging effects on sleep-wake regulation.

Previously, a small population of DA neurons (~1,000 cells in rats) in the dorsal raphe nucleus (DRN; or ''A10 dc'' or ''ventral/ ventrolateral periaqueductal gray''; herein referred to as the DRN^{DA}) (Hokfelt et al., 1984; Descarries et al., 1986; Dougalis et al., 2012) was observed to be wake promoting (Lu et al., 2006). Chemical lesion of these cells precipitated profound hypersomnia (~20% increase in sleep), while prolonged wakefulness elicited increased *c-fos* expression (Lu et al., 2006; but see Leger et al., 2010). Compared to other DA populations, little is known about the natural dynamics of DRN^{DA} cells, such as whether their activity contributes to the valuation of external cues and whether this valuation is predictive of the corresponding behavioral response. Contrary to VTA^{DA}-driven reward circuits, optogenetic activation of DRN^{DA} neurons fails to reinforce operant responding (McDevitt et al., 2014) but instead conveys a negative affective state and

promotes social seeking via a negative reinforcement mechanism (Matthews et al., 2016). Given these seemingly disparate roles of DRN^{DA} cells, namely to promote wakefulness (Lu et al., 2006) and encode a ‘‘loneliness-like’’ state (Matthews et al., 2016), we hypothesized that DRN^{DA} neurons may signal arousal on a more general level, including awakening from sleep, maintenance of wakefulness, and promoting arousal in response to behaviorally relevant cues.

Here, we performed longitudinal monitoring of DRN^{DA} activity by calcium imaging via fiber photometry (Gunaydin et al., 2014) and of sleep-wake states via electroencephalography (EEG) and electromyography (EMG) recordings, in conjunction with optogenetics and chemogenetics for reversible, spatially specific control of neural activity (Rajasethupathy et al., 2016; Urban and Roth, 2015). We found that DRN^{DA} neurons are wake-active, showing higher population activity during wakefulness over sleep states, and that endogenous DRN^{DA} activity correlates with state transitions and with external stimulus-driven behaviors. Furthermore, reversible and bi-directional manipulations of DRN^{DA} firing support the sufficiency and necessity of these neurons in promoting vigilance and arousal. Taken together, our results provide evidence that DRN^{DA} pathways provide a circuit for modulating behavioral states and salience-induced arousal in mammals.

3.3 Results

DRN^{DA} Neurons Are Activated by Arousal-Provoking Salient Cues

To investigate the natural dynamics of DRN^{DA} neurons during awake-behaving states, we monitored DRN^{DA} population activity in subjects exposed to a diverse array of salient stimuli and environmental settings. In vivo activity of DRN^{DA} neurons was recorded using fiber photometry (Gunaydin et al., 2014), which can measure bulk Ca^{2+}-dependent fluorescence of GCaMP6, a genetically encoded calcium indicator (Chen et al., 2013), through a single optical fiber positioned in deep brain structures (Figures S1A, S1G, and S1H). Our photometry setup utilized a 490 nm beam to activate Ca^{2+}-dependent GCaMP6 fluorescence, as well as a 405 nm beam to image an isosbestic reference signal, which compensates for photo-bleaching and movement-related artifacts (Lerner et al., 2015). For specific targeting of DRN^{DA} neurons, we stereotaxically injected an adeno-associated virus (AAV) encoding GCaMP6f in a Cre-dependent manner (AAV5-Syn-FLEX-GCaMP6f) into the DRN of tyrosine hydroxylase (TH)::IRES-Cre mice (Figures 1A and 1B). Control animals were injected with AAV encoding the fluorescent marker EGFP (AAV5-hSyn-DIO-EGFP). An optical fiber was implanted over the DRN to acquire population fluorescence emitted from DRN^{DA} neurons (Figures 1A and S1A). We confirmed that GCaMP6f-expressing neurons emitted dynamic fluorescence fluctuations, while EGFP-expressing cells showed minimal fluorescence variation (Figures S1B and S1C).

We quantified the efficiency and specificity of GCaMP6f+ neurons in the DRN of TH-Cre mice. Transfection was highly efficient (94.2%, n = 407/432 neurons). Similar to previous

reports that used the identical mouse line or others targeting TH or the *Slc6a3* promoter (Matthews et al., 2016), 74.9% (n = 407/543) of GCaMP6f+ neurons were co-localized with TH in the DRN. These neurons are not noradrenergic, as they lack dopamine beta-hydroxylase, which converts dopamine to norepinephrine (Nagatsu et al., 1979). Importantly, GCaMP6f+ or TH+ neurons never overlapped with serotonergic neurons (Figures 1B and S1D; Lu et al., 2006; Matthews et al., 2016), a major population in the DRN that is hypothesized to regulate arousal states (Jouvet, 1999). It is possible that GCaMP6f+/TH- neurons may express TH at a level below immunohistochemical detection limit but sufficient to drive Cre expression.

We first tested $DRN^{DA\text{-}GCaMP6f}$ mice in a social interaction paradigm, in which physical contact with conspecifics after social isolation has been demonstrated to activate DRN^{DA} neurons (Matthews et al., 2016). We observed the robust activation of DRN^{DA} neurons in single-housed male $DRN^{DA\text{-}GCaMP6f}$ mice when they first interacted with female intruders (Figures 1C and 1D). Similar activation was observed with juvenile mice (Figure S2A; Movie S1; Matthews et al., 2016) and also when they displayed aggressive behavior toward adult male intruders (Figure S2B). Beyond social interaction, we also observed prominent DRN^{DA} activity when mice consumed palatable food (Figures 1E and 1F; Movie S2). To further characterize the valence tuning of DRN^{DA} cells, we also challenged $DRN^{DA\text{-}GCaMP6f}$ mice in assays with negative contexts. Surprisingly, DRN^{DA} neurons showed phasic activation upon delivery of unexpected electric footshocks (Figures 1G and 1H), air puffs (Figure S2C), or motivated responding (mobility/struggling) in tail suspension tests (Figure S2D) and during investigation of predator odor TMT (component of fox urine; Figure

S2E). Furthermore, they showed sustained activation when subjects were physically restrained (Figure S2F).

In contrast, DRN^{DA} activity showed minimal change when mice interacted with novel or familiar objects (Figures 1I–1L, first encounters), which are less salient than social targets, food, or aversive cues. Indeed, DRN^{DA} activation during female interaction, chocolate consumption, and footshock was significantly larger than that during object investigation (Figure 1M). Furthermore, the second and third bouts of female interaction and aggressive behavior continued to provoke a significant elevation in DRN^{DA} activity, whereas it remained relatively unchanged from baseline with repeated novel object encounters, suggesting rapid habituation toward physically salient but motivationally neutral cues (Figures S2G–S2I).

These findings did not vary with subject social history, as similar patterns of DRN^{DA} activation were seen in group-housed mice (Figures S2J–S2L). Furthermore, DRN^{DA} neuronal activation was not correlated with locomotion, which argues against the observed DRN^{DA} activity resulting from the motor response alone (Figures S2M–S2O). Taken together, these findings suggest that DRN^{DA} neurons are activated by a broad array of arousal-provoking stimuli, paralleling animals' heightened environmental awareness that accompanies exposure to such motivationally salient stimuli.

DRN^{DA} Population Activity Correlates with Sleep-Wake States

That DRN^{DA} neurons were activated by exposure to a variety of salient cues expands their previous description as a socio-centric pathway (Matthews et al., 2016). It seems plausible that DRN^{DA} neurons convey more generalized arousal signals across broad temporal scales, especially given that chemogenetic activation promotes analgesia (Li et al., 2016) and selective lesion causes hypersomnia (Lu et al., 2006).

To test this hypothesis, we prepared TH-Cre mice for simultaneous and synchronized recording of $DRN^{DA\text{-}GCaMP6s}$ fluorescence (AAV5-Syn-FLEX-GCaMP6s, EGFP for control animals; DRN optical fiber insertion; Figures 2A and 2B) and polysomnography signals (implantation of EEG electrodes and EMG wires; Figure 2A). Sleep-wake states, which were manually classified in 5 s windows based on the visual and spectral characteristics of the EEG/EMG signals, were correlated to fluctuations in DRN^{DA} population activity (Figures 2C and S3A). Variations in fluorescent signal were absent in control $DRN^{DA\text{-}EGFP}$ mice (Figures 2D and S3B), and viral delivery of transgenes (here and in all subsequent experiments) did not alter the basic sleep-wake architecture (Figures S1E and S1F).

To record DRN^{DA} activity over many episodes of distinct sleep-wake states, we collected fiber photometry and EEG/EMG across the entire light (inactive) phase (Figure 2E). $DRN^{DA\text{-}GCaMP6s}$ mice showed normal EEG spectral characteristics and sleep-wake patterns, even in the presence of GCaMP6s excitation light (Figures S3C and S3D). Over long recording sessions, GCaMP6s bleaching was observed, but it could be effectively removed by subtracting the linearly scaled control signal from 405 nm excitation (Figure S3E). To examine the correlation of DRN^{DA} activity with sleep-wake states, we calculated the area

under the curve (AUC) for non-overlapping 5 s windows of photometry data during each state as an index of the estimated DRN^{DA} population firing rate (Figure 2F). AUC values were significantly higher during wakefulness (Figure 2G). For further characterization, Ca^{2+} peak events were detected (Figure S3F), and their quantitative features were compared across states. The peak amplitude and summed AUC values of detected events were highest during wakefulness, but there was no significant difference in their frequency or duration across distinct states (Figures S3G–S3J). Altogether, these results suggest that DRN^{DA} neurons are wake-active and that their activity profile correlates with arousal states.

To examine the temporal dynamics of DRN^{DA} activity during each state, we normalized the variable durations of sleep-wake states to a unit-less time from 0 (onset) to 1 (offset) and accordingly down-sampled the normalized photometry traces. During wakefulness, DRN^{DA} population fluorescence peaked soon after wake onset and gradually decreased toward wake offset (Figure 2H). Indeed, the DRN^{DA} activity at the early 20^{th} percentile of a wake episode was significantly larger than at the late 20^{th} percentile (Figure 2I). In contrast, DRN^{DA} activity was continuously suppressed during NREM sleep and showed minimal variations during REM sleep (Figure 2H). We additionally verified that wake episodes whose durations were similar to sleep episodes demonstrated similar dynamics (Figure S3K), suggesting that the observed DRN^{DA} wake dynamics did not originate from photobleaching over time. In sum, the activity level of DRN^{DA} populations not only varies across sleep-wake states but also shows dynamic changes within wakefulness, showing the

highest activity after wake onset and gradual decrease toward sleep onset.

Next, we examined DRN^{DA} activity during state transitions. DRN^{DA} fluorescence increased significantly at NREM to wake (Figure 3A; when wake duration >60 s). There was no significant fluorescence change at REM-to-wake transitions (Figure 3B; when wake duration >60 s). Conversely, DRN^{DA} activity decreased when animals fell asleep (Figure 3C). We also observed a gradual increase of DRN^{DA} activity across NREM-to-REM transitions (Figure 3D). When a brief period of wake (<15 s) intervened in transition from REM to NREM, DRN^{DA} activity exhibited a corresponding decrease across the brief wake and NREM onset (Figure S3L).

Interestingly, we observed that the duration of wake episodes varied as a function of the change in DRN^{DA} activity across the wake onset. The net fluctuation in DRN^{DA} fluorescence across sleep-to-wake transitions (from both NREM and REM) was significantly larger when mice were awake for a longer period (‘‘long’’: >60 s) than when mice were briefly awake (‘‘short’’: <30 s; ‘‘intermediate’’: between 30 and 60 s; Figures 3E and 3F). This suggests that DRN^{DA} activity at wake onset is positively correlated with the duration of the following wake episode. In sum, these results provide correlative evidence that endogenous DRN^{DA} firing is highest during wakefulness and that DRN^{DA} activity is dynamic across state transitions.

Optogenetic Activation of DRN^{DA} Neurons Promotes Wakefulness

To reveal a causal relationship between DRN^{DA} activity and wakefulness, we tested for sufficiency using a Cre-dependent excitatory opsin to stimulate transduced DRN^{DA} cells (AAV5-Ef1a-DIO-ChR2-eYFP, EGFP for controls; polysomnography for stage classification; Figures 4A and 4B). ChR2-eYFP expression was limited to the DRN and caudal linear nucleus, and never found in retrorubral field or VTA (Figures S4N and S4O). To avoid potential ceiling effects, we applied optogenetic stimulation to DRN^{DA} neurons during the light phase (Figure 4C). As endogenous firing characteristics of DRN^{DA} cells are unknown (one neuron reported by juxtacellular recording [Schweimer and Ungless, 2010]), we used stimulus parameters commonly adopted for photoactivation of ventral midbrain DA neurons (Tsai et al., 2009), which operate in phasic and tonic firing modes. We applied both phasic (a train of ten 30 Hz pulses, 10 ms pulse width, every 5 s) and tonic (continuous 2 Hz pulses, 10 ms pulse width) stimulation patterns (Figures 4C and S4D). These specific parameters were designed to expose subjects to the same total number of light pulses with distinct temporal structures. We verified that DRN^{DA} neurons were capable of faithfully following phasic pulse trains in whole-cell patch clamp recordings (Figure S4A).

Two minutes of phasic stimulation caused immediate transitions to and maintenance of wakefulness from both NREM and REM sleep in $DRN^{DA\text{-}ChR2}$ mice, but not in control $DRN^{DA\text{-}EGFP}$ mice (Figures 4D–4F, S4B, and S4C). By contrast, 2 min of tonic stimulation could only induce waking from REM sleep (Figures S4D–S4G). Because phasic stimulation more reliably evoked stage changes, we employed this paradigm in subsequent experiments. Phasic activation was effective in inducing immediate NREM-to-wake

transitions even after 4 hr of sleep deprivation, suggesting that DRN^{DA} activation can promote instantaneous arousal in the face of high sleep pressure (Figure 4G). Phasic stimulation caused a significant change in cortical EEG in $DRN^{DA\text{-}ChR2}$, but not in control $DRN^{DA\text{-}EGFP}$ mice, as revealed by spectral analysis (Figures 4H, 4I, S4H, and S4I); delta (0.5–4 Hz) and high-frequency (40–100 Hz) EEG powers were decreased and increased, respectively, upon DRN^{DA} activation (Figures 4J and 4K).

We next sought to examine the effect of longer, sustained activation of DRN^{DA} neurons on behavioral states. A 1 hr epoch of phasic stimulation was applied 4 hr into the subject's light phase when sleep pressure is high. Photostimulation resulted in a net increase in time awake relative to unstimulated epochs, due to the extension of wake episodes (Figures 4L and 4M). Spectral analysis revealed that delta (0.5–4 Hz) power was significantly diminished while high-frequency (40–100 Hz) activity was enhanced in ChR2-expressing mice (Figures 4N–4P). This spectral change from DRN^{DA} activation could not be attributed to increased locomotion, which can also affect cortical activity and arousal (Vinck et al., 2015), because optogenetic manipulations did not affect locomotion in either the light or dark phase (open field test; Figure S4L). Moreover, the sustained increase in wakefulness from DRN^{DA} activation was directly mediated by DA, as systemic administration of D1 and D2 receptor antagonists (SCH-23390 and eticlopride, respectively, 1 mg/kg) prior to stimulation abolished the wake-promoting effect of phasic stimulation in $DRN^{DA\text{-}ChR2}$ mice but caused no overall effect in control mice (Figures S4J–S4K).

In sum, phasic stimulation of DRN^{DA} neurons can affect sleep-wake state patterning and

promote arousal by inducing immediate sleep-to-wake transitions and prolonging wake duration. DRN^{DA} activity also causes electrocortical arousal, bi-directionally modulating low- and high-frequency rhythms across both minutes-short and hour-long temporal scales.

Chemogenetic Inhibition of DRN^{DA} Neurons Reduces Wakefulness

To interrogate the necessity of DRN^{DA} signaling for wake maintenance, we used a chemogenetic (Urban and Roth, 2015) approach to reversibly inhibit DRN^{DA} activity during polysomnographic recordings (Figure 5A). Here, DRN^{DA} cell recruitment via expression of the inhibitory DREADD (AAV2-hSyn-DIO-hM4Di-mCherry; Figures 5A and 5B) rather than the analogous opsin is not limited to light spread from optical fibers, and long-term suppression of DRN^{DA} activity carries no potential for phototoxicity. We confirmed with ex vivo whole-cell patch-clamp recordings that bath application of 1 mM clozapine-N-oxide (CNO) reversibly reduced the firing of hM4Di-expressing DRN^{DA} neurons via hyperpolarization but showed no effect on EGFP-positive cells in control mice (Figures S5B–S5E). We also verified that the hM4Di vector was not anterogradely or retrogradely transported from the DRN to other TH+ neurons (across a 4-week window; Figures S5F–S5I), some of which have been shown to have reciprocal connections (Lu et al., 2006).

$DRN^{DA\text{-}hM4Di}$ and $DRN^{DA\text{-}EGFP}$ mice were habituated to experimenter handling for three days prior to intraperitoneal injection of saline or CNO (1 mg/kg) 3 hr into their dark (active) cycle, and EEG/EMG recordings took place for 2 hr afterward (Figure 5C).

Compared to saline, CNO injection led to a marked reduction in wakefulness (Figures 5D and 5E). At the group level, DRN^{DA} inhibition decreased the time spent in wakefulness and increased NREM sleep time (Figure 5F). Specifically, CNO injection into the $DRN^{DA\text{-}hM4Di}$ mice increased NREM sleep duration (Figure 5G) but had no effect on the number of episodes of each state (Figure 5H). Importantly, saline or CNO injection into control mice did not affect sleep-wake proportions (Figures 5F–5H). A change was also evident in cortical EEG (Figure 5I); contrary to optogenetic activation, chemogenetic inhibition was associated with increased delta (0.5–4 Hz) power (Figure 5J) and decreased high-frequency (40–100 Hz) activity (Figure 5K) relative to vehicle injection. To test whether CNO-induced sleep-wake states have normal EEG architecture, we verified that the EEG spectrum in each state after CNO injection was not distinguishable from those after saline injection (Figures S5J–S5L). Thus, our findings indicate that DRN^{DA} neuronal activity is required for supporting wakefulness in normal physiological conditions.

DRN^{DA} Neuronal Activity Supports Wakefulness in the Presence of Salient Stimuli

Since diverse salient stimuli activated DRN^{DA} neurons (Figure 1) and their firing promoted wakefulness (Figures 4 and 5), we asked whether DRN^{DA} neurons are necessary for maintaining arousal in the face of environmental salience by chemogenetically inhibiting their activity (Figure 6A). We introduced female mouse and predator odor TMT to the subject's home cage during the dark cycle while monitoring behavioral states. These two stimuli, which were shown to induce robust DRN^{DA} activity (Figures 1C, 1D, and S2E), hold ethological relevance, and are of opposite valence. CNO injection into the $DRN^{DA\text{-}}$

^{hM4Di} mice reduced the time spent awake and promoted NREM sleep in both assays, contrary to other conditions where mice remained awake (Figures 6B and 6C). More broadly, DRN^{DA} inhibition during these assays caused a shift in cortical EEG spectra; CNO treatment of DRN$^{DA\text{-}hM4Di}$ mice led to an increase in delta (0.5–4 Hz) power and decreases in high-theta (8–12 Hz) and high-frequency (40–100 Hz) power relative to saline condition, which was absent in control mice (Figures 6D–6G).

We further asked if the unexpected presentation of arousing or alerting stimuli (e.g., loud noises) during sleep could induce immediate wake transitions with DRN^{DA} firing. DRN$^{DA\text{-}GCaMP6s}$ mice were exposed to randomized auditory stimuli (65 dB, 2–5 kHz, 2 Hz pulse frequency, 250 ms width, 10 s duration) throughout their light phase while recording GCaMP6s fluorescence and EEG/EMG signals (Figure S6A). We observed time-locked DRN^{DA} activity upon tone onset, which was most prominent when subjects immediately (within 10 s) switched from sleep to wake (Figures S6B and S6C). There was no detectable difference in DRN^{DA} activity increase between NREM- and REM-to-wake transitions (Figures S6D and S6E). To test for a causal contribution of DRN^{DA} activity to cued arousal, we repeated the above experiment on mice expressing archaerhodopsin-3 (Arch; Mattis et al., 2011), which allows for time-locked reversible inhibition (Figures S6F and S6G). When DRN^{DA} neurons were exposed to a continuous 20 s light pulse (532 nm, 10 mW) centered on tone delivery (70 dB), the probability of cued waking from NREM (Figures S6H–S6K), but not from REM sleep (Figures S6L–S6O), significantly decreased. DRN^{DA} inhibition did not completely block NREM-to-wake transitions, which suggests that multiple pathways likely work together to sustain full arousal, including, but not limited

to, noradrenergic or cholinergic neurons (Aston-Jones and Bloom, 1981; Xu et al., 2015). In sum, these data indicate that DRN^{DA} activity is required for maintaining salience-induced wakefulness and for triggering cued waking from sleep.

3.4 Discussion

Using simultaneous calcium imaging and polysomnography in conjunction with optogenetic and chemogenetic manipulations, we demonstrated that DRN^{DA} neurons respond to external salient events of positive and negative valence, show correlative fluctuations at the population level across distinct sleep-wake states, and promote wakefulness. Furthermore, DRN^{DA} activity is necessary to maintain normal levels of wakefulness and support arousal in response to the perception of salient stimuli. These findings support a role for wake-promoting DRN^{DA} neurons that parallels the arousal-promoting function of isolated DA cells in invertebrates (Pimentel et al., 2016), as well as a more expansive role for DRN^{DA} signaling beyond promoting social interaction via negative reinforcement (Matthews et al., 2016) or mediating anti-nociceptive effects (Li et al., 2016).

Our photometry data demonstrate not only that social interaction robustly enhances DRN^{DA} spiking (female interaction, male intruder; Figures 1 and S2), akin to previous findings (juvenile interaction; Matthews et al., 2016), but also that these neurons respond to the perception of highly salient, non-social stimuli (Figures 1 and S2). DRN^{DA} activation by a wide variety of rewarding and aversive stimuli, both social and non-social, occurred irrespective of the subject's social history, as the stimulus-evoked change in DRN^{DA} fluorescence was not influenced by chronic separation from cage-mates (Figures S2J–S2M). Given the subtleties in how various forms of social deprivation (e.g., maternal separation, acute or chronic social isolation) can differentially alter physiology and

behavior (George et al., 2010; Whitaker et al., 2013), the extent to which a subject's social environment and rank causes plasticity in DRN^{DA} neurons will require further investigation. Based on the documented heterogeneity of ventral midbrain DA groups (Bromberg-Martin et al., 2010; Morales and Margolis, 2017), it is plausible that DRN^{DA} cells may also be heterogeneous and individually tuned to specific classes of stimuli. For example, some DRN^{DA} neurons may play a general role in social engagement or may be more susceptible to changes in social history, while other subsets may fire selectively for arousing, non-social stimuli. Since we and Matthews et al. (2016) used different fiber-placement methods (angled versus perpendicular, respectively), we may have sampled distinct, non-overlapping DRN^{DA} subsets.

Matthews et al. (2016) further demonstrated that DRN^{DA} neurons signal aversion, a trend that was also corroborated, albeit weakly, by our data (Figure S4M). This is in stark contrast with wake-promoting VTA^{DA} neurons, whose activity supports robust place preference and operant responding (Tsai et al., 2009; Witten et al., 2011). That neural circuits may be involved in two seemingly unrelated roles, valence encoding and sleep-wake regulation, is not unique to midbrain DA groups; wake-promoting LC NA neurons and CRH inputs also convey negative valence (McCall et al., 2015). Considering the involvement of hypocretin and VTA^{DA} systems in reward behavior (Espana, 2012; Wise, 2004), there may be dichotomous wake-promoting pathways signaling positive or negative valence upon their activation. That DRN^{DA} neurons can simultaneously send arousal and anti-nociceptive signals (Li et al., 2016) can be understood by considering DRN^{DA} connectivity with the bed nucleus of stria terminalis (BNST; Figure S4Q), which is a critical regulator of pain

perception (Minami and Ide, 2015).

Compared to ventral midbrain DA counterparts (Schultz, 1997; Ungless et al., 2004; Matsumoto and Hikosaka, 2009; Cohen et al., 2012; Lerner et al., 2015; Kim et al., 2016), the natural dynamics of DRN^{DA} neurons are much less characterized. Due to their relative low number and shared projection targets, DRN^{DA} neurons have been assumed to be functionally similar to VTA^{DA} neurons and hence termed the dorso-caudal extension of the VTA (A10) or A10 dc group (Hokfelt et al., 1984). Several pieces of evidence argue against their treatment as a mere extension of the VTA. Unlike the well-studied dorsal or lateral VTA^{DA} neurons, which fire bursts in response to rewarding or reward-predicting stimuli and are inhibited by punishment (Schultz, 1997; Ungless et al., 2004; Cohen et al., 2012; Kim et al., 2016), or the ventromedial VTA^{DA} neurons, which are selectively excited by aversive stimuli (Brischoux et al., 2009), DRN^{DA} neurons appear to be activated by any alerting or salient stimulus, regardless of valence (Figures 1 and S2). Also, they appear to be minimally affected by physically salient but motivationally neutral cues, such as novel or familiar objects (Figure 1). Since both rewarding and aversive stimuli elicit arousal and motivated responding, the VTA^{DA} system may address this challenge of dual positive (Schultz, 1997) and negative (Brischoux et al., 2009; Matsumoto and Hikosaka, 2009; Zweifel et al., 2011) valence coding in part through segregating to functionally and electrophysiologically distinct subgroups split across anatomical gradients (Brischoux et al., 2009; Bromberg-Martin et al., 2010) or projection targets (Lammel et al., 2011). The DRN^{DA} population, from our observations, showed bimodal activation at the population level, responding to both positive and negative stimuli. Whether individual DRN^{DA} neurons

are uniformly excited by positive and negative valence (therefore encoding salience), or whether they are oppositely tuned and intermingled within the DRN, will require future single-cell recording techniques.

DRN^{DA} and VTA^{DA} populations diverge significantly in downstream targets, which may help to explain their functional heterogeneity. Optogenetic excitation of VTA^{DA} neurons, especially those projecting to the nucleus accumbens, supports both appetitive conditioning and positive reinforcement behavior (Wise, 2004; Witten et al., 2011; Steinberg et al., 2014), whereas stimulation of DRN^{DA} neurons produces neutral or mild aversion (Figure S4M; Matthews et al., 2016). These observations may be indicative of differences in downstream connectivity between these neuronal populations. Although DRN^{DA} and VTA^{DA} neurons share overlap in some of their downstream targets (e.g., the prefrontal cortex and the basolateral amygdala), DA neurons projecting to cortical and striatal regions predominantly arise from the VTA (Bjorklund and Dunnett, 2007). DRN^{DA} terminals, however, are biased toward the extended amygdala, such as the BNST and central nucleus of the amygdala (CeA) (Figures S4P–S4S; Hasue and Shammah-Lagnado, 2002). Thus, as a major source of excitatory DA drive to the BNST and CeA (Matthews et al., 2016), two regions known to bi-directionally affect motivated behavior and regulate complex emotional states (Jennings et al., 2013), DRN^{DA} neurons are uniquely positioned to provide excitatory signals about environmental salience and internal arousal state to downstream nuclei, which can in turn initiate appropriate behavior, including triggering vigilance or patterning sleep-wake states.

Although DA has been implicated in sleep-wake regulation by pharmacological (Lin et al., 1992), genetic (Wisor et al., 2001), and clinical (Lima, 2013) studies, the precise circuits mediating such actions have been elusive. Single-unit recordings of VTA^{DA} and SNc^{DA} neurons have indicated that they do not change their mean firing rate across distinct sleep-wake states (Miller et al., 1983; Dahan et al., 2007). Here, we show that DRN^{DA} neurons are wake-active (Figures 2 and 3), whereas VTA^{DA} neurons exhibited increased burst firing or Ca^{2+} signals during REM sleep over wakefulness (Dahan et al., 2007; Eban-Rothschild et al., 2016). While the role of VTA^{DA} firing during REM sleep remains elusive, optogenetic activation of VTA^{DA} neurons can promote behavioral and electrocortical arousal (Eban-Rothschild et al., 2016; Taylor et al., 2016). Unlike the DRN^{DA} or VTA^{DA} populations, other DA groups appear to promote sleep rather than wakefulness. For example, chemical lesion of the SNc^{DA} neurons projecting to the dorsal striatum (DS) promotes wakefulness, and optogenetic stimulation of SNc^{DA} terminals in the DS increases NREM sleep (Qiu et al., 2016). Outside the midbrain, A13 zona incerta DA neurons express *c-fos* after REM sleep rebound (Leger et al., 2010). Taken together, these studies indicate that anatomically segregated DA populations may play functionally heterogeneous or even opposing roles in regulating sleep-wake states, and the DRN^{DA} as well as VTA^{DA} systems represent key arousal-promoting DA populations.

As shown here (Figures 6 and S6), external factors can influence sleep-wake patterns, and DRN^{DA} neurons contribute to these processes. Our findings that DRN^{DA} activity tracks the arousal states over broad temporal scales and that DRN^{DA} neurons respond to salient external cues position the DRN^{DA} system at the interface between internal (e.g., wake/sleep

drive) and external (e.g., salient stimuli) influences in regulating sleep-wake states. While this evolutionarily conserved trait is advantageous for organism survival, its dysfunction may have negative implications in humans, in which sleep disorders triggered by the malfunctioning of arousal-promoting circuits represent a highly morbid societal burden (Sanford et al., 2015). DRN^{DA} neurons are not well studied in humans, but it has been shown that they degenerate in patients with multiple systems atrophy and Lewy body dementia, which commonly cause excessive daytime sleepiness (Benarroch et al., 2009). Going forward, therapeutic strategies targeting DRN^{DA} activity may have utility in the treatment of primary sleep-wake disorders and sleep/arousal disturbances secondary to myriad neuropsychiatric diseases (Sateia et al., 2000), including major depressive disorder, bipolar affective disorder, and schizophrenia.

3.5 Main figures

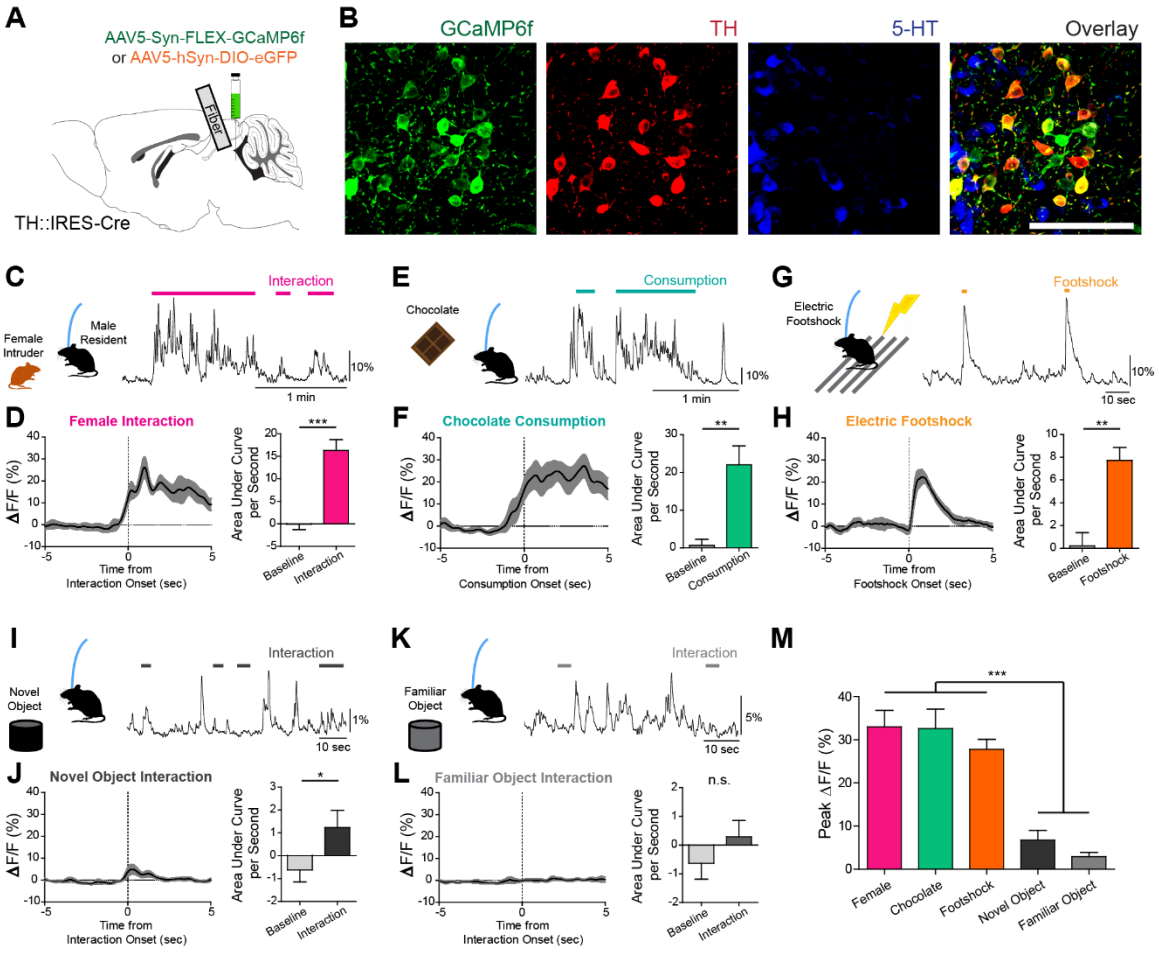

Figure 1. DRN^{DA} Neurons Are Activated upon Exposure to Salient Stimuli or Behavioral Challenge. (A) TH-Cre mice were injected with AAV5-Syn-FLEX-GCaMP6f or AAV5-hSyn-DIO-EGFP and implanted with an optical fiber into the DRN for fiber photometry. **(B)** Confocal images of GCaMP6f+ (green) neurons show co-localization with TH+ neurons (red), but no overlap with 5-HT+ neurons (blue). Scale bar, 100 mm. **(C)** Social interaction between a male DRN$^{DA\text{-}GCaMP6f}$ resident mouse and a female intruder were associated with increased DRN^{DA} activity; the trace is a representative recording with interaction bouts indicated. **(D)** Left: female interaction caused an increase in fluorescence

at the onset (first interactions only). Right: quantification of the area under the curve per second (AUC) during the interaction (0–5 s) shows that social interaction caused significant increase in DRN^{DA} activity from baseline (-5 to 0 s) (n = 7 $DRN^{DA\text{-}GCaMP6f}$ mice; paired t test, $t_6 = 11.97$, ***$p < 0.001$). **(E)** Chocolate consumption by a $DRN^{DA\text{-}GCaMP6f}$ mouse increased DRN^{DA} activity; representative recording. **(F)** Left: DRN^{DA} activity was increased upon chocolate consumption. Right: AUC quantification during consumption (0–5 s) compared with baseline (-5 to 0 s) shows that food consumption is associated with significant fluorescence increase (n = 7 $DRN^{DA\text{-}GCaMP6f}$ mice; paired t test, $t_6 = 4.273$, **$p < 0.01$). **(G)** Electric footshocks (0.25 mA, 1 s) were delivered; representative DRN^{DA} trace during two consecutive footshocks. **(H)** Left: footshock induced phasic DRN^{DA} activation. Right: DRN^{DA} activity after footshock (0–5 s) was significantly increased relative to baseline (-5 to 0 s) (n = 7 $DRN^{DA\text{-}GCaMP6f}$ mice; paired t test, $t_6 = 5.763$, **$p < 0.01$). **(I)** $DRN^{DA\text{-}GCaMP6f}$ mouse was allowed to interact with a novel object; representative recording during interactions. **(J)** Left: first interaction of a novel object was associated with DRN^{DA} activity increase. Right: DRN^{DA} activity after first interaction (0-5 s) was significantly increased relative to baseline (-5 to 0 s) (n = 7 $DRN^{DA\text{-}GCaMP6f}$ mice; paired t test, $t_6 = 3.614$, *$p < 0.05$). **(K)** A familiar object was introduced; representative DRN^{DA} trace with interaction bouts. **(L)** Left: first interaction bout was not associated with any change in DRN^{DA} fluorescence. Right: there was no change in DRN^{DA} activity across familiar object interaction (n = 7 $DRN^{DA\text{-}GCaMP6f}$ mice; paired t test, $t_6 = 2.205$, $p > 0.05$). **(M)** Peak DRN^{DA} fluorescence values during female interaction, chocolate

consumption, and electric footshocks were significantly higher than those during novel and familiar object interaction (n = 7 $DRN^{DA\text{-}GCaMP6f}$ mice; one-way ANOVA, $F_{4,30} = 22.77$, $p < 0.0001$, Bonferroni post hoc analysis, ***$p < 0.001$). Data represent mean ± SEM.

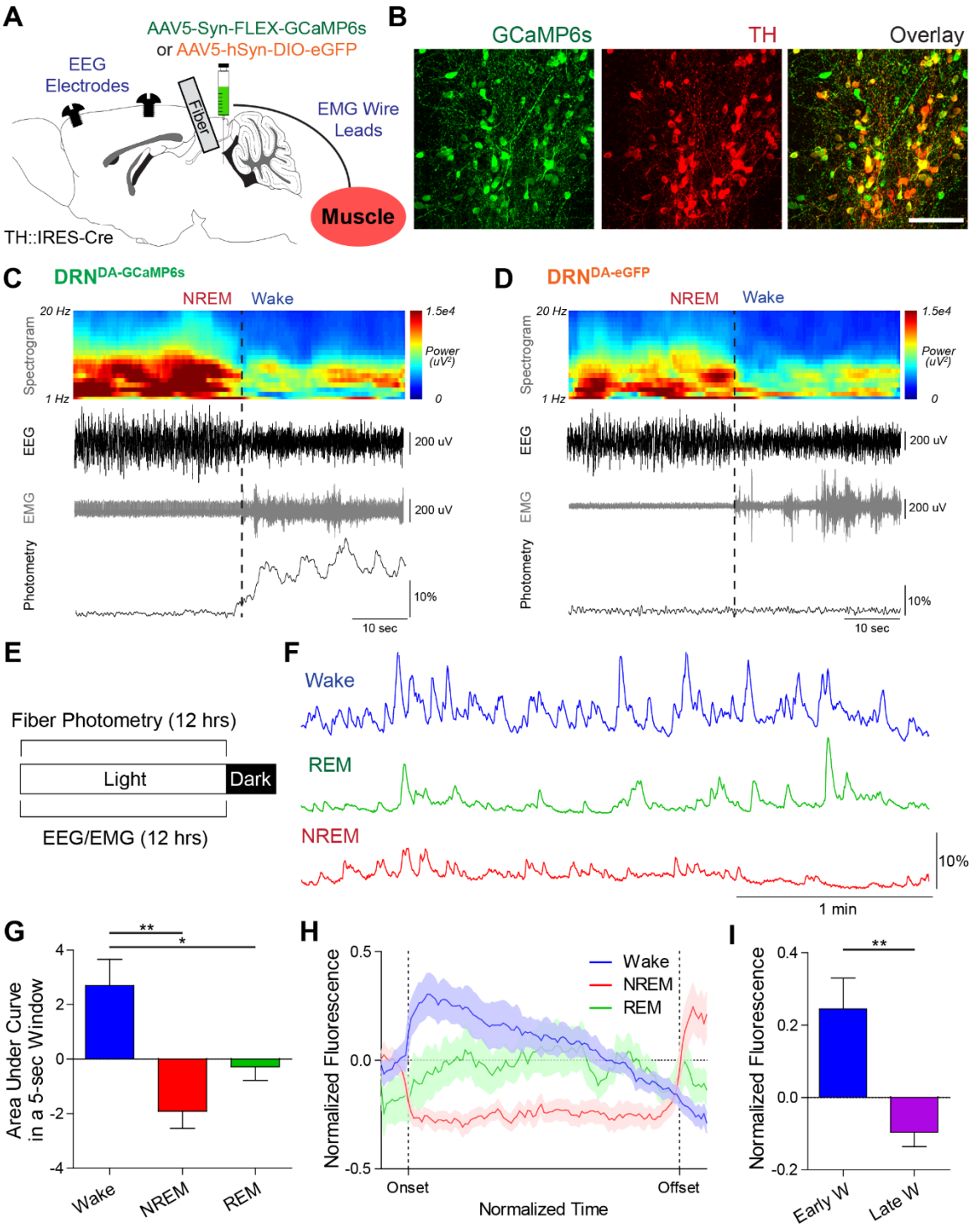

Figure 2. Simultaneous Fiber Photometry and EEG/EMG Recordings Reveal a Correlation between DRN^{DA} Neuronal Activity and Sleep-Wake States. (A) In

addition to fiber photometry, EEG screw electrodes and EMG wires were implanted to classify sleep-wake states. **(B)** Representative confocal images of GCaMP6s+ neurons (green) co-localized with TH+ neurons (red). Scale bar, 100 mm. **(C)** Representative example of an NREM-to-wake transition from a $DRN^{DA\text{-}GCaMP6s}$ mouse with EEG spectrogram, EEG, EMG, and photometry traces. Note DRN^{DA} fluorescence was increased at the wake onset, when EEG desynchronized from delta (0.5–4 Hz) and EMG amplitude increased. **(D)** Same as (C), but from a $DRN^{DA\text{-}EGFP}$ mouse. No change in photometry was observed. **(E)** Synchronized photometry and EEG/EMG recordings were performed during the entire light phase. **(F)** Representative photometry traces at distinct sleep-wake states (blue, wake; green, REM sleep; red, NREM sleep). **(G)** Quantification of AUC per 5 s window revealed higher DRN^{DA} activity during wakefulness over NREM and REM sleep (n = 6 $DRN^{DA\text{-}GCaMP6s}$ mice; one-way ANOVA, $F_{2,15} = 10.58$, $p < 0.01$; Bonferroni post hoc analysis, *$p < 0.05$, **$p < 0.01$). **(H)** Temporal dynamics of normalized DRN^{DA} activity during wake (blue), NREM (red), and REM (green) episodes within normalized time. **(I)** Normalized DRN^{DA} activity at early wake (first 20^{th} percentile) was significantly increased from late wake period (last 20^{th} percentile) (n = 6 $DRN^{DA\text{-}GCaMP6s}$ mice; paired t test, $t_5 = 5.672$, **$p < 0.01$). Data represent mean ± SEM.

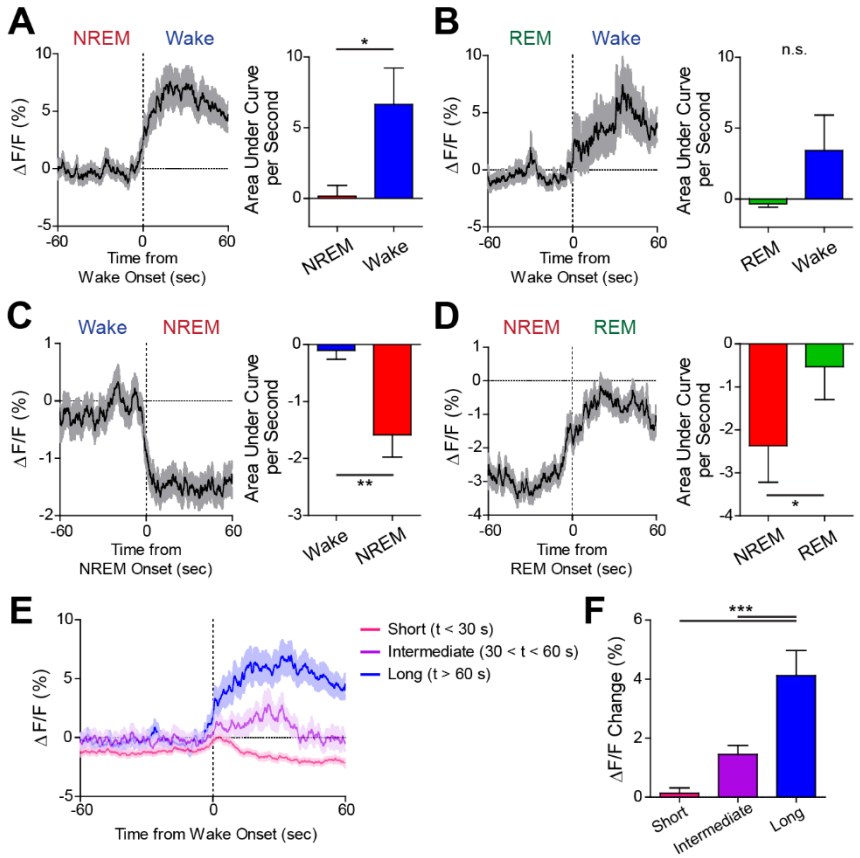

Figure 3. DRN^{DA} Neuronal Dynamics across State Transitions. (A) Left: DRN^{DA} activity increased across NREM-to-wake transitions. Right: DRN^{DA} activity after transitions (wake) was significantly greater than before transitions (NREM) (n = 6 DRN$^{DA\text{-}GCaMP6s}$ mice; paired t test, $t_5 = 3.052$, *p < 0.05). **(B)** Left: DRN^{DA} activity did not change across REM-to-wake transitions. Right: DRN^{DA} fluorescence was not different across transitions (n = 6 DRN$^{DA\text{-}GCaMP6s}$ mice; paired t test, $t_5 = 1.556$, p > 0.1). **(C)** Left: DRN^{DA} activity decreased at wake-to-NREM transitions. Right: the AUC values after transitions (NREM) were significantly lower than before transitions (wake) (n = 6 DRN$^{DA\text{-}GCaMP6s}$ mice; paired t test, $t_5 = 4.516$, **p < 0.01). **(D)** Left: DRN^{DA} fluorescence increased across NREM-to-REM transitions. Right: DRN^{DA} activity significantly increased during NREM

to REM transitions (n = 6 $DRN^{DA\text{-}GCaMP6s}$ mice; paired t test, $t_5 = 3.192$, *$p < 0.05$). **(E)** DRN^{DA} activity increase across sleep-to-wake transitions was more prominent when mice spent longer time awake (> 60 s, blue) than when mice were awake for intermediate (between 30 and 60 s, purple) or short (< 30 s, pink) period. **(F)** Fluorescence increase across wake onsets was significantly larger for long-duration wake episodes than for intermediate- or short-duration wake episodes (n = 366 short, 158 intermediate, and 185 long wake episodes; one-way ANOVA, $F_{2,706} = 21.85$, $p < 0.0001$; Bonferroni post hoc analysis, ***$p < 0.001$). Data represent mean ± SEM.

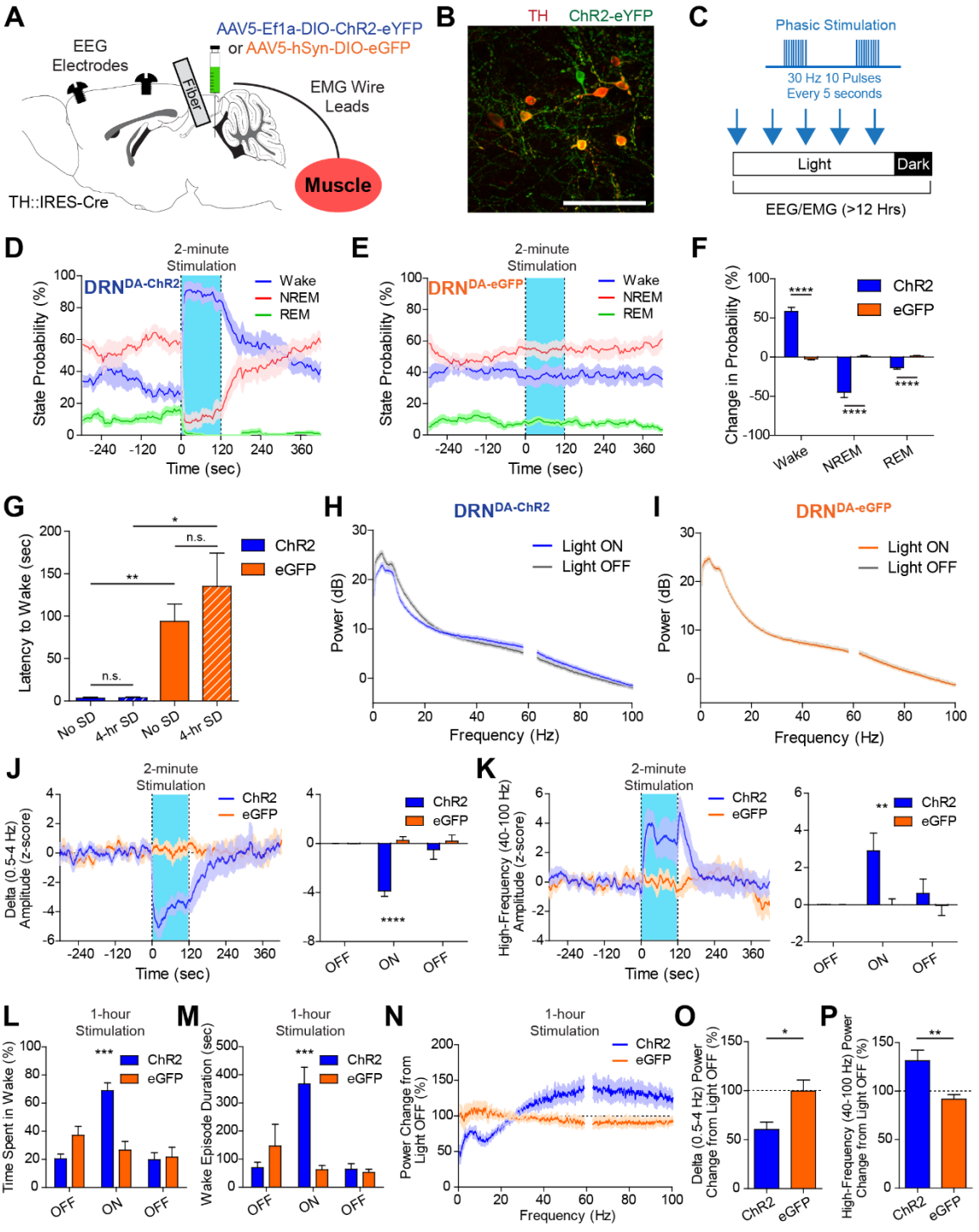

Figure 4. Optogenetic Stimulation of DRN^{DA} Neurons Promotes Wakefulness. (A) TH-Cre mice injected with AAV5-Ef1a-DIO-ChR2-eYFP or AAV5-hSyn-DIO-EGFP and

implanted with an optical fiber received optogenetic stimulation during sleep-wake state monitoring. **(B)** Confocal images of ChR2-eYFP+ neurons (green) co-localized with TH+ neurons (red). Scale bar, 100 mm. **(C)** Two-minute blocks (blue arrows) of phasic stimulations were delivered with intervals of 20 to 25 min throughout the light phase to photo-activate DRN^{DA} neurons. **(D)** Probability of being awake was dramatically increased upon onset of the phasic stimulation, with concurrent reduction of both NREM and REM state probability in $DRN^{DA\text{-}ChR2}$ mice. **(E)** Same as (D), but no change was observed in $DRN^{DA\text{-}EGFP}$ mice. **(F)** The increase in wake probability in $DRN^{DA\text{-}ChR2}$ mice compared with $DRN^{DA\text{-}EGFP}$ mice was significant, as were the decreases in NREM and REM sleep probability ($n = 8$ per group; unpaired t test, $^{****}p < 0.0001$). **(G)** There was no difference in the latency to wake onset even after 4 hr of sleep deprivation in both groups ($n = 4$ per group; paired t test, $p > 0.2$). Regardless of sleep deprivation, latency to wake after stimulation was significantly shorter in $DRN^{DA\text{-}ChR2}$ mice compared to controls (unpaired t test, $^{*}p < 0.05$, $^{**}p < 0.01$). **(H)** Power spectral density of frontal EEG shows reduced power in low-frequency range and increased power in high-frequency range during light ON (blue) compared to light OFF (gray) conditions in $DRN^{DA\text{-}ChR2}$ mice. **(I)** Same as (H), but power spectral density showed no difference across light ON (orange) and OFF (gray) conditions in $DRN^{DA\text{-}EGFP}$ mice. **(J)** Left: time-varying spectral analysis showed that the amplitude of delta (0.5–4 Hz) rhythms was decreased upon phasic stimulation. Right: delta amplitude during the light ON epoch was significantly decreased compared to baseline OFF epochs ($n = 8$ per group; two-way ANOVA revealed group 3 epoch interaction, $F_{2,26} = 17.06$, $p < 0.0001$; Bonferroni post hoc analysis, $^{****}p < 0.0001$). **(K)** Left: the

amplitude of high-frequency (40–100 Hz) rhythms was increased upon phasic stimulation. Right: high-frequency amplitude was significantly increased during the light ON epoch compared to the OFF epochs (n = 8 per group; two-way ANOVA revealed group 3 epoch interaction, $F_{2,26} = 5.096$, $p < 0.05$; Bonferroni post hoc analysis, $^{**}p < 0.01$). **(L)** 1 hr of phasic DRN^{DA} stimulation significantly increased the time spent in wakefulness during the light ON hour compared to the light OFF hours (n = 6 per group; two-way ANOVA revealed group 3 epoch interaction, $F_{2,20} = 15.99$, $p < 0.0001$; Bonferroni post hoc analysis, $^{***}p < 0.001$). **(M)** 1 hr of phasic stimulation significantly increased the duration of wake episodes (n = 6 per group; two-way ANOVA revealed group 3 epoch interaction, $F_{2,20} = 12.16$, $p < 0.001$; Bonferroni post hoc analysis, $^{***}p < 0.001$). **(N)** Power spectral density revealed decrease in low-frequency power and increase in high-frequency power in $DRN^{DA\text{-}ChR2}$ mice during light ON compared to the light OFF hours, but no changes were observed in $DRN^{DA\text{-}EGFP}$ mice. **(O)** Stimulation-induced delta (0.5–4 Hz) power reduction was significantly larger in $DRN^{DA\text{-}ChR2}$ mice (n = 6 per group; unpaired t test, $^{*}p < 0.05$). **(P)** Stimulation-induced high-frequency (40–100 Hz) power increase was significantly larger in $DRN^{DA\text{-}ChR2}$ mice (n = 6 per group; unpaired t test, $^{**}p < 0.01$). Data represent mean ± SEM.

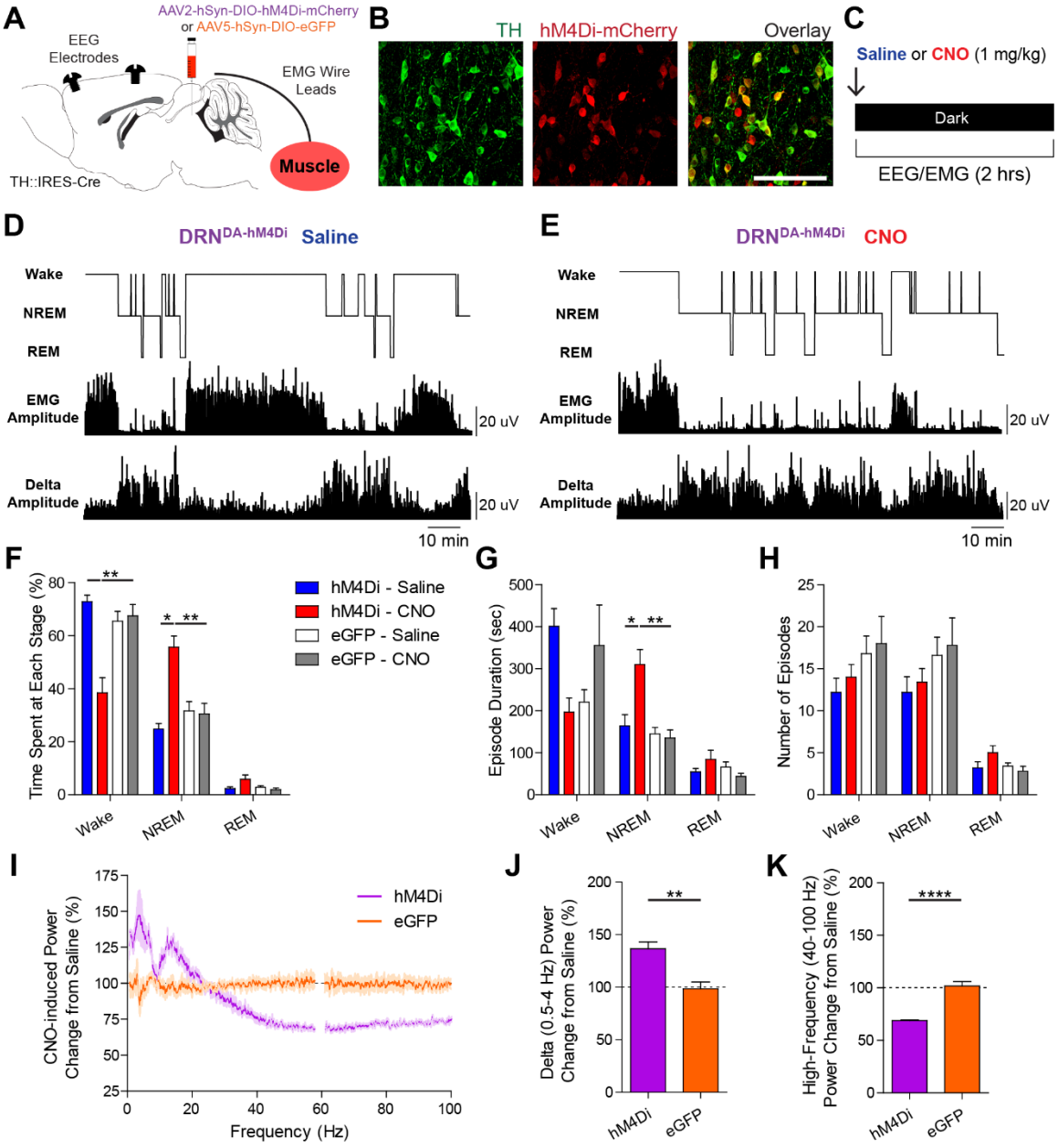

Figure 5. Chemogenetic Inhibition of DRN^{DA} Neurons Reduces Wakefulness. (A) AAV2-hSyn-DIO-hM4Di-mCherry or EGFP vectors were injected to the DRN of TH-Cre mice, and EEG/EMG electrodes were implanted for sleep-wake state classification. **(B)** Confocal images of TH+ (green) neurons co-localized with hM4Di-mCherry (red) expression. Scale bar, 100 mm. **(C)** Saline or CNO (1 mg/kg) was intraperitoneally

injected to inhibit DRN^{DA} neurons during the dark phase. EEG/EMG recordings were performed for 2 hr afterward. **(D)** Representative hypnogram (top), EMG amplitude (middle, in 5 s windows), and delta amplitude (bottom, in 5 s windows) from a $DRN^{DA\text{-}hM4Di}$ mouse after saline injection. **(E)** Same as (D), but with CNO injection. CNO injection caused reduced wakefulness, accompanied by lower EMG and higher delta amplitudes. **(F)** CNO injections into the $DRN^{DA\text{-}hM4Di}$ mice decreased the time spent in wake and increased the time spent in NREM sleep (n = 5 per group; two-way ANOVA revealed a group 3 drug interaction in wake and NREM, $F_{1,19}$ [wake] = 20.96, $p < 0.01$, $F_{1,19}$ [NREM] = 28.34, $p < 0.001$, $F_{1,19}$ [REM] = 2.07, $p > 0.1$; Bonferroni post hoc analysis, *$p < 0.05$, **$p < 0.01$). **(G)** Duration of NREM sleep was significantly increased when $DRN^{DA\text{-}hM4Di}$ mice were administered with CNO (n = 5 per group; two-way ANOVA revealed a group 3 drug interaction in NREM, $F_{1,19}$ [wake] = 3.84, $p > 0.05$, $F_{1,19}$ [NREM] = 10.78, $p < 0.05$, $F_{1,19}$ [REM] = 0.26, $p > 0.6$; Bonferroni post hoc analysis, **$p < 0.01$, *$p < 0.05$). **(H)** There was no difference in the number of episodes in all states (n = 5 per group; two-way ANOVA revealed no group 3 drug interaction, $F_{1,19}$ [wake] = 0.88, $F_{1,19}$ [NREM] = 0.52, $F_{1,19}$ [REM] = 0.55, all $p > 0.3$). **(I)** Power spectral density analysis revealed CNO-induced increase in low-frequency power and decrease in high-frequency power in $DRN^{DA\text{-}hM4Di}$ mice with respect to saline condition, but no change in controls. **(J)** CNO-induced delta (0.5–4 Hz) power increase was significantly larger in $DRN^{DA\text{-}hM4Di}$ mice compared to controls (n = 5 per group; unpaired t test, **$p < 0.01$). (K) CNO-induced high-frequency (40–100 Hz) power decrease was significantly larger in $DRN^{DA\text{-}hM4Di}$ mice compared to controls (n = 5 per group; unpaired t test, ****$p < 0.0001$). Data represent mean ± SEM.

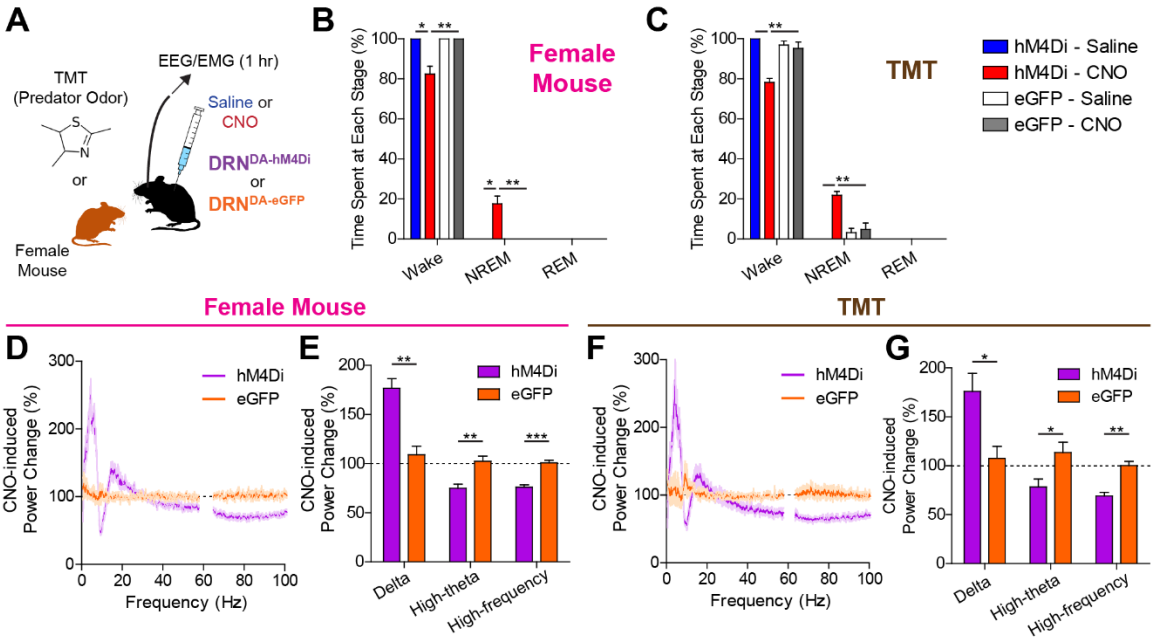

Figure 6. DRN^{DA} Firing Supports Wakefulness upon Exposure to Salient Stimuli. (A) DRN$^{DA\text{-}hM4Di}$ and DRN$^{DA\text{-}EGFP}$ mice were systemically administered with saline or CNO (1 mg/kg) 45 min prior to the introduction of a female mouse or a filter paper with predator odor TMT. EEG/EMG recordings were carried out for 1 hr after salient stimuli presentation. **(B)** While the introduction of a female mouse induced robust wakefulness in other conditions, CNO-injected DRN$^{DA\text{-}hM4Di}$ mice spent significantly reduced time in wakefulness at the cost of NREM sleep (n = 4 per group; two-way ANOVA revealed a group 3 drug interaction, $F_{1,15}$ [wake, NREM] = 20.83, $p < 0.01$, Bonferroni post hoc analysis, *$p < 0.05$, *$p < 0.01$). **(C)** Similar to (B), but a filter paper with predator odor TMT was introduced to home-cages. Compared to other conditions, CNO-injected DRN$^{DA\text{-}hM4Di}$ mice spent significantly reduced time in wakefulness and increased time in NREM sleep (n = 4 per group; two-way ANOVA revealed a group 3 drug interaction, $F_{1,15}$ [wake, NREM] = 26.88, $p < 0.01$, Bonferroni post hoc analysis, **$p < 0.01$). **(D)** Power spectral

density analysis during female mouse interaction revealed CNO-induced increase in low-frequency power and decrease in high-theta (8–12 Hz) and high-frequency power in $DRN^{DA\text{-}hM4Di}$ mice with respect to the saline condition but no change in control mice. **(E)** CNO-induced increase in delta (0.5–4 Hz) power and decrease in high-theta (8–12 Hz) and high-frequency (40–100 Hz) power were significantly larger in $DRN^{DA\text{-}hM4Di}$ mice than in controls (n = 4 per group; unpaired t test, $^{**}p < 0.01$, $^{***}p < 0.001$). **(F)** Same as (D), but for the TMT condition. A similar trend was observed as (D). **(G)** CNO-induced increase in delta (0.5–4 Hz) power and decrease in high-theta (8–12 Hz) and high-frequency (40–100 Hz) power were significantly larger in $DRN^{DA\text{-}hM4Di}$ mice than in controls (n = 4 per group; unpaired t test, $^{*}p < 0.05$, $^{**}p < 0.01$). Data represent mean ± SEM.

3.6 Supplementary figures

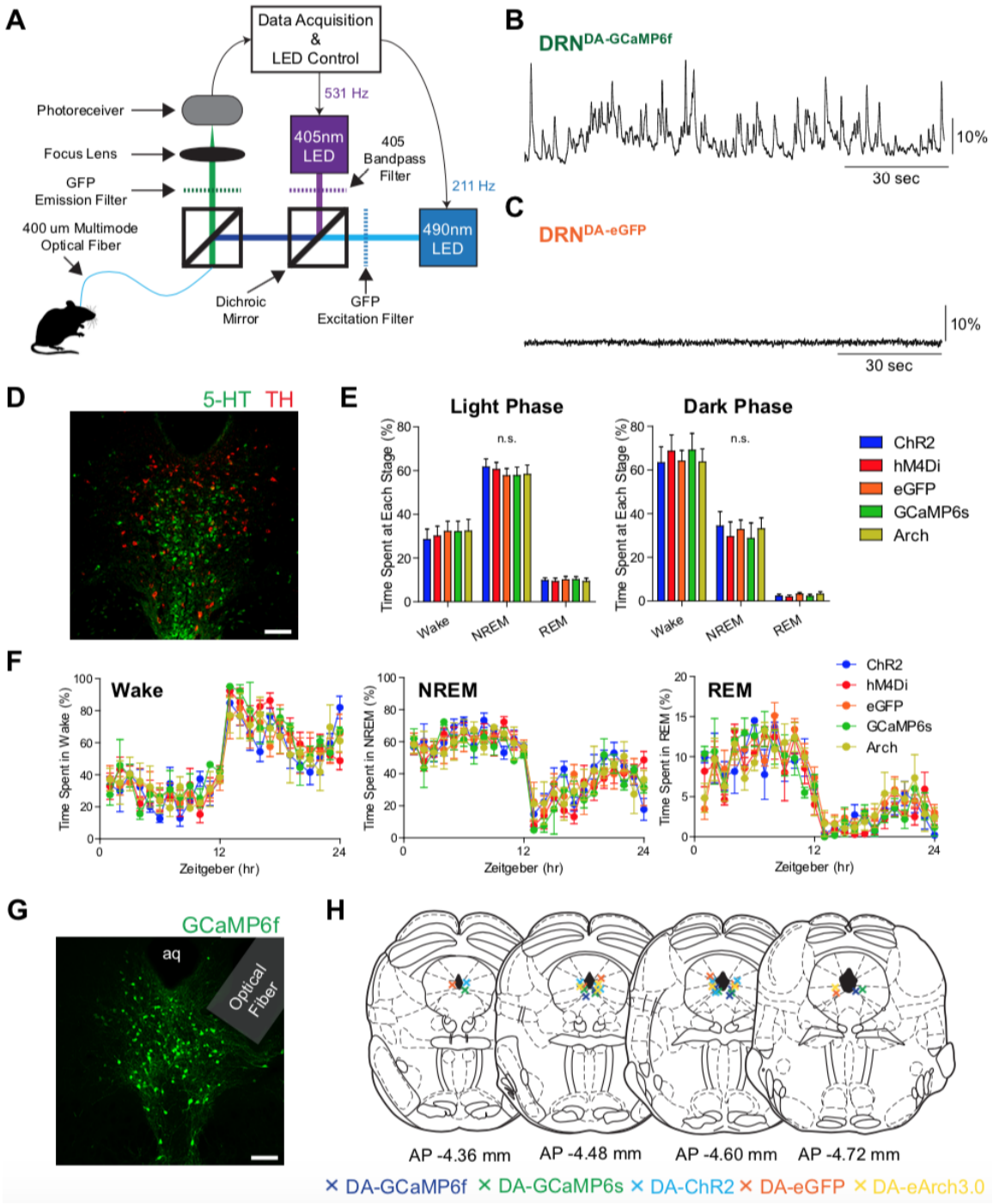

Supplementary Figure 1: related to all main figures. (A) Schematic of a fiber photometry

setup. See Supplementary Experimental Procedures for details. **(B)** Representative trace from a $DRN^{DA\text{-}GCaMP6f}$ mouse that shows dynamic Ca^{2+}-dependent fluorescence across time. **(C)** Representative trace from a $DRN^{DA\text{-}eGFP}$ mouse. Notice minimal fluctuations in fluorescence. **(D)** Confocal image of serotonin (5-HT, green) and dopamine (TH, red) neurons in the DRN. Notice that there is no overlap between the two populations and that the number of TH+ neurons is far less than that of 5-HT+ neurons. Scale bar is 100 μm. **(E)** Viral expression of diverse transgenes did not affect normal sleep-wake architecture both in light (left) and dark (right) phases ($n = 4$ per group; one-way ANOVA, all $p > 0.2$). **(F)** Time spent in each state per hour in 24-hour recordings: Wake (left), NREM (middle), and REM sleep (right). **(G)** Representative confocal image of GCaMP6f+ neurons in the DRN and the location of fiber-tip (in this case, for fiber photometry). Scale bar is 100 μm. **(H)** Histologically verified fiber-tip locations of $DRN^{DA\text{-}GCaMP6f}$ (dark blue), $DRN^{DA\text{-}GCaMP6s}$ (green), $DRN^{DA\text{-}ChR2}$ (sky blue), $DRN^{DA\text{-}eGFP}$ (orange), and $DRN^{DA\text{-}Arch}$ (yellow) mice.

Data are represented as mean ± s.e.m.

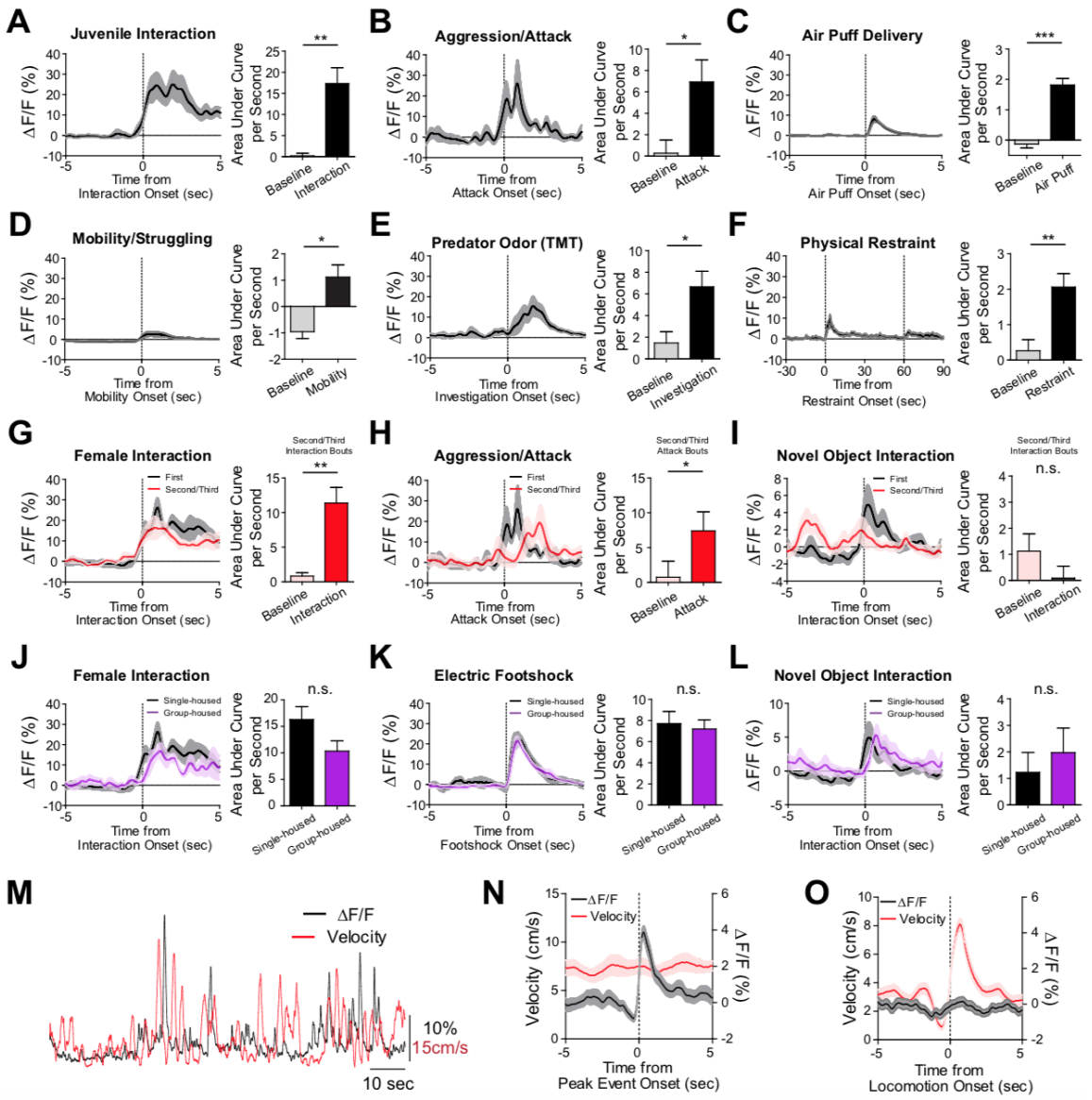

Supplementary Figure 2: related to Figure 1. (A) Left, social interaction between a male $DRN^{DA\text{-}GCaMP6f}$ resident mouse and a male juvenile intruder were associated with increased DRN^{DA} activity. Right, quantification of the area under the curve per second (AUC) showed that DRN^{DA} activity during first interaction (0 – 5 s) was significantly increased compared with baseline (-5 – 0 s) (n = 7 $DRN^{DA\text{-}GCaMP6f}$ mice, paired t-test, $t_6 = 4.679$, **$p < 0.01$). **(B)** Left, attack/fight bouts (first bout only) between a male $DRN^{DA\text{-}GCaMP6f}$ resident and an adult

intruder were associated with increased DRN^{DA} activity. Right, DRN^{DA} activity during attack (0 – 5 s) was significantly increased relative to baseline (-5 – 0 s) (n = 4 $DRN^{DA\text{-}GCaMP6f}$ mice, paired t-test, $t_3 = 4.993$, *$p < 0.05$). **(C)** Left, brief air puffs (<1 s) were intermittently delivered to the tail of a $DRN^{DA\text{-}GCAMP6f}$ mouse, which caused time-locked DRN^{DA} fluorescence increase. Right, DRN^{DA} activity after air puff delivery (0 – 5 s) was significantly increased relative to baseline (-5 – 0 s) (n = 7 $DRN_{DA\text{-}GCaMP6f}$ mice; paired t-test, $t_6 = 7.518$, ***$p < 0.001$). **(D)** Left, fiber photometry recording of $DRN^{DA\text{-}GCaMP6f}$ mice undergoing a 5-minute tail suspension test. DRN^{DA} neurons showed time-locked activation at the onset of mobility or struggling. Right, AUC values during mobility (0 – 5 s) were significantly increased compared with baseline (-5 – 0 s) (n = 7 $DRN^{DA\text{-}GCaMP6f}$ mice, paired t-test, $t_6 = 3.044$, *$p < 0.05$). **(E)** Left, investigation of predator odor TMT was associated with increase in DRN^{DA} activity. Right, quantification of the AUC showed that there was significant difference in DRN^{DA} activity between interaction (0 – 5 s) and baseline (-5 – 0 s) (n = 7 $DRN^{DA\text{-}GCaMP6f}$ mice, paired t-test, $t_6 = 2.653$, *$p < 0.05$). **(F)** Left, there was a prolonged increase in DRN^{DA} neuronal activity while a $DRN^{DA\text{-}GCaMP6f}$ mouse was restrained or immobilized. Right, sustained activation of DRN^{DA} neurons was observed throughout the restraint period (0 – 60 s), compared baseline (-60 – 0 s) (n = 6 $DRN^{DA\text{-}GCaMP6f}$ mice, paired t-test, $t_5 = 5.444$, **$p < 0.01$). **(G)** Left, averaged DRN^{DA} activity was increased during second and third interaction bouts (red trace), when a resident male $DRN^{DA\text{-}GCaMP6f}$ mouse was investigating a female intruder. Photometry data from first interaction (black trace, Fig 1D) was also illustrated for comparison. Right, AUC values during second and third interaction bouts (0 – 5 s) were significantly increased relative to baseline (-5 – 0 s) (n = 7 $DRN^{DA\text{-}GCaMP6f}$ mice, paired t-test, $t_6 = 4.437$, **$p < 0.01$). **(H)** Left, averaged DRN^{DA} activity

was increased during the second and third episodes of aggression (red trace) by a resident male $DRN^{DA\text{-}GCaMP6f}$ mouse against a male intruder. Photometry data from the first attack episode (black trace, Fig. S2B) was also illustrated for comparison. Right, quantification of AUC revealed that DRN^{DA} activity during the second and third episodes of attack (0 – 5 s) was significantly increased relative to baseline (-5 – 0 s) (n = 4 $DRN^{DA\text{-}GCaMP6f}$ mice, paired t-test, $t_3 = 3.235$, $^*p < 0.05$). **(I)** Left, averaged DRN^{DA} activity during the second and third investigation bouts (red trace) in novel object interaction assays was not different from preceding baseline. Photometry data from first interaction bout (black trace, Fig. 1J) was also illustrated for comparison. Right, quantification of the area under the curve per second (AUC) showed that DRN^{DA} activity during the second and third interactions with a novel object (0 – 5 s) was not significantly increased compared with baseline (-5 – 0 s) (n = 7 $DRN^{DA\text{-}GCaMP6f}$ mice, paired t-test, $t_6 = 2.406$, $p > 0.05$). **(J)** Left, a robust increase in DRN^{DA} activity during the first interaction bout with a female mouse was observed in both single-housed (black, Fig. 1D) and group-housed (purple) mice. Right, quantification of AUC values during interaction (0 – 5 s) from single-housed and group-housed mice showed that there was no significant difference in DRN^{DA} activity based on housing conditions (n = 7 single-housed, n = 4 group-housed $DRN^{DA\text{-}GCaMP6f}$ mice; unpaired t-test, $p > 0.1$). **(K)** Left, time-locked DRN^{DA} activation was present when single-housed (black, Fig. 1H) and group-housed (purple) mice received unexpected electric footshocks. Right, AUC values during footshock delivery did not differ between single- and group-housed mice (n = 7 single-housed, n = 4 group-housed $DRN^{DA\text{-}GCaMP6f}$ mice; unpaired t-test, $p > 0.7$). **(L)** Left, small DRN^{DA} activation was observed in the first interaction bout with a novel object in both single-housed (black, Fig. 1J) and group-housed (purple) mice. Right, AUC values during novel object

interaction were not distinct between single- and group-housed mice (n = 7 single-housed, n = 4 group-housed $DRN^{DA\text{-}GCaMP6f}$ mice; unpaired t-test, $p > 0.5$). **(M)** Representative fiber photometry recording (black: fluorescence trace) and real-time locomotion tracking (red: velocity) for a $DRN^{DA\text{-}GCaMP6f}$ mouse during the open field test. Notice the lack of temporal correlation between two signals. **(N)** Averaged velocities aligned by detected Ca^{2+} peak event onset showed that increased DRN^{DA} activity is not associated with any change in velocity. **(O)** Averaged DRN^{DA} activity aligned by detected locomotion onset revealed that locomotion onset (indexed by increase of velocity) was not associated with a change in DRN^{DA} fluorescence. Data are represented as mean ± s.e.m.

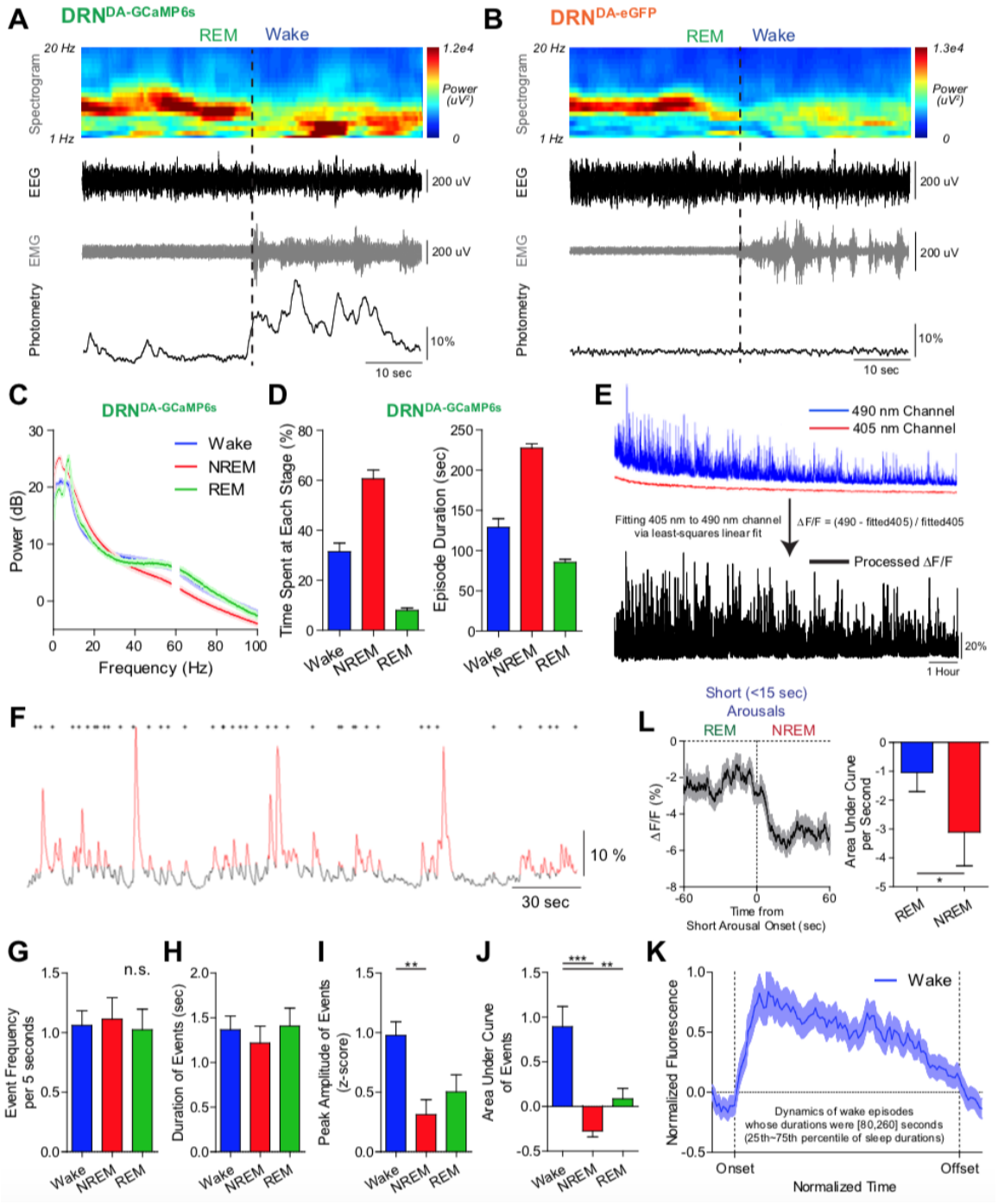

Supplementary Figure 3: related to Figure 2 and 3. (A) Representative example of a REM-to-wake transition from a DRN$^{DA\text{-}GCaMP6s}$ mouse with EEG spectrogram, EEG, EMG, and fiber photometry traces. Note that DRN^{DA} fluorescence was increased at the wake onset,

when EEG shifted from theta oscillations (5-10 Hz) to desynchronized rhythms and EMG amplitude abruptly increased. **(B)** Same as (A), but from a $DRN^{DA\text{-}eGFP}$ mouse. No change in fiber photometry signal is observed. **(C)** Power spectral density plots of $DRN^{DA\text{-}GCaMP6s}$ mice at each state: wake (blue), NREM (red), and REM (green). Notice that they show normal spectral EEG characteristics at each state: wake is characterized by smaller low-frequency activity and elevated high-frequency activity, NREM is characterized by high delta or slow wave (0.5-4 Hz) activity with suppressed high-frequency rhythms, and REM is associated with high theta (5-10 Hz) peak with elevated high-frequency activity. **(D)** Even with constant LED light exposure for exciting GCaMP6s, $DRN^{DA\text{-}GCaMP6s}$ mice showed normal sleep-wake architecture during light phase when synchronized photometry and EEG/EMG recordings were performed. For comparison, please see Fig. S1E. **(E)** After aligning the linearly scaled control 405 nm signal (red) with the 490 nm signal (blue), no noticeable decay was detected in the quality or signal-to-noise ratio of an extended photometry trace (black, 12-hour recording). **(F)** A representative photometry recording from a $DRN^{DA\text{-}GCaMP6s}$ mouse, with examples of automatically detected Ca^{2+} peak events (red). Detection onsets are denoted with black asterisks. **(G)** The frequency of detected peak events per 5-second window did not vary across sleep-wake states (n = 6 $DRN^{DA\text{-}GCaMP6s}$ mice; one-way ANOVA, $F_{2,15} = 0.07802$, $p > 0.9$). **(H)** Duration of the detected peak events did not vary significantly across sleep-wake states (n = 6 $DRN^{DA\text{-}GCaMP6s}$ mice; one-way ANOVA, $F_{2,15} = 0.2999$, $p > 0.7$). **(I)** Amplitude (z-scored) of the detected peak events was significantly increased in wake compared to NREM sleep (n = 6 $DRN^{DA\text{-}GCaMP6s}$ mice; one-way ANOVA, $F_{2,15} = 7.144$, $p < 0.01$; Post-hoc Bonferroni Analysis, $^{**}p < 0.01$) **(J)** Summed area under curve values within a 5-sec window was significantly increased at wake state over NREM and REM sleep (n = 6 $DRN^{DA\text{-}}$

^{GCaMP6s} mice; one-way ANOVA, $F_{2,15} = 15.59$, $p < 0.001$; Post-hoc Bonferroni Analysis, $^{**}p < 0.01$, $^{***}p < 0.001$). **(K)** Left, when mice made transitions from REM sleep to NREM sleep through a short period of arousal (wake shorter than 15 seconds), the DRN^{DA} activity decreased. Right, Quantification of the area under the curve per second showed that DRN^{DA} activity was significantly lower after transitions than before transitions (n = 6 $DRN^{DA\text{-}GCaMP6s}$ mice, paired t-test, $t_5 = 2.823$, $^{*}p < 0.05$). Data are represented as mean ± s.e.m.

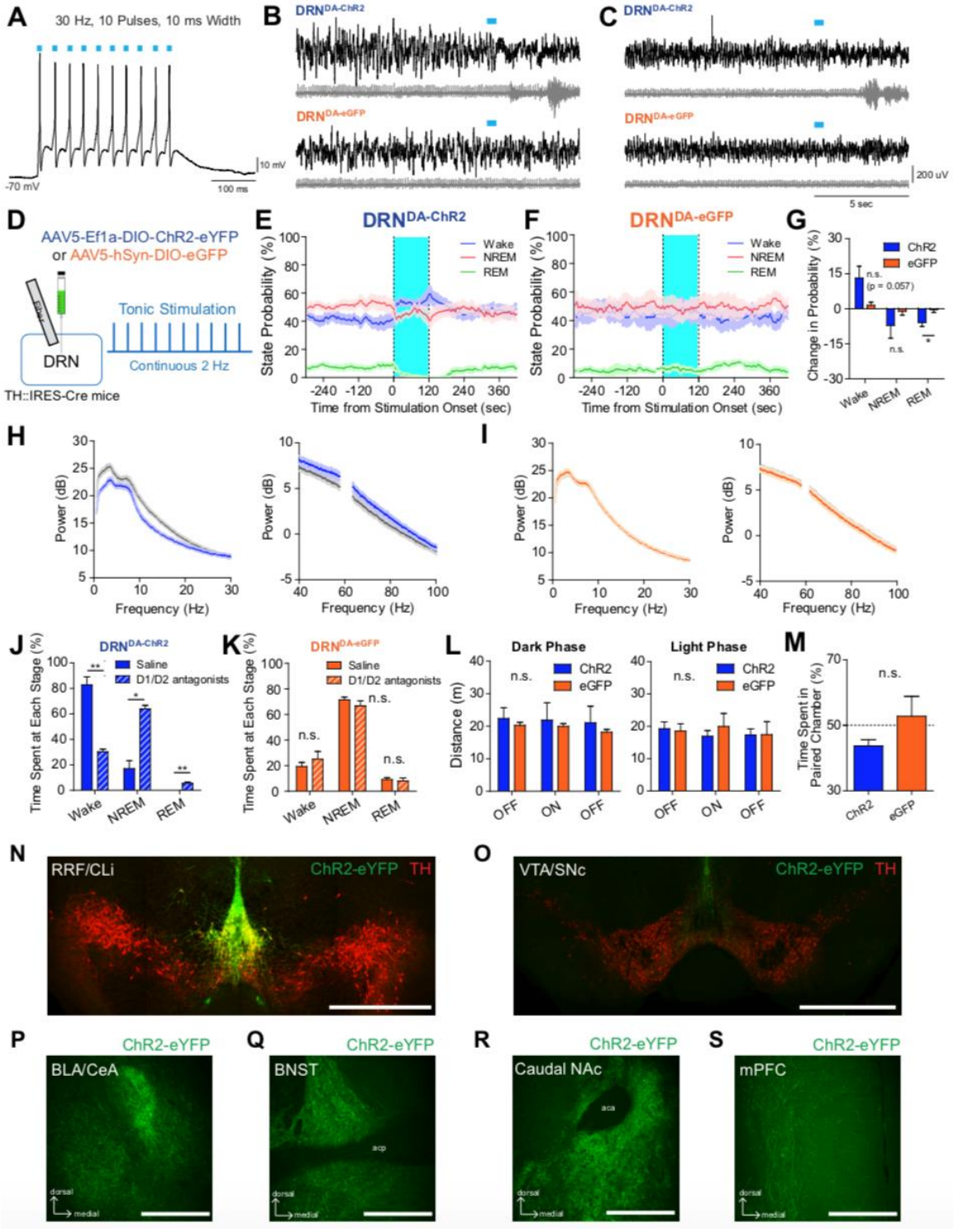

Supplementary Figure 4, related to Figure 4. (A) Ex vivo patch clamp recording demonstrated that DRN^{DA} neurons could faithfully follow our parameters of phasic

stimulation (30 Hz, 10 pulses, 10 ms pulse width). **(B)** Representative EEG (black) and EMG (gray) recordings when phasic DRN^{DA} stimulation caused immediate (<5 second) NREM-to-wake transitions in a $DRN^{DA\text{-}ChR2}$ mouse. Notice the termination of slow delta waves and abrupt increase of muscle activity after a phasic pulse. The same phasic stimulation paradigm did not cause any state changes in a $DRN^{DA\text{-}eGFP}$ mouse. **(C)** Same as (B), but when phasic stimulation occurred during REM sleep. **(D)** Two-minute tonic stimulations (continuous 2 Hz pulses for 2 minutes, 10 ms pulse width) were delivered every 20-25 minutes to $DRN^{DA\text{-}ChR2}$ and $DRN^{DA\text{-}eGFP}$ mice. **(E)** Tonic stimulation caused a small increase in the wake probability and a small decrease in the NREM and REM probability in $DRN^{DA\text{-}ChR2}$ mice. **(F)** No changes were observed upon tonic stimulation in $DRN^{DA\text{-}eGFP}$ mice. **(G)** REM state probability was significantly decreased in $DRN^{DA\text{-}ChR2}$ mice compared to $DRN^{DA\text{-}eGFP}$ mice (n = 8 $DRN^{DA\text{-}ChR2}$ mice, n = 7 $DRN^{DA\text{-}eGFP}$ mice; unpaired t-test, $*p < 0.05$). Although $DRN^{DA\text{-}ChR2}$ mice appeared to spend more time in the wake state, this trend did not reach statistical significance (unpaired t-test, $p = 0.057$). There were no significant differences in NREM state probability change between two groups (unpaired t-test, $p > 0.3$). **(H)** Power spectral density of $DRN^{DA\text{-}ChR2}$ mice (see Figure 4H), but divided into low (0.5-30 Hz) and high (40-100 Hz) frequency ranges for better visualization. **(I)** Same as (H), but for power spectral density of $DRN^{DA\text{-}eGFP}$ mice (see Figure 4I). **(J)** Wake-promoting effect of DRN^{DA} activation was abolished with systemic administration of D1 and D2 receptor antagonists. D1/D2 antagonists injection resulted in a significant decrease of the time spent awake (n = 4 $DRN^{DA\text{-}ChR2}$ mice; paired t-test, $t_3 = 7.161$, $**p<0.01$) and a significant increase in the time spent in NREM (paired t-test, $t_3 = 5.796$, $*p<0.05$) and REM sleep (paired t-test, $t_3 = 6.673$, $**p<0.01$), compared to saline injection. **(K)** $DRN^{DA\text{-}eGFP}$ mice showed no

significant change in the time spent in any state (n = 4 $DRN^{DA\text{-}eGFP}$ mice, paired t-test, all p>0.4) after systemic administration of saline or D1/D2 antagonists. **(L)** $DRN^{DA\text{-}ChR2}$ and $DRN^{DA\text{-}eGFP}$ mice underwent the open field test at the dark and light phases to examine the causal effect of DRN^{DA} activation with locomotion. There was no difference in distance traveled in the open field between the two mouse groups across light OFF and ON epochs in both phases (n = 6 per group; two-way ANOVA revealed no light x epoch interaction in both phases, $F_{2,20}$ (dark) = 0.089, p > 0.9, $F_{2,20}$ (light) = 2.088, p > 0.1). **(M)** Real-time place preference/aversion assay with $DRN^{DA\text{-}ChR2}$ and $DRN^{DA\text{-}eGFP}$ mice demonstrated that $DRN^{DA\text{-}ChR2}$ mice spent less time in the chamber paired with phasic light stimulation, but this trend for place aversion was not statistically different from $DRN^{DA\text{-}eGFP}$ mice group place preference/aversion (n = 6 per group; unpaired t-test, p > 0.1). **(N)** Virus injection into the DRN results in the transgene expression in the caudal linear nucleus (CLi) but not in the retrotrubral field (RRF). Scale bar is 1 mm. **(O)** Virus injection into the DRN does not result in cell-body expression, but show fibers (originating from DRN) in the VTA or SNc. Scale bar is 1 mm. **(P)** ChR2-eYFP fibers were found in the basolateral amygdala (BLA) and the central nucleus of the amygdala (CeA). **(Q)** Bed nucleus of the stria terminalis (BNST). **(R)** Caudal part of nucleus accumbens (NAc). **(S)** Medial prefrontal cortex (mPFC). All scale bars from (P) to (S) are 500 μm. Data are represented as mean ± s.e.m.

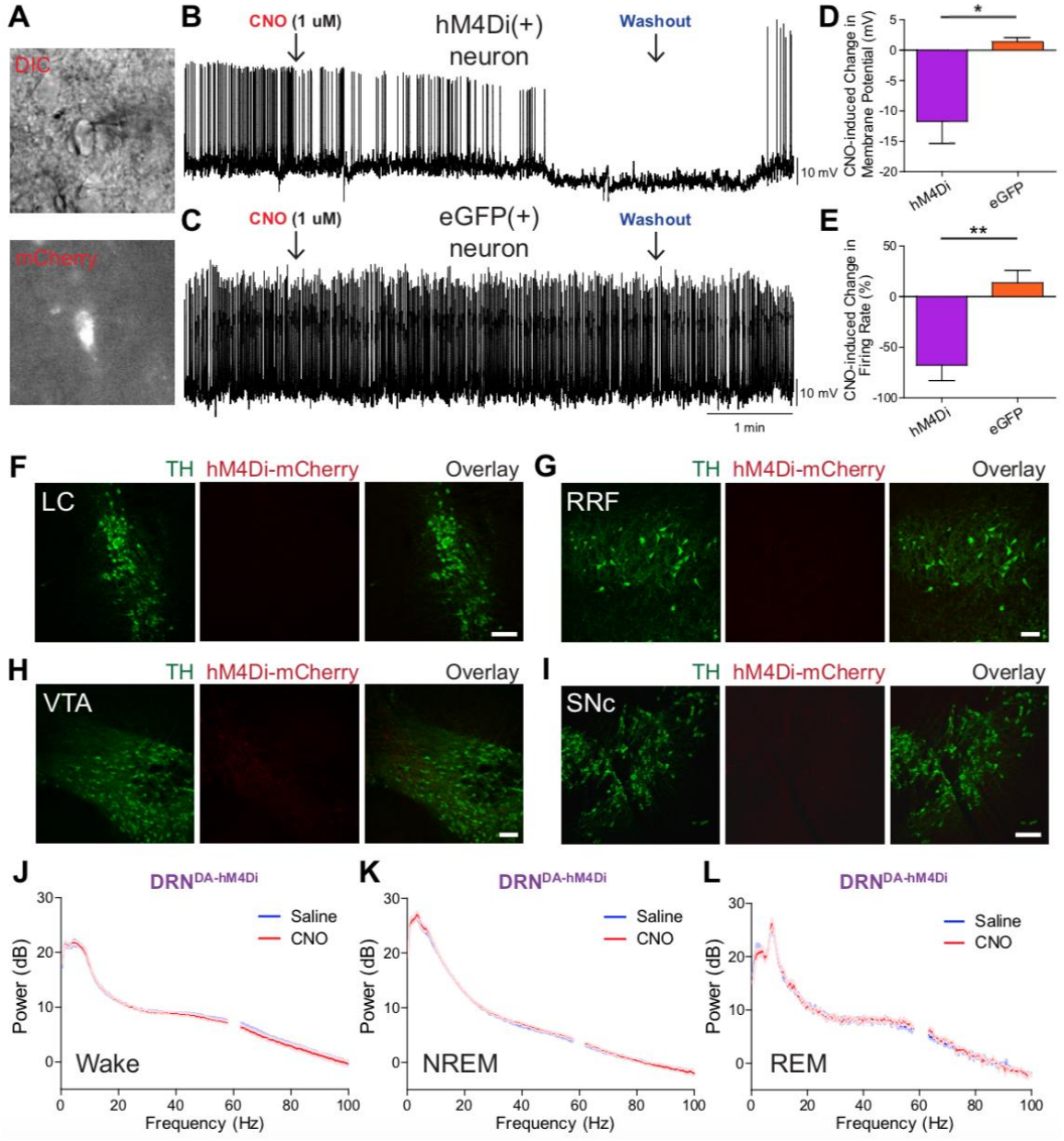

Supplementary Figure 5, related to Figure 5. (A) Images of DIC (upper) and fluorescence (lower) from a patched DRN^{DA} neuron expressing hM4Di-mCherry. **(B)** Representative example recording of membrane potentials from an hM4Di+ DRN^{DA} neuron. Bath application of CNO (1 uM) resulted in hyperpolarization and a reduction of neuronal firing, which was recovered after washout. Holding potential was at -45 mV. **(C)** Same as (B), but

for an eGFP+ DRN^{DA} neuron. Notice that there was no detectable change in membrane potential or firing rate. Holding potential was at -45 mV. **(D)** Application of CNO reduced the membrane potential of hM4Di+ neurons, but not in eGFP+ neurons. (n = 4 cells each; unpaired t-test, *p < 0.05). Baseline was defined as 1-minute epoch before CNO application, and CNO induced change was quantified from 2 to 4 minutes after CNO bath application. **(E)** Firing rate was significantly reduced with CNO application in hM4Di+ neurons, relative to eGFP+ neurons (n = 4 cells each; unpaired t-test, **p < 0.01). **(F-I)** Stereotaxic injection of AAV2-hSyn-DIO-hM4Di-mCherry (red) vectors into the DRN of TH-Cre mice did not result in anterograde or retrograde transport to other TH+ neurons (green) in **(F)** locus coeruleus (LC), **(G)** retrorubral field (RRF), **(H)** ventral tegmental area (VTA), and **(I)** substantia nigra pars compacta (SNc) after one month. Axonal fibers (presumably coming from the DRN^{DA} neurons) were shown, but no cell body expression was present in these areas. Scale bars are 100 um. **(J)** Power spectral density during wakefulness from $DRN^{DA\text{-}hM4Di}$ mice after saline (blue) and CNO (red) injection. Notice that EEG spectra after CNO delivery were not distinct from saline controls. **(K)** Same as (J), but for NREM sleep. **(L)** Same as (J), but for REM sleep. Data are represented as mean ± s.e.m.

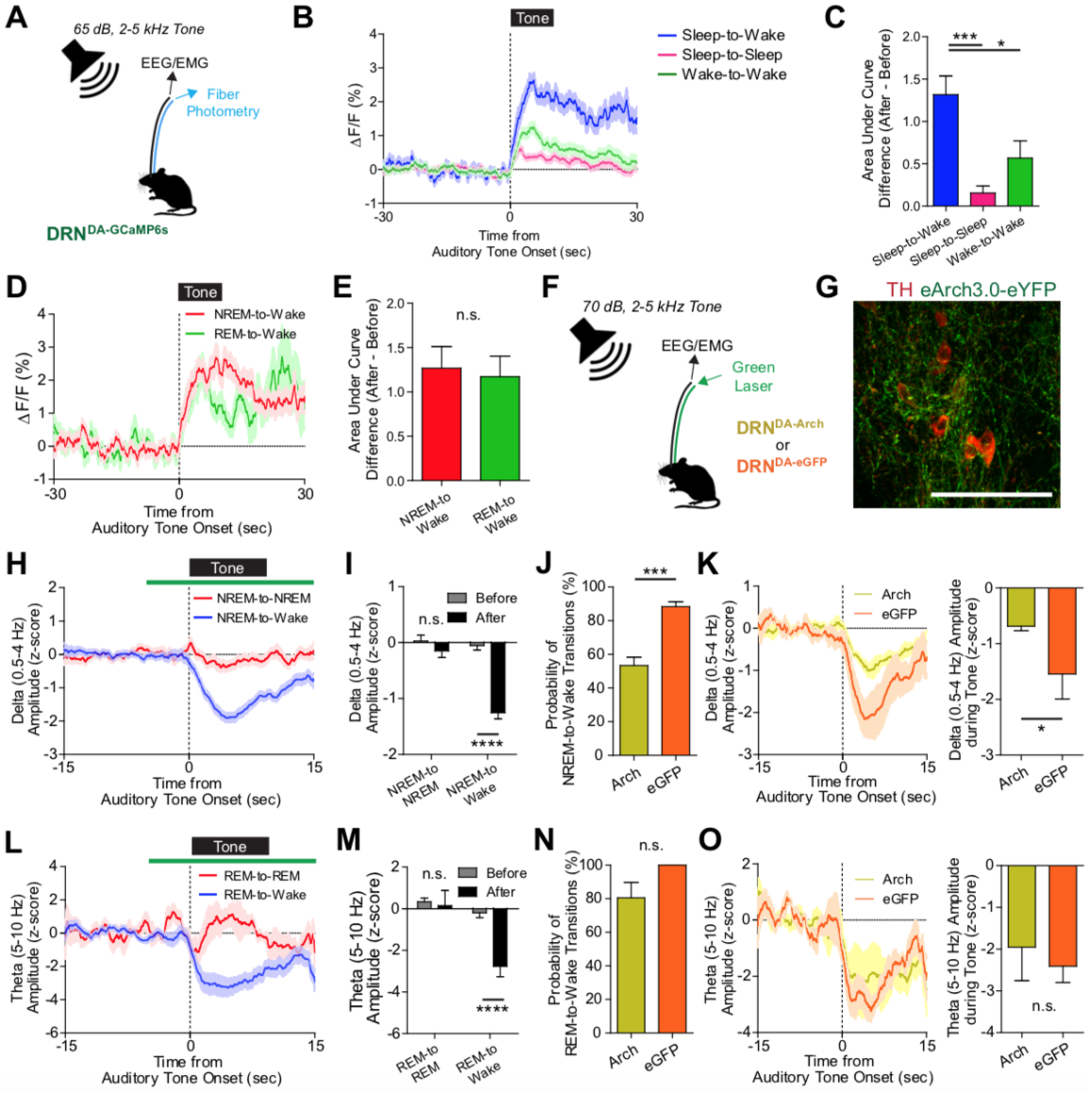

Supplementary Figure 6, related to Figure 6. (A) Fiber photometry and EEG/EMG recordings were performed in DRN$^{DA\text{-}GCaMP6s}$ mice. Arousing auditory tones (65 dB, 2-5 kHz, 2 Hz pulse frequency, 250 ms pulse, for 10 seconds) were randomly triggered during the light phase. **(B)** The presentation of auditory cues was associated with a time-locked increase in DRN^{DA} activity, especially in sleep-to-wake transitions. **(C)** DRN^{DA} activity change, as indexed by the difference in the area under the curve between before (-30-0 s) and after (0-

30 s) tone presentation, was larger when the auditory tone induced sleep-to-wake transitions (within 10 seconds) than when it was turned on during the wake state or when it failed to cause sleep-to-wake transitions (n = 7 $DRN^{DA\text{-}GCaMP6s}$ mice; one-way ANOVA, $F_{2,18} = 10.79$, $p < 0.001$, Bonferroni post-hoc analysis, *$p < 0.05$, ***$p < 0.001$). **(D)** Increased DRN^{DA} population activity was observed when arousing tones woke up $DRN^{DA\text{-}GCaMP6s}$ mice from NREM (red) or REM (green) sleep states. **(E)** The time-locked increase in DRN^{DA} activity upon auditory tone presentation did not vary according to the type of sleep-to-wake transitions (NREM-to-wake versus REM-to wake; n = 7 $DRN^{DA\text{-}GCaMP6s}$ mice, paired t-test, $t_6 = 1.4094$, $p > 0.2$). **(F)** EEG/EMG monitoring was performed with $DRN^{DA\text{-}Arch}$ or $DRN^{DA\text{-}hM4Di}$ mice while auditory tones (70 dB) were turned on during the light phase. Green laser (532 nm) was applied for 20 seconds surrounding the tonal stimuli for time-locked DRN^{DA} inhibition. **(G)** Confocal images of Arch+ (green) neurons co-localized with TH (red) expression. Scale bar is 100 μm. **(H)** There was a noticeable decrease in delta (0.5-4 Hz) amplitude in NREM-to-wake trials (blue), when auditory cues successfully caused wake transitions from NREM sleep, whereas there was minimal change of delta (0.5-4 Hz) amplitude in NREM-to-NREM trials (red), when auditory cues failed to cause wake transitions from NREM. Data are pooled together from both $DRN^{DA\text{-}Arch}$ and $DRN^{DA\text{-}eGFP}$ mice. **(I)** There was no difference in delta (0.5-4 Hz) amplitude before and after tones in NREM-to-NREM trials (n = 67 trials; paired t-test, $t_{66} = 1.310$, $p > 0.1$). However, there was significant decrease in delta (0.5-4 Hz) amplitude across tones in NREM-to-wake trials (n = 123 trials; paired t-test, $t_{122} = 10.58$, ***$p < 0.0001$). **(J)** There was a noticeable decrease in theta (5-10 Hz) amplitude in REM-to-wake trials (blue), when auditory cues successfully caused wake transitions from REM sleep, while there was minimal change of theta (5-10 Hz)

amplitude in REM-to-REM trials (red), when auditory cues failed to cause wake transitions from REM trials. Data are pooled together from both $DRN^{DA\text{-}Arch}$ and $DRN^{DA\text{-}eGFP}$ mice. **(K)** There was no difference in theta (5-10 Hz) amplitude before and after tones in REM-to-REM trials (n = 5 trials; paired t-test, $t_4 = 0.2832$, $p > 0.7$). However, there was significant decrease in theta amplitude across tones in REM-to-wake trials (n = 30 trials; paired t-test, $t_{29} = 5.786$, ***$p < 0.0001$). **(L)** The probability of NREM-to-wake transitions upon auditory tones was significantly lower in $DRN^{DA\text{-}Arch}$ mice compared to $DRN^{DA\text{-}eGFP}$ mice (n = 6 $DRN^{DA\text{-}Arch}$ mice, n = 4 $DRN^{DA\text{-}eGFP}$ mice; unpaired t-test, $p < 0.001$). **(M)** Left, delta (0.5-4 Hz) amplitude decrease was less prominent in $DRN^{DA\text{-}Arch}$ mice compared to control mice. Right, delta (0.5-4 Hz) amplitude during the tone was significantly higher in $DRN^{DA\text{-}Arch}$ mice than $DRN^{DA\text{-}eGFP}$ controls (n = 6 $DRN^{DA\text{-}Arch}$ mice, n = 4 $DRN^{DA\text{-}eGFP}$ mice; unpaired t-test, *$p < 0.05$). **(N)** The probability of REM-to-wake transitions upon auditory tones presentation was not different between $DRN^{DA\text{-}Arch}$ and $DRN^{DA\text{-}eGFP}$ mice (n = 6 $DRN^{DA\text{-}Arch}$ mice, n = 4 $DRN^{DA\text{-}eGFP}$ mice; unpaired t-test, $p > 0.1$). **(O)** Left, the decrease in theta (5-10 Hz) amplitude was similar between $DRN^{DA\text{-}Arch}$ and $DRN^{DA\text{-}eGFP}$ mice. Right, there was no statistically detectable difference in the theta (5-10 Hz) amplitude between groups during the tone presentation (n = 6 $DRN^{DA\text{-}Arch}$ mice, n = 4 $DRN^{DA\text{-}eGFP}$ mice; unpaired t-test, $p > 0.6$).

3.7 Supplementary movie captions

Supplementary Movie 1. DRN^{DA} neuronal activity increases upon social contact with a juvenile mouse, related to Figure 1. DRN^{DA} neuronal activity was recorded with fiber photometry while a TH-Cre mouse expressing GCaMP6f was in his home cage and a novel juvenile mouse was introduced. The corresponding DRN^{DA} fluorescence (upper right) shows increased activity upon contact with or investigation of the juvenile mouse.

Supplementary Movie 2. DRN^{DA} activity increases during the consumption of palatable food, related to Figure 1. DRN^{DA} neuronal activity was recorded with fiber photometry while a TH-Cre mouse expressing GCaMP6f was exploring in a novel empty cage and palatable food (peanut butter chocolate) was introduced to a corner. The corresponding DRN^{DA} fluorescence (upper right) shows increased activity upon investigation and consumption of the food.

3.8 Materials and methods

Key Resources Table

REAGENTS or RESOURCE	SOURCE	IDENTIFIER
Antibodies		
Chicken polyclonal anti-TH	Aves Labs	Cat#: TYH
Rabbit polyclonal anti-TH	Santa Cruz	Cat#: sc-14007
Chicken polyclonal anti-GFP	Aves Labs	Cat#: GFP-1020
Goat polyclonal anti-5HT	Immunostar	Cat#: 20079
Rabbit polyclonal anti-mCherry	Abcam	Cat#: ab167453
Anti-chicken Alexa Fluor 488	Jackson ImmunoResearch	Cat#: 703-545-155
Anti-rabbit Alexa Fluor 488	Jackson ImmunoResearch	Cat#: 711-545-152
Anti-goat Rhodamine Red-X	Jackson ImmunoResearch	Cat#: 705-297-003
Anti-rabbit Rhodamine Red-X	Jackson ImmunoResearch	Cat#: 711-297-003
Anti-rabbit Alexa Fluor 647	Jackson ImmunoResearch	Cat#: 711-607-003
Anti-chicken Alexa Fluor 647	Jackson ImmunoResearch	Cat#: 703-606-155
Chemicals		
Clozapine-N-oxide	Enzo Life Science	Cat#: BML-NS105
Experimental Models: Organisms/Strains		
Mouse: TH::IRES-Cre	European Mouse Mutant Archive	EM::00254
Recombinant DNA		
AAV5-Syn-FLEX-GCaMP6f	Penn Vector Core	AV-5-PV2819
AAV5-Syn-FLEX-GCaMP6s	Penn Vector Core	AV-5-PV2821
AAV5-Ef1a-DIO-ChR2(H134R)-eYFP	UNC Vector Core	N/A
AAV5-Ef1a-DIO-eArch3.0-eYFP	UNC Vector Core	N/A
AAV5-hSyn-DIO-eGFP	UNC Vector Core	N/A
AAV2-hSyn-DIO-hM4Di-mCherry	UNC Vector Core/Addgene	N/A
Software and Algorithms		
MATLAB R2014a	Mathworks	N/A
pClamp 10.4	Molecular Devices	N/A
SleepSign 3.0	Kissei Comtec	N/A
EthoVision XT10	Noldus Information Technology	N/A
ABETII	Lafayette Instrument	N/A
Prism 5.0	GraphPad Software	N/A
Illustrator CS6	Adobe	N/A

Experimental Model and Subject Details

Tyrosine hydroxylase (TH)::IRES-Cre knock-in mice (Lindeberg et al., 2004) were obtained from the European Mouse Mutant Archive (EM::00254) and crossed with wild-type C57BL/6N mice. We exclusively used male heterozygote mice for fiber photometry during behaviors and used both male and female heterozygote mice for other experiments with EEG/EMG. After weaning, animals were group-housed until they were 3-4 months old. Upon the completion of any surgical procedures, mice were allowed to recover from anesthesia on a heating-pad, and then they were transferred, singly-housed (or group-housed for the group-housed cohort) to a new residence room for full recovery (2-4 weeks) prior to the start of any behavioral experiments or habituation to EEG/EMG tethers. In this residence/procedure room, subjects were housed on a 12 h: 12 h light/dark cycle (light off at 6AM, light on at 6PM) with *ad libitum* access to food and water. Animal husbandry and all experimental procedures involving animal subjects were approved by the Institutional Animal Care and Use Committee (IACUC) and by the Office of Laboratory Animal Resources at the California Institute of Technology under IACUC protocol 1672.

Surgeries for viral delivery, optical fiber and EEG/EMG implantation

General surgical procedures and viral delivery

Mice were anesthetized with isoflurane gas/carbogen mixture (5% for induction and 1.5-2% for maintenance during surgery) and placed to a stereotaxic frame (David Kopf Instruments, CA, USA). After shaving their hair and sterilizing the skin with chlorohexidine, a midline incision was made with a sterile scalpel. The skull surface was wiped and cleaned with autoclaved cotton swabs. Bregma and lambda were identified and leveled to be on the same

z-axis. Small craniotomy holes were made for 20 degree angled injection of viruses and optical fiber implantation over the dorsal raphe nucleus (DRN, antero-posterior (AP) axis: -4.65 mm, medio-lateral (ML) axis: ±1.2 mm, relative to Bregma). Adeno-associated viral vectors (AAV, see below for details) were injected to the DRN (AP -4.6 mm, ML ±1.2 mm, dorso-ventral (DV) -2.95 mm, at a 20 degree angle relative to vertical axis from the left and right sides). Viral injection was performed using a blunt 35-gauge microinjection needle within a 10 uL microsyringe (NanoFil, World Precision Instruments, FL, USA), which was controlled by a microsyringe pump (UMP3, World Precision Instruments) connected to a controller (Micro4, World Precision Instruments). 0.3-0.5 uL of AAV was infused per site at a rate of 50 nL per min. Following injection, the needle/syringe was held in the same location for an additional 10 minutes to allow further diffusion. To prevent potential backflow, the needle/syringe was slowly withdrawn over approximately 10 minutes.

EEG and EMG implantation

To implant the EEG/EMG apparatus, three additional craniotomy holes were made in frontal (for first EEG channel; AP +2.0 mm, ML +0.7 mm), central (for second EEG channel; AP -1.3 mm, ML +1.3 mm) and lateral parietal (for reference and ground; AP -3.5 mm, ML -2.5 mm) regions with a drill bit (#73, 105-0240.340, Kyocera, Kyoto, Japan). 0.10'' electrodes with wire leads (8403, Pinnacle Technology Inc., KS, USA) were screwed to the craniotomy holes. With the leads from the screw electrodes held away from the surface of the skull to prevent accidental glue application, a thin layer of adhesive cement (C&B Metabond, Parkell Inc., NY, USA) was applied on the skull surface to secure the screw electrodes. Another thin layer of dental cement (51458, Stoelting Co., IL, USA) was additionally applied until it

covered screw heads. The EEG/EMG headmount (8201, Pinnacle Technology Inc.) was then affixed on the dental cement layer and lead wires from screw electrodes were connected to the headmount. Silver epoxy (MG Chemicals, BC, Canada) was applied to ensure electrical conduction between lead wires and the headmount. Additional layer of dental cement was applied to secure the headmount to the animal's head. Finally, EMG leads from the headmount were inserted into the trapezius muscles and then the incision was closed.

Optical fiber implantation (for fiber photometry and optogenetic experiments)

Following virus infusion, an optical ferrule/fiber with cut length of 4 mm and diameter of 300 um (for optogenetics, NA 0.37, home-made) or 400 um (for fiber photometry, NA 0.48, Doric lenses, Quebec, QC, Canada) was firmly mounted to a stereotaxic holder (1766AP, David Kopf Instruments, CA, USA). An optical ferrule/fiber was then inserted to the DRN (AP -4.6 mm, ML ±1.2 mm, DV -2.5~2.7 mm, at a 20 degree angle relative to vertical axis from either left or right side) through a craniotomy hole, and stopped 200 (for fiber photometry) or 500 um (for optogenetics) above the viral injection site. A thin layer of adhesive cement was applied on the skull surface to strongly hold the ferrule/fiber. After adhesive cement was completely dried, a thick layer of pink dental cement was applied to build a robust head cap.

Viral constructs

For fiber photometry experiments, 0.5 uL of AAV serotype 5 encoding GCaMP6f or GCaMP6s (Chen et al., 2013) under synapsin promoter and Cre-dependent FLEX switch (AAV5-Syn-FLEX-GCaMP6f or GCaMP6s, 1.0-1.5 X 10^{13} genome copies/mL) was

unilaterally injected. GCaMP6 viruses were packaged and purchased from the University of Pennsylvania Vector Core (Philadelphia, PA, USA). For optogenetic activation experiments, 0.3 uL of AAV serotype 5 encoding ChR2-eYFP under Ef1a promoter and double-floxed inverse open reading frame (DIO) (AAV5-Ef1a-DIO-ChR2(h134R)-eYFP, 4.5 X 10^{12} genome copies/mL) was bilaterally injected. For chemogenetic experiments, 0.3 uL of AAV serotype 2 encoding hM4Di-mCherry under human synapsin promoter and DIO switch (AAV2-hSyn-DIO-hM4Di-mCherry, 4.0 - 5.0 X 10^{12} genome copies/mL) was bilaterally injected. For optogenetic inhibition experiments, 0.5 uL of AAV serotype 5 encoding eArch3.0-eYFP under Ef1a promoter and DIO frame (AAV5-Ef1a-DIO-eArch3.0-eYFP, 3.4 X 10^{12} genome copies/mL) was bilaterally injected. For control animals, 0.5 uL of AAV5-hSyn-DIO-eGFP (4.7 X 10^{12} genome copies/mL) was bilaterally injected. ChR2-eYFP, hM4Di-mCherry, eArch3.0-eYFP and eGFP viruses were packaged and purchased from the University of North Carolina Vector Core (Chapel Hill, NC, USA). hM4Di-mCherry vector was also purchased from Addgene (Cambridge, MA, USA).

Fiber photometry

Fiber photometry is a method of measuring population Ca^{2+} sensitive fluorescence from genetically defined cell types in deep brain structures, such as TH-expressing neurons in the DRN, using a single optical fiber for both excitation and emission in freely moving mice (Gunaydin et al., 2014). We based our photometry design from previous literature (Lerner et al., 2015; Calipari et al., 2016) with a few modifications. Two wavelength LEDs (490 nm for GCaMP6 excitation and 405 nm for isosbestic wavelength excitation, M490F1 and M405F1, Thorlabs Inc.,NJ, USA) were modulated at two different frequencies (211 Hz for

490 nm, 531 Hz for 405 nm), which were controlled by a real-time processor (RX8-2, Tucker David Technologies, FL, USA) and a custom-written software (provided by Drs. Karl Deisseroth and Tom Davidson at Stanford University). The emission signal from 405 nm illumination was shown to be Ca^{2+}-independent with GCaMP6 and to mostly reflected bleaching and motion artifacts (Lerner et al., 2015; Kim et al., 2016): thus, this signal serves as a control reference signal. 490 nm and 405 nm excitation lights were passed through GFP and violet cleanup excitation filters (FF02-472/30-25 and FF01-400/40-25, Semrock, NY, USA) respectively, and reflected off dichroic mirrors (DMLP425 and MD498, Thorlabs). Excitation light was coupled into a low auto-fluorescence 400 um patch cord (0.48 NA, 2 m cable length, Doric lenses) with a high NA coupler/collimator (F240FC-A, Thorlabs). Another end of the patch cord was connected to a ceramic optical ferrule/fiber (1.25 mm diameter ferrule, 400 um fiber core diameter) implanted on animals. The LED powers for either excitation wavelength was measured with a power meter (PM100D, Thorlabs) and set to be 50-80 uW at the end of patch cord. GCaMP6 emission signals were collected through the patch cord and collimator and passed through a dichroic mirror (MD498, Thorlabs) and a GFP emission filter (MF525-39, Thorlabs) to reach a femtowatt photoreceiver (Model 2151, Newport Co., Irvine, CA, USA) using a focusing lens (62-561, Edmunds Optics, Barrington, NJ, USA). Photoreceiver signals were relayed into a RX8-2 processor through a BNC cable and were demodulated into two signals, corresponding to each LED excitation wavelength based on its modulation frequency. These outputs were digitized at a sampling rate of 382 Hz and low-pass filtered at 15 Hz. One digital input channel was additionally acquired to record any TTL pulses from an external source in order to synchronize transients with

EEG/EMG, video recording, or behavioral events. Custom-written software was used to control data acquisition and signal visualization.

Behavioral experiments

All behavioral experiments involving fiber photometry were performed at least 2 weeks after viral injection. Behavioral tests with optogenetics were performed at least 4 weeks after surgery to allow maximal transgene expression. Mice underwent the following assays during their dark phase (10AM-5PM) in their residence room, unless otherwise stated.

Resident-intruder assay

Mice with an implanted optical fiber were connected to a patch cord for recording of fiber photometry. After connection, mice were placed back into their home cages and habituated to the open cage setup for 10 minutes. After habituation, a juvenile male (3-4 weeks old), adult female (2-3 months old), or adult male (2-3 months old) mouse was introduced as an intruder into each home cage. Video recording was performed and synchronized with fiber photometry signals. After 5 minutes, the intruder mouse was removed from the home cage. The behavior of resident mice, such as investigation and attack (observed only towards adult males), was manually scored by an experimenter.

Novel object interaction assay

The novel object interaction test setup is almost identical to the resident-intruder assay, but a distinct novel object was placed into the center of the empty cages instead of an intruder mouse. To run the test, mice were connected to the photometry patch cord, and habituated to

being tethered in the open empty cage environment. Then, a novel object was introduced, and the subject was allowed to freely explore the object for a 5-minute test session. Behavior scoring was manually performed to identify interaction bouts, which consist of the subject approaching, sniffing, and/or touching of the object with forelimbs.

Familiar object interaction assay

This assay is similar to the novel object interaction assay described above, except that the designated familiar object (similar size and characteristics as used for the novel objects) was placed into the subject's home cage 5 days prior to photometry recording sessions.

Feeding assay

Two days before the experiment, the palatable food treat (approximately 1 g of peanut butter chocolate pieces (Reese's peanut butter cups)) was presented to each mouse for consumption. After connecting the mouse to the patch cord, they were placed to a clean, empty cage. After 5 minutes of habituation, approximately 2 g of treats in a small weighing boat were introduced into one of the cage corners. All tested subjects approached and consumed the treat after variable delays. Leftover treats were removed after 10 minutes. Video recordings were manually scored to identify food consumption bouts.

Air puff

Mice were connected to a patch cord and placed to a clean empty cage without any bedding. Mice were allowed to explore and habituate for 5 minutes. Six brief (<1 s) air puffs were applied to the tail using a compressed air duster with an inter-puff interval of 30-60 seconds.

TTL pulses were sent to the fiber photometry digital input channel for time stamping when air puffs were applied.

Unpredictable delivery of electric footshocks

Mice were connected to a patch cord and placed inside an operant chamber (Lafayette Instruments, IN, USA). Mice were allowed to explore and habituate to the operant box for 10 minutes. Two mild footshocks (0.3 mA, 1 second) were delivered with intervals about 30 seconds. TTL pulses were sent to the fiber photometry digital input channel for accurate time stamping.

Exposure to predator odor

Mice were connected to a patch cord and put to a clean empty cage. They were allowed to explore for 5 minutes to habituate to the environment. After photometry recording started, a filter paper applied with 10 uL of 2,3,5-trimethyl-3-thiazoline (TMT, a component of fox urine, SRQ Bio, Inc, FL, USA) was introduced at the corner. Simultaneous photometry video recordings were performed to identify the time point of odor investigation.

Restraint/Immobilization

A test subject was connected to a patch cord and placed to a clean empty cage. A 5-minute habituation session was conducted in which the subject was allowed to freely explore the cage. At the start of fiber photometry recording, 3 minutes of baseline was obtained. Then, taking care not to cause significant pain to the subject, a trained experimenter restrained the subject for one minute by placing gentle pressure on the mouse body with the left hand and

immobilizing the tail with the right hand. All subjects engaged in active struggling and escape behaviors. Recordings were terminated after 3 minutes of recovery.

Tail suspension test

Mice were connected to a patch cord, and the tail was placed between strips of common lab tape that were affixed to a horizontal bar that was suspended about 50 cm from the ground. We additionally put a lightweight (~1 g) plastic cylinder around the tail to prevent the mouse from climbing onto the tail. Synchronized fiber photometry and video recordings were performed for 5 minutes, and video was manually and blindly scored to pinpoint "mobility" bouts during which the animals struggled by moving their bodies.

Open field test

Mice were connected to a patch cord and transferred to the open field box (50 cm x 50 cm x 25 cm) that contained a video camera positioned above the behavioral arena to track the position and velocity of subject mice. Mice were habituated for 10-15 minutes prior to the start of testing. Locomotor activity tracking by a video camera was controlled by Ethovision XT 9 software (Noldus Information Technology, Wageningen, Netherlands). Fiber photometry and video recordings were synchronized via TTL pulses generated by the Noldus USB-IO box. Recording sessions lasted for 15 minutes. Fiber photometry experiments took place during the subjects' dark phase (10AM-5PM). For optogenetic experiments, open field tests were performed during both the dark phase (9AM-1PM) and light phase (6PM-10PM) to examine whether locomotion varied across the circadian cycle. The order of open field test sessions during dark and light phases was counter-balanced.

Real time place preference/aversion assay

A subject was connected to a patch cord and transferred to the open field box (50 cm x 25 cm x 25 cm), which was divided into left and right compartments. The subject was given free access to explore the two compartments for 30 minutes. However, upon entering the "paired chamber", the subject received phasic bursts of optogenetic stimulation (30 Hz, 10 pulses, 10 ms pulse width, every 5 seconds). The side paired with optogenetic stimulation was counter-balanced. Ethovision XT 9 software (Noldus) was used to track the movement and location of mice. As a dependent variable, time spent in the paired compartment was quantified.

EEG/EMG data acquisition, processing, and sleep-wake state classification

After EEG/EMG implantation surgery, animals were single-housed for four weeks in a regular mouse cage for recovery and transgene expression. Mice were then transferred to a transparent cylindrical cage (12'' diameter and 12" height) and connected to a customized pre-amplifier (10x gain, 0.5 Hz high-pass filter, 10 Hz high-pass filter for EMG; Pinnacle Technology Inc., Lawrence, KS, USA) and a commutator (8204, Pinnacle Technology Inc.) for freely moving recordings. They were habituated for at least seven days to the recording setup before beginning any experiments. At the 7^{th} day, four animals were randomly selected per group (depending on the viral transgene they expressed) and 24-hr baseline recordings were performed to test whether viral transgene expression or other experimental artifacts altered mice's sleep-wake architecture. Food and water were available *ad libitum*. EEG/EMG signals were digitized through the OmniPlex System (Plexon, TX, USA) with a sampling

rate of 1,000 Hz in most experiments, or through Pinnacle Sirenia Acquisition (Pinnacle Technology Inc, KS, USA) with a sampling rate of 400 Hz (for 24-hr baseline recordings and chemogenetic experiments in presence of salient stimuli). Mice with lost EEG and EMG signals were excluded from the experiment; very occasionally, some mice showed a low signal-to-noise ratio or unintelligible EEG/EMG traces.

Data acquired in Plexon's or Pinnacle proprietary file format (.pl2 or .pvfs) were converted to the European data format (.edf) with MATLAB (MathWorks, MA, USA) using the EEGLAB plug-in (Schwartz Center for Computational Neuroscience, La Jolla, CA, USA). Polysomnographic EEG/EMG recordings were loaded and scored to corresponding behavioral states using sleep analysis software (SleepSign for Animal, Kissei Comtec Co., Nagano, Japan).

Sleep-wake state classification is manually performed based on visual and spectral signatures of EEG and EMG signals. We assigned each state during consecutive non-overlapping 5-second windows. We defined wakefulness as desynchronized, low-amplitude, and high frequency EEG rhythms with elevated EMG activity. We defined NREM sleep as synchronized, high-amplitude, and low frequency (<4 Hz) EEG activity with lower tonic EMG tone. We defined REM sleep as containing prominent theta (6-10 Hz) oscillations on EEG and minimal EMG activity. All sleep-wake state scorings were performed by an experimenter (J.R.C.), who was blind to the type of expressed transgenes and experimental conditions.

Optogenetic and chemogenetic modulation of behavioral states and locomotion

For optogenetic experiments, one side of a patch cord (1.25 mm ceramic ferrule, 300 um diameter, Doric lenses) was connected to the implanted optical ferrule/fiber with another side (FC/PC connector) connected to a swivel commutator (fiber-optic rotary joints, FRJ_1x1_FC-FC, Doric lenses) to allow free movement. Another patch cord was connected from the commutator to a 473 nm laser (MLL-FN-473nm/150mW, Changchun New Industries Optoelectronics Technology, Changchun, China). The intensity of laser beam was measured with an optical power meter (PM100D, Thorlabs) and set to be 10 mW at the tip. Laser output was controlled by a TTL pulse generator (OTPG4, Doric lenses) via a BNC cable. For phasic stimulation, ten 30-Hz, 10-ms pulses were applied every 5 seconds. For tonic stimulation, continuous 2-Hz, 10-ms pulses were used. These phasic and tonic parameters were chosen to have the same number of pulses for a given duration but with distinct temporal pattern. Both phasic and tonic patterns of stimulation were applied for 2 minutes with intervals of 20-25 minutes. Animals used for optogenetic experiments were always connected to the preamplifier and Plexon system to continuously acquire EEG and EMG signals for sleep-wake state classification. TTL signals for controlling laser output were split and input into the Plexon acquisition system through an analog input for accurate time stamping of triggered stimulation. All optogenetic experiments with EEG/EMG monitoring were carried out during the light phase (6 PM-6 AM).

To test whether the wake-promoting effect of DRN^{DA} activation was mediated by direct action of DA, $DRN^{DA\text{-}ChR2}$ or $DRN^{DA\text{-}eGFP}$ mice habituated to the recording setup were systemically administered with the dopamine receptor antagonists SCH-23390 (a selective

D1 antagonist, 1 mg/kg) and eticlopride (a selective D2 antagonist, 1 mg/kg) 45 minutes before the onset of light phase. The concentration of these dopamine antagonists was selected based on previous literatures (Burgess et al., 2010; Eban-Rothschild et al., 2016). For controls, we injected sterile saline at the same circadian time. EEG/EMG recording and phasic optogenetic stimulation started at the light phase onset and lasted for 2 hours.

To study whether the wake-promoting effect of optogenetic DRN^{DA} stimulation is influenced by homeostatic sleep pressure, $DRN^{DA\text{-}ChR2}$ or $DRN^{DA\text{-}eGFP}$ mice were sleep deprived for 0 or 4 hours by gentle handling (Palchykova et al., 2006; Eban-Rothchild et al., 2016). The order of experiments (0 or 4-hour deprivation) was counter-balanced across animals. For sleep deprivation, mice were continuously monitored by an experimenter (with EEG and EMG recordings turned on). Mice were softly touched by a brush whenever they become motionless and/or exhibited reduced EMG tone or absent EMG bursts. After the sleep deprivation procedure, two phasic bursts (30 Hz, 15 pulses, 10 ms width, 5-second interval) were applied about 5~10 minutes after they entered into NREM sleep, and the latency to wake transitions was measured.

To study the causal effect of increased DRN^{DA} activity on locomotion, we performed the open field test with $DRN^{DA\text{-}ChR2}$ and $DRN^{DA\text{-}eGFP}$ mice. Procedures and experimental equipment were similar those described above for open field testing during fiber photometry. Mice were first habituated in the open field for 20 minutes, and the video recording was obtained while tracking the position of the test subject mice. After acquiring 20 minutes of baseline activity (not including habituation), laser stimulation (phasic or tonic patterns) was

was delivered for 5 minutes. After stimulation, five additional minutes were recorded. Throughout testing, distance travelled during 5-minute epochs of before, during, and after stimulation were analyzed.

For chemogenetic experiments, animals with hM4Di-mCherry or eGFP injection were connected to the data acquisition system for EEG and EMG signals. Animals were habituated to experimenter handling for 3-4 days before any experiments commenced. Saline or clozapine-N-oxide (CNO, selective ligand for hM4Di, 1 mg/kg dissolved in saline; Enzo Life Sciences Inc., Exeter, UK) was intraperitoneally injected immediately prior to the start of testing at 9 AM (3 hours after dark phase onset). Recordings were carried out for 2 hours following injection.

To test whether DRN^{DA} neuronal activity is required for wake maintenance after exposure to salient environmental stimuli, $DRN^{DA\text{-}hM4Di}$ or $DRN^{DA\text{-}eGFP}$ mice (which were already habituated to experimenter's handling) were first injected with saline or CNO (1 mg/kg) 45 minutes before testing. Then, a female mouse (contained in an inverted wire cup, and thus not directly accessible for mounting) or a filter paper with predator odor TMT was introduced into the recording cage. We chose these two stimuli because they are of opposite valence (positive versus negative) and were shown effective in inducing robust DRN^{DA} neuronal activity (See Fig. 1 and S2). EEG/EMG recording began right after introduction of the salient stimulus and lasted for 1 hour.

Auditory cue arousal test

To examine whether DRN^{DA} firing mediates cue-induced arousal from sleep, we performed simultaneous recording of fiber photometry and EEG/EMG signals on $DRN^{DA\text{-}GCaMP6s}$ mice. On each experimental day, recordings began at the light phase onset (6PM). Auditory tonal stimuli (65 dB; 2, 3, or 5 kHz frequency; 2-Hz pulse; 250-ms pulse width, 10-second duration) were randomly applied during the first half of the light phase (for 6 hours) with a minimum inter-trial interval of 15 minutes from a speaker located adjacent to the testing cages. In order to limit habituation to specific tonal frequencies, three different tones were administered in random order with a 33.3% probability for each frequency. The speaker was placed 30 cm away from the cage, and the auditory tone intensity inside the cylindrical cage was calibrated with a sound meter (Digital Sound Level Meter, Foneso, Shenzhen, China) before the beginning of each session with mice temporarily removed from the room. TTL pulses were generated when auditory cues were turned on and inputted onto the Plexon data acquisition system for accurate time stamping.

Sleep-wake states were classified as described above by an experimenter (J.R.C.) who was blind to the experimental conditions. Depending on the behavioral consequence of auditory cues, each trial was classified as 1) sleep-to-wake transitions (further divided from NREM or from REM sleep), 2) sleep-to-sleep (when auditory cue failed to induce wakefulness), and 3) wake-to-wake (auditory stimuli that were administered during wakefulness) cases. In order for the data to be scored as sleep-to-wake transitions, animals had to show at least 3 seconds of wake EEG and EMG signs (EEG: desynchronized from delta or theta rhythm, EMG: sudden phasic elevation of muscle activity) within 10 seconds of the auditory cue onset. If these criteria were not met, they were categorized as sleep-to-sleep cases.

To test for the necessity of DRN^{DA} firing in auditory cue-induced arousal from sleep, we inhibited DRN^{DA} neurons in a time-locked manner with the inhibitory proton pump eArch3.0 (Arch). The experimental setup was identical to the procedure described above, except that we used slightly higher intensity tone (70 dB) to avoid possible floor effects and that 20 seconds of 532 nm green laser (10 mW at the tip) was continuously applied surrounding the tone presentation (starting 5 seconds before the tone, terminating 5 seconds after the end of the tone) to the $DRN^{DA\text{-}Arch}$ or $DRN^{DA\text{-}eGFP}$ mice. Only data epochs when auditory cues were turned on during NREM or REM sleep were considered and we manually reviewed whether auditory tones caused wake transitions (see above for specific criteria). If cues successfully woke up the animal, they were categorized as 'NREM-to-Wake' or 'REM-to-Wake' trials. If tones did not lead to immediate wake transitions, they were categorized as 'NREM-to-NREM' or 'REM-to-REM' trials. To confirm that sleep-related oscillations (delta for NREM and theta for REM) were not perturbed in 'NREM-to-NREM' and 'REM-to-REM' trials, we calculated the delta and theta amplitude for NREM and REM, respectively, and determine whether there were any changes across the tone onset (see Figure S6H-S6K).

Data analysis

Fiber photometry data processing and analysis

Acquired data files were loaded and processed with custom-written codes in MATLAB. Pre-processing was performed as previously described (Lerner et al., 2015). Fiber photometry traces from 490 and 405 nm excitation wavelengths were first low-pass filtered at 2 Hz using a 4^{th} order Butterworth filter with zero-phase distortion. To calculate $\Delta F/F$, a least-squares

linear fit was applied to 405-nm signal and aligned to the 490-nm signal. The fitted 405-nm signal was subtracted from the 490-nm signal and then divided by the fitted 405-nm signal again to yield the ΔF/F time-series.

To visualize peri-event photometry traces, ΔF/F data epochs were extracted around immediately before and after relevant behavioral events (e.g. event onsets identified by either video scoring or TTL pulses) and averaged. For statistical comparison between baseline and behavior, areas under the curve (AUC) per second values were calculated for given conditions. Similarly, to visualize Ca^{2+} fluorescence change across state transitions, the temporal locations of state transitions were identified, and 120 seconds of photometry traces around the transition time points were extracted and averaged. AUC was also calculated to compare DRN^{DA} population activity before and after transitions. We performed analyses for NREM-to-wake, REM-to-wake, wake-to-NREM, and NREM-to-REM transitions. We excluded other possible combinations as rodents rarely transit directly from REM to NREM, and none of the tested mice showed wake-to-REM transitions, which is a common feature of narcolepsy. We termed periods of less than 15 seconds of wakefulness after REM state as "short arousal" and we separately plotted these transitions as "REM-to-short arousal-to-NREM".

To detect Ca^{2+} peak events from photometry traces and quantify them across sleep-wake states, we first normalized the trace using z-score and then high-pass filtered at 0.01 Hz using 2^{nd} order butterworth filter with zero-phase distortion to eliminate possible low frequency fluctuations across states. Then we detected prominent Ca^{2+} peak events with an amplitude

threshold, which was defined as the 75th percentile of the entire photometry data amplitude distribution. This percentile threshold was heuristically chosen because the photometry amplitude distribution is positively skewed and does not follow Gaussian distribution, which makes it more sensitive to the presence of outliers (such as during Ca^{2+} peak events). For quantification of these detected events, we calculated 1) peak amplitude, 2) duration (from detection onset to offset), 3) frequency or number of events in a 5-second window, and 4) summed AUC values of detected events in a 5-second window.

In order to account for inter-subject variability in amplitude during investigations into the temporal dynamics of DRN^{DA} activity during each behavioral state from onset to offset, we first converted the fluorescence traces into z-scores (calculated from the entire traces). Next, photometry traces from each state including 10% of the trace before and after were cropped and down-sampled to 120 points in order to normalize the timescale. This allowed us to project variable length photometry traces containing z-score normalized fluorescence changes onto the normalized time of -0.1 to 1.1, where 0 notes the onset and 1 notes the offset of a wake or sleep episode.

To examine any correlation between DRN^{DA} activity and locomotion, we obtained the synchronized recordings of fiber photometry and video tracking. To test if increased DRN^{DA} activity is associated with any change in locomotion, we detected prominent Ca^{2+} peak events as previously described above, extracted 10 seconds of velocity traces around peak event onsets, and then averaged. Conversely, to test if initiation of locomotion is associated increased DRN^{DA} activity, we detected locomotion onset similarly as the Ca^{2+} peak events

(but with 65th percentile as an amplitude threshold), extracted 10 seconds of photometry traces around locomotion onsets, and then averaged.

EEG spectrogram

To visualize spectral and temporal profiles of EEG activity across distinct behavioral states, we decomposed EEG into time-frequency plan using Morlet wavelet. EEG data epoch of interest was convolved with a complex Morlet wavelet, $w(t, f_0)$, having a Gaussian shape both in the time (σ_t) and frequency (σ_f) domain around its central frequency, f_0:

$$w(t, f_0) = (\frac{\sigma_t}{\pi})^{-1/2}\, exp\left(-\frac{t^2}{2{\sigma_t}^2}\right) exp(2i\pi f_0 t), \text{ where } \sigma_f = 1/2\pi\sigma_t.$$

A wavelet family was characterized by a constant (f_0/σ_f) ratio of 6 from 1 to 20 Hz in 1 Hz steps. The time-varying energy of the signal, $E(t, f_0)$, is defined as the squared norm of the convolution product of a complex wavelet $w(t, f_0)$, with the signal *s*(*t*): $E(t, f_0) = |w(t, f_0) \times s(t)|^2$. Time-varying energy is then smoothed by a moving average filter with span of 2 seconds for each frequency step to enhance visualization.

Calculation of EEG frequency band

To extract time-varying amplitude of a certain EEG frequency band (e.g. 0.5-4 Hz for delta, 5-10 Hz for theta, and 40-100 Hz for high-frequency - notch filter was applied from 58 to 62 Hz before calculating high-frequency activity amplitude to avoid any contribution from 60 Hz line noise), the signal of interest was first band-pass filtered using a 2nd order Butterworth filter. A zero-phase shift filter was used to prevent any phase distortion. Instantaneous amplitude was obtained by taking the absolute value of the Hilbert transform of the band-

passed signal. EEG frequency band amplitude signals were smoothed by a moving average filter (with 10-second window for Figure 4 and S4 and with 2-second window for Figure 6 and S6) and then normalized using z-score with respect to the baseline. EEG data epochs containing high-amplitude artifacts were excluded from analysis.

Power spectral density

Power spectral density was estimated for EEG data using a Welch's method. We used a 5-second window size and 50% overlap to estimate power from 0.5 to 100 Hz (except from 58 to 62 Hz). For 1-hour chronic optogenetic stimulation, spectral power changes during optogenetic stimulation with respect to the baseline (1 hour before the stimulation) were obtained for both $DRN^{DA\text{-}ChR2}$ and $DRN^{DA\text{-}eGFP}$ mice. For chemogenetic experiments, spectral power changes of CNO conditions from saline conditions were calculated at each frequency step. EEG data epochs with high-amplitude artifacts were excluded from analysis.

Efficiency and specificity of GCaMP6f+ expression

Efficiency was defined as "the number of GCaMP6f+ *and* TH+ neurons out of the total number of TH+ neurons". Specificity was defined as "the number of GCaMP6f+ *and* TH+ neurons out of the total number of GCaMP6f+ neurons".

Ex vivo electrophysiology

Electrophysiological recordings were performed as previously described (Xiao et al., 2016) to check the functionality of optogenetic and chemogenetic constructs. In brief, TH-cre mice expressing ChR2-eYFP or hM4Di-mCherry were euthanized with carbon dioxide and

transcardially perfused with ice-cold sucrose-based cutting solution saturated with 95% O2 / 5% CO2 (carbogen) that contained (mM) 85 NaCl, 75 sucrose, 2.5 KCl, 1.25 NaH_2PO_4, 4.0 $MgCl_2$, 0.5 $CaCl_2$, 24 $NaHCO_3$ and 25 glucose. The brain was removed and 250-μm coronal slices that contained the DRN were prepared in oxygenated cutting solution using a vibratome (VT-1200, Leica Biosystems, IL, USA). Slices were recovered at 32 °C for one hour prior to recording in carbogenated ACSF containing (mM): 125 NaCl, 2.5 KCl, 1.2 NaH_2PO_4, 1.2 $MgCl_2$, 2.4 $CaCl_2$, 26 $NaHCO_3$, and 11 glucose. Slices were transferred to the recording chamber and perfused (1.5 - 2.0 ml/min) with carbogen-saturated ACSF at 32 ± 0.5 °C. Whole-cell patch clamp recordings of fluorescently tagged (TH+) DRN neurons were obtained using a MultiClamp 700B amplifier (Molecular Devices, CA, USA) and a Digidata 1440 analog-to-digital converter (Molecular Devices). Data were sampled at 10 kHz and filtered at 2 kHz with Clampex 10.4 (Molecular Devices). Patch electrodes had resistance of 4 - 6 MΩ and were filled with a potassium gluconate intrapipette solution (mM): 135 K gluconate, 5 KCl, 5 EGTA, 0.5 $CaCl_2$, 10 HEPES, 2 Mg-ATP, and 0.1 GTP. Electrophysiological data were analyzed with Clampfit 10.4 (Molecular Devices). For Figure S4A, light-evoked currents (voltage clamp) and action potentials (current clamp) were evoked by ten of 30 Hz (10 ms pulse width) blue (420-455 nm) light delivered by an LED light source (Lumencor, OR, USA) in neurons held at -70mV. Once we patched hM4Di-mCherry+ or eGFP+ DRN^{DA} cells (Figure S5A-S5E), neuronal firing was evoked by depolarizing the membrane potential to -45 mV in current clamp mode. After collecting baseline for ~2 minutes, 1 μM of CNO was applied to the bath for neuronal silencing. After 3-4 minutes, CNO was washed out.

Histology

Perfusion

Mice were euthanized with CO_2 and transcardially perfused with 20 mL of ice-cold 1x PBS with heparin (10 U/mL) and then with 30 mL of ice-cold 4% PFA in 1x PBS. Mouse brains were carefully removed from the skull and post-fixed in 4% PFA at 4 °C overnight. The 4% PFA solution was switched to 1x PBS in the morning. Brains were sectioned into 50 μm coronal slices with a vibratome (VT1200, Leica Biosystems, IL, USA). Slices were stored in 1x PBS at 4 °C until immunohistochemical processing.

Immunohistochemistry

Brain sections were incubated in a 1x PBS solution containing 0.1% Triton X and 10% normal donkey serum (NDS; Jackson ImmunoResearch, PA, USA) with primary antibodies (see below for details) at 4 °C overnight. Afterwards, sections were thoroughly washed four times (15 minutes each) in 1x PBS and temporarily stored at 4 °C. Sections were then transferred into a secondary cocktail, which included 1xPBS with 0.1% Triton-X, 10% NDS with secondary antibodies (see below for details), and stored at 4 °C overnight. The next morning, sections were again washed by 1x PBS solution four times (15 minutes each), mounted on glass microscope slides (Adhesion Superfrost Plus Glass Slides, #5075-Plus, Brain Research Laboratories, MA, USA), dried, and cover-slipped with a DAPI-containing mounting media (Fluoromount G with DAPI, 00-4959-52, eBioscience, CA, USA).

Antibodies

For primary antibodies, anti-chicken TH (1:500; TYH, Aves Labs, OR, USA), anti-rabbit TH (1:500; sc-14007, Santa Cruz Biotechnology, CA, USA), anti-chicken GFP (1:500; GFP-1020, Aves Labs), anti-goat 5HT (1:1000; 20079, ImmunoStar, WI, USA), and anti-rabbit mCherry (1:500; ab167453, Abcam, Cambridge, UK) were used. For secondary antibodies, anti-chicken/rabbit Alexa Fluor 488 (1:500; 703-545-155, 711-545-152, Jackson ImmunoResearch), anti-goat/rabbit Rhodamine Red-X (1:500; 705-297-003, 711-297-003, Jackson ImmunoResearch), and anti-rabbit/chicken Alexa Fluor 647 (1:500, 711-607-003, 703-606-155, Jackson ImmunoResearch) were used.

Confocal microscopy imaging

Fluorescent images from brain tissue were acquired by a LSM 780 confocal microscope (Carl Zeiss, Jena, Germany). We used a 10x Plan Apochromat air objective (NA 0.45), 25x Plan Apochromat water immersion objective (NA 1.2) and 4 laser wavelengths (405 nm, 488 nm, 561 nm, and 633 nm). Image acquisition was controlled by Zen 2011 software (Zeiss), which also allowed automated z-stacking, tiling, and maximum intensity projection. Images were not further processed.

Quantification and Statistical Analysis

All data are represented as mean ± s.e.m. Sample sizes were determined to be comparable to previous studies that used optogenetics or chemogenetics to study neural circuits of sleep and wake state regulation (Carter et al., 2010; Xu et al., 2015). All statistical analyses were performed with in-built functions of the Statistics and Machine Learning toolbox in MATLAB (Mathworks) or Prism (GraphPad). Paired and unpaired t-tests were used for

single value comparisons. One-way ANOVA was used to compare more than two groups. Two-way repeated measures ANOVA was used to perform group comparisons with multiple measurements. Data is considered to be statistically significant if $p < 0.05$. We used Bonferroni correction to control for multiple comparisons where appropriate.

3.9 Additional information

AUTHOR CONTRIBUTIONS

J.R.C., J.B.T., and V.G. conceived and designed the project. J.R.C. performed and collected data from EEG/EMG recording, fiber photometry, and optogenetic, chemogenetic, and behavioral experiments. C.X. and J.E.R. performed ex vivo slice recordings. J.R.C., J.B.T., and V.G. analyzed data and made figures. J.R.C. and A.G. assembled the fiber photometry setup and wrote scripts for processing. J.R.C. and L.R.B. set up the EEG and EMG recording system. J.R.C., J.B.T., and V.G. wrote the manuscript with significant contributions from J.E.R. and L.R.B. All authors read and approved the final manuscript. V.G. supervised all aspects of the project.

ACKNOWLEDGMENTS

We would like to acknowledge Drs. Karl Deisseroth and Tom Davidson for the fiber photometry setup. We appreciate the entire Gradinaru lab and Dr. David Anderson for helpful discussions. This work was supported by the NIH (Director's New Innovator grants IDP20D017782-01 and PECASE), the NIH/ NIA (grants 1R01AG047664-01 and NIH BRAIN 1U01NS090577), the Heritage Medical Research Institute (HMRI-15-09-01), the Pew Charitable Trust (00026171), the Michael J. Fox Foundation (RRIA 2013), Caltech-GIST (CG2013), and the Sloan Foundation (FR2015-65471, to V.G.). J.B.T. is a Colvin postdoctoral fellow. J.E.R. is supported by the Children's Tumor Foundation (2016-01-006). C.X. was partly supported by the Michael J. Fox Foundation.

3.10 Reference

Aston-Jones, G., and Bloom, F.E. (1981). Activity of norepinephrine-containing locus coeruleus neurons in behaving rats anticipates fluctuations in the sleep-waking cycle. J. Neurosci. 1, 876–886.

Benarroch, E.E., Schmeichel, A.M., Dugger, B.N., Sandroni, P., Parisi, J.E., and Low, P.A. (2009). Dopamine cell loss in the periaqueductal gray in multiple system atrophy and Lewy body dementia. Neurology 73, 106–112.

Bjorklund, A., and Dunnett, S.B. (2007). Dopamine neuron systems in the brain: an update. Trends Neurosci. 30, 194–202.

Brischoux, F., Chakraborty, S., Brierley, D.I., and Ungless, M.A. (2009). Phasic excitation of dopamine neurons in ventral VTA by noxious stimuli. Proc. Natl. Acad. Sci. USA 106, 4894–4899.

Bromberg-Martin, E.S., Matsumoto, M., and Hikosaka, O. (2010). Dopamine in motivational control: rewarding, aversive, and alerting. Neuron 68, 815–834.

Brown, R.E., Basheer, R., McKenna, J.T., Strecker, R.E., and McCarley, R.W. (2012). Control of sleep and wakefulness. Physiol. Rev. 92, 1087–1187.

Chen, T.W., Wardill, T.J., Sun, Y., Pulver, S.R., Renninger, S.L., Baohan, A., Schreiter, E.R., Kerr, R.A., Orger, M.B., Jayaraman, V., et al. (2013). Ultrasensitive fluorescent proteins for imaging neuronal activity. Nature 499, 295–300.

Cohen, J.Y., Haesler, S., Vong, L., Lowell, B.B., and Uchida, N. (2012). Neuron- type-specific signals for reward and punishment in the ventral tegmental area. Nature 482, 85–88.

Daberkow, D.P., Brown, H.D., Bunner, K.D., Kraniotis, S.A., Doellman, M.A., Ragozzino, M.E., Garris, P.A., and Roitman, M.F. (2013). Amphetamine paradoxically augments exocytotic dopamine release and phasic dopamine signals. J. Neurosci. 33, 452–463.

Dahan, L., Astier, B., Vautrelle, N., Urbain, N., Kocsis, B., and Chouvet, G. (2007). Prominent burst firing of dopaminergic neurons in the ventral tegmental area during paradoxical sleep. Neuropsychopharmacology 32, 1232–1241.

Descarries, L., Berthelet, F., Garcia, S., and Beaudet, A. (1986). Dopaminergic projection from nucleus raphe dorsalis to neostriatum in the rat. J. Comp. Neurol. 249, 511–520, 484–515.

Dougalis, A.G., Matthews, G.A., Bishop, M.W., Brischoux, F., Kobayashi, K., and Ungless, M.A. (2012). Functional properties of dopamine neurons and co-expression of vasoactive intestinal polypeptide in the dorsal raphe nucleus and ventro-lateral periaqueductal grey. Eur. J. Neurosci. 36, 3322–3332.

Eban-Rothschild, A., Rothschild, G., Giardino, W.J., Jones, J.R., and de Lecea, L. (2016). VTA dopaminergic neurons regulate ethologically relevant sleep-wake behaviors. Nat. Neurosci. 19, 1356–1366.

Espan˜ a, R.A. (2012). Hypocretin/orexin involvement in reward and reinforcement. Vitam. Horm. 89, 185–208.

Garey, J., Goodwillie, A., Frohlich, J., Morgan, M., Gustafsson, J.A., Smithies, O., Korach, K.S., Ogawa, S., and Pfaff, D.W. (2003). Genetic contributions to generalized arousal of brain and behavior. Proc. Natl. Acad. Sci. USA 100, 11019–11022.

George, E.D., Bordner, K.A., Elwafi, H.M., and Simen, A.A. (2010). Maternal separation

with early weaning: a novel mouse model of early life neglect. BMC Neurosci. 11, 123.

Gjerstad, M.D., Wentzel-Larsen, T., Aarsland, D., and Larsen, J.P. (2007). Insomnia in Parkinson's disease: frequency and progression over time. J. Neurol. Neurosurg. Psychiatry 78, 476–479.

Gunaydin, L.A., Grosenick, L., Finkelstein, J.C., Kauvar, I.V., Fenno, L.E., Adhikari, A., Lammel, S., Mirzabekov, J.J., Airan, R.D., Zalocusky, K.A., et al. (2014). Natural neural projection dynamics underlying social behavior. Cell 157, 1535–1551.

Hasue, R.H., and Shammah-Lagnado, S.J. (2002). Origin of the dopaminergic innervation of the central extended amygdala and accumbens shell: a combined retrograde tracing and immunohistochemical study in the rat. J. Comp. Neurol. 454, 15–33.

Hokfelt, T., Martensson, R., Bjorklund, A., Kleinau, S., and Goldstein, M. (1984). Distribution Maps of Tyrosine-Hydroxylase-Immunoreactive Neurons in the Rat Brain (Elsevier).

Jennings, J.H., Sparta, D.R., Stamatakis, A.M., Ung, R.L., Pleil, K.E., Kash, T.L., and Stuber, G.D. (2013). Distinct extended amygdala circuits for divergent motivational states. Nature 496, 224–228.

Jones, B.E. (1991). Paradoxical sleep and its chemical/structural substrates in the brain. Neuroscience 40, 637–656.

Jouvet, M. (1999). Sleep and serotonin: an unfinished story. Neuropsychopharmacology 21 (2, Suppl), 24S–27S.

Kim, C.K., Yang, S.J., Pichamoorthy, N., Young, N.P., Kauvar, I., Jennings, J.H., Lerner, T.N., Berndt, A., Lee, S.Y., Ramakrishnan, C., et al. (2016). Simultaneous fast

measurement of circuit dynamics at multiple sites across the mammalian brain. Nat. Methods 13, 325–328.

Lammel, S., Ion, D.I., Roeper, J., and Malenka, R.C. (2011). Projection-specific modulation of dopamine neuron synapses by aversive and rewarding stimuli. Neuron 70, 855–862.

Lammel, S., Lim, B.K., Ran, C., Huang, K.W., Betley, M.J., Tye, K.M., Deisseroth, K., and Malenka, R.C. (2012). Input-specific control of reward and aversion in the ventral tegmental area. Nature 491, 212–217.

Lammel, S., Lim, B.K., and Malenka, R.C. (2014). Reward and aversion in a heterogeneous midbrain dopamine system. Neuropharmacology 76 (Pt B), 351–359.

Leger, L., Sapin, E., Goutagny, R., Peyron, C., Salvert, D., Fort, P., and Luppi, P.H. (2010). Dopaminergic neurons expressing Fos during waking and paradoxical sleep in the rat. J. Chem. Neuroanat. 39, 262–271.

Lerner, T.N., Shilyansky, C., Davidson, T.J., Evans, K.E., Beier, K.T., Zalocusky, K.A., Crow, A.K., Malenka, R.C., Luo, L., Tomer, R., and Deisseroth, K. (2015). Intact-brain analyses reveal distinct information carried by SNc dopamine subcircuits. Cell 162, 635–647.

Li, C., Sugam, J.A., Lowery-Gionta, E.G., McElligott, Z.A., McCall, N.M., Lopez, A.J., McKlveen, J.M., Pleil, K.E., and Kash, T.L. (2016). Mu opioid receptor modulation of dopamine neurons in the periaqueductal gray/ dorsal raphe: a role in regulation of pain. Neuropsychopharmacology 41, 2122–2132.

Lima, M.M. (2013). Sleep disturbances in Parkinson's disease: the contribution of dopamine in REM sleep regulation. Sleep Med. Rev. 17, 367–375.

Lin, J.S., Roussel, B., Akaoka, H., Fort, P., Debilly, G., and Jouvet, M. (1992). Role of catecholamines in the modafinil and amphetamine induced wakefulness, a comparative pharmacological study in the cat. Brain Res. 591, 319–326.

Lu, J., Jhou, T.C., and Saper, C.B. (2006). Identification of wake-active dopaminergic neurons in the ventral periaqueductal gray matter. J. Neurosci. 26, 193–202.

Margolis, E.B., Mitchell, J.M., Ishikawa, J., Hjelmstad, G.O., and Fields, H.L. (2008). Midbrain dopamine neurons: projection target determines action potential duration and dopamine D(2) receptor inhibition. J. Neurosci. 28, 8908–8913.

Matsumoto, M., and Hikosaka, O. (2009). Two types of dopamine neuron distinctly convey positive and negative motivational signals. Nature 459, 837–841.

Matthews, G.A., Nieh, E.H., Vander Weele, C.M., Halbert, S.A., Pradhan, R.V., Yosafat, A.S., Glober, G.F., Izadmehr, E.M., Thomas, R.E., Lacy, G.D., et al. (2016). Dorsal raphe dopamine neurons represent the experience of social isolation. Cell 164, 617–631.

Mattis, J., Tye, K.M., Ferenczi, E.A., Ramakrishnan, C., O'Shea, D.J., Prakash, R., Gunaydin, L.A., Hyun, M., Fenno, L.E., Gradinaru, V., et al. (2011). Principles for applying optogenetic tools derived from direct comparative analysis of microbial opsins. Nat. Methods 9, 159–172.

McCall, J.G., Al-Hasani, R., Siuda, E.R., Hong, D.Y., Norris, A.J., Ford, C.P., and Bruchas, M.R. (2015). CRH engagement of the locus coeruleus noradrenergic system mediates stress-induced anxiety. Neuron 87, 605–620.

McDevitt, R.A., Tiran-Cappello, A., Shen, H., Balderas, I., Britt, J.P., Marino, R.A., Chung, S.L., Richie, C.T., Harvey, B.K., and Bonci, A. (2014). Serotonergic versus nonserotonergic dorsal raphe projection neurons: differential participation in reward

circuitry. Cell Rep. 8, 1857–1869.

Miller, J.D., Farber, J., Gatz, P., Roffwarg, H., and German, D.C. (1983). Activity of mesencephalic dopamine and non-dopamine neurons across stages of sleep and walking in the rat. Brain Res. 273, 133–141.

Minami, M., and Ide, S. (2015). How does pain induce negative emotion? Role of the bed nucleus of the stria terminalis in pain-induced place aversion. Curr. Mol. Med. 15, 184–190.

Morales, M., and Margolis, E.B. (2017). Ventral tegmental area: cellular heterogeneity, connectivity and behaviour. Nat. Rev. Neurosci. 18, 73–85.

Nagatsu, I., Inagaki, S., Kondo, Y., Karasawa, N., and Nagatsu, T. (1979). Immunofluorescent studies on the localization of tyrosine hydroxylase and dopamine-beta-hydroxylase in the mes-, di-, and telencephalon of the rat using unperfused fresh fronzen section. Acta Histochem. Cytochem. 12, 20–37.

Pimentel, D., Donlea, J.M., Talbot, C.B., Song, S.M., Thurston, A.J., and Miesenbo¨ck, G. (2016). Operation of a homeostatic sleep switch. Nature 536, 333–337.

Pinto, L., Goard, M.J., Estandian, D., Xu, M., Kwan, A.C., Lee, S.H., Harrison, T.C., Feng, G., and Dan, Y. (2013). Fast modulation of visual perception by basal forebrain cholinergic neurons. Nat. Neurosci. 16, 1857–1863.

Poulin, J.F., Zou, J., Drouin-Ouellet, J., Kim, K.Y., Cicchetti, F., and Awatramani, R.B. (2014). Defining midbrain dopaminergic neuron diversity by single-cell gene expression profiling. Cell Rep. 9, 930–943.

Qiu, M.H., Yao, Q.L., Vetrivelan, R., Chen, M.C., and Lu, J. (2016). Nigrostriatal dopamine action on globus pallidus regulates sleep. Cereb. Cortex 26, 1430–1439.

Qu, W.M., Huang, Z.L., Xu, X.H., Matsumoto, N., and Urade, Y. (2008). Dopaminergic D1 and D2 receptors are essential for the arousal effect of modafinil. J. Neurosci. 28, 8462–8469.

Rajasethupathy, P., Ferenczi, E., and Deisseroth, K. (2016). Targeting neural circuits. Cell 165, 524–534.

Sakurai, T., Amemiya, A., Ishii, M., Matsuzaki, I., Chemelli, R.M., Tanaka, H., Williams, S.C., Richardson, J.A., Kozlowski, G.P., Wilson, S., et al. (1998). Orexins and orexin receptors: a family of hypothalamic neuropeptides and G protein-coupled receptors that regulate feeding behavior. Cell 92, 573–585.

Sanford, L.D., Suchecki, D., and Meerlo, P. (2015). Stress, arousal, and sleep. Curr. Top. Behav. Neurosci. 25, 379–410.

Sateia, M.J., Greenough, G., and Nowell, P. (2000). Sleep in neuropsychiatric disorders. Semin. Clin. Neuropsychiatry 5, 227–237.

Schultz, W. (1997). Dopamine neurons and their role in reward mechanisms. Curr. Opin. Neurobiol. 7, 191–197.

Schweimer, J.V., and Ungless, M.A. (2010). Phasic responses in dorsal raphe serotonin neurons to noxious stimuli. Neuroscience 171, 1209–1215.

Steinberg, E.E., Boivin, J.R., Saunders, B.T., Witten, I.B., Deisseroth, K., and Janak, P.H. (2014). Positive reinforcement mediated by midbrain dopamine neurons requires D1 and D2 receptor activation in the nucleus accumbens. PLoS ONE 9, e94771.

Szymusiak, R., and McGinty, D. (2008). Hypothalamic regulation of sleep and arousal. Ann. N Y Acad. Sci. 1129, 275–286.

Takahashi, K., Kayama, Y., Lin, J.S., and Sakai, K. (2010). Locus coeruleus neuronal

activity during the sleep-waking cycle in mice. Neuroscience 169, 1115–1126.

Taylor, N.E., Van Dort, C.J., Kenny, J.D., Pei, J., Guidera, J.A., Vlasov, K.Y., Lee, J.T., Boyden, E.S., Brown, E.N., and Solt, K. (2016). Optogenetic activation of dopamine neurons in the ventral tegmental area induces reanimation from general anesthesia. Proc. Natl. Acad. Sci. USA 113, 12826–12831.

Tsai, H.C., Zhang, F., Adamantidis, A., Stuber, G.D., Bonci, A., de Lecea, L., and Deisseroth, K. (2009). Phasic firing in dopaminergic neurons is sufficient for behavioral conditioning. Science 324, 1080–1084.

Ungless, M.A., Magill, P.J., and Bolam, J.P. (2004). Uniform inhibition of dopamine neurons in the ventral tegmental area by aversive stimuli. Science 303, 2040–2042.

Urban, D.J., and Roth, B.L. (2015). DREADDs (designer receptors exclusively activated by designer drugs): chemogenetic tools with therapeutic utility. Annu. Rev. Pharmacol. Toxicol. 55, 399–417. Vinck, M., Batista-Brito, R., Knoblich, U., and Cardin, J.A. (2015). Arousal and locomotion make distinct contributions to cortical activity patterns and visual encoding. Neuron 86, 740–754.

Whitaker, L.R., Degoulet, M., and Morikawa, H. (2013). Social deprivation enhances VTA synaptic plasticity and drug-induced contextual learning. Neuron 77, 335–345. Winsky-Sommerer, R., Boutrel, B., and de Lecea, L. (2005). Stress and arousal: the corticotrophin-releasing factor/hypocretin circuitry. Mol. Neurobiol. 32, 285–294.

Wise, R.A. (2004). Dopamine, learning and motivation. Nat. Rev. Neurosci. 5, 483–494.

Wisor, J.P., Nishino, S., Sora, I., Uhl, G.H., Mignot, E., and Edgar, D.M. (2001). Dopaminergic role in stimulant-induced wakefulness. J. Neurosci. 21, 1787–1794.

Witten, I.B., Steinberg, E.E., Lee, S.Y., Davidson, T.J., Zalocusky, K.A., Brodsky, M., Yizhar, O., Cho, S.L., Gong, S., Ramakrishnan, C., et al. (2011). Recombinase-driver rat lines: tools, techniques, and optogenetic application to dopamine-mediated reinforcement. Neuron 72, 721–733.

Xu, M., Chung, S., Zhang, S., Zhong, P., Ma, C., Chang, W.C., Weissbourd, B., Sakai, N., Luo, L., Nishino, S., and Dan, Y. (2015). Basal forebrain circuit for sleep-wake control. Nat. Neurosci. 18, 1641–1647.

Zweifel, L.S., Fadok, J.P., Argilli, E., Garelick, M.G., Jones, G.L., Dickerson, T.M., Allen, J.M., Mizumori, S.J., Bonci, A., and Palmiter, R.D. (2011). Activation of dopamine neurons is critical for aversive conditioning and prevention of generalized anxiety. Nat. Neurosci. 14, 620–626.

Chapter 4

DORSAL RAPHE DOPAMINE NEURONS SIGNAL MOTIVATIONAL SALIENCE

4.1 Summary

The previous chapter demonstrated that DRN^{DA} neurons are critical mediators of sleep-wake regulation and promote behavioral arousal. Then what do these neurons encode or signal while animals are awake? That DRN^{DA} neurons were robustly activated for any environmental stimuli with positive or negative valence, but not with neutral value, suggests these neurons may encode motivational salience. To further address this idea, mice were trained for appetitive and aversive classical conditioning tasks during fiber photometry recordings, where they learned associations between originally neutral cues and positive or negative outcomes. Across associative learning, initially unresponsive DRN^{DA} neurons developed positive response to cues paired with both positive and negative outcomes. After extinction learning, DRN^{DA} neurons no longer responded to the previously paired cues. Further experiments demonstrated that DRN^{DA} neurons signal unsigned prediction error, showing enhanced neural activity for unexpected outcomes over fully expected ones. These salience responses were also sensitive to animal's internal motivational state, as response to reward-predicting cues were diminished after satiety. Altogether, these data suggest that DRN^{DA} neurons encode or signal motivational salience of environmental cues at the population level.

4.2 DRN^{DA} dynamics during classical conditioning

In the previous chapter, I have shown with fiber photometry recordings that DRN^{DA} neuronal activity fluctuates across distinct sleep and wake states and that its activity is highest during wakefulness and suppressed in sleep stages. However, the level of arousal fluctuates even within wakefulness: for example, animals can be highly aroused and hence motivated to perform goal-directed behavior when they face with rewarding (such as food or social targets) or aversive (such as predator odor, threat, or pain) stimuli. Therefore, whether DRN^{DA} neurons also respond to arousal-provoking stimuli or situation during wakefulness is a naturally extended question to be addressed. Indeed, Figure 1 and S2 in the Chapter III demonstrated that DRN^{DA} neurons were activated by diverse arrays of motivationally salient stimuli or during motivated responding to such situation, regardless of their value (i.e., whether they are rewarding or aversive). This leads to a hypothesis that DRN^{DA} neurons encode motivational salience (i.e., absolute of motivational value), distinct from lateral VTA^{DA} or medial SNc^{DA} neurons that signal motivational valence (Bromberg-Martin et al., 2010).

To further address this idea, I trained TH-Cre mice expressing a novel genetically encoded calcium indicator jGCaMP7f (Dana et al., 2018) in the DRN^{DA} neurons for classical conditioning tasks. While freely moving inside an operant chamber, mice were presented with two auditory tones as conditioned stimuli (CS; 5 kHz beeping at 4 Hz or continuous white noise) and salience or valence of these CS was manipulated by pairing with positive, negative, or neutral outcome at different stages. In the first stage, mice underwent

"appetitive learning" phase where tone A was paired with 5% sucrose water delivery (50 uL per trial) and tone B had no outcome (Figure 1A). Across repeated sessions, mice fully learned the association between tone A and reward, as demonstrated by increased anticipatory licks (licking after CS onset and even before reward is available) in response to reward-predicting tone A over neutral tone B (Figure 1B). After appetitive learning phase, mice underwent "aversive learning", where tone A no longer predicted sucrose water delivery and tone B signaled the delivery of aversive footshocks (0.4 mA for 1 sec; Figure 1C). Mice were able to learn the shifts in valence of CS and appropriately responded to it, showing increased freezing behavior to tone B over now-neutral tone A (Figure 1D). Finally, mice underwent "extinction learning" phase, where salience or valence of both tone A and tone B was removed by pairing with no outcome.

Across the three separate stages of classical conditioning tasks, motivational valence and salience of CS were modulated, which have no intrinsic values before associative learning (i.e., auditory tones do not trigger any type of response or motivated behavior). For example, originally neutral tone A became salient and positive in valence after appetitive learning and later became neutral after aversive learning and extinction (Figure 1). Tone B was neutral until appetitive learning phase but became salient and negative in valence after aversive learning and later became neutral again across extinction (Figure 1). It has been shown that valence-encoding lateral VTA^{DA} or medial SNc^{DA} neurons develop positive, phasic responses to reward-predicting cues and reward itself, while showing inhibition or suppression of firing upon punishment or predicting cues (Schultz et al., 1997; Bromberg-Martin et al., 2010; Cohen et al., 2012). I hypothesized that, if DRN^{DA} neurons neurons are

functionally distinct from valence-encoding DA neurons and indeed signal motivational salience, it would develop positive responses to both reward- and punishment-predictive cues across learning.

Before learning occurs (1st session of appetitive conditioning), DRN^{DA} neuronal responses to both CS types were present but small, and their amplitude increase was not differentiable until mice consumed delivered sucrose water after predictive cues and showed robust fluorescence increase (Figure 2A), consistent with the previous finding that DRN^{DA} activity increased during reward consumption (Cho et al., 2017). Across appetitive learning, reward-predicting cues (tone A) developed phasic, positive response, while no-outcome cues (tone B) elicited negligible fluorescence change (Figure 2B). Reward consumption-related DRN^{DA} fluorescence increase was also present, but its amplitude was smaller than predictive cue response (Figure 2B). After aversive learning, however, the fluorescence amplitude of tone A, which predicted no outcome at this stage, was greatly diminished, while punishment-predicting tone B developed sustained, positive response, as well as phasic fluorescence increase upon footshock delivery (Figure 2C; Cho et al., 2017). After extinction where both of CS types predicted no outcome and their valence became neutral, DRN^{DA} response to those cues were almost completely abolished (Figure 2D). Quantification of CS-evoked DRN^{DA} dynamics at each stage indicated that DRN^{DA} neurons developed cue responses only when they are paired to both positive and negative outcomes (Figure 2E). This suggests that DRN^{DA} neurons track the dynamic nature of motivational salience attributed to environmental cues, rather than specific valence.

4.3 DRN^{DA} neurons encode unsigned prediction error

One of the key features in DA signaling is that ventral midbrain DA neurons encode reward prediction error (RPE), calculating the difference between the reward and its prediction (Schultz et al., 1997). In other words, unexpected reward elicits enhanced DA neuronal firing (positive prediction error), a fully predicted reward induces small or no response, and the omission of an expected reward produces a depression or inhibition of firing (negative prediction error). RPE serves as a key mechanism for reinforcement learning by monitoring error between prediction and outcome and providing feedback update (Schultz, 2016). RPE encoding in VTA^{DA} neurons was also shown to play causal roles in cue-reward learning in rodents (Steinberg et al., 2013).

Whether RPE encoding property is generalizable to or different in other DA populations in the brain remains largely unknown. To address this question, I performed prediction error experiments during fiber photometry recordings of DRN^{DA} neurons in $DRN^{DA\text{-}jGCaMP7f}$ mice, after they fully learned the association between cues and positive or negative outcome. After appetitive learning phase, mice underwent reward prediction error experiments where reward was provided after predictive cue (“expected”, 10 trials per session), but in some cases, reward became available without any predictive cues in a randomized order (“unexpected”, 5 trials per session; Figure 3A). Similarly, after aversive learning phase, mice underwent punishment prediction error experiments, where unpredicted footshocks were given without cues (3 trials per session; first, second and last) as well as normal CS-shock paired trials (10 trials; Figure 3A). It is hypothesized that

unexpected reward and punishment would carry stronger salience than expected ones, even though the amount of reward or the current amplitude of footshock was kept identical (Figure 3B).

Similar to RPE-encoding ventral midbrain DA neurons (Schultz et al., 1997), DRN^{DA} neurons also demonstrated positive prediction error dynamics for reward: unexpected reward consumption elicited higher DRN^{DA} fluorescence than expected consumption after predictive cues (Figure 3C). Interestingly, DRN^{DA} neurons showed similar encoding strategy for punishment: unexpected footshock induced higher DRN^{DA} fluorescence than expected ones delivered after predictive cues. These results indicate that DRN^{DA} neurons signal unsigned prediction error, showing higher neural activity towards unexpected salient events.

As RPE-encoding DA neurons also show negative prediction error where they show depression of neural activity below the baseline for unexpectedly omitted reward (Schultz et al., 1997), I have also performed unexpected omission experiments for both reward and punishment during photometry recording of DRN^{DA} neurons. In "unexpected reward omission" experiment, reward-predictive cues were turned on to signal sucrose water, but its delivery was omitted in a few, random-ordered trials (5 out of 15 total trials; Figure 4A). Photometry recordings demonstrated that, in expected trials, there were robust DRN^{DA} fluorescence increase for both CS and sucrose consumption, similar to "after appetitive learning" (Figure 2B). However, when reward was omitted, CS-evoked DRN^{DA} neural activity slowly decayed back to the baseline level, showing no evidence of reduced firing

or inhibition below the baseline (Figure 4B). Similarly, in "unexpected footshock omission" experiment (Figure 4C), CS-induced DRN^{DA} fluorescence slowly decreased down to the baseline level when shocks were unpredictably omitted (Figure 4D). As it was demonstrated that slow Ca^{2+} kinetics from GCaMP6 can also report inhibition-related depression upon unexpected reward omission in VTA^{DA} neurons (Saunders et al., 2018), these results suggest that DRN^{DA} neurons may not encode negative prediction error for salient stimuli with suppression of neural activity like classically described RPE-encoding neurons.

4.4 DRN^{DA} neurons are modulated by internal motivational state

Motivational salience attributed to environmental cues can be dynamic in nature. In other words, the same objects can be perceived less (or more) salient depending on animal's need or motivational state. For example, salience of water or food is contingent on the animal's internal state: if thirsty or hungry, they perceive it as highly salient, which may drive approach behavior for consumption. But when fully sated, they may not perceive it as motivationally salient and simply ignore it. Related to this question, I asked whether DRN^{DA} neuronal response to motivational salience can be modulated by internal motivational state or physiological need.

After appetitive learning phase in classical conditioning experiments (Figure 1A), mice underwent the half of appetitive conditioning sessions (tone A predicted reward delivery and tone B predicted no outcome) when thirsty and later completed the other half after fully sated (Figure 5A). To induce satiety in animals, mice were given free access to regular and sucrose water for three hours in-between. It is hypothesized that same reward cues (tone A) may be perceived less motivationally salient to animals when sated (Figure 5B), manifested as less reward consumption in behavior and less activated DRN^{DA} fluorescence to reward-predicting cues.

Indeed, mice were highly motivated to obtain reward only when they were thirsty (Figure 5C and 5D): they even showed baseline licks (0.5~1 Hz) before any cues were available. They could discriminate reward-predicting tone A to neutral tone B, showing increased

anticipatory licks only to reward-predictive CS. After satiety, baseline licking was absent and mice no longer showed anticipatory licks in response to reward-predictive cues. Mice consumed reward only in a subset of trials in satiety condition, showing slightly increased lick rate well after sucrose water was available. Overall, motivated behavior (anticipatory licks in response to reward-predicting cues) was greatly reduced from thirsty to sated state (Figure 5D).

At the neuronal level, DRN^{DA} responses to reward-predicting cues and reward consumption were present in both conditions, but the CS-evoked DRN^{DA} fluorescence was significantly diminished when mice were sated (Figure 5E and 5F). On contrary, DRN^{DA} response to nothing-predicting tone B was absent and not different across two conditions. These behavioral and neuronal data suggest that motivational salience of same environmental cues can be modulated by animal's internal state or physiological need, and DRN^{DA} neuronal response can faithfully follow the changed perception of motivational salience.

4.5 Future directions

Fiber photometry recordings during classical conditioning and prediction error experiments suggest that DRN^{DA} neurons encode or signal motivational salience, rather than valence or value. While this finding is novel and complements on the recently described functional heterogeneity of DA system, one natural weakness of this data is that fiber photometry records the bulk fluorescence from all GCaMP-expressing neurons under the optical fiber, providing the neuronal dynamics only at the population level. Therefore, potential heterogeneity within DRN^{DA} populations, if any, cannot be addressed with this method. There can be multiple scenarios on what may occur at the single-cell level (Figure 6A): for example, most of individual, responsive DRN^{DA} neurons may fire in synchronized manner and behave like its population sum. It is equally plausible that DRN^{DA} neurons are divided into two functional clusters, one signaling positive valence and another promoting negative valence. Alternatively, salience- and valence-encoding DA neurons can be intermingled within DRN populations. All of these scenarios can lead to same qualitative results in population recordings as I have observed. To address these possibilities, it is required to optically record DRN^{DA} neurons at the single-cell level with surgically implanted gradient index (GRIN) lens and multi-photon microscope (Otis et al., 2017; McHenry et al., 2017).

To achieve this goal, my lab and Dr. Daniel Wagenaar at the Caltech Neurotechnology Center worked together to build a customized two-photon microscope (Figure 6B). To image single DRN^{DA} neurons, Cre-dependent adeno-associated virus encoding GCaMP6m

(Chen et al., 2013) was injected into the DRN of TH-Cre mice and GRIN lens was implanted (0.5 mm diameter, 8.4 mm length, Inscopix; with 25-degree angle from lateral side; Figure 6C). Mice were habituated to the head-fixation setup while waiting for optimal GCaMP6m expression. Individual DRN^{DA} neurons could be visualized with this method and fluorescence traces for each cell could be extracted from manually hand-drawn region of interest (Figure 6D). Preliminary data showed that majority of recorded DRN^{DA} neurons respond positively to un-cued delivery and consumption of sucrose water (Figure 6E). Immediate future plan with this single-cell resolution imaging technique is to perform same classical conditioning procedures (Figure 1) while maintaining the same field of view, in order to investigate the encoding properties (whether they signal salience or certain valence) of DRN^{DA} neurons at the single-cell level. It is also of interest to examine how DRN^{DA} neurons can modulate downstream neuronal processing in the extended amygdala regions. It would be viable to record individual neurons in the central amygdala or the bed nucleus of stria terminalis where DRN^{DA} neurons heavily project to (Matthews et al., 2016; Cho et al., 2017) and investigate how they respond to salient stimuli, while modulating DRN^{DA} neurons with optogenetics or chemogenetics. Those experiments are forthcoming and will help disclose original and novel insights on how salience-signaling DRN^{DA} neurons affect circuit dynamics in the downstream forebrain regions and effectively promote the appropriate behavioral response to salient stimuli.

4.6 Figures

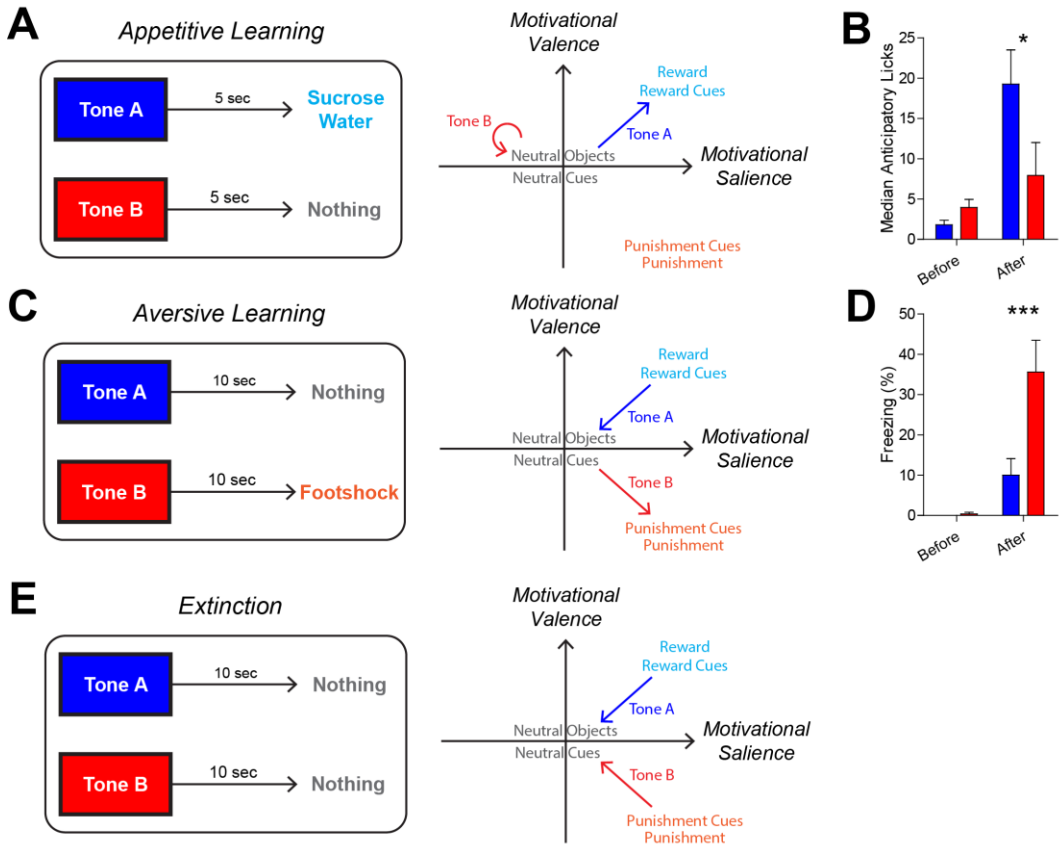

Figure 1. Classical conditioning procedures. (A) At the first stage, mice underwent appetitive learning where auditory tone A predicted the delivery of 5% sucrose water 5 seconds after onset and tone B was paired with no outcome. Therefore, tone A became motivationally salient (x-axis) and positive in valence (y-axis), while tone B remained neutral. **(B)** After learning, mice were able to discriminate reward-predicting cues from nothing-predicting cues by showing increased anticipatory licks to tone A over tone B (n = 5 $DRN^{DA\text{-}jGCaMP7f}$ mice; two-way repeated measures ANOVA revealed trend in interaction, $F = 4.583$ and $p = 0.0647$, and significance in time effect, $F = 11.54$ and $p = 0.0094$. Post-hoc Bonferroni tests, $*p < 0.05$). **(C)** After appetitive learning, mice

underwent aversive learning phase where tone A (previously paired with sucrose water) no longer had outcome and tone B predicted the delivery of a footshock (0.4 mA, 1 sec) after 10 seconds of cue presentation. Therefore, tone A was reduced in both salience and valence dimensions and became neutral, while tone B became salient and negative in valence. **(D)** After aversive learning, mice were able to discriminate aversive shock-predicting cues over neutral cues by showing increased freezing to tone B, which was paired with footshocks (n = 5 $DRN^{DA\text{-}jGCaMP7f}$ mice; two-way repeated measures ANOVA revealed significance in interaction, $F = 10.41$ and $p = 0.0121$, and in time effect, $F = 32.15$ and $p = 0.0005$. Post-hoc Bonferroni tests, ***$p < 0.001$). **(E)** Finally, mice underwent extinction learning where both of tone A and B predicted no outcome. By extinction, both salience and valences of tone A and B became close to zero or neutral.

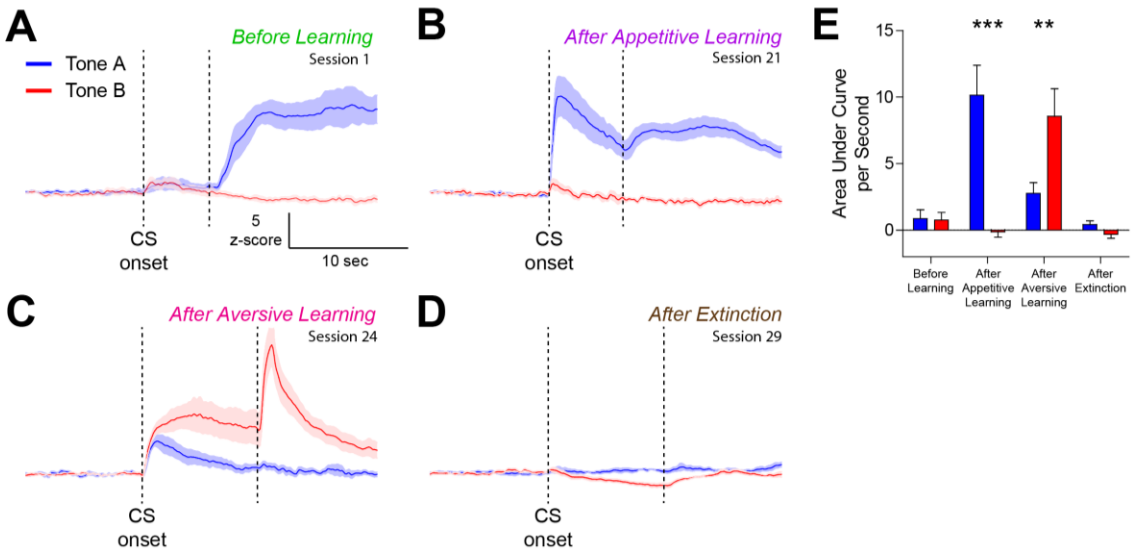

Figure 2. DRN^{DA} dynamics during classical conditioning. (A) Before learning, both tone A (blue) and tone B (red) showed only small, non-differentiable increase of DRN^{DA} activity from the baseline after conditioned stimuli (CS) onset (first dashed line). DRN^{DA} fluorescence was increased upon reward consumption (second dashed line) only after tone A. **(B)** After appetitive learning, DRN^{DA} neurons showed positive, phasic response to reward-predicting tone A, but showed negligible response to tone B paired with no outcome. Reward consumption-related response was also observed. **(C)** After aversive learning, DRN^{DA} neurons showed higher and more positive response to shock-predicting tone A than now nothing-predicting tone A. Strong phasic response was recorded upon the delivery of footshocks after tone B. **(D)** After extinction, DRN^{DA} neurons did not show significant responses for both tones, although there was small negative activity to tone B which was previously paired to punishment. **(E)** Quantification of cue (tone) responses with calculating the area under curve (AUC, per second) showed that DRN^{DA} neurons developed significantly enhanced responses to reward-predicting cues after appetitive

learning and to punishment-predicting cues after aversive learning, both significantly higher than pre-learning or after extinction (n = 5 $DRN^{DA\text{-}jGCaMP7f}$ mice; two-way repeated measures ANOVA revealed significance in interaction, $F = 15.78$ and $p < 0.0001$, and in time effect, $F = 11.63$ and $p < 0.0001$. Post-hoc Bonferroni tests, ***$p < 0.001$, **$p < 0.01$).

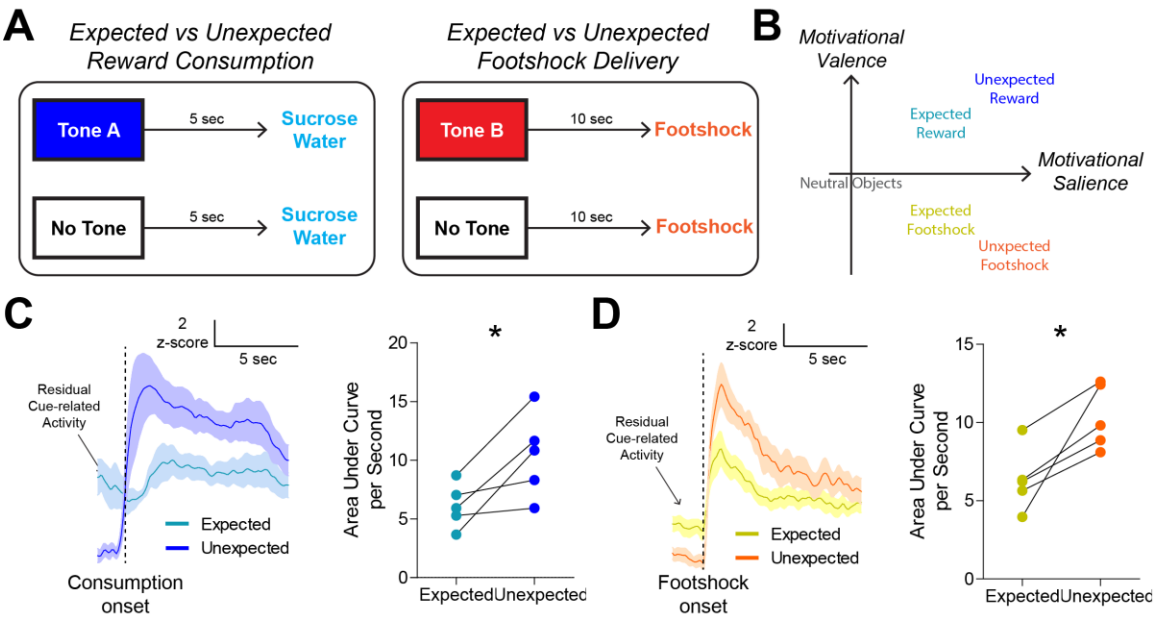

Figure 3. DRN^{DA} neurons encode unsigned prediction error. (A) Procedures for prediction error experiment. *Left*; After appetitive learning, reward prediction experiment was performed: while reward-predicting tone A was turned on to signal reward delivery, same amount of sucrose water was delivered without any predictive cues in a few random trials. *Right*; After aversive learning, punishment prediction experiment was performed: while punishment-predicting tone B was turned on to trigger footshock delivery, same footshock was delievered without any predictive cues in a few random trials. **(B)** Prediction error experiments enables comparison of DRN^{DA} neuronal response to expected and unexpected outcomes. It is hypothesized that unexpected reward or punishment (without predictive cues) is more salient and also stronger (more positive or more negative) in a valence dimension. **(C)** *Left*; DRN^{DA} response to unexpected rewards (darker blue) was larger than that to fully expected rewards (lighter blue), when aligned to consumption or lick onset. The last five trials were analyzed for expected condition. *Right*; the quantification of AUC confirmed that DRN^{DA} response to unexpected rewards was

significantly larger than that to expected rewards (n = 5 $DRN^{DA\text{-}jGCaMP7f}$ mice; paired t-test, $t_4 = 3.091$, $p = 0.0365$. *$p < 0.05$). **(D)** *Left*; DRN^{DA} response to unexpected punishment (orange) was larger than that to fully expected punishment (yellow). Last five trials were analyzed for expected condition. *Right*; the quantification of AUC confirmed that DRN^{DA} response to unexpected footshock was significantly higher than that expected (n = 5 $DRN^{DA\text{-}jGCaMP7f}$ mice; paired t-test, $t_4 = 3.586$, $p = 0.0230$. *$p < 0.05$).

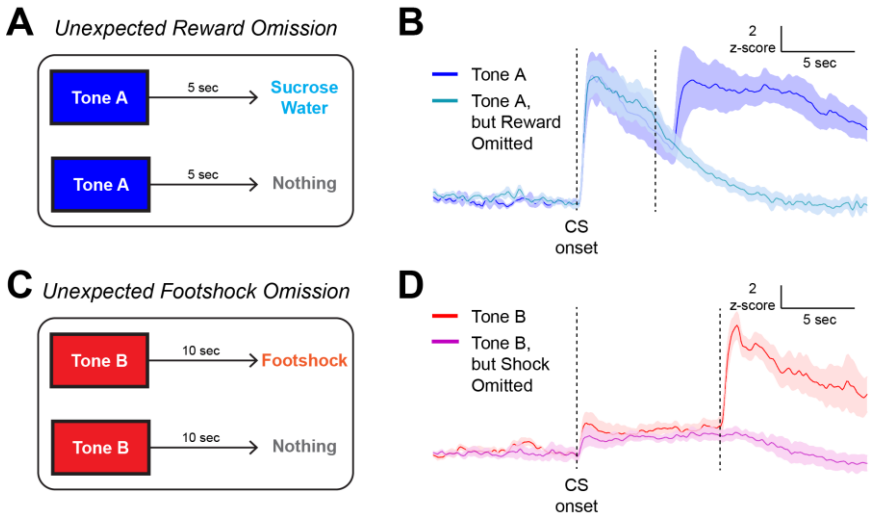

Figure 4. DRN^{DA} response to unexpected omission. (A) In unexpected reward omission experiments after appetitive learning, tone A was turned on to predict the delivery of sucrose water as expected. In some trials, however, tone A was turn on without outcome and reward delivery was omitted. **(B)** DRN^{DA} response to unexpected reward omission. Tone A elicited non-differentiable, positive cue responses to both cases. When reward was delivered as expected, mice consumed it and DRN^{DA} activity was increased. When it was unexpectedly omitted, DRN^{DA} fluorescence slowly converged to baseline. Last five trials were analyzed for expected condition. **(C)** In unexpected punishment omission experiments after aversive learning, tone B was turned on to predict the delivery of a footshock. In some trials, however, tone B was turn on but footshock delivery was omitted. **(D)** DRN^{DA} response to unexpected footshock omission. Tone B elicited non-differentiable, positive cue responses to both cases. When footshock was delivered as expected, DRN^{DA} activity was sharply increased. When it was unexpectedly omitted, DRN^{DA} fluorescence slowly went back down to baseline. Last five trials were analyzed for expected condition.

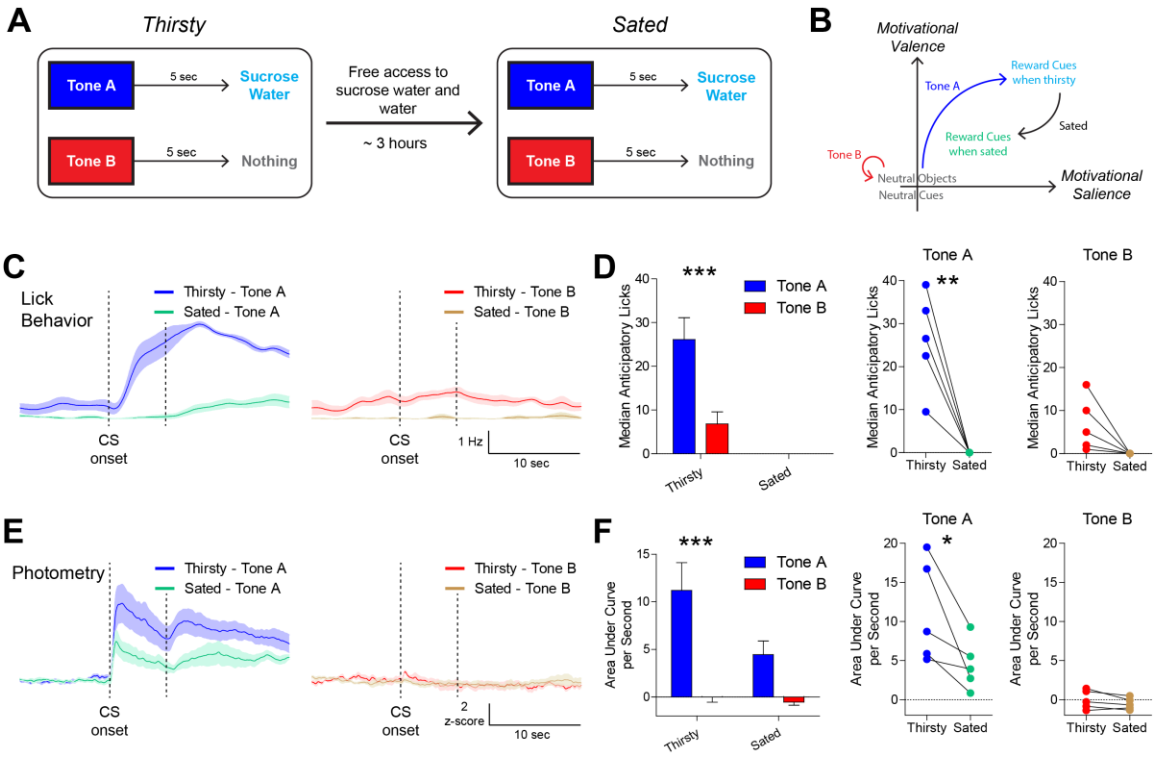

Figure 5. DRN^{DA} response to reward-predicting cues can be modulated by internal motivational state. (A) To examine if DRN^{DA} response can be affected by internal state or physiological needs, appetitive conditioning sessions were separately performed first during thirsty state and later during sated state. **(B)** It is hypothesized that reward cues can be perceived more saliently when mice are thirsty compared to sated as they are more motivated to consume reward after predictive cues. **(C)** Behavioral (lick) data with respect to cue (tone) onsets. When thirsty (blue on left for tone A, red on right for tone B), mice demonstrated increased baseline licks before CS onset and showed anticipatory licks only after reward-predicting tone A. After satiety, baseline licks (green on left for tone A, brown on right for tone B) or anticipatory licks were no longer observed. **(D)** Quantification of lick behavior. *Left*; Anticipatory licks were present when thirsty and were increased for reward-predicting tone A over nothing-predicting tone B (n = 5 DRN$^{DA\text{-}jGCaMP7f}$ mice; two-

way repeated measures ANOVA revealed significance in interaction, $F = 11.33$ and $p < 0.0098$, and in time effect, $F = 32.93$ and $p = 0.0004$. Post-hoc Bonferroni tests, ***$p < 0.001$). *Middle*; Anticipatory licks to tone A was significantly increased when thirsty than sated (n = 5 $DRN^{DA\text{-}jGCaMP7f}$ mice; paired t-test, $t_4 = 5.206$, $p = 0.0065$, **$p < 0.01$). *Right*; Anticipatory licks to tone B was not different from two conditions (n = 5 $DRN^{DA\text{-}jGCaMP7f}$ mice; paired t-test, $t_4 = 2.444$, $p = 0.0709$). **(E)** DRN^{DA} dynamics to cues during thirst and satiety. DRN^{DA} response to reward-predicting tone A became smaller after satiety. There was no difference in DRN^{DA} response to tone B with no outcome. **(F)** Quantification of photometry data. *Left*; DRN^{DA} fluorescence to tone A was significantly increased during thirst compared to satiety (n = 5 $DRN^{DA\text{-}jGCaMP7f}$ mice; two-way repeated measures ANOVA revealed significance in interaction, $F = 6.875$ and $p < 0.0306$, and in time effect, $F = 9.384$ and $p = 0.0155$. Post-hoc Bonferroni tests, ***$p < 0.001$). *Middle*; DRN^{DA} response to tone A was significantly higher while thirsty compared to sated (n = 5 $DRN^{DA\text{-}jGCaMP7f}$ mice; paired t-test, $t_4 = 2.865$, $p = 0.0457$, *$p < 0.05$). *Right*; DRN^{DA} response to tone B was not different between two conditions (n = 5 $DRN^{DA\text{-}jGCaMP7f}$ mice; paired t-test, $t_4 = 1.790$, $p = 0.1479$).

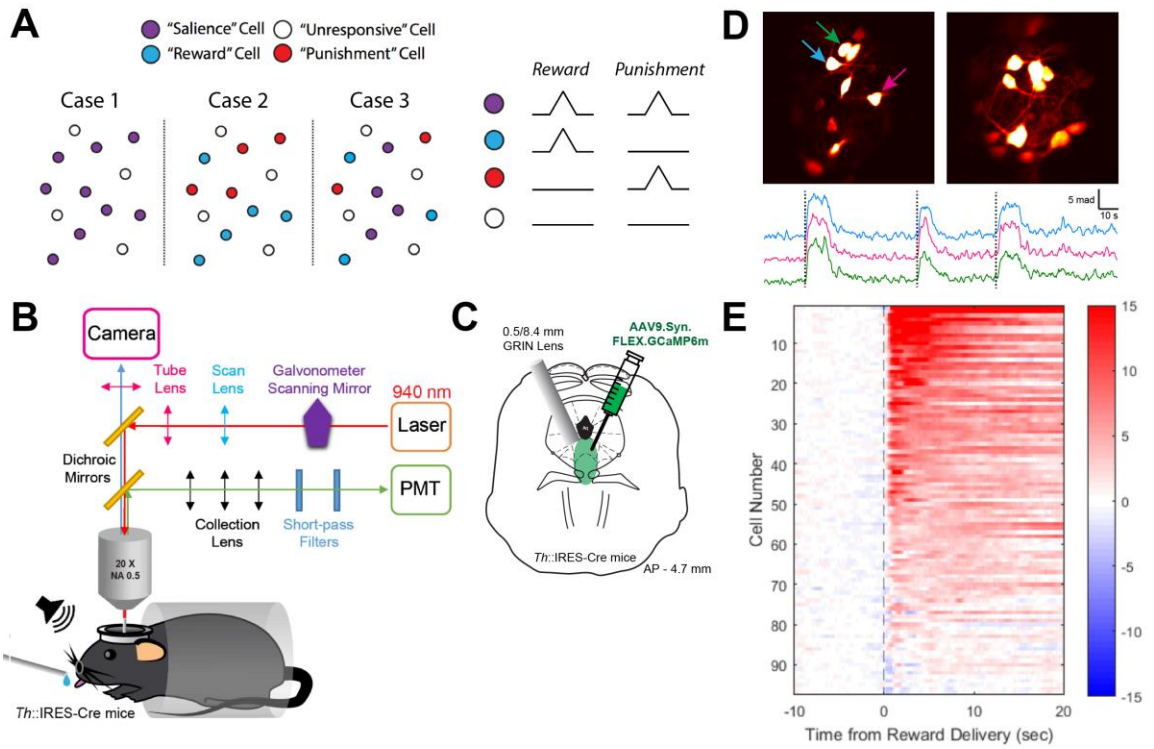

Figure 6. Deep brain two-photon imaging of DRN^{DA} neurons at the single cell level. **(A)** While DRN^{DA} neurons track motivational salience at the population level, single cell correlates could be diverse. In case 1, most of responsive DRN^{DA} neurons encode salience similar to its population sum. In case 2, DRN^{DA} neurons are divided into two functional groups tune to opposite valence. In case 3, salience- and valence-encoding cells are intermingled. **(B)** Schematic of two-photon microscope and imaging when a mouse is head-fixed under the objective. **(C)** Schematic of GRIN lens surgery for two-photon imaging. Cre-dependent AAV carrying GCaMP6m was stereotaxically injected into the DRN and GRIN lens is implanted. **(D)** Representative fields of view (standard deviation projection map) from 2 DRN$^{DA\text{-}GCaMP6m}$ mice. Fluorescence traces from three arrowed neurons were extracted. Vertical lines indicate sucrose water delivery. (E) Majority of DRN^{DA} neurons

(74.2%, 72 out of 97 cells from 7 $DRN^{DA\text{-}GCaMP6m}$ mice) were significantly activated from baseline (paired t-test, FDR correction, significance at $q < 0.05$).

4.7 Reference

Bromberg-Martin, E.S., Matsumoto, M., and Hikosaka, O. (2010). Dopamine in motivational control: rewarding, aversive, and alerting. Neuron 68, 815–834.

Chen, T.W., Wardill, T.J., Sun, Y., Pulver, S.R., Renninger, S.L., Baohan, A., Schreiter, E.R., Kerr, R.A., Orger, M.B., Jayaraman, V., et al. (2013). Ultrasensitive fluorescent proteins for imaging neuronal activity. Nature 499, 295–300.

Cho, J.R. et al. (2017). Dorsal Raphe Dopamine Neurons Modulate Arousal and Promote Wakefulness by Salient Stimuli. Neuron 94, 1205–1219.e8.

Cohen, J.Y., Haesler, S., Vong, L., Lowell, B.B., and Uchida, N. (2012). Neuron- type-specific signals for reward and punishment in the ventral tegmental area. Nature 482, 85–88.

Dana, H. et al (2018). High-performance GFP-based calcium indicators for imaging activity in neuronal populations and microcompartments. bioRxiv 434589.

McHenry, J.A. et al. (2017). Hormonal gain control of a medial preoptic area social reward circuit. Nat Neurosci. 20(3), 449-458.

Otis, J.M. et al. (2017). Prefrontal cortex output circuits guide reward seeking through divergent cue encoding. Nature 543(7643), 103-107.

Saunders, B.T., Richard, J.M., Margolis, E.B., Janak, P.H. (2018). Dopamine neurons create Pavlovian conditioned stimuli with circuit-defined motivational properties. Nat Neurosci. 21(8), 1072-1083.

Schultz, W., Dayan, P., Montague, P.R. (1997). A neural substrate of prediction and reward. Science 275(5306), 1593-9.

Schultz, W. (2016). Dopamine reward prediction error coding. Dialogues Clin. Neurosci. 18(1), 23-32.

Steinberg, E.E. et al. (2013). A causal link between prediction errors, dopamine neurons and learning. Nat Neurosci. 16(7), 966-73.